Attosecond dynamics of collective electron effects in nanostructures and molecules

Benjamin Förg

München 2017

Attosecond dynamics of collective electron effects in nanostructures and molecules

Benjamin Förg

Dissertation
an der Fakultät für Physik
der Ludwig–Maximilians–Universität
München

vorgelegt von
Benjamin Förg

München, den 06.12.2017

Erstgutachter: Prof. Dr. Matthias Kling
Zweitgutachter: PD. Dr. Vladislav Yakovlev
Tag der mündlichen Prüfung: 23. Januar 2018

Zusammenfassung

In der vorliegenden Arbeit werden mehrere zeitaufgelöste, experimentelle Studien über die Dynamik kollektiver Elektronenphänomene vorgestellt. Im ersten Teil der Messungen wird versucht, die Dynamik von Oberflächenplasmonen (SPP) offenzulegen, die als kohärente Anregung an Grenzflächen zwischen Metallen und Dielektrika in Erscheinung treten. Die Experimente nutzen ein Pump-Probe Schema, wobei der Pumppuls einen wenige Zyklen umfassenden Laserpuls im nah-infraroten Spektralbereich darstellt, der die SPPs an einem nanostrukturierten Gitter erzeugt. Ausgehend vom Gitter breiten sich die SPPs in Richtung einer Nanospitze aus, an der das elektrische Feld der Plasmonen adiabatisch fokussiert und eingegrenzt wird. Mit einem zweiten, zeitlich verzögerten Laserpuls, der im Folgenden als Probepuls bezeichnet ist und eine direkte Kopie des Pumppulses darstellt, wird das elektrische Feld der SPPs untersucht. Die Überlagerung des elektrischen SPP-Feldes mit dem Probepuls führt zur Multi-Photonen Ionisation (MPI) der metallischen Probe. Aus der Ionisationsrate, die von der zeitlichen Verzögerung zwischen Pump- und Probepuls abhängt, ergibt sich die Dynamik von SPP und Probepuls als Faltung beider elektrischer Felder.

Um eine zeitliche Auflösung auf der Attosekunden-Zeitskala ($1\,\mathrm{as} = 10^{-18}\,\mathrm{s}$) zu ermöglichen, wurden weiterführende Untersuchungen durchgeführt, die die Anwendbarkeit des Attosekunden Streakings bei nanoskaligen elektrischen Feldern demonstrieren. Die Pilotexperimente wurden an konisch verjüngten Gold (Au) Nanodrähten durchgeführt. Dabei wurden die Proben von einem wenige Zyklen umfassenden Laserstrahl im nah-infraroten Spektralbereich beleuchtet, wodurch aus der Überlagerung von einfallendem und gestreutem Laserstrahl ein charakteristisches Nahfeld entsteht. Ein synchronisierter Attosekundenlaserstrahl im extremen ultravioletten (XUV) Spektralbereich führt zur Emission von Photoelektronen vom Nanodraht. Nach Propagation durch das elektrische Nahfeld wurde die kinetische Energie der Photoelektronen gemessen, die grundsätzlich von der zeitlichen Verzögerung zwischen XUV und NIR Laserstrahl abhängt. Im aufgenommen Spektrogramm der Photoelektronen zeigt sich die eindeutige Signatur des Nahfeldes, das im Vergleich zum einfallenden NIR Laserstrahl phasenverschoben erscheint. Die experimentellen Ergebnisse werden durch theoretische Simulationen, die die spezifische Probengeometrie berücksichtigen, unterstützt. Basierend auf Trajektorien Rechnungen, werden allgemeingültige Bedingungen an den experimentellen Aufbau sowie die Probengeometrie formuliert, unter denen die Untersuchung von nanoskaligen elektrischen Feldern möglich ist.

Der dritte Teilbereich der Experimente untersucht den fundamentalen Einfluss kollektiver Elektroneneffekte auf die zeitliche Verzögerung der Photoionisation von gasförmigen Ethyliodidmolekülen unter Anwendung der Attosekunden Streaking-Methode. Die Photonenenergie des XUV Pulses wurde dabei so gewählt, dass die Ionisation im Bereich der Riesenresonanz der 4d-Elektronenschale des Iods erfolgt. Die Experimente, die bei verschiedenen XUV Photonenenergien durchgeführt wurden, offenbaren einen deutlichen Anstieg der Verzögerung der Photoionisation in Richtung niedrigerer XUV Energien. Um die zeitliche Verzögerung zu erklären, werden unterschiedliche theoretische Ansätze verfolgt, wobei semi-klassische, *ab initio* und Quanten-Streurechnungen durchgeführt werden. Neben den kollektiven Elektroneneffekten werden auch mögliche Einflüsse der Molekülorbitale diskutiert.

Abstract

In this work several time-resolved experimental studies on collective electron phenomena are presented. The first set of measurements aims to reveal the dynamics of surface plasmon polaritons (SPP), which emerge as coherent excitation of quasi-free conduction band electrons at a metal-dielectric-interface. The experiments employ a pump-probe scheme, where a few-cycle near-infrared (NIR) laser pulse, considered as pump beam, excites SPPs at a nanostructure grating. After propagation towards a nanoscale apex, where adiabatic focusing and localization is observed, the SPP electric field is probed by a second few-cycle laser field with variable delay, which constitutes a direct replica of the pump beam. The cross-correlation of SPP and near-infrared probe beam at the apex facilitates multi-photon ionization (MPI) from the metal sample and allows to obtain the convoluted temporal dynamics of both electric fields from the delay-dependent photoionization yield.

To achieve temporal resolution on the attosecond ($1\,\mathrm{as} = 10^{-18}\,\mathrm{s}$) scale, consecutive studies are performed to demonstrate the applicability of the attosecond streaking technique to nanoscale electric near-fields. These proof-of-principle measurements are conducted on tapered gold (Au) nanowires, which are illuminated by a few-cycle near-infrared laser pulse. The superposition of incident and scattered laser field gives rise to a characteristic near-field at the streaking target surface. A synchronized, extreme-ultraviolet (XUV) laser pulse of attosecond temporal duration generates photoelectrons from the target, whose final kinetic energy is modulated whilst propagating through the electric near-field. Acquisition of delay-dependent photoelectron energy spectra unambiguously shows the signature of the nanoscale near field, which appears phase shifted relative to the incident laser field. Experimental findings are supported by theoretical simulations, which consider the specific target geometry. Based on trajectory calculations, generic prerequisites on the experimental setup and target geometry are formulated to facilitate sampling of nanoscale electric fields with attosecond temporal resolution.

In the third set of experiments, the fundamental influence of collective electron effects on photoionization delays is investigated using the attosecond streaking technique on gaseous ethyl iodide molecules. Here, the photon energy of the extreme-ultraviolet radiation is chosen to overlap with the giant dipole resonance of the 4d shell in atomic iodine. The resulting photoionization delays are referenced by a simultaneous streaking measurement on atomic neon. The experiments, performed at different XUV photon energies, reveal a drastic increase of photoionization delays with decreasing XUV photon energy. To explain the observed temporal delays, simulations at different levels of theory are performed, including *ab initio*, quantum scattering and semi-classical calculations. Besides collective electron effects, the influence from molecular orbitals on the obtained photoionization delays is discussed.

Contents

List of Figures

List of Tables

Chapter 1

Introduction

Interactions of electrons, amongst each other or with their surrounding, are underlying a plethora of physical processes and thereby determine the macroscopically observed features in all states of matter. Optical transmission and reflectivity, magnetism or thermal and electrical conductivity name only a few characteristics, which are to a large extent established by the electronic properties of materials. Even beyond, electron interactions govern the formation, transition and break-up of chemical bonds, which, as a result, have profound implications on biological processes. Accordingly, microscopic understanding of electron interactions is highly desirable and crucial for technical developments in various disciplines, ranging from electrical engineering and material science to chemistry and life science. Firm insight into electron interactions demands investigation on their natural spatial and temporal scales, which involves characterization on the Angstrom ($1\,\text{Å} = 10^{-10}\,\text{m}$) and attosecond ($1\,\text{as} = 10^{-18}\,\text{s}$) level. Spatial resolution down to the sub-nanometer range is reliably achieved by numerous instrumentations, e.g. atomic force microscope (AFM) and transmission or scanning electron microscope (TEM, SEM). The ability to resolve dynamics on the attosecond temporal scale was gained only less than two decades ago, marking the advent of attosecond physics [1], which led subsequently to the development of experimental and theoretical tools [2, 3] required for a self-contained attosecond metrology [4, 5].

The generation of high-harmonic radiation from intense near-infrared, few-cycle laser fields by Macklin *et al.* [6] forms the cornerstone for the research field of attosecond physics and led to the first experimental demonstration of ultrashort laser pulses with attosecond duration [7]. While the latter observation involves pulse trains, the realization of isolated attosecond pulses by Hentschel *et al.* [4] initiated the implementation of the attosecond streak camera [8], which allows pump-probe-measurements with unprecedented temporal resolution. Besides the full characterization of attosecond [9] and few-cycle laser pulses [10] in the time domain, the attosecond streaking technique was likewise applied to investigate electron dynamics in various physical processes including Auger decay [11], tunneling [12, 13], photoionization from gaseous [14] or solid state targets [15–17] and electronic transport or screening effects in solids [18].

Based on the findings from previous experimental studies, which are considerably well explained in the single active electron approximation (SAE), the focus of time-resolved measurements moves gradually to more complex target systems, where the electron dynamics is strongly affected by collective electron effects. The motivation for intensified basic research on this topic is self-evident from the variety of material properties and phenomena, e.g. superconductivity [19], magnetism [20] or metal-insulator transitions [21], which derive from collective

electron interactions. As an important step in this direction, Ossiander *et al.* published recently pioneering studies on the dynamics of correlated systems, where they investigated the photoionization delay from helium atoms (He) based on the attosecond streaking approach: between photoionization from the He ground state and the photoemission from its excited (shake-up) state, Ossiander *et al.* reveal a timing difference of minimum 5 as [22], depending on the excess energy of emitted photoelectrons. This finding is in perfect agreement with theoretical predictions from *ab initio* simulations [23].

In this thesis pump-probe-measurements on nanostructures and molecules are conducted, aiming to investigate the dynamics of collective electron interactions in the respective target system. Especially in case of nanostructured sample geometries, a growing interest in time-resolved studies is perceptive, apparent from the multitude of recent experimental and theoretical reports (see e.g. Refs. [24, 25] for an overview). Motivation behind the growing interest in collective electron dynamics of nanostructures lies in their vast importance for technical applications: surface plasmon polaritons (SPP), emerging as collective electron excitation at the surface of metallic nanostructures, allow to confine electromagnetic radiation to nanometer dimensions [26], which is well below the diffraction limit of conventional focusing. Concomitant with the field confinement is typically a significant field enhancement, which may yield several orders of magnitude [27], depending on the respective target geometry. Based on theses features, SPPs promise to bridge the gap between different spatial scales of ultrafast photonic devices [28, 29] and conventional semiconductor circuitry [30, 31]. Merging both technologies offers the development of novel electronic devices, which link the large diversity of silicon-based circuitry with ultrafast switching speeds in the petahertz range, which is 5 - 6 orders of magnitude larger than state-of-the-art electronics. One goal of this thesis is to study the dynamics of surface plasmon polaritons in pump-probe experiments and extract its fundamental temporal properties. Even beyond, the measurements presented in this thesis aim to demonstrate experimental techniques, which facilitate the full characterization of nanoscale electric fields in the time-domain with sub-cycle resolution.

Experiments on collective electron effects in nanostructures involve several millions of atoms, which demands typically strong assumptions in theoretical calculations, while target systems, restricted to the single or few-atom limit, are generally captured to high accuracy with reduced complexity. In contrast to isolated atoms, molecular compounds allow to shape electron interactions by choosing specific constituents, which allows to verify individual facets of theoretical modeling. Accordingly, the second branch of this thesis considers attosecond streaking experiments on molecular targets to resolve its underlying electron dynamics. Generally, extensive studies on electron dynamics in molecules are motivated by the primary goal to obtain active control and the ability of steering electron processes in molecular compounds, which would have an unprecedented impact on chemistry and life sciences [32]. While the first pump-probe measurement on molecular targets with attosecond precision by Sansone *et al.* was performed on the simplest molecule H_2, subsequent experiments considered already polyatomic molecules [33, 34]. In contrast to previous reports, the measurements presented in this thesis are conducted on molecular targets, in the presence of collective electron interactions: the photoionization cross section of the ethyl iodide 4d shell is strongly enhanced for photon energies around 90 eV, which is the typical signature of a giant dipole resonance (GDR) [35], where collective electron interactions play an essential role [36]. The influence of collective electron effects on photoionization delays is conversely debated at the current stage [37, 38]. Accordingly, the attosecond streaking measurements, performed within the scope of this thesis, aim to resolve remaining discrepancies in theoretical model calculations, while residual

effects of collective electron interactions and influences from molecular constituents on fundamental photoionization delays are elaborated.

Following this introduction into the topic, chapter 2 describes the theoretical foundations and general principles of the employed measurement techniques. Details on the experimental infrastructure, including specifics on the target fabrication process, follow in chapter 3. Pump-probe-measurements on the dynamics of surface plasmon polaritons are described in chapter 4, where the findings are discussed in view of peculiarities of the experimental setup. Results on the first experimental demonstration of sub-cycle temporal characterization of nanoscale electric fields are presented in chapter 5, together with detailed theoretical simulations. Achievements on the investigation of photoionization delays from molecular targets are shown in chapter 6, where the outcome is discussed in consideration of collective electron effects and influences from molecular constituents. Finally, all results are concluded and summarized in chapter 7.

List of publications with high relevance to the results presented in this thesis

(**1**) B. Förg, J. Schötz, W. Schweinberger, L.Ortmann, T. Zimmermann, L. Pi, S. Biswas, D. Baykusheva, A. Masood, I. Liontos, A. Kamal, N. G. Kling , H.-J. Wörner, M. Alharbi, F. Krausz, A. S. Landsman, A.M. Azzeer, and M. F. Kling, "Photoemission chronoscopy for broadband resonances in molecules", *in preparation*, 2017.

(**2**) J. Schötz, B. Förg, W. Schweinberger, S. Biswas, A. Masood, I. Liontos, A. Kamal, N.G. Kling , H.-J. Wörner, M. Alharbi, F. Krausz, A. M. Azzeer, and M. F. Kling, "Attosecond Phase Optimization", *in preparation*, 2017.

(**3**) M. F. Ciappina, J. A. Pérez-Hernández, A. S. Landsman, W. A. Okell , S. Zherebtsov, B. Förg, J. Schötz, L. Seiffert , T. Fennel, T. Shaaran, T. Zimmermann, A. Chacón, R. Guichard, A. Zaïr, J. W. G. Tisch, J. P. Marangos, T. Witting, A. Braun, S. A. Maier, L. Roso, M. Krüger, P. Hommelhoff, M. F. Kling, F. Krausz and M. Lewenstein "Attosecond physics at the nanoscale", *Reports on Progress in Physics*, vol. 80, no. 5, pp. 054401, 2017.

(**4**) J. Schötz, B. Förg, M. Förster, W. A. Okell, M. Stockman, F. Krausz, P. Hommelhoff, and M. F. Kling "Reconstruction of nanoscale near fields by attosecond streaking", *IEEE Journal of Selected Topics in Quantum Electronics*, vol. 23, no. 3. pp. 1-11, 2017.

(**5**) B. Förg, J. Schötz, F. Süßmann, M. Förster, M. Krüger, B. Ahn, W. A. Okell, K. Wintersperger, S. Zherebtsov, A. Guggenmos, V. Pervak, A. Kessel, S. A. Trushin, A. M. Azzeer, M. I. Stockman, D.Kim, F.Krausz, P.Hommelhoff, and M. F. Kling, "Attosecond nanoscale near-field sampling", *Nature Communications*, vol. 7, no. 3. pp. 11717, 2016.

Other publications

(**6**) Q. Liu, P. Rupp, B. Förg, J. Schötz, F. Süßmann, W. A. Okell, J. Passig, J. Tiggesbäumker, K.-H. Meiwes-Broer, L. Seiffert, T. Fennel, E. Rühl, M. Förster, P. Hommelhoff, S. Zherebtsov, and M. F. Kling "Photoemission from Nanomaterials in Strong Few-Cycle Laser Fields", *Nano-Optics: Principles Enabling Basic Research and Applications*, pp. 283-299, 2017

(**7**) A. Schmehl, T. Mairoser, A. Herrnberger, C. Stephanos, S. Maier, B. Förg, B. Wiedemann, P. Böni, J. Mannhart, and W. Kreuzpaintner, "Design and realization of a sputter deposition system for the in situ- and in operando-use in polarized neutron reflectometry experiments", *Nuclear Instruments and Methods in Physics Research Section A*, *accepted*, 2017.

(**8**) P. Rupp, L. Seiffert, Q. Liu, F. Süßmann, B. Ahn, B. Förg, C. G. Schäfer, M. Gallei, V. Mondes, A. Kessel, S. A. Trushin, C. Graf, E. Rühl, J. Lee, M. S. Kim, D. Kim, T. Fennel, M. F. Kling, and S. Zherebtsov, "Quenching of material dependence in few-cycle driven electron acceleration from nanoparticles under many-particle charge interaction", *Journal of Modern Optics*, vol. 64, no. 10-11, pp. 993-1003, 2017.

(**9**) B. Ahn, J. Schötz, M. Kang, W. A. Okell, S. Mitra, B. Förg, S. Zherebtsov, F. Süßmann, C. Burger, M. Kübel, C. Liu, A. Wirth, E. Di Fabrizio, H. Yanagisawa, D. Kim, B. Kim, and M. F. Kling, "Attosecond-controlled photoemission from metal nanowire tips in the few-electron regime", *APL Photonics*, vol. 2, no. 3, pp. 036104, 2017.

(**10**) H. Li, N. G. Kling, B. Förg, J. Stierle, A. Kessel, S. A. Trushin, M. F. Kling, and S. Kaziannis, "Carrier-envelope phase dependence of the directional fragmentation and hydrogen migration in toluene in few-cycle laser fields", *Structural Dynamics*, vol. 3, no. 4, pp. 043206, 2016.

(**11**) B. Ahn, J. Schötz, W. A. Okell, F. Süßmann, B. Förg, S. C. Kim, M. F. Kling, and D. Kim, "Optimization of a nanotip on a surface for the ultrafast probing of propagating surface plasmons", *Optics Express*, vol. 24, no. 1, pp. 92-101, 2016.

(**12**) H. Li, A. S. Alnaser, X. M. Tong, K. J. Betsch, M. Kübel, T. Pischke, B. Förg, J. Schötz, F. Süßmann, S. Zherebtsov, B. Bergues, A. Kessel, S. A. Trushin, A. M. Azzeer, and M. F. Kling, "Intensity dependence of the attosecond control of the dissociative ionization of D_2", *Journal of Physics B: Atomic, Molecular and Optical Physics*, vol. 47, no. 12, pp. 124020, 2014.

(**13**) R. Jany, C. Richter, C. Woltmann, G. Pfanzelt, B. Förg, M. Rommel, T. Reindl, U. Waizmann, J. Weis, J. A. Mundy, D. A. Muller, H. Boschker, J. Mannhart, "Monolithically integrated circuits from functional oxides", *Advanced Materials Interfaces*, vol. 1, no.1, 2014.

(**14**) B. Förg, C. Richter, J. Mannhart, "Field-effect devices utilizing $LaAlO_3$-$SrTiO_3$ interfaces", *Applied Physics Letters*, vol. 100, no.5, pp. 053506, 2012.

Chapter 2

Theoretical Foundations

The following chapter briefly introduces the most important theoretical background underlying the experiments presented in this thesis. While the first section concentrates on the mathematical foundation of the description of ultrashort laser pulses, the second part is dedicated to laser-matter interactions, relevant for this thesis. The last part introduces attosecond metrology. In favor of a small description, typically no detailed derivations of relations are presented. More details are found in cited articles, reviews and book chapters, listed in the bibliography.

2.1 Ultrashort Laser Pulses

2.1.1 Mathematical Description

Cornerstone for the description of oscillating electric fields are Maxwell's equations [39]

$$\nabla \cdot \mathbf{D} = \rho \,, \tag{2.1a}$$

$$\nabla \cdot \mathbf{B} = 0 \,, \tag{2.1b}$$

$$\nabla \times \mathbf{E} = -\frac{\partial \mathbf{B}}{\partial t} \,, \tag{2.1c}$$

$$\nabla \times \mathbf{H} = \mathbf{J} + \frac{\partial \mathbf{D}}{\partial t} \,, \tag{2.1d}$$

which connect the electric and magnetic fields $\mathbf{E}$ and $\mathbf{H}$, dielectric displacement $\mathbf{D}$ and magnetic induction $\mathbf{B}$ with the charge and current density ρ, $\mathbf{J}$. Considering an electric laser field propagating in a homogeneous medium, no external charge or current density is present, i.e. $\rho\,, \mathbf{J} = 0$. Generally, the dielectric displacement $\mathbf{D}$ and the magnetic field $\mathbf{H}$ for homogeneous media are expressed as

$$\mathbf{D} = \epsilon_0 \epsilon \mathbf{E} \,, \tag{2.2a}$$

$$\mathbf{B} = \mu_0 \mu \mathbf{H} \,, \tag{2.2b}$$

where ϵ_0, ϵ represent the vacuum and relative permittivity and μ_0, μ yield the vacuum and relative magnetic permeability. For the propagation in vacuum, the values of relative permittivity and permeability equal one. Under consideration of Eqs. (2.2a) and (2.2b), the Maxwell equations yield the generic wave equation [40]

$$\nabla \times \nabla \mathbf{E} = \nabla(\nabla \mathbf{E}) - \Delta \mathbf{E} = -\frac{\partial^2 \mathbf{D}}{\partial t^2} \quad . \tag{2.3}$$

With the definition of the speed of light in vacuum $c_0 = 1 / \sqrt{\epsilon_0 \mu_0}$ and under consideration of Eqs. (2.1a) and (2.2a), the wave equation for transversal electric fields simplifies to

$$\left(\Delta - \frac{1}{c_0^2} \frac{\partial^2}{\partial t^2} \right) \mathbf{E}(\mathbf{r}, t) = 0 \qquad . \tag{2.4}$$

Since any electromagnetic wave in time and space must fulfill the above differential equation, the temporal evolution of laser pulses for a fixed point in space is conveniently described by a harmonic oscillation with Gaussian envelope function

$$E(t) = E_0 \cdot \exp\left[-2 \ln(2) \left(\frac{t}{\tau} \right)^2 \right] \cdot \exp\left[-\mathrm{i}\, \Phi(t) \right] \qquad , \tag{2.5}$$

where E_0 is the maximum electric field strength, τ represents the pulse duration and $\Phi(t)$ describes the generic time-dependent phase term. The absolute value of the electric field determines the laser intensity, given by $I(t) = c\, \epsilon_0\, |E(t)|^2$.

From its description in the temporal domain, the laser pulse's spectral properties are directly obtained by a Fourier transform

$$\tilde{E}(\omega) = \int_{-\infty}^{\infty} E(t) \exp\left[i\omega t \right] dt \qquad . \tag{2.6}$$

Since Gaussian functions are invariant under Fourier transformation, in the spectral domain, the laser pulse is again described by a Gaussian function given as

$$\tilde{E}(\omega) = \tilde{E}_0 \cdot \exp\left[-2 \ln(2) \left(\frac{\omega - \omega_0}{\Delta\omega} \right)^2 \right] \cdot \exp\left[i\, \Phi(\omega) \right] \qquad , \tag{2.7}$$

where $\tilde{E}_0$ and $\Delta\omega$ represent the spectral amplitude and bandwidth, ω_0 denotes the central laser frequency and $\Phi(\omega)$ describes the spectral phase. Assuming a slowly varying function, the spectral phase can be expanded into a Taylor series about the central frequency ω_0

$$\Phi(\omega) = \varphi_{\mathrm{CE}} + (\omega - \omega_0) \cdot T_g + \sum_{n=2}^{\infty} \frac{\varphi_n}{n!} \cdot (\omega - \omega_0)^n \qquad , \tag{2.8}$$

where φ_{CE} and T_g represent the carrier-envelope phase (CEP) and group delay, while the parameters φ_n denote the n-th derivative of the spectral phase at ω_0 with respect to angular frequency

$$\varphi_n = \left. \frac{\partial^n \Phi(\omega)}{\partial \omega^n} \right|_{\omega_0} \qquad . \tag{2.9}$$

The CEP can be defined for any laser pulse and its physical importance only comes into play with approaching the few-cycle regime, where the pulse terminates after only a few (typically < 3) oscillations. Accordingly, for optical wavelengths, pulse durations up to 7 fs are considered as few-cycle pulses. Since φ_{CE} describes the phase shift between the Gaussian envelope function and the harmonic oscillation of the laser pulse, the CEP affects the maximum electric field strength. Typically, field-sensitive physical processes are strongly dependent on the carrier-envelope phase. Accordingly, techniques for its measurement and control, as will be presented in Sec. 3.2.1, are essential in ultrafast laser physics.

From the temporal and spectral width, the time-bandwidth-product (TBP) can be calculated. For laser fields, described by Gaussian envelope function, where higher order phase terms are zero, the TBP yields a minimum of [40]

$$\tau \cdot \frac{\Delta\omega}{2\pi} = 0.44 \qquad . \tag{2.10}$$

Accordingly, the above relation allows to estimate the shortest possible pulse duration based on the spectral width of the laser field. Assuming a central wavelength of 800 nm, a few-cycle pulse of $\tau = 5\,\mathrm{fs}$ demands around 190 nm spectral width.

2.1.2 Temporal Characterization

Since durations of ultrashort laser pulses are commonly found in the range of femtoseconds, their direct characterization using electronic devices is not feasible. One possible approach are autocorrelation (AC) measurements, which represent a self-referenced technique, where a time-delayed replica of the laser pulse to be measured is employed to obtain the pulse duration. Both beams are spatially overlapped in a nonlinear medium, where the second harmonic (SHG) of the two input pulses is generated [41, 42]. The delay-dependent SHG intensity, i.e. the autocorrelation signal, which is detected by a photodiode is accordingly described by

$$I_{\mathrm{IAC}}(\tau) \propto \int_{-\infty}^{\infty} I(t)\, I(t-\tau) dt \qquad , \tag{2.11}$$

where τ is the delay between pulse and replica, and $I(t)$, $I(t-\tau)$ represent the intensity of the laser pulse and its replica, respectively. Based on an assumption for the temporal envelope, the pulse duration is hereafter retrieved from the width of the autocorrelation trace. Due to the high sensitivity to the assumed temporal envelope of the laser pulse, pulse durations as extracted from auto-correlation measurements are prone to large uncertainties. Additionally, the influence of higher order phase distortions is not unambiguously revealed, since AC traces are always symmetric in time.

The fringe-resolved autocorrelation (FRAC) represents an advanced technique compared to intensity autocorrelation (IAC). Experimentally obtained FRAC traces are presented in the following chapter and illustrated in Figs. 3.7 and 3.8 for measurements with the laser system used in the experiments. In fringe-resolved autocorrelators, the beampath is designed collinear and realized as Michelson interferometer, where geometrical smearing effects can be neglected [43]. The intensity of the second harmonic signal, detected by a photodiode is then determined by the electric fields of two superimposed pulses [44]

$$I_{\mathrm{F}RAC}(\tau) \propto \int_{-\infty}^{\infty} \left| \left[E(t) + E(t-\tau)\right]^2 \right|^2 dt \qquad . \tag{2.12}$$

The interference of the two laser pulses yields an oscillatory autocorrelation trace, where the oscillation period is determined by the central wavelength λ_{c} of the laser field, which is deduced from a spectral measurement. The fringe spacing in FRAC traces is given by

$$\Delta\tau_{\mathrm{fringe}} = \frac{\lambda_{\mathrm{c}}}{2\, c_0} \qquad . \tag{2.13}$$

For the known fringe spacing, the full-width at half-maximum (FWHM) of the FRAC trace is obtained by counting the number N of fringes, exceeding the half-maximum. Based on the

deconvolution factor D_{FRAC}, which takes the expected temporal envelope of the laser pulse into account (≈ 1.7 for Gaussian pulse envelopes [44]), the pulse duration τ is calculated from the number of fringes N within the FWHM range of the FRAC trace

$$\tau = \frac{N \cdot \Delta\tau_{\mathrm{fringe}}}{D_{\mathrm{FRAC}}} \ . \tag{2.14}$$

Similar to IAC and FRAC measurements, where the pulse to be measured is self-referenced to its own replica, cross-correlation measurements are conceptually identical, where two different pulses are superimposed. However, in cross-correlation measurements, the temporal envelope of one pulse must be known.

In the few-femtosecond regime, the reliable measurement of pulse durations via auto- and crosscorrelation experiments is difficult, since already small deviations in dispersion affect the pulse shapes significantly. Especially for the interferometric FRAC measurements, proper dispersion management for the individual arms is indispensable [43]. In addition, for the broad spectral width of ultrashort pulses, the phase-matching for second harmonic generation must be preserved. The latter typically demands to decrease the crystal thickness, for the price of reduced signal intensities. While theoretical considerations revealed that the full amplitude and phase information can be retrieved from iterative autocorrelation measurements [45, 46], the experimental realization, especially for ultrashort laser pulses in the few-femtosecond regime is cumbersome and the results are still prone to large error margins [47].

More sophisticated methods for retrieval of ultrashort laser pulse durations include the frequency-resolved optical gating (FROG) [48] technique and spectral phase interferometry for direct electric-field reconstruction (SPIDER) [49]. Both methods can be applied to laser pulses in the few-femtosecond regime [50, 51]. Besides the higher reliability and accuracy in the temporal characterization of ultrashort laser pulses, the main advantage of FROG and SPIDER derives from the full retrieval of the spectral phase information. Thereby higher order phase distortions can be experimentally determined which allows to undertake direct means for compensation.

2.2 Laser-Matter Interaction

2.2.1 Plamonics

Plasmonic excitations arise from the interaction between light pulses and metallic media, where delocalized electrons in the valence band respond to the oscillating electric laser field. As illustrated in full detail in Ref. [26], the dispersion relation for plasmonic excitations can be derived from Maxwell's equations, given by Eqs. (2.1a) – (2.1d), under consideration of the specific properties of metallic materials, where charge and current densities are generally not zero. Here, the wave equation according to Eq. (2.3) is described by

$$\mathbf{k}(\mathbf{k} \cdot \mathbf{E}) - k^2 \cdot \mathbf{E} = -\epsilon(\mathbf{k}, \omega)\frac{\omega^2}{c_0^2}\mathbf{E} \qquad , \tag{2.15}$$

where $\mathbf{k}$ represents the wave vector pointing in the laser propagation direction with an absolute value of $k = \omega \,/\, c_0$. While longitudinal waves demand $\epsilon(\mathbf{k}, \omega) = 0$, transversal waves with $\mathbf{k} \cdot \mathbf{E} = 0$ are represented by the dispersion relation [26]

$$k^2 = \epsilon(\mathbf{k}, \omega) \cdot \frac{\omega^2}{c_0^2} \qquad . \tag{2.16}$$

For isotropic and nonmagnetic media, the dielectric function $\epsilon(\mathbf{k}, \omega)$ of a metal, where delocalized electrons are modeled as free electron gas based on Drude's theory, is expressed by

$$\epsilon(\omega) = 1 - \frac{\omega_P^2}{\omega^2 + i\gamma\omega} \quad . \tag{2.17}$$

where γ is the electron collision frequency and $\omega_P^2 = n_e e^2/\epsilon_0 m_e$ defines the plasma frequency, given by the number of free electrons n_e and the electron's mass m_e and charge e. Inherent to the above dispersion relation is, that within the application of Maxwell's equations the metal's polarization $\mathbf{P}$ is assumed as linearly depending on the electric field strength, i.e. $\mathbf{P} = \epsilon_0(\epsilon - 1)\mathbf{E}$, while higher order contributions are substantially smaller and can be neglected. In addition, the dielectric function according to Eq. (2.17) represents a spatially local result, where the wavelength of the electric laser field is expected to be much larger than the typical dimensions of the metallic systems. However, for nanoscale geometries, the plasmon wavelength can for example approach the electron's mean free path, for which spatial dispersion effects need to be considered. Also, the simple assumption of a free-electron gas regardless of the metal's band structure breaks down for high energetic photons, which facilitate interband transitions. For large frequencies in the range of ω_P, the damping factor $\gamma\omega$ is typically small and the dielectric functions yields

$$\epsilon(\omega) \xrightarrow[\gamma\omega \to 0]{} 1 - \frac{\omega_P^2}{\omega^2} \quad . \tag{2.18}$$

Therefore, the dispersion relation in the high-frequency limit results as

$$\omega^2 = \omega_P^2 + k^2\, c_0^2 \quad . \tag{2.19}$$

The propagation of transversal waves with frequencies $\omega < \omega_P$ is not supported by a free electron gas, whereas for waves of frequencies above the limiting plasma frequency, metals become gradually transparent. For electric fields that oscillate right at the plasma frequency, the dispersion relation of the Drude gas yields $\epsilon(\omega) = 0$, which, under consideration of Eq. (2.15), allows for the propagation of a longitudinal plasmon mode.

Surface Plasmon Polaritons

While the propagation of transversal plasmonic excitations in an idealized free electron gas is not possible, macroscopic metal-dielectric interfaces support bound modes also under the condition of $\omega < \omega_P$. The appearance of so-called surface plasmon polaritons (SPPs) follows as solution to Maxwell's equations (2.1a)−(2.1d), taking electric and magnetic field's boundary conditions at the metal-dielectric-interface into account. The detailed derivation, demonstrated e.g. in Ref. [26], reveals that only transverse magnetic (TM) modes exist at the interface, while transverse electric (TE) modes are not feasible. The dispersion relation for surface plasmon polaritons on an infinite interface, as illustrated in Fig. 2.1 (a), is described by [52]

$$\omega = c_0 \cdot k_{\mathrm{SPP}} \sqrt{\frac{\epsilon_m + \epsilon_d}{\epsilon_m \cdot \epsilon_d}} = \frac{c_0 \cdot k_{\mathrm{SPP}}}{n_{\mathrm{SPP}}} \quad , \tag{2.20}$$

where k_{SPP} represents the wave vector of the SPP, while ϵ_m and ϵ_d describe the dielectric functions for the metal and dielectric medium, which are in general both complex valued. In

the last step, the generic definition of the refractive index n_{SPP} is applied to the dispersion relation. Based on the refractive index, the SPP group velocity can be calculated, yielding

$$v_{\mathrm{group}} = c_0 \cdot \left[\frac{d(n_{\mathrm{SPP}}\,\omega)}{d\omega}\right]^{-1} \quad . \tag{2.21}$$

In figure. 2.1 (b) the dispersion relations of photons (black dashed line) and an ideal conductor (blue solid line) are displayed, where the metal's dielectric function is described according to Eq. (2.18). For large frequencies, i.e. $\omega > \omega_{\mathrm{P}}$, the metal's dispersion relation is described by Eq. (2.19), where propagation of transversal fields through the metal is possible. Below the metal's plasma frequency, SPPs can propagate along the metal-vacuum-interface, where the SPP wave vector becomes infinite while approaching the maximum SPP frequency, represented by $\omega_{\mathrm{P}}/\sqrt{1+\epsilon_d}$, and indicated by the black dotted line. For real metallic systems, where damping effects need to be considered, the dispersion relation is altered significantly, as illustrated in the inset of Fig. 2.1 (b) for an Au-vacuum (green solid line) and Au-SiO_2-interface (red solid line). As can be observed, for small SPP wave vectors, the group velocity is close to the speed of light, while for large wave vectors the group velocities reduce significantly. Due to damping effects, there is a maximum SPP wave vector for which bound SPP excitations can propagate along the interface.

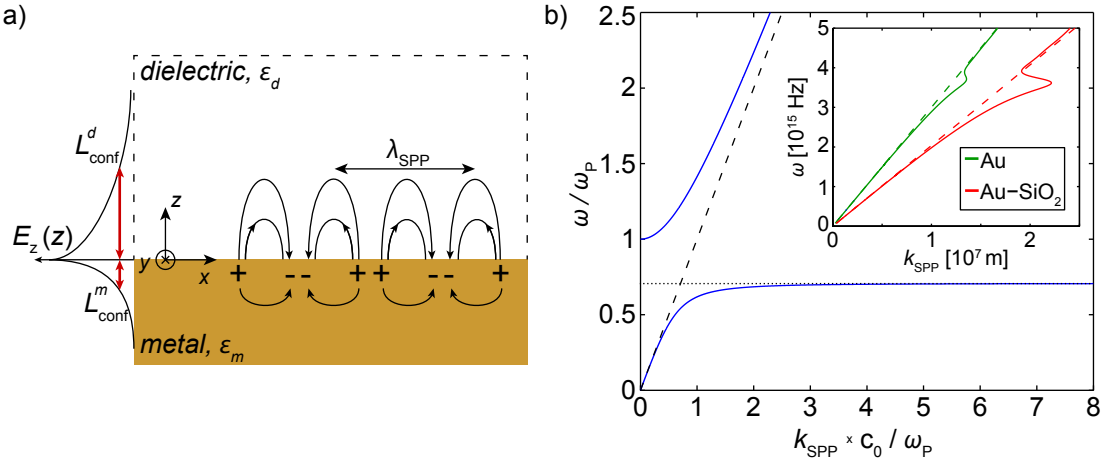

Figure 2.1: SPP dispersion relation. In **(a)** the general geometry for an SPP propagating along an infinite metal-dielectric interface is displayed. The resulting dispersion relation for an ideal conductor is illustrated in **(b)**, where the black dashed line represents the dispersion relation of photons. The inset shows the calculated dispersion relations for an Au-vacuum (blue solid line) and Au-silica-interface (red solid line), where the refractive index for Au is taken from Ref. [53] and the plasma frequency is obtained with $\omega_{\mathrm{P}}^{\mathrm{Au}} = 1.35 \times 10^{16}\,\mathrm{s}^{-1}$ [54]. The respective dispersion relations for photons in vacuum and silica are displayed as dashed lines.

The SPP electric field is confined to the interface with an exponential decay in perpendicular direction, where the decay lengths L^m_{conf}, L^d_{conf} into the metallic and dielectric half space reads as [26]

$$L^{m,d}_{\mathrm{conf}} = \left| \left(k^2_{\mathrm{SPP}} - \epsilon_{m,d} \cdot \frac{\omega^2}{c_0^2} \right)^{-\frac{1}{2}} \right| \quad . \tag{2.22}$$

The SPP propagation length correlates with the confinement to the interface, which demands generally a trade-off between strong confinement and large propagation distances. For real metals, the imaginary part in the dielectric function determines the SPP damping, where the propagation length equals $L_{\mathrm{prop}} = 1/(2\,\mathrm{Im}[\epsilon_m])$, defined as $1/e$ decay length of the SPP intensity.

The SPP dispersion relation depends in general on the respective geometry: the analytical solution of Maxwell's equations for an infinite cylindrical geometry of radius r yields an axially symmetric SPP mode of refractive index n_{SPP}, determined by the condition [55]

$$\frac{\epsilon_m}{\kappa_m}\frac{I_1(k_0\kappa_m r)}{I_0(k_0\kappa_m r)} + \frac{\epsilon_d}{\kappa_d}\frac{K_1(k_0\kappa_d r)}{K_0(\kappa_0\kappa_d r)} = 0 \tag{2.23}$$

where $I_{0,1}$ and $K_{0,1}$ specify the modified Bessel functions of first and second kind, $k_0 = \omega/c_0$ defines the wave vector in vacuum, while $\kappa_{m,d} = \sqrt{n_{\mathrm{SPP}} - \epsilon_{\mathrm{m,d}}}$ introduces the SPP refractive index. Since tapered nanowire geometries can be locally approximated by a cylindrical geometry, the above equation is also employed to calculate the refractive index of conical nanotips in dependence of its local radius. For large radii, the requirement reproduces n_{SPP} for flat surfaces as resulting from Eq. (2.20), while for small radii, the refractive index is approximated by [55]

$$n_{\mathrm{SPP}}(r) \approx \frac{1}{k_0 r}\left[-\frac{\epsilon_{\mathrm{m}}}{2\,\epsilon_{\mathrm{d}}}\left(\log\sqrt{-\frac{4\,\epsilon_{\mathrm{m}}}{\epsilon_{\mathrm{d}}}} - \gamma_{\mathrm{E}}\right)\right]^{-1/2} \quad , \tag{2.24}$$

where γ_{E} represents the Euler constant. In case of a tapered nanowire geometry, the SPP group velocity reduces whilst approaching the singularity at the apex. Given that the SPP propagation length y is parametrized by the local radius, i.e. $y = y(r)$, the geometrically introduced group delay, which references to the propagation along a macroscopic surface, can be calculated

$$\Delta t_{\mathrm{group}} = \int_0^{y_{\mathrm{prop}}} \frac{dy}{v_{\mathrm{group}}\left(y(r)\right)} - \left.\frac{y_{\mathrm{prop}}}{v_{\mathrm{group}}}\right|_{r=\infty} \quad , \tag{2.25}$$

where y_{prop} equals the SPP propagation length on the respective geometry.

Excitation of SPPs via Grating Structures

The SPP dispersion relation reveals that for any macroscopic metal-dielectric-interface the vacuum wave vector is smaller than the SPP wave vector, i.e. $k_0 \leq k_{\mathrm{SPP}}$. Due to this wave vector mismatch, the direct excitation of surface plasmon polaritons by photon irradiation is not feasible. Instead, the mismatch must be compensated to achieve phase-matching conditions for which besides prism coupling [56, 57] and near-field excitation [58], also the coupling via diffraction gratings [59] is an efficient approach. Assuming a grating constant g, the condition for ideal phase matching writes as [26]

$$k_{\mathrm{SPP}} = k_0 \sin\theta \pm m\frac{2\pi}{g}\,, \qquad m \in \mathbb{N} \tag{2.26}$$

where θ describes the angle of incidence relative to the grating surface normal and m represents the grating's mode number. The coupling efficiency depends sensitively on the grating's geometry, e.g. duty cycle and groove's (ridge's) depth (height) and width [60, 61]. However, concerning coupling efficiency, no systematic difference between groove and ridge type gratings

are reported [62]. While the relation of beam size and lateral dimensions of the grating influences its functionality, it was shown that already five grating periods can be enough to achieve more than 40 % coupling efficiency [62]. For increasing depth, each groove can be interpreted as cavity for the surface plasmon polariton, which thereby experiences strong localization. These effects are already observed for considerably small groove depths exceeding 20 Å [26]. Besides SPP excitation of via grating geometries, surface roughness acts in a similar fashion. However, the stochastic allocation of surface corrugation does typically not support the emergence of directed, coherent surface plasmon polaritons. Nevertheless, localization effects can yield drastically enhanced field intensities in the vicinity of rough surfaces [63].

2.2.2 Photoionization in Laser Fields

Since all experiments performed in the framework of this thesis rely on photoionization, a thorough understanding of this physical process is essential. While early experiments [64] on photoemission were restricted to low field strengths, pulsed laser fields and tight focusing offer the opportunity to explore also the strong field regime. Based on the theoretical work on photoionization of atoms by Keldysh [65], the distinction between both regimes relies on the dimensionless Keldysh parameter

$$\gamma = \sqrt{\frac{I_p}{2\,U_p}} \qquad , \tag{2.27}$$

where I_p defines the ionization potential of the respective atom, and U_p is the ponderomotive potential. The latter yields the cycle averaged kinetic energy of a free electron in the presence of an oscillatory electric field:

$$U_p = \frac{1}{2} m_\mathrm{e} \left\langle v(t)^2 \right\rangle = \frac{e^2\,E_0^2}{4 m_\mathrm{e}\,\omega^2} \qquad , \tag{2.28}$$

with m_e, $v(t)$ and e being the electron mass, velocity and charge, while E_0 and ω represent the peak amplitude and central frequency of the respective electric field. The Keldysh theory can be extended from atomic species to metallic targets, by replacing the ionization potential I_p with the respective work function ϕ of the metal [66]. Based on the Keldysh parameter, Perelomov, Popov and Terent'ev calculated the ionization probability of atoms by integrating over all possible many-photon processes [67, 68]. Under consideration of linearly polarized light, the cycle-averaged photoemission yield is determined by

$$P(\gamma) \propto \exp\left[-\frac{2\phi}{\hbar\omega} \cdot \left[\left(1 + \frac{1}{2\gamma^2}\right) \operatorname{arsinh}(\gamma) - \frac{\sqrt{(1+\gamma^2)}}{2\gamma}\right]\right] \qquad . \tag{2.29}$$

The above equation represents a generalized expression of the photoemission rate, where $\gamma \gg 1$ and $\gamma \ll 1$ distinguishes between the weak and strong field photoemission regimes.

Weak Field Regime

In the weak field regime, characterized by $\gamma \gg 1$, the photoionization from atomic or metallic targets is modeled within the framework of perturbation theory, where the inner-atomic potentials are typically orders of magnitude larger than the field strength of weak laser fields at high frequencies. For photon energies, which are smaller than the binding potential an integer

number n of multiple photons is accumulated for the photoemission of an electron [69], as schematically illustrated in Fig. 2.2 (a). Therefore, the weak field regime is also referred to as multiphoton ionization (MPI). The photoelectron's kinetic energy is herein described by

$$E_{\mathrm{kin}} = n\,\hbar\omega - I_p \qquad , \tag{2.30}$$

where n typically yields the smallest integer that is necessary to overcome the potential barrier. Accordingly, the photoemission rate w_{MPI} is calculated in lowest order perturbation theory (LOPT) [70]

$$w_{\mathrm{MPI}} = \sigma_n I_0^n \qquad . \tag{2.31}$$

with σ_n and I_0 being the ionization cross section for the absorption of n photons and the electric field intensity. Accordingly, Einstein's theoretical considerations [71] on the photoelectric effect, discovered by Hertz [64], represents the limiting case of single photon excitation, i.e. linear light-matter interaction. The non-linear regime with $n > 1$ demands intensities, which can be reached by tight focusing of pulsed laser fields.

The photoemission rate described in Eq. (2.31) is readily derived from Keldysh's theory. Since for $\gamma \gg 1$, the exponent can be approximated with $\operatorname{arsinh}(\gamma) \approx \ln(2\,\gamma)$, the photoionization probability simplifies to [72]

$$P(\gamma) \sim \exp\left[-\frac{2\,I_p}{\hbar\omega}\ln(2\,\gamma)\right] \sim \left(\frac{1}{2\,\gamma}\right)^{2\,I_p\,/\,(\hbar\omega)} \sim E_0^{2\cdot[I_p\,/\,(\hbar\omega)]} \qquad . \tag{2.32}$$

Since in the case of low frequency fields, the exponent $I_p\,/\,(\hbar\omega)$ yields approximately the number n of necessary photons and E_0^2 is identified as the laser intensity, the above result is in agreement with Eq. (2.31).

With increasing laser field intensity and frequency, where $\gamma \to 1$, electrons absorb more photons than the minimum required number necessary to overcome the ionization potential [74], as illustrated in Fig. 2.2 (b). The kinetic energy of such above threshold ionized (ATI) electrons yields

$$E_{\mathrm{kin}} = (n+s)\,\hbar\omega - I_p \qquad , \tag{2.33}$$

with s representing the number of absorbed photons above the necessary threshold number n. For increasing field intensities, the laser electric field strength becomes comparable to the inner-atomic potentials and additional effects, like AC-Stark shifts and peak-suppression (channel closing) must be considered [75], as well as specific photoionization resonances of the targets [76].

Strong Field Regime

The strong-field regime is characterized by $\gamma \ll 1$, with large laser field strength at low frequencies. Since the external electric laser fields are found on the same scale as inner-atomic fields, the atom potential well is modulated significantly. As illustrated in Fig. 2.3 (a), where the dashed gray line represents the unperturbed atomic potential, the potential barrier is lowered in the presence of strong electric laser fields, indicated by the blue solid line, and electrons can leave the atom in a tunneling process.

Based on the Keldysh theory, the photoionization probability can be evaluated for $\gamma \ll 1$, where

$$\operatorname{arsinh}(\gamma) \approx \gamma - \frac{\gamma^3}{6} \qquad . \tag{2.34}$$

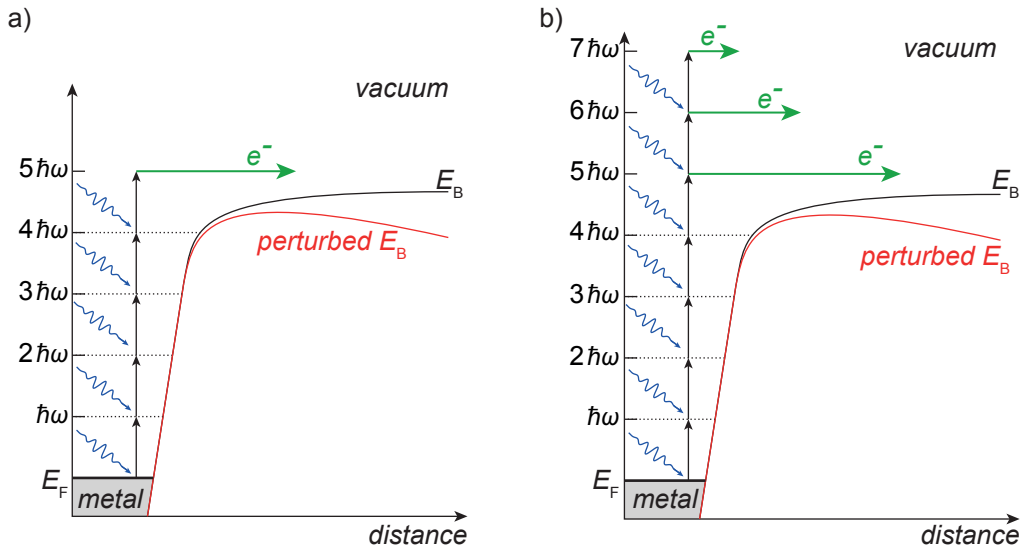

Figure 2.2: Scheme of weak-field photoionization. In **(a)** the multiphoton ionization process from a metal target is schematically displayed, where $n = 5$ photons of energy $\hbar\omega$ are accumulated by electrons at the Fermi-level E_F, to overcome the binding potential E_B. The presence of the NIR laser field perturbs the binding potential, illustrated by the red solid line. In **(b)** the above threshold ionization is illustrated, where electrons accumulate additionally $s \leq 3$ photons. With increasing s, the photoemission yield decreases, represented by the length of the green arrow. Reprinted from [73].

Using Eq. (2.34), the photoionization probability as expressed in Eq. (2.29) simplifies to [72]

$$P(\gamma) \sim \exp\left(-\frac{2\,I_p}{\hbar\omega}\cdot\frac{2\,\gamma}{3}\right) \sim \exp\left(-\frac{4\,\sqrt{2m_\mathrm{e}}\,I_p^{3/2}}{3\,e\hbar E_0}\right) \quad , \tag{2.35}$$

which is qualitatively identical with the derived Ammosov-Delone-Krainov (ADK) photoionization rate [77]. Due to its exponential dependency, the ADK rate is highly sensitive to the electric field strength, which can vary significantly for few-cycle laser pulses of different CEP as has been demonstrated in several experiments on nanostructured solids [78, 79].

2.3 Attosecond Metrology

2.3.1 Attosecond Pulse Generation

High-Harmonic Generation

High-brilliance, attosecond-duration laser pulses are typically produced in a high harmonic generation (HHG) process. As discussed above, the photoionization yield in the strong-field regime, expressed by Eq. (2.35), depends exponentially on the laser electric field strength. Accordingly, the photoemission of electrons is likewise restricted to a sub-cycle time-window in the attosecond domain, centered around the maximum field amplitudes of the femtosecond laser pulse [7, 80].

However, the dynamics in strong-field photoemission is not finished with the ionization process, but followed by the photoelectron's propagation in the respective laser field. Classical

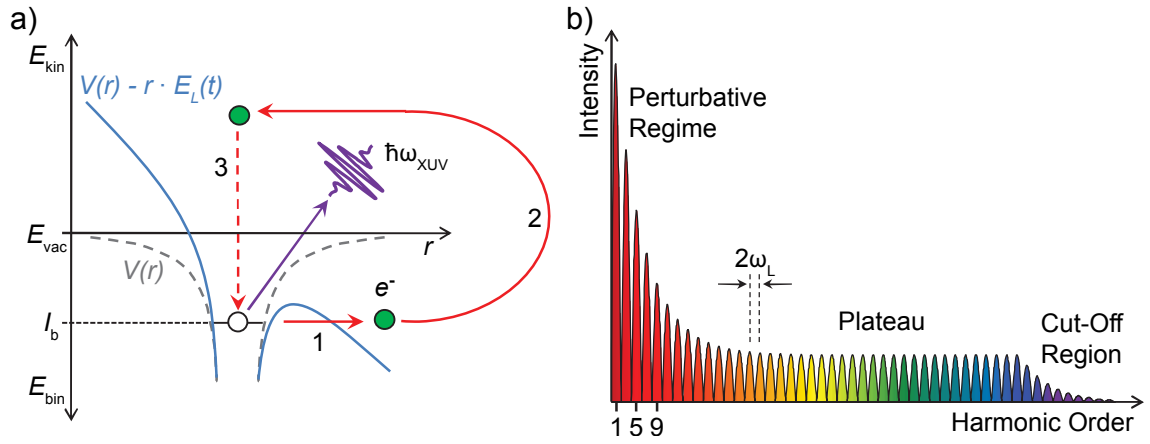

Figure 2.3: Schematic illustration of three step model and high harmonic spectrum. In **(a)** the three step model of high harmonic generation is schematically illustrated. The electron e^- is photoionized (1), propagates in the electric field (2) and finally recombines (3) with the ionic core, thereby generating a high energetic photon $\hbar\omega_{\mathrm{XUV}}$. The photoionization is initiated by the external field, which lowers the atomic potenial $V(r)$ considerably. The resulting harmonics spectrum is displayed in **(b)**, where only odd harmonics are generated, separated by twice the photon energy of the driving laser field $2\,\omega_{\mathrm{L}}$. Reprinted from [81].

calculations predict that electrons leaving the electric field without scattering after emission, reach a maximum final kinetic energy of $E_{\mathrm{kin}}^{\mathrm{max}} = 2\,U_p$ [82]. However, experiments revealed significantly higher photoelectron energies upon strong-field photoemission [83], whose occurrence is explained by the simple man's model (SMM) by Corkum [84], where the strong-field photoemission process is divided, as displayed in Fig. 2.3 (a), into three subsequent steps:

1. Photoionization in the strong-field regime via tunneling ionization.
2. Propagation of photoelectrons in the electric field and back-acceleration towards the ionic core.
3. Interaction between electron and the ionized atom.

Besides recombination with the ion, inelastic or elastic scattering events are observed in the last step. The latter gives rise to high-energetic electrons with a maximum kinetic energy of $E_{\mathrm{kin}}^{\mathrm{max}} = 10.0007\,U_p + 0.538\,I_p$ [82, 85], which is obtained from solving the time-dependent Schrödinger equation (TDSE). In contrast, inelastic scattering events can result in photoemission of additional electrons, occurring as non-sequential double ionization (NSDI) [86]. For attosecond pulse generation, the most important interaction process is the electron's recombination with the ionized atom, where high-energetic photons are produced, referred to as high harmonic generation [6, 87–90]. In case of noble gas atoms, the inversion symmetry restricts HHG to odd harmonics, while for different media, e.g. bulk crystals [91] and molecules [92], or strongly inhomogeneous electric fields [93] also even harmonics can be observed. Since the electron photoemission is restricted to fractions of the driving laser's cycle duration, their recombinations at each half-cycle yields a train of attosecond pulses [94].

The qualitative dependence of a high harmonics spectrum, schematically illustrated in Fig. 2.3 (b), is fully explained by quantum mechanical considerations [95], where the exponential decay for low-order harmonics is predicted already by perturbation theory. In agreement

with the simple man's model, the highest harmonic orders in the cut-off regime yield maximum photon energies of [96]

$$E_{\mathrm{XUV}} = \hbar\omega_{\mathrm{XUV}} = 3.17\,U_p + I_p \qquad . \tag{2.36}$$

For few-cycle laser fields, centered at 750 nm with intensity around $5 \cdot 10^{14}\,\mathrm{W\,cm^{-2}}$, as can be achieved in experiments described in this thesis, the ponderomotive potential yields $U_p \approx 25\,\mathrm{eV}$. Accordingly, the HHG-cut-off using neon as driving gas allows photon energies beyond 100 eV, which is considered the extreme ultra-violet (XUV) regime.

The maximum electron energy, as stated in Eq. (2.36), is only achieved for electrons of specific emission and recombination times t_0 and t', while electrons, which recombine before or after t' follow so-called short and long trajectories. For both trajectory types, the maximum electron or XUV-photon energy is reduced, with attosecond pulses from short (long) trajectories being positively (negatively) chirped. This so-called atto-chirp can be compensated by dispersion management of the HHG process itself [97] or by placing material of appropriate dispersion in the beam path of the attosecond pulse [98–100]. Since HHG in multi-cycle driving fields occurs at each half-cycle, a train of attosecond pulses emerges, which is spaced by half of the oscillation period in the time-domain picture. In the Fourier domain, the spectral intensity forms an equidistant frequency comb of odd harmonics, as illustrated schematically in Fig. 2.3 (b), where the harmonics are separated by twice the laser frequency of the driving laser field.

Phase-matching of Attosecond Pulse Generation

The generation of high-brilliance Fourier-limited attosecond pulses demands, besides knowledge of the microscopic picture and the single atom response, a detailed understanding of the generation process on a macroscopic level. To establish the attosecond pulse generation as coherent process, ideally for multiple harmonic orders simultaneously, the phases of individual attosecond pulses, originating from multiple atoms must match. The later requirement demands that wavevectors of newly generated harmonics at specific position within the generation volume are equal to the wavevector of the propagating attosecond pulse. A simple derivation of the phase-mismatch in attosecond pulse generation was given by Balcou *et al.*, who considered the Gouy phase shift, i.e. the geometrical phase variation of the driving laser field, together with the intrinsic phase accumulated by the photoelectron during propagation in the Coulomb field of its ion superimposed with the NIR laser field [101]. The intrinsic phase variation depends not only on the harmonic order and NIR laser intensity, but also on the respective trajectory type, which can be employed to support attosecond pulse generation from specific trajectories via phase-matching [102]. Since the geometrical phase variation is always negative, the intrinsic phase contribution, which changes sign while going through the NIR focal spot should be positive to compensate the phase mismatch. Accordingly, best phase-matching conditions are expected for harmonics generated downstream of the NIR laser focus. A numerical analysis by Gaarde *et al.* reveals that phase matching of long trajectories is generally in favor for harmonics generated close to the NIR laser focus, whereas in case of short trajectories better phase-matching is achieved at a distance of about one Rayleigh length apart from the focal spot [102]. Since the intrinsic phase of short trajectories in comparison to long trajectories is less sensitive on the harmonic order or the position within the NIR laser focus, phase-matching of several harmonics is easier achieved by short trajectories. Also, the spatial profile of the attosecond laser beam is found to vary for different electron pathways, where long path trajectories yield an annular beam profile, while short path trajectories result

in mostly collimated beam shapes [101, 103].

A more detailed description, including the dispersion effects of free-electrons ionized in the target gas and in addition to dispersion effects and reabsorption processes due to gas atoms, was given by Gaarde, Tate and Schafer [102, 104]. However, results from dispersion effects are more difficult to predict, since the free-electron density follows the electric field strength and is accordingly strongly time dependent [102].

Isolation of Single Attosecond Pulses

For pump-probe measurements, the isolation of a single attosecond pulse is a crucial prerequisite. The first report on isolated attosecond pulses (IAP) was given by Hentschel *et al.* who employed phase-stabilized few-cycle pulses as driving laser field together with amplitude gating of the high harmonic spectrum [4]. To current date, IAPs are realized based on numerous isolation methods, including polarization gating [105, 106], ionization gating [107], multi-color gating methods [108–111] and also spatiotemporal gating approaches [112] (for a review see Ref. [113]).

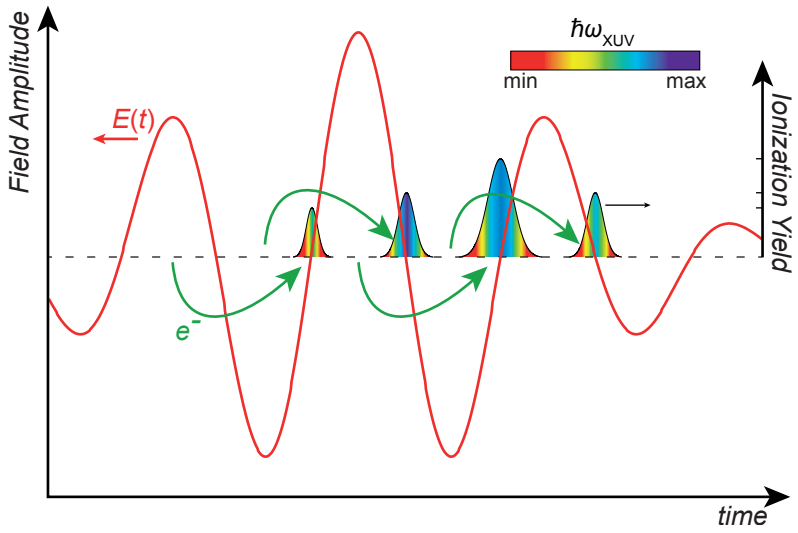

Figure 2.4: Schematic illustration of attosecond pulse generation. In multiple-cycle laser fields, depicted by the red solid line, streaking targets are ionized at several half-cycles. Subsequently to their ionization, free electrons (green solid lines) are propagated in the laser field, thereby gaining kinetic energy. Upon recombination with the ionic core around the field's zero crossings, high-energetic photons are generated. The ionization yield and thereby the XUV photon flux is maximized for electrons, ionized at the half cycle of maximum laser field amplitude as indicated by the magnitude of the XUV photon bursts. In contrast, maximum XUV photon energies, represented by the respective color, are reached by electrons which are propagated during the maximum laser field half-cycle. Using an appropriate bandpass filter, e.g. multilayer mirror, the maximum XUV photon energy range is selected and yields, for cosine-like few-cycle laser fields, an isolated attosecond pulse. Adapted from [3].

Experiments performed in the framework of this thesis, rely mostly on the amplitude gating technique, while the crossover towards the ionization gating regime with increasing laser intensities is fluent. As elaborated above and illustrated schematically in Fig. 2.4, for multiple-

cycle driving lasers, harmonics generated at different half-cycles yield a train of attosecond pulses. Since short and long trajectories generate photons of equal XUV energies at different times, even single cycle laser fields cannot generate isolated attosecond pulses ranging over the full harmonics spectrum. However, selecting the highest photon-energies in the cut-off region, which are generated only within a small window of recombination times, an isolated attosecond pulse can be selected. For filtering, multilayer coatings are employed [114], where the spectral width and central energy is controlled by the number of multilayers and their individual thickness. In the photon energy range of 70 to 90 eV, alternating layers of molybdenum (Mo) and silicon (Si) typically reach a reasonable reflectivity of several ten percents.

While single cycle laser fields achieve optimum brilliance in amplitude gating, also CE-phase stabilized few-cycle pulses can generate IAPs. Here, the single cycle regime is mimicked for $\varphi_{\mathrm{CE}} = 0$, for which the maximum electric field amplitude is only reached once within few-cycle pulse duration.

2.3.2 Attosecond Streaking Technique

Attosecond Streak Camera

Attosecond streaking spectroscopy is widely employed for the full temporal characterization of attosecond pulses or to determine the dynamics of ultrafast processes in the attosecond time domain. This experimental technique relies on the generation of an electron pulse via XUV-photoionization by the isolated attosecond pulse. Generally, it is assumed that the electron pulse represents an exact replica of the IAP, which typically holds for attosecond pulses of small spectral bandwidth and central energy far from photoionization resonances of the specific streaking targets. In conventional streak cameras the electron pulse is spatially deflected by a fast-varying electric field, where the temporal structure of the electron pulse is encoded onto the lateral shift of the electrons. In contrast the attosecond streaking camera, where the fast-varying electric field is typically realized by the few-cycle pulse driving the HHG, detects the change in electron's kinetic energy instead of their spatial deflection. Besides a full quantum mechanical derivation, e.g. in Ref. [115], the working principle of the attosecond streak camera can be understood classically, where the electron dynamics result from Newton's equations of motion [8]. Accordingly, the electron velocity yields

$$\mathbf{v}(t) = \mathbf{v}_0 - \int_{t_i}^{t} \frac{e}{m_e} \mathbf{E}(t')dt' \qquad , \tag{2.37}$$

where $\mathbf{v}_0$ represents the electrons initial velocity, with $|\mathbf{v}_0| = \sqrt{2W_0 \,/\, m_e}$, while t_i, $\mathbf{E}(t)$ describe the ionization time and the electric field of the few-cycle laser pulse. The electrons initial kinetic energy W_0 is derived from the streaking target's ionization potential and the XUV photon energy as $W_0 = \hbar\omega_{\mathrm{XUV}} - I_p$. Here, the few-cycle laser field is assumed to be homogeneous in space, which is typically a good approximation for gas phase streaking experiments with XUV photon energies on the order of 100 eV. Introducing the electric field vector potential, defined by $\mathbf{E}(t) = -\partial\mathbf{A}(t) \,/\, \partial t$ and considering pulsed electric fields which vanish for $t \to \infty$, the photoelectron's final velocity yields

$$\mathbf{v}_f(t_i) = \mathbf{v}_0 - \frac{e}{m_e}\mathbf{A}(t_i) \qquad . \tag{2.38}$$

Accordingly, the final velocity is fully determined by the ionization's initial conditions. Typically the ponderomotive potential of the streaking laser field is significantly lower than the free

electrons energy for which $W_0/2 > U_p$ is fulfilled. Based on Eq. (2.38), under the assumption of a linearly polarized laser field and propagation along the laser polarization direction, the electron's kinetic energy yields [8, 116]

$$E_{\mathrm{kin}}(t_i) = \frac{1}{2}m_e v_0^2 - e v_0 A(t_i) + \frac{e^2}{2m_e}A^2(t_i) \approx \frac{1}{2}m_e v_0^2 - e v_0 A(t_i) \quad . \tag{2.39}$$

Since the vector potential of typically applied NIR field intensities in this thesis of around $10^{12}\,\mathrm{W\,cm^{-2}}$ is small, the quadratic term in the above derivation is negligible [117]. Accordingly, the electron's kinetic energy shift follows the negative vector potential of the few-cycle laser field at the moment of ionization, described by

$$\Delta E_{\mathrm{kin}}(t_i) = -A(t_i)\sqrt{\frac{2e^2}{m_e}(\hbar\omega_{\mathrm{XUV}} - I_p)} \quad . \tag{2.40}$$

The acquisition of a streaking spectrogram, where the photoelectron kinetic energy is recorded as a function of the delay between the XUV attosecond and the streaking pulse allows for a full characterization of the NIR few-cycle laser field in the time domain [10]. The temporal structure of the attosecond pulse is derived from the energy spectrum of photoelectrons [9]: as illustrated in Fig. 2.5 (a), electron pulses of the same duration, but ionized at different times yield different spectral widths after the interaction with the NIR laser field. While the expected spectral width for Fourier-limited XUV pulses can be expressed analytically [8], higher order phase contributions of the attosecond pulse result in distortions of the streaking spectrograms. Exemplary, the influence of chirped attosecond pulses is displayed in Fig. 2.5 (b), where positive chirp yields an increased photoelectron bandwidth for rising electric fields, while the spectral width is decreased for falling NIR field strength. For negatively chirped attosecond pulses, the dependence is vice versa. Based on these considerations, a retrieval algorithm can be employed to extract the full temporal waveform of the attosecond pulse and the streaking NIR laser field [118].

Streaking of Highly Localized Electric Fields

In the section above, it was demonstrated that besides the temporal structure of the attosecond pulse, the streak camera offers a full time-domain characterization of the few-cycle NIR field in phase and amplitude. The applied assumption of a homogeneous field distribution is a reasonable approach, since photoelectrons in the range of 100 eV, as common for streaking experiments, propagate less than $10\,\mathrm{nm\,fs^{-1}}$, while NIR focal spot sizes are on the order of tens of microns. Theoretical calculations, e.g. in Refs. [120–125] investigated the implications of highly localized electric fields on the streaking field retrieval based on the attosecond streak camera. Only recently Schötz *et al.* demonstrated a generalized approach for the reconstruction of nanoscale electric fields, where they considered an NIR laser field that scatters at a metallic nanotarget geometry [126]. Here, the spatial dependence of the scattered field is modeled by an exponential decay with the characteristic near-field decay length l_{nf}. Without limitations, in the following only the one dimensional case is considered. Accordingly, the streaking field E_{st}, experienced by electrons during the streaking process, results as superposition of incident NIR laser field and scattered field

$$E_{\mathrm{st}}(x,t) = E_{\mathrm{NIR}}(t) + E_{\mathrm{scat}}(t)\cdot\exp\left[-\frac{x}{l_{\mathrm{nf}}}\right] \quad , \tag{2.41}$$

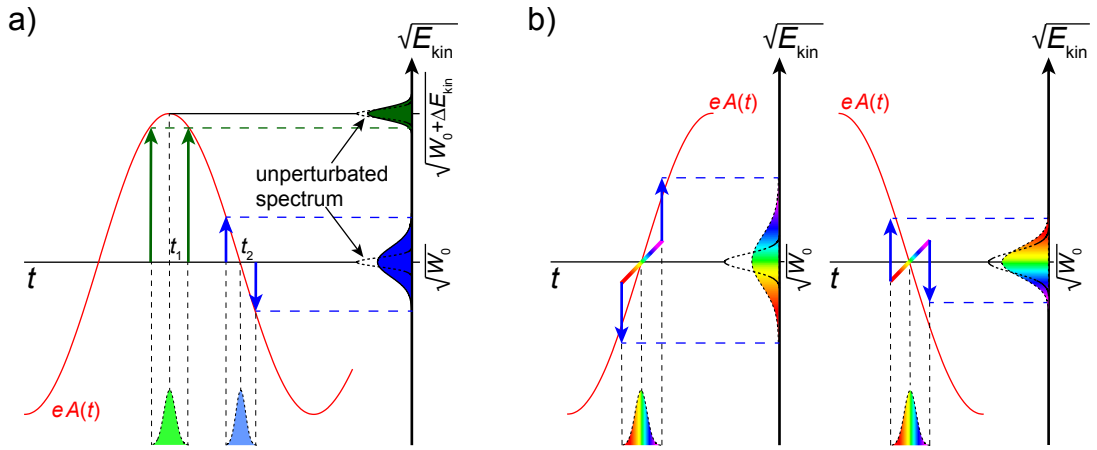

Figure 2.5: Schematic illustration of the streak camera. In **(a)** the interaction of the vector potential $\mathbf{A}(t)$ and electron pulses of identical duration, but generated at different times t_1 and t_2, is shown. Compared to the unperturbed spectrum, the streaking yields a broadening of the observed photoelectron spectrum. The effect of a negatively chirped attosecond pulse is displayed in **(b)**, where the streaking spectrum for rising vector potential is significantly broadened as compared to the unperturbed and unchirped case. Streaking in falling vector potentials yields a reduced spectral width. Adapted from [119].

where E_{NIR} and E_{scat} describe the homogeneous NIR laser field and scattered field, respectively. Commonly in streaking experiments, the photoelectrons initial energy on the order of 100 eV is much larger than the energy gain induced by propagating in the electric fields, which typically yields less than 10 eV. Therefore, in zeroth order approximation, the electron position can be described through the initial velocity as $x = v_0 \cdot (t - t_i)$, while we neglect the influence of the near-field on the electron velocity. Based on these approximations, Newton's equation of motion can be solved, which is for convenience performed in the Fourier domain. Accordingly, the photoelectron's final velocity, as derived in Eq. (2.38), yields

$$v_f(\omega) = i\omega \frac{e}{m_e} \cdot E_{\mathrm{st}}(\omega) \quad , \tag{2.42}$$

where $E_{\mathrm{st}}(\omega)$ represents the electric near field in the Fourier domain. As demonstrated in Ref. [126], the near field is expressed by

$$E_{\mathrm{st}}(\omega) = \frac{E_{\mathrm{NIR}}(\omega) + E_{\mathrm{scat}}(\omega)}{1 - i\frac{1}{2\pi\delta(\omega)}} + \frac{E_{\mathrm{NIR}}(\omega)}{1 + i2\pi\delta(\omega)} \quad , \tag{2.43}$$

where the adiabaticity parameter δ is defined by

$$\delta(\omega) = \frac{l_{\mathrm{nf}} \cdot \omega}{v_0} = \frac{l_{\mathrm{nf}}}{v_0 \cdot T_0} = \frac{T_{\mathrm{esc}}}{T_0} \quad , \tag{2.44}$$

with T_0, T_{esc} representing the duration of a single NIR laser cycle and the near-field escape time of the photoelectron. Identifying the sum $E_{\mathrm{NIR}}(\omega) + E_{\mathrm{scat}}(\omega)$ as the near field on the sample surface at $x = 0$, and introducing the surface-field function f_{surf} and incident-field function f_0, by

$$f_{\mathrm{surf}}(\delta) = \left(1 - i \cdot \frac{1}{2\pi \cdot \delta}\right)^{-1} , \tag{2.45a}$$

$$f_0(\delta) = (1 + i \cdot 2\pi \cdot \delta)^{-1} , \tag{2.45b}$$

the expression for the streaking field simplifies to

$$E_{\mathrm{st}}(\omega) = f_{\mathrm{surf}}(\delta) \cdot E_{\mathrm{surf}}(\omega) + f_0(\delta) \cdot E_{\mathrm{NIR}}(\omega) \quad . \tag{2.46}$$

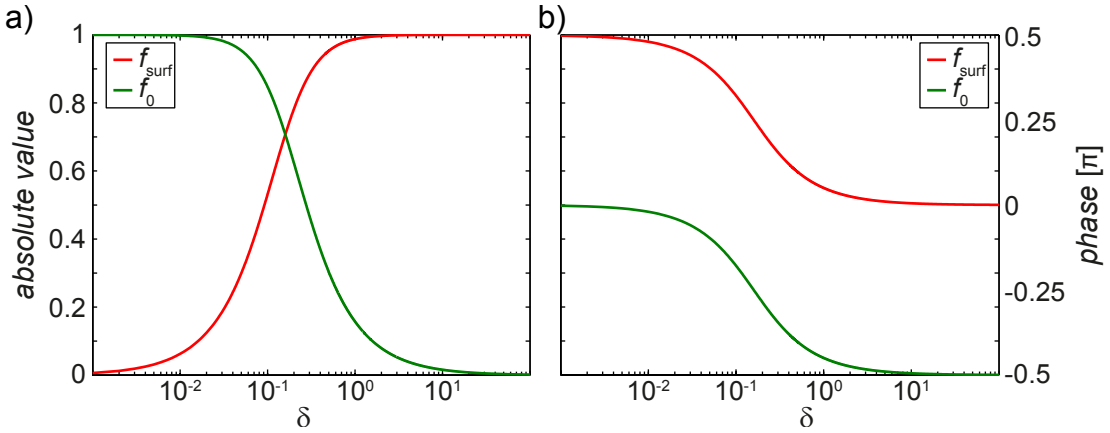

Figure 2.6: Streaking in nanoscale electric fields. In **(a)** the absolute value of the surface-field function and incident-field function is displayed, while in **(b)** the respective phase values in dependence of the adiabaticity parameter are illustrated. Based on the δ-values three different streaking regimes can be distinguished (as explained in the text). Adapted from [126].

The effect of spatially confined streaking fields is illustrated in Figs. 2.6 (a) and (b), where the absolute value and phase of the surface-field and incident field function is plotted in dependence of the adiabaticity parameter. As apparent from the figures, three different regimes can be distinguished

i. Ponderomotive streaking regime with $\delta \gg 1$
The time it takes the electron to leave the near field is much larger than the duration of an optical cycle. Therefore, the electron effectively probes a quasi-homogeneous field. Since the absolute value f_{surf} is close to unity, while it's phase is almost zero, the streaking field is determined by the surface electric field. Accordingly, the streaking trace is described by the vector potential of the surface electric field which allows to retrieve its full amplitude and phase information.

ii. Intermediate regime with $\delta \approx 1$
The intermediate regime determines the transition between the ponderomotive and instantaneous regime. Here, the photoelectrons leave the near-field too fast to consider the streaking field as spatially homogeneous, while electrons are too slow to describe the streaking field by a time-independent static field.

iii. Instantaneous streaking regime with $\delta \ll 1$
In this case photoelectrons leave the near field within a small fraction of an optical cycle, i.e. quasi instantaneous. Despite the surface-field function approaches zero for small δ-values, photoelectrons can be strongly influenced by the surface field, since large field enhancement factors are observed for nanostructured geometries. Given that the streaking field is governed by the surface field, i.e. $f_{\mathrm{surf}}(\delta) \cdot E_{\mathrm{surf}}(\omega) \gg f_0(\delta) \cdot E_{\mathrm{NIR}}(\omega)$,

the streaking trace phase is shifted by π with respect to the surface electric field. Accordingly, the streaking trace is not determined by the vector potential but directly by the nanoscale electric surface field. Generally, the exact phase and amplitude of the streaking trace in the instantaneous regime depends sensitively on the ratio between the contributions of the incident laser field and surface electric field.

Accordingly, prior to the analysis, the streaking regime must be determined by estimating the actual adiabaticity parameter for the experimental setup. For sufficiently small XUV photon energies, the streaking regime is typically found in the ponderomotive regime, resembling to good approximation, the case of homogeneous electric near fields.

Correspondence of Photoionization Delays and Streaking Experiments

The advent of the attosecond streaking technique allowed to investigate, amongst others, the photoionization process with unprecedented temporal resolution, which revealed an apparent delay for emission from different electron initial states in atoms [14] and solids [15, 16]. However, these findings pose questions on the physical interpretation of such time delays and demand a microscopic explanation of their origin.

Due to its nature, the photoionization process is typically discussed in the realm of quantum mechanics (QM). While time was initially considered a quantum mechanical operator [127], where time-delays would result from the associated eigenvalues, Wolfgang Pauli [128] argued that time represents not an operator but rather a parameter, which is nowadays widely accepted [129]. The theoretical foundations for the explanation of time delays in the photoionization process were derived by Eugene P. Wigner, who investigated the influence of a scattering potential on the propagation of a free particle [130]. In the QM picture, the free particle acquires an additional energy-dependent phase $\eta(E)$ during the scattering process. Compared to the non-interaction case, the particle after interaction appears delayed, where the time-delay under application of the stationary phase approximation is given by [129]

$$\tau_{\mathrm{W}} = \hbar \frac{\partial \eta(E)}{\partial E} \quad , \tag{2.47}$$

and is typically referred to as Wigner delay or Eisenbud-Wigner-Smith (EWS) delay [131–133]. In the derivation, a short-ranged scattering potential is intrinsically assumed, which is a reasonable approximation for the atomic binding potential. Since the photoionization can be considered a half-scattering process, the observed time delays are typically explained as Wigner-type delays. Transitions from different initial states generally experience different scattering potentials for which different phase shifts are accumulated. Therefore, the most generic description of the EWS delays in photoionization is given by [131]

$$\tau_{\mathrm{EWS}}^{i \to f}(E, \theta, \varphi) = \frac{d}{dE} \arg \left[\langle \psi_f(E, \theta, \varphi) | \mathbf{d} | \psi_i \rangle \right] \quad , \tag{2.48}$$

where $\mathbf{d}$ represents the dipole transition operator, while ψ_i and ψ_f describe the electron's initial and final state wave functions, where the latter generally depends on the solid angle (θ, φ).

In attosecond streaking experiments, the observed measurement result t_{S}, referred to as streaking delay, does not represent the pure EWS-delay as defined in Eq. (2.48). Instead several contributions add phase shifts to the ionized electrons, thereby changing the observed streaking delay. Most generally, for atomic streaking targets, major contributions include [134]

i Coulomb-laser-coupling (CLC): t_{CLC}
The presence of the NIR streaking field yields an additional phase shift to the propagating photoelectron. Thereby the measurement method itself affects the observed time-delays. Moreover, the ionic residual of the initially neutral streaking target features a Coulomb potential, which adds an additional Coulomb-phase [135, 136].
A classical calculation estimates the induced time shift from the photoelectron's propagation in the NIR laser field with superimposed Coulomb-like electric field by [134]

$$t_{\mathrm{CLC}} = \frac{Z}{(2E)^{3/2}} \left[2 - \ln(E \cdot T_{\mathrm{IR}})\right] \qquad , \tag{2.49}$$

where Z denotes the nuclear charge of the target ion, E represents the photoelectron final energy and T_{IR} stands for the NIR laser period. Most importantly, this approximation is found to be independent of the respective NIR intensity or pulse duration.

ii Initial state effects: t^{i}_{dLC}
Streaking targets with non-vanishing dipole moments $\mathbf{d}_{\mathrm{target}}$ (either permanent or induced by the NIR laser field) interact with the NIR laser field prior to the photoionization. Similar to the Stark-effect, the initial state energies are shifted by the interaction between dipole moment and NIR laser field, which in turn induces a phase shift

$$\eta_{\mathrm{dLC}} = -\mathbf{d}_{\mathrm{target}} \cdot \int_{t}^{-\infty} \mathbf{E}_{\mathrm{NIR}}(t')dt' \qquad . \tag{2.50}$$

From the phase shift the resulting time-shift can be calculated as outlined above.

iii Final state effects: t^{f}_{dLC}
Similar to the previous case, where the streaking target's polarization gives rise to additional phase shifts, final state effects, which consider the streaking target after photoionization, can alter the streaking delays significantly. A prominent example is the photoionization of many-electron targets, where the correlation between emitted photoelectrons and bound electrons of the same (intraband) or different shells (intershell) changes the photoelectron's final kinetic energy and thereby its phase, respectively the observed streaking delay [134, 137]. In theory, the accurate incorporation of electron correlation is difficult, since non-stationary theories, e.g. random phase approximation with exchange (RPAE) [37] or many-body perturbation theory (MBPT) [138] need to be applied.

Accordingly, in the atomic case, the observed streaking delay is in general described by

$$t_{\mathrm{S}} = \tau_{\mathrm{EWS}} + t_{\mathrm{CLC}} + t^{i}_{\mathrm{dLC}} + t^{f}_{\mathrm{dLC}} \qquad . \tag{2.51}$$

Streaking measurements of solid state systems are typically more complex, where a multitude of phase shift contributions need to be respected (see e.g. Refs. [15,16,18,139–146]). Not only the bandstructure will affect the photoelectron propagation, but also many-body interactions, e.g. photoelectron's scattering at the lattice or delocalized electrons, electron-hole screening or plasmon interactions are more pronounced compared to the atomic case, due to the large number of particles. Depending on the experimental setup, the NIR laser field can be screened inside the streaking target, for which electron propagation effects to the target's surface and accurate screening lengths need to be considered. Nevertheless, experimental streaking measurements offer the opportunity to validate theoretical models and to extract benchmarks for

the strength of correlations.

The lack of an absolute time, which is universal to measurements of any dynamical process, requires a reference system to gauge the measurement results. For streaking spectroscopy, the latter demands typically the photoionization from two independent targets, which allows to measure the time delay between ionization from one target with respect to the other.

Chapter 3

Experimental Techniques

The following chapter introduces the main experimental techniques that were used throughout the thesis. The first section presents details on the fabrication process of nanostructured samples that were used in the time-resolved measurements of plasmonic excitations (presented in chapter 4). The samples are fabricated according to our requirements by cooperating research groups in the framework of joint activities.

The second and third section concentrate on explaining the different experimental setups for attosecond streaking spectroscopy. Experiments presented in this thesis were conducted using attosecond beamlines. The commission and, subsequently, the characterization of the beamline in the Attosecond Science Laboratory (ASL) was a major task within this thesis. The general introduction into attosecond beamline design is given taking the ASL-beamline as an example. Moreover, the individual parameter range for the ASL-beamline is presented. The streaking on nanostructured targets has been performed using the attosecond beamline AS-5, commissioned already in 2012. Here, I will restrict the descriptions on reconstructions, necessary to meet the requirements for nanostrucutre streaking experiments. A detailed presentation of the AS-5 design can be found elsewhere [116, 147, 148].

3.1 Fabrication and Characterization of Nanostructures

For the experiments on the temporal dynamics of excitations of plasmonic nanostructures, three different sample geometries are in the focus of the investigations presented in this thesis. The different geometries can be interpreted as an evolution in terms of complexity and number of nanosize features. While the first sample generation is extensively studied, experiments on the latest sample generation are currently still at an early stage.

3.1.1 Etched Metal Nanotips

Metallic nanotips, where the tip apex radius yields about 100 nm, are fabricated by our collaborators in the group of Peter Hommelhoff[1]. In the Hommelhoff group, laser-induced electron emission studies from similar kind of samples were performed to investigate electron recollision processes on attosecond timescales. In their experiments they demonstrated attosecond control of electron photoemission using the CEP of few-cycle laser pulses as a tuning knob [72,149]. Moreover, they proved the possibility to extract near-field information on a nanoscale spatial

[1]Prof. Peter Hommelhoff; Lehrstuhl für Laserphysik; Staudtstraße 1; 91058 Erlangen, Germany

resolution using the photoemitted electron as a probe [150].

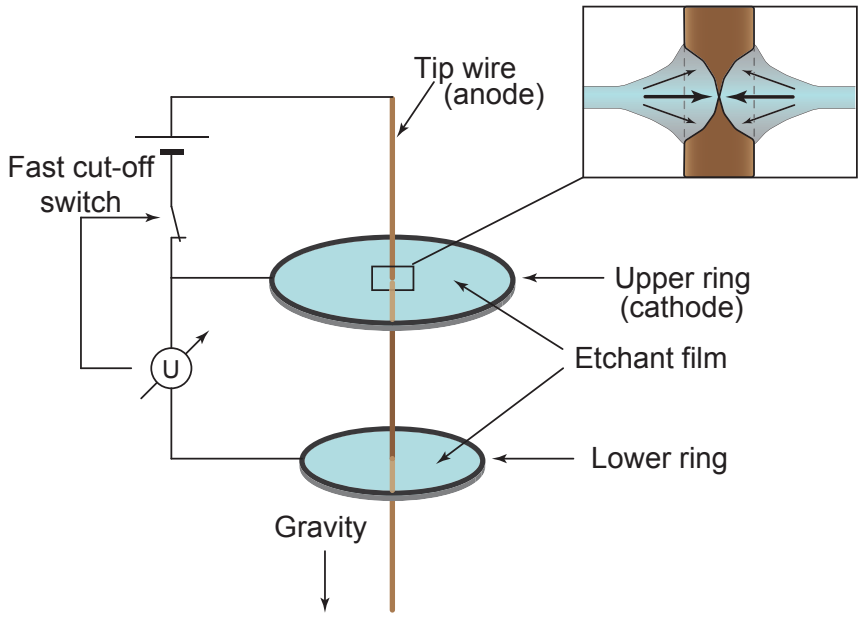

Figure 3.1: Schematic illustration of the double-lamellae drop-off technique. The wire, serving as anode, is mounted vertically between two conducting rings, that are wetted by a thin film of etchant solution. Applying a voltage between the upper ring and the wire initiates the etching process. When the etching process is finished, the lower part of the wire is attracted from gravity and breaks the film in the lower ring. An electronic circuit detects the breaking of the film and initiates the switch-off of supply voltage. Depending on the supply voltage and switch-off delay, apex radii r_{apex} range between 5 nm – 200 nm using this technique. Adapted from [72].

Etched nanotip samples were used in streaking experiments, where we could demonstrate the ability to resolve attosecond dynamics of nanoscale electrical fields [151]. The samples are fabricated from a thin, polycrystalline gold nanowire with a diameter of 100 µm in a so-called double-lamella drop-off technique as illustrated in Fig. 3.1 [150]. The gold (Au) wire[2] is mounted vertically, centering two electrode rings with a relative distance of 0.5 cm and a diameter of 0.5 – 1.0 cm. For gold tips the cathode material is platinum[3]. By dipping the rings into an etchant solution, two thin films build up inside the cathodes. Hereafter, a potential difference (typically about 10 V DC) is applied between the upper ring and the wire to start the electrochemical etching process. A 90 % aqueous solution of KCl is used as etchant, initiating the following processes [152–154]:

$$\begin{aligned} \mathrm{Au} + 4\,\mathrm{Cl}^- &\longrightarrow \mathrm{AuCl}_4^- + 3\,e^- , & E_0 &= 1.002\,\mathrm{V} , \\ \mathrm{Au} + 2\,\mathrm{Cl}^- &\longrightarrow \mathrm{AuCl}_2^- + e^- , & E_0 &= 1.154\,\mathrm{V} , \\ \mathrm{AuCl}_2^- + 2\,\mathrm{Cl}^- &\longrightarrow \mathrm{AuCl}_4^- + 2\,e^- , & E_0 &= 0.926\,\mathrm{V} . \end{aligned}$$

Under the influence of gravity, the micro-wire breaks eventually and destroys the lower etchant film, which is detected by an electronic circuit, shutting off the etching supply voltage. The

[2] Alfa Aesar, 99.998 % purity metals basis
[3] Alfa Aesar, 99.95 % purity metals basis, annealed

shut-off time of the voltage switch determines the sharpness of the tip apex that starts to blunt after the micro-wire breaks [155,156]. Figures 3.2 (a) and (b) show a typical sample, produced by the double-lamella drop-off technique. Coarse characterization with a microscope reveals a shiny surface, indicating the high surface quality. The SEM micrograph, shown in Fig. 3.2 (b) demonstrates the uniform shape down to the nanometer scale. Using the double-lamella drop-off for gold tip production, apex radii r_{apex} were found to vary within $5\,\mathrm{nm} - 200\,\mathrm{nm}$, while full opening angles between 6°-12° are reported [150].

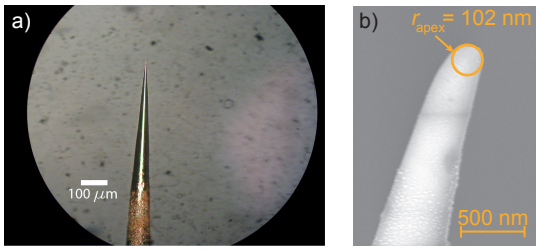

Figure 3.2: Optical image and scanning electron micrograph of a nanotip sample. Coarse investigation of the sample quality using an optical microscope **(a)** demonstrates a smooth and shiny surface. From SEM micrographs, shown in **(b)**, the apex radius $r_{\mathrm{apex}} \approx 100\,\mathrm{nm}$ is estimated. Adapted from [150, 151].

3.1.2 Grating Supertip Samples

Grating supertip samples are fabricated in cooperation with the group of Enzo Di Fabrizio[4]. In Di Fabrizio's group grating supertip samples were fabricated to investigate the possibility of hot electron-injection through a Schottky-type contact into a semiconductor [157] via excitation by a surface plasmon polariton. The plasmons are excited on a diffraction grating written into the nanostructure and are subsequently guided and focused onto the sharp supertip apex. As a result of the adiabatic focusing, surface-plasmon-to-hot-electron conversion efficiencies of 30 % are reported in striking contrast to previous studies ranging around 1 % conversion efficiency. In experiments of the DiFabrizio group, the SPPs are excited by three distinct laser frequencies each with a small spectral width. Therefore, each grating was optimized for a single wavelength only.

The samples (see Fig. 3.3) that have been fabricated in the framework of our collaboration use the same manufacturing procedure as described in Ref. [157] and the according supplementary information. The base is a commercial atomic force microscopy (AFM) tip[5] fabricated from n-type silicon, placed on a cantilever. The grating is written by focussed ion beam (FIB) milling. Depending on the milling current density, the lateral dimensions of the grating, i.e. groove width and spacing, are realized with a typical resolution in the range of 5 nm. The maximum resolution for the depth of the grooves is typically around 15 nm. In a second step, after defining the grating features, the AFM cone is coated with gold via sputtering. The third step involves the growth of a platinum needle on top of the AFM-cone-tip (refered to as *super-tip*) by electron-beam induced deposition (EBID). The super tip with a base radius of about 300 nm extends roughly $1\,\mu\mathrm{m} - 2\,\mu\mathrm{m}$ from the AFM cone with an apex radius $< 10\,\mathrm{nm}$. In a last step the whole nanostructured sample is again coated by thin Au

[4] Prof. Enzo Di Fabrizio; King Abdullah University of Science and Technology; Bldg. 3; 23955-6900 Thuwal, Saudi-Arabia

[5] μmasch, csc 38

layer via mild Argon-Ion (Ar^+) sputtering. In addition the last step comprises a smoothing of the transition from AFM-cone to super-tip.

As illustrated in Fig. 3.3 (b), for our sample, the cone height is about 18.5 µm with a full opening angle of about 42°. The grating is formed out of nine grooves that are equally spaced by 1.3 µm (see Fig. 3.3 (c)) with a grating duty-cycle of 0.2 (here, duty-cycle is defined as the ratio between groove width and grating constant). For the given cone opening angle and using Eq. (2.2.1), the calculated optimum excitation wavelength is about 633 nm. The super-tip, displayed in Fig. 3.3 (d), extends about 1500 nm from the AFM-tip.

The main goal we pursued with experiments on the grating supertip samples was to observe the dynamics of propagating surface plasmon polaritons. While the first sample geometry focuses on the generation of localized enhanced fields at the tip apex, the second sample geometry concentrates on adiabatic nanofocusing of propagating surface plasmons. In the second sample generation, the surface plasmons are excited on a grating structure from where they propagate towards the super-tip apex. The adiabatic focusing enhances the surface plasmon towards the supertip, where the SPP is probed on the apex.

3.1.3 Chirped Grating Structures

Chirped grating samples are fabricated in a collaboration with Stefano Cabrini[6] and his group. Experiments on chirped grating samples aim at resolving the attosecond dynamics of plasmonic excitations and the control of their temporal and spatial properties. While chirped gratings with varying grating constants are used to shape the temporal properties of SPPs, the spatial properties are altered by so called fan-grating structures [158–160]. Since plasmonic transport in information technology is considered to speed up electronics, understanding the plasmon dynamics could help bridging the gap from conventional circuitry towards petahertz electronics [161].

The samples, as illustrated in Figs. 3.4 and 3.5, are fabricated using a crossed-beam FIB-SEM setup[7]. The basis forms a thin Au wire with a diameter of 100 µm[8]. The manufacturing process can be divided into four steps: during the first step a plane surface of 100 µm × 100 µm is generated by cutting on the side of the wire. The first step uses a high ion current density of 10 nA cm^{-2}. For the poor confinement of the high current density, the surface shows a high surface roughness (see Fig. 3.4 (b)). In a second step the surface is polished with FIB, reducing the current density in four consecutive polishing steps as shown in Fig. 3.4 (c). As a third step another part of basic Au wire is cut such that a wedged geometry with a full opening angle in the range of $10° - 40°$ is achieved. At the intersect between the two cross section, an apex radius r_{apex} between 50 nm − 200 nm is formed, where the SPP excitations get adiabatically enhanced. The last step involves etching of the gratings into the smoothed surface. Here, two different kinds of samples were fabricated, namely fan-type gratings to introduce spatial chirp to the SPP and chirped gratings for temporal shaping of the SPP. In both cases the width of the gratings was kept unchanged to be about 10 µm, resembling the approximate focal spot size in the AS-5 setup (see also Sec. 3.3). For both grating types the spacing as well as the duty cycle is varied, for investigating different degrees of spatial or temporal chirping. Moreover, the distance between grating and edge, measured as the

[6] Prof. Stefano Cabrini; Lawrence Berkeley National Lab; 1 Cyclotron Road; Berkeley CA 94720
[7] Carl Zeiss AG™, Crossbeam 1540 EsB
[8] Goodfellow GmbH, 99.99 % purity metals basis, annealed

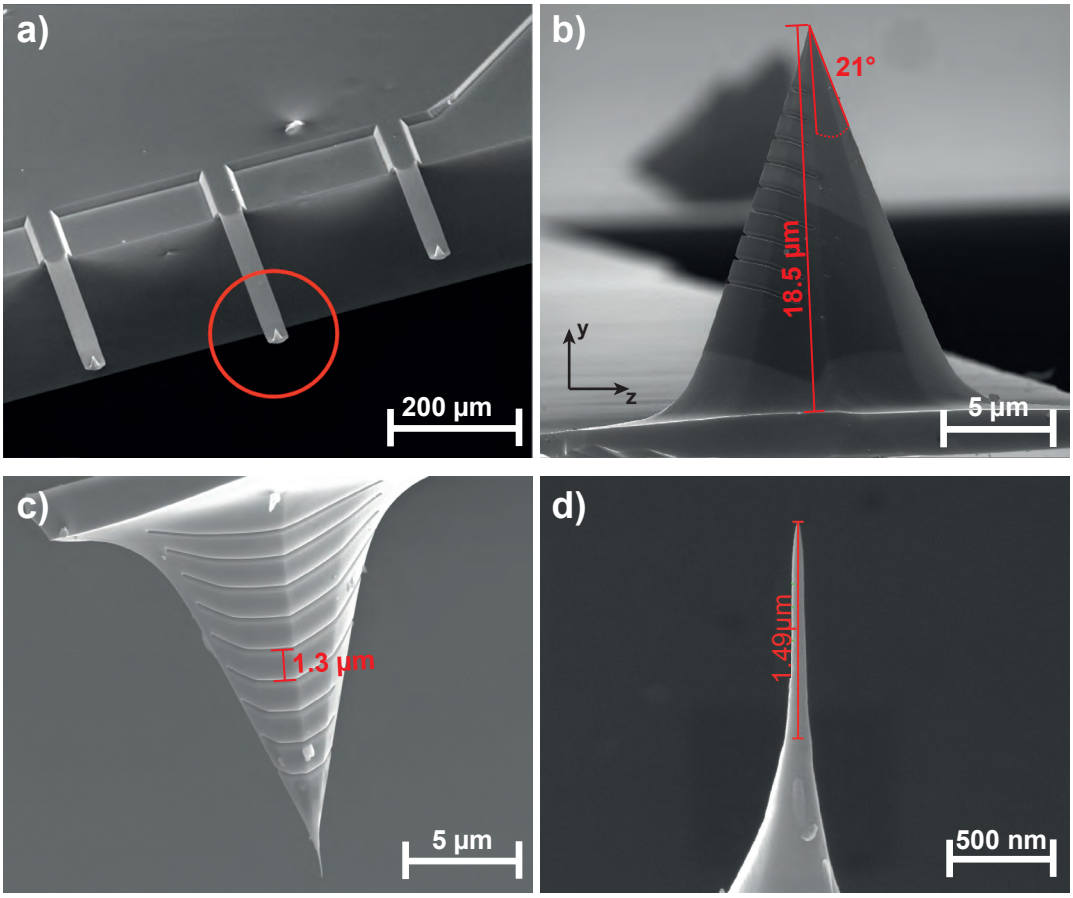

Figure 3.3: SEM micrographs of the grating supertip geometry. The samples use a commercial AFM cantilever as basis for fabrication. The silicon chip **(a)** carries several cantilevers, such that different geometrical structures (i.e different gratings, different supertips) can be realized on a single holder. In the SEM image, a red circle marks the cantilever with the imprinted geometry shown in **(b)** – **(d)**. The pyramidal AFM tip **(b)** has typically a full opening angle of 42°. For phase matching with incident light, a grating is imprinted onto the AFM cone. The grating constant of 1.3 µm **(c)** with a duty-cycle of 0.2 is chosen to match $\lambda = 633\,\text{nm}$ for laser propagation parallel to z-axis. Excited SPPs propagate along the cone to the supertip apex **(d)**, where adiabatic focussing results in field enhancement at the apex. Surface imperfections and contamination, as can be seen in **(c)**, can couple the propagating SPP to the far-field and thereby reduce the propagation distance of SPPs. Courtesy of Enzo Di Fabrizio, adapted from [148].

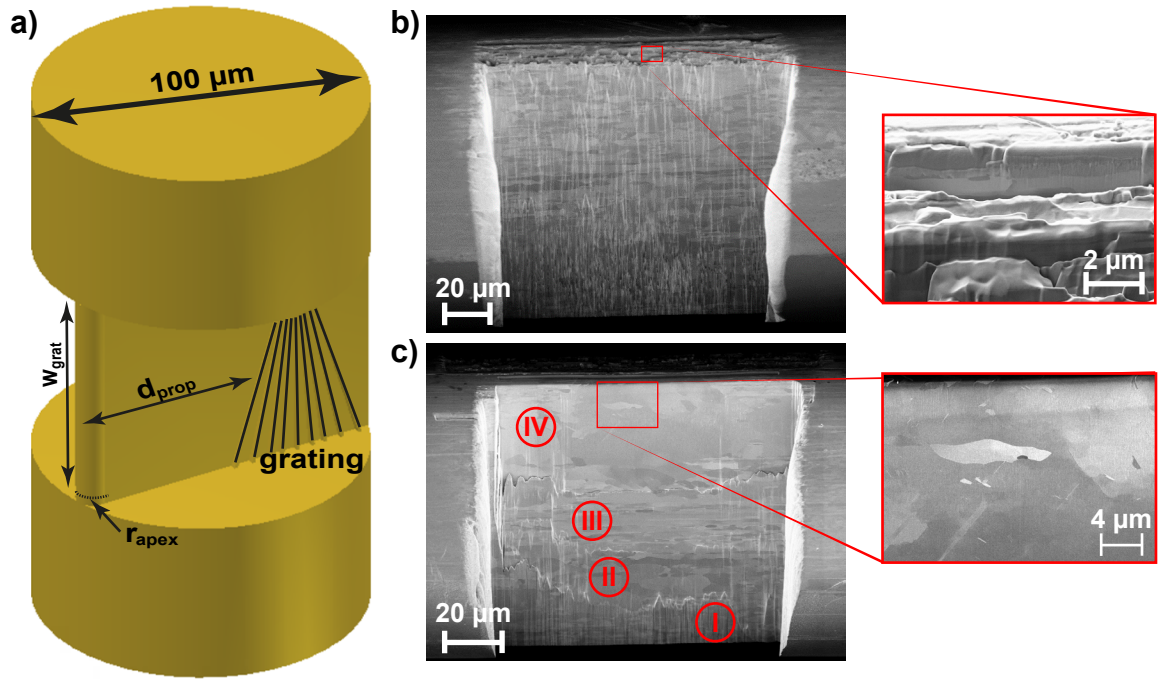

Figure 3.4: Fabrication process of chirped grating samples. Subfigure (**a**) illustrates the sample geometry fabricated from a polycrystalline Au wire by FIB milling. The grating is written on an atomically smooth surface plane (typically 100 µm × 100 µm) that is prepared in a preceding cross section of the Au wire. The propagation distance d_{prop} is altered between 2 µm − 10 µm, while the grating width $w_{\mathrm{grat}} = 10\,\mu\mathrm{m}$ is constant for different nanosamples, matching the focal spot size of our experimental setup. A cross sectional cut at 10° − 40° relative to the grating plane, forms an apex with radius r_{apex} between 50 nm and 200 nm. Different steps of the surface preparation are shown in (**b**) and (**c**). FIB-milling of micron scale surface requires high dose rates resulting in a rough surface texture (**b**). For smoothing the surface, the current density was stepwise reduced from 10 nA cm^{-2}, 5 nA cm^{-2} and 1 nA cm^{-2} to 500 pA cm^{-2}. The varying surface roughness is imprinted as terraces, labeled by I to IV in **(c)**.

distance from the edge to the closest grating stripe is changed for multiple samples in the range between 2 µm and 15 µm. A typical sample geometry, hosting two fan-type gratings and a reference grating, is shown in Fig. 3.5. The reference grating period is optimized to match a laser wavelength of 720 nm for perpendicular incidence. In contrast the fan-type grating phase-matches a continuous spectrum ranging from 540 nm to 1.6 µm, in principle.

3.2 ASL Setup

The Attosecond Science Laboratory was opened in February 2015 as the first attosecond science facility in the arabic world [162]. The ASL-infrastructure, comprised of the laser system and the attosecond pump-probe appartus, was build up within less than one and a half years and was fully commissioned shortly after the laboratory opening in July 2015. The implementation and build-up has been a major part of this thesis.

In the following subchapters, I will explain technical details on the laser system and necessary information for its working principle before focusing on the operating mode of the ASL attosecond beamline.

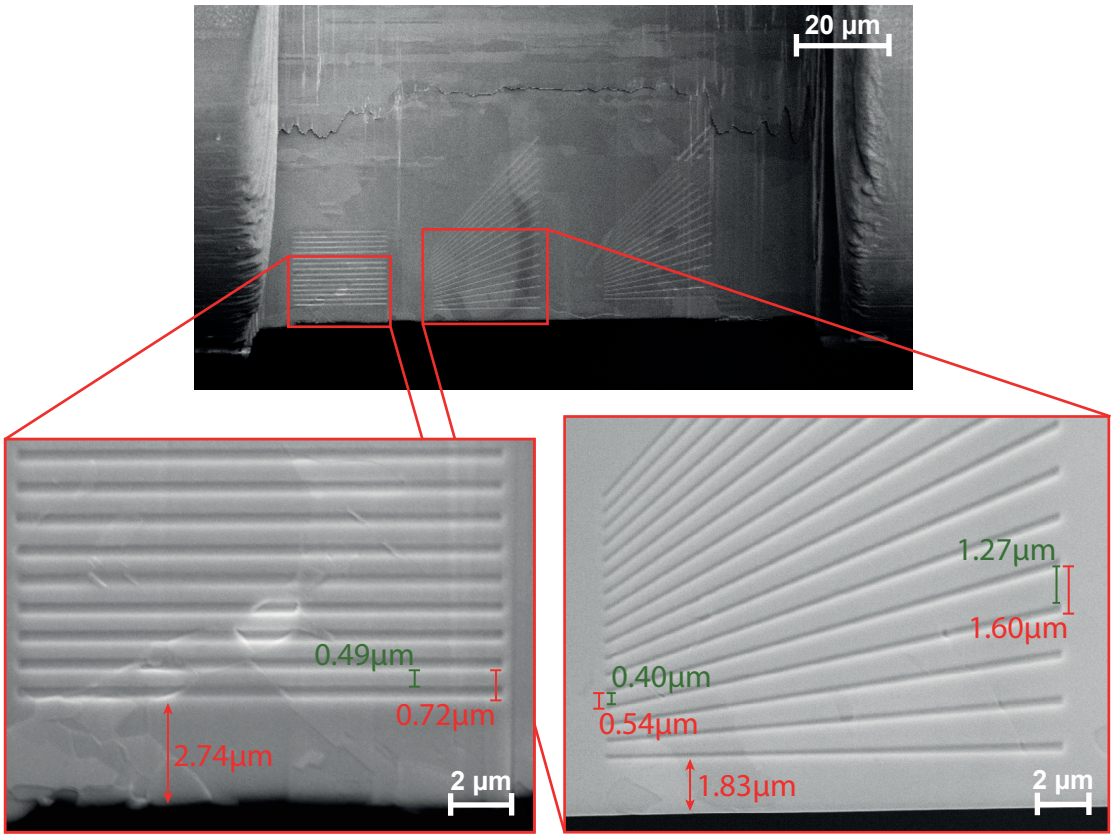

Figure 3.5: SEM micrographs of the chirped grating geometry. SEM micrographs with two detailed sections of a finished chirped grating sample. The imprinted grating resembles a fan-type grating (right) together with a linear reference grating (left). A single sample hosts several gratings with differing properties (i.e. duty cycle, propagation distance, grating period and depth). The fan-type grating is optimized for excitation wavelength ranging from 540 nm − 1.6 µm, while the reference grating is optimized for 720 nm.

3.2.1 Laser System

At ASL we use a titanium sapphire (Ti:Sa) laser system for the generation of few-cycle pulses. The low-power oscillator output is amplified by chirped pulse amplification (CPA) and hereafter spectrally broadenend via self-phase modulation (SPM) in a hollow-core fiber. Finally the fiber output is temporally compressed with a chirped mirror compressor, compensating also higher order phase distortions.

Oscillator

The Ti:Sa oscillator[9] generates the broadband seed for subsequent amplification. Its optical layout is displayed in Fig. 3.6 (a). The oscillator is pumped by a continuous-wave diode-pumped solid state laser system[10] (cw-DPSS laser) emitting an etalon-filtered single frequency of 532 nm. The pump-beam, focussed into the crystal by a lens (**L1**), is pointing stabilized using a piezo-mirror (**PM**) and a position sensitive quadrant diode (**QD**). The pumping power

[9] Spectra-Physics™; rainbow™ DFG seed
[10] Coherent Inc.; Verdi V6 UNO

applied to the oscillator crystal is altered to stabilize the carrier-envelope phase (CEP), using an acousto-optic modulator (**AOM**) for control and a **Fast Loop** device[11] for measuring CEP-drifts. For pulsed operation, the intra-cavity dispersion (using the wedges **W1**) is optimized for Kerr-lens mode locking. The pulses leave the cavity through the output coupler (**OC**) with about 12.5 % transmission and are temporally compressed by a chirped mirror compressor (**CPM1**).

The typical output spectrum is shown in figure 3.7 (a). The spectral bandwidth, exceeding 250 nm and centered around 800 nm, supports pulse durations of $\tau_{\mathrm{Osc}} = 5.7\,\mathrm{fs}$ (assuming Fourier-limited pulses). With an averaged output power of 300 mW and repetition rate of 75 MHz, pulse energies in the range of 4 nJ are feasible, in line with previous reports on comparable laser systems [163–165].

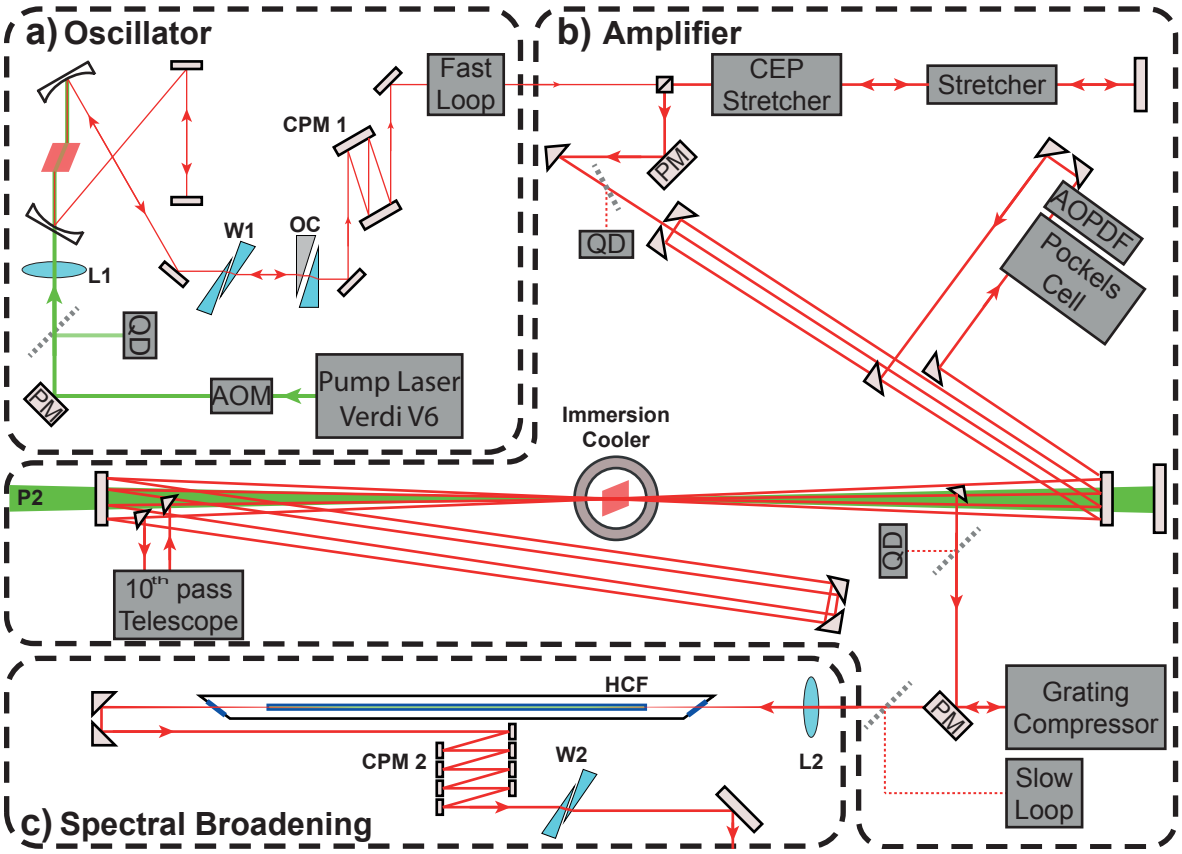

Figure 3.6: Illustration of the ASL laser setup. The laser system used to generate few-cycle pulses, is divided into three parts, the oscillator (**a**), amplifier stage (**b**) and spectral broadening (**c**).

Amplifier

As illustrated in Fig. 3.6, the pulses from the oscillator are directly traversed to the amplifier system[12]. To prevent damage to the amplifier crystal, the seed pulses are stretched to about

[11] Menlo Systems GmbH, XPS 800 Femtosecond Phase Stabilization
[12] Spectra-Physics™; FEMTOPOWER™ compact PRO HP/HR 3 kHz

12 ps in a SF-57 glass piece (**Stretcher**). The stretcher setup includes a moveable double-prism (**CEP Stretcher**) for controlling slow drifts in CEP, based on the **Slow-loop** signal. For amplification, the Ti:Sa crystal is pumped by 20 W optical power from a pulsed DPSS, single-frequency ($\lambda = 532\,\text{nm}$) laser system[13] (**P2**), operating at a repetition rate of 3 kHz. Piezo-controlled mirrors (**PM**) and quadrant diodes (**QD**) stabilize the seed beam through the multipass. In addition, aperture masks filter the beam profile spatially before every pass through the crystal, to reduce amplified spontaneous emission (ASE).

Before the fifth pass, up to which the full oscillator pulse train is amplified, the beam passes through the **Pockels Cell**. There, with proper triggering, single pulses at the repetition rate of the amplifier pump laser are selected. Subsequently, the pulses propagate through an acousto-optic programmable dispersive filter[14] (**AOPDF**), which shapes the spectral amplitude and phase to reduce nonlinear effects as gain-narrowing and conserve a larger bandwidth for short pulse generation. As displayed in Fig. 3.7 (a), despite the AOPDF, the amplification reduces the spectral bandwidth significantly to about 50 nm FWHM, lengthening the FL-pulse duration to $\tau_{\text{amp}}^{\text{FL}} \sim 18\,\text{fs}$ after the amplifier.
In another 5 passes, the isolated pulses are amplified to the final pulse energy of 800 µJ. Reflection gratings (**Grating Compressor**) compress the pulses in time to durations of $\tau_{\text{amp}} = 25.4\,\text{fs}$ full-width half-maximum, as can be calculated with Eq. (2.14) from the FRAC-trace displayed in Fig. 3.7 (b). The discrepancy between Fourier-limited and experimentally observed pulse durations must be attributed to residual phase distortions, that could not be fully compensated with the AOPDF. The grating distance is controlled with a micrometer screw for fine-adjustment of group delay dispersion (GDD). A small fraction of the amplified, compressed pulses is fed to the **Slow Loop** device[15], to compensate CEP jitter introduced from the amplifier. Together with the **CEP Stretcher** fluctuations below 40 Hz can be compensated.

Spectral Broadening and Pulse Compression

For generation of few-cycle pulses, the spectral bandwidth is increased via self-phase modulation in a hollow core fiber [116, 147, 150, 162]. As illustrated in Fig. 3.6 (c) the amplifier output is focused by a lens of $f = 1.5\,\text{m}$ (**L2**) into a fused silica hollow core fiber with an inner diameter $d_{\text{inner}} = 250\,\mu\text{m}$ and an approximate length of 1.0 m. With a static filling of neon gas at 1.0 bar, the spectral full width at half maximum exceeds 300 nm, as depicted in Fig. 3.8 (a). The Fourier-limited pulse duration of $\tau_{\text{fiber}}^{\text{FL}} = 3.9\,\text{fs}$, is equal to roughly 1.7 optical cycles.

Spectral broadening in HCFs leads to phase distortions, which are compensated by a set of low-loss chirped mirrors (**CPM2**). Residual imperfections in the phase compensation result in a temporal waveform differing from the Fourier-limit pulse duration: from fringe-resolved autocorrelation measurements the pulse duration is calculated to be around $\tau_{\text{fiber}} = 4.7\,\text{fs}$. The finite pedestal in the FRAC trace, as observed in Fig. 3.8 (b), indicates a non-ideal third-order compensation, which results in pre- or post-pulses in the temporal waveform.
The experimentally achieved fiber transmission can be in the range of 67 %. After the chirped-mirror compressor with a a typical transmission higher than 95 %, the few-cycle pulse energy, usable for HHG, is around 450 µJ.

[13] Photonics Industries International Inc.; DM 30 Q-Switched DPSS Laser
[14] FASTLITE; Dazzler
[15] Menlo Systems GmbH; APS 800 Amplifier Phase Stabilization

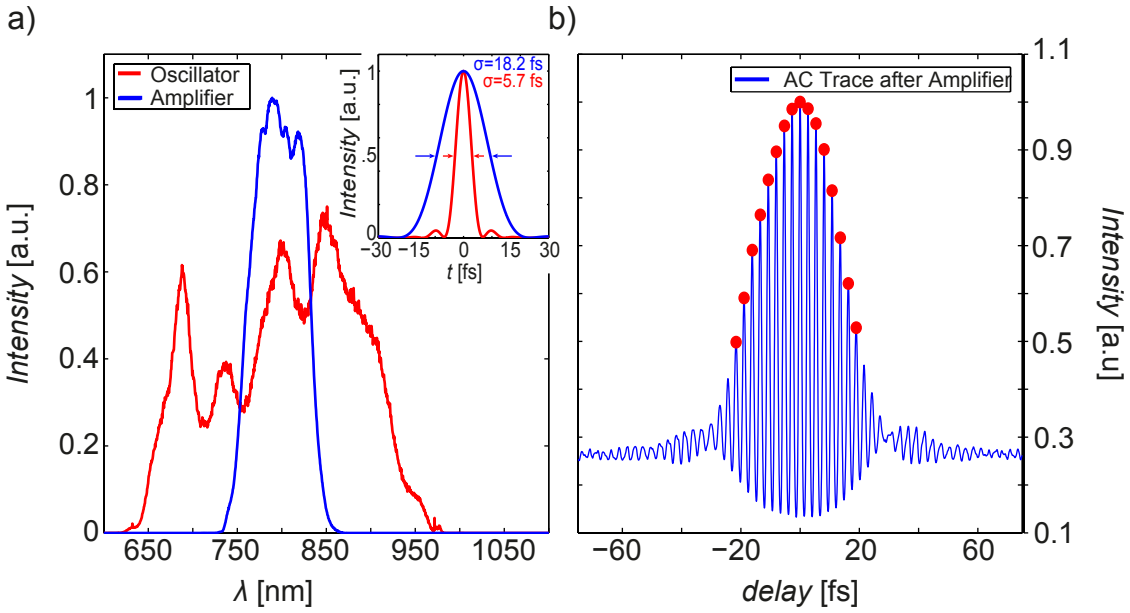

Figure 3.7: Amplifier and oscillator output spectra. The left panel **(a)** shows the normalized output spectra of the oscillator (red) and amplifier (blue). The inset shows the Fourier-limited pulse durations for the given spectra of $\tau_{\mathrm{osc}}^{\mathrm{FL}} = 5.7\,\mathrm{fs}$ and $\tau_{\mathrm{amp}}^{\mathrm{FL}} = 18.2\,\mathrm{fs}$ for oscillator and amplifier, respectively. From the FRAC trace, displayed in **(b)**, an experimentally obtained pulse duration of $\tau_{\mathrm{amp}} = 25.4\,\mathrm{fs}$ is retrieved for the amplifier output.

CEP Stabilization

The stabilization of the CEP is a crucial point for the feasibility of attosecond streaking experiments. Drifts and instabilities directly or indirectly affecting the CEP of the laser pulses can be manifold. Conclusively, searching the source of an unstable CEP can be a time-consuming and frustrating process, that is nevertheless highly necessary. Stabilizing the CEP is divided into two parts, where the first directly applies a lock-in-technique to the oscillator cavity, typically referred to as *fast-loop* stabilization. The second measures the CEP as close as possible to the experimental setup and tries to account for CEP fluctuations accumulated in the beam path, typically referred to as *slow-loop* stabilization.

In the temporal domain, the output of a mode-locked laser cavity is observed as a train of pulses, where each pulse is fully described by a Gaussian envelope function, carrier frequency ω_0 and a CE-offset phase φ_{CE}, where the latter describes the offset between envelope function and the carrier wave. Transferred into the spectral domain, the cavity output is described by a frequency comb, where the different modes have a fixed spacing, given by the laser repetition rate $f_{\mathrm{rep}} = 1/T$, where T is the duration of a cavity round trip (see Fig. 3.9). A difference of the CE-offset phase $\Delta\varphi_{\mathrm{CE}}$ for consecutive pulses, gives rises to a carrier-offset frequency

$$f_{\mathrm{offset}} = f_{\mathrm{rep}} \frac{\Delta\varphi_{\mathrm{CE}}}{2\pi} \tag{3.1}$$

which fixes the frequency comb in the Fourier domain [166]. Each mode ν_m, contained in the amplification profile is accordingly described by the repetition rate, the carrier-offset frequency and an integer number m, as $\nu_m = f_{\mathrm{offset}} + m \cdot f_{\mathrm{rep}}$.

Techniques for stabilizing the CEP at ASL, rely on the heterdyne mixture of different

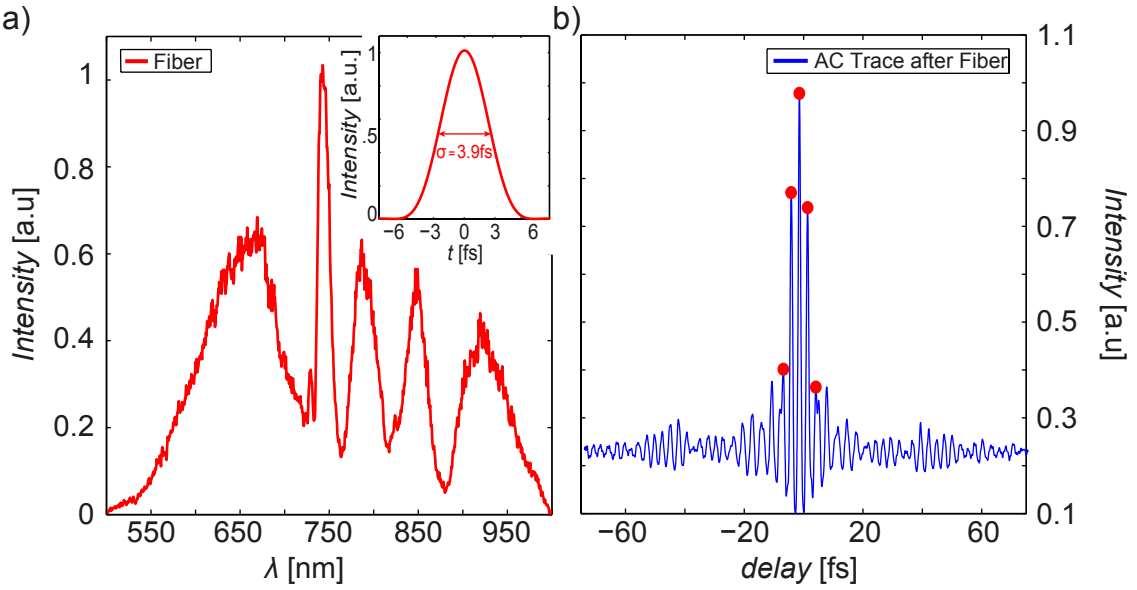

Figure 3.8: Fiber output spectrum and FRAC trace. On the left a typical output spectrum of the fiber system is shown **(a)**. The inset displays the calculated pulse duration for the given spectral width assuming ideal phase compensation (i.e. Fourier-limited pulses). The left panel **(b)** shows the measured FRAC trace after compressing the fiber output using low-loss chirped-mirrors. From the measurement $\tau_{\text{fiber}} = 4.7\,\text{fs}$ is calculated.

spectral components. In the *fast-loop* detection scheme, illustrated in Fig. 3.9 (a), the difference frequency (DFG) spectrum of the fundamental amplification profile is generated, for which the offset frequency vanishes:

$$f_{\text{diff}} = (j f_{\text{rep}} + f_{\text{offset}}) - (k f_{\text{rep}} + f_{\text{offset}}) = (j-k) f_{\text{rep}} \,. \tag{3.2}$$

Given an octave spanning amplification profile, the DFG modes overlap with the fundamental spectrum. Two neighboring modes in the spectral overlap ($j-k=l$) of DFG and fundamental yield a beat signal, which directly provides the offset frequency

$$f_{\text{beat}}^{\text{DFG}} = f_{\text{diff}} - f_l = (n-m-k) f_{\text{rep}} + f_{\text{offset}} = f_{\text{offset}} \,. \tag{3.3}$$

Stabilizing the beat signal f_{beat} therefore results in CEP-stable pulse trains. For practical reasons the offset frequency is locked to an integer fraction of the repetition rate $f_{\text{offset}} = f_{\text{rep}}/n$ causing every n-th pulse to have an identical CEP.

In the *fast-loop*-stabilization scheme used at ASL, the difference frequency is generated using a periodically-poled lithium niobate crystal (PPLN). While the crystal optimizes the phase matching conditions for DFG, it additionally broadens the oscillator spectrum by self-phase modulation. Accordingly, the mixture of the DFG with the long wavelength components results in higher beat-signal amplitudes. The beat signal is filtered from the oscillator spectrum by a long-pass filter and detected with a fast IR-photodiode. Locking-electronics compare the beat-signal frequency with an integer fraction of the repetition rate. The repetition rate f_{rep} is detected by a photodiode inside the oscillator housing and electronically divided to the appropriate fraction (here $f_{\text{rep}}/4$). Based on the difference between these two signals, the electronics calculate an error-signal, corresponding to the time-integrated difference. The error signal serves as the feedback signal to the acousto-optic modulator (AOM) changing the

pumping power into the cavity and thereby the CEP-slip of the laser pulse train [167].

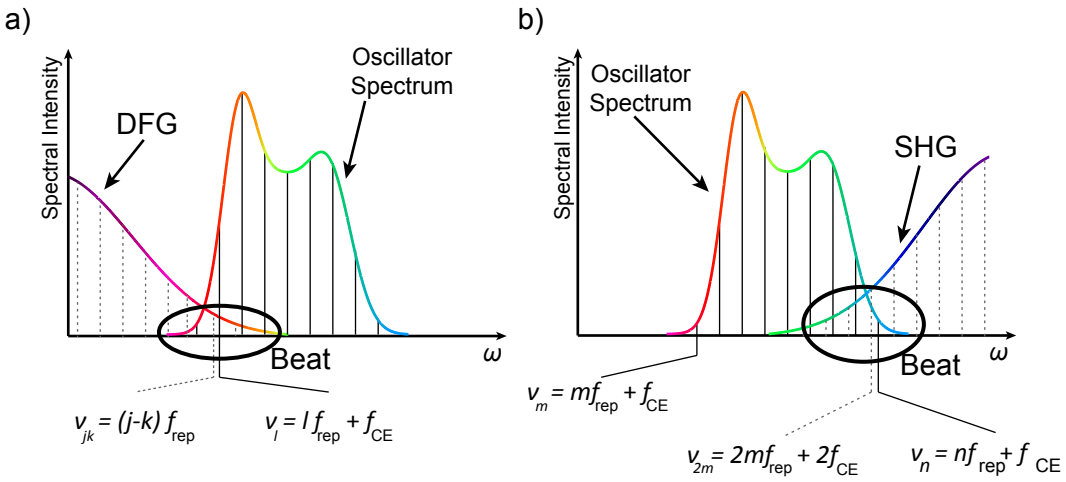

Figure 3.9: Principles of CEP Stabilization. The illustrated oscillator output spectrum contains several modes. Via heterdyne mixture of the fundamental spectrum with components generated by DFG **(a)** or SHG **(b)**, the CEP can be retrieved and stabilized. Adapted from [168].

The typical locking-time achievable at ASL is in the range of $5\,\mathrm{h} - 12\,\mathrm{h}$, depending on the daily stability of the system. Hereafter, the difference between beat signal and reference is too large to be compensated within the feedback-loop bandwidth of the PI-regulator and has to be pre-adjusted manually changing the intra-cavity dispersion.

As for the *fast-loop* scheme, the *slow-loop*-stabilization relies on the heterodyne mixture of different spectral components. As displayed in Fig. 3.9 (b), for the *slow-loop* stabilization, the second harmonic (SHG) is generated from the fundamental laser spectrum. Given that the fundamental spectral width exceeds an octave, the SHG signal will spectrally overlap with the fundamental. Since in an SHG process, the offset frequency f_{offset} is preserved, modes contained in the SHG comb have the form

$$f_{\mathrm{SHG}} = 2 \cdot (m f_{\mathrm{rep}} + f_{\mathrm{offset}})\,. \tag{3.4}$$

Heterodyne mixture of neighboring modes, i.e. $n = 2m$, in the region of spectral overlap between fundamental and second harmonic, will generate a beat signal according to

$$f_{\mathrm{beat}}^{\mathrm{SHG}} = f_{\mathrm{SHG}} - f_n = 2m f_{\mathrm{rep}} + 2 f_{\mathrm{offset}} - 2n f_{\mathrm{rep}} - f_{\mathrm{offset}} = f_{\mathrm{offset}}\,. \tag{3.5}$$

In contrast to the *fast-loop*-stabilization, the *slow-loop*-scheme at ASL uses spectral interferometry to detect the CEP. Here, a small fraction of the compressed multi-path output ($\leq 10\,\mu\mathrm{J}$) is used for CEP detection. The beampath is shown in Fig. 3.10 (a). The signal pulses are attenuated using a rotatable neutral density filter (**ND**) and focused ($\mathbf{L}_1$) into a 1 mm-thick sapphire plate (**SP**) for spectral broadening. The polarization is adjusted using a halfwave plate (**WP**). The spectrally broadend pulses are focussed ($\mathbf{L}_2$) into a 500 µm-thin β-barium borate crystal (**BBO**) where the second harmonic is generated (SHG) from the long-wavelength infrared-part of the spectrum. A rotatable polarizer (**RB**) is used to project the fundamental blue part and SHG onto the same projection axis and balances the intensities

of both contributions. The pulses are spectrally filtered, cutting out the long wavelength components and are focused into a **spectrometer**, where the spectral intensity $I(\omega)$ is detected. For the spectral region, where fundamental and second harmonic overlap, the spectrometer signal yields

$$I(\omega) = I_f(\omega) + I_{2f}(\omega) + \sqrt{I_f(\omega) I_{2f}(\omega)} \cos(\phi_f(\omega) - \phi_{2f}(\omega) + \omega\tau + \varphi_{\mathrm{CE}}) \quad , \tag{3.6}$$

where $\phi_f(\omega)$, $\phi_{2f}(\omega)$ and φ_{CE} are phases of the fundamental, SHG and the CE-phase, respectively, while $I_f(\omega)$ and $I_{2f}(\omega)$ represent the intensity of the fundamental and second harmonic. The temporal delay τ between fundamental and SHG changes the modulation frequency imposed on the spectral intensity. While $\omega\tau$ is determined by the experimental setup, it can generally not be measured with the demanded accuracy to evaluate φ_{CE} directly from the intensity modulation.

A measurement of the spectral intensity taken at ASL is displayed in Fig. 3.10 (b). Fourier transformation of the spectrometer signal retrieves the modulation frequency, determined by the CEP. However, the delay τ between fundamental and SHG signal must be controlled to meet the spectral resolution of the interferometer at the region of spectral overlap. Since $\omega\tau$ is fixed, stabilizing the CEP is equivalent to stabilizing the modulation frequency imposed on the spectral intensity. The latter is achieved with a PID regulator, calculating a feedback voltage to the **CEP Stretcher**-stage (Fig. 3.6), which controls dispersion via the insertion of a glass prism in the beampath.

In the ASL, CEP stability reaches values in the range of $\sigma^{\mathrm{rms}} = 447\,\mathrm{mrad}$ and can be stabilized as long as the fast-loop locks the CE phase (see Fig. 3.10 (c) and (d)). The typical bandwidth of the PID regulator for the ASL configuration is in the range of 40 Hz. The major drawback of the ASL slow-loop system is the position inside of the amplifier, reducing the compensation of CEP drifts to the beam path inside the amplifier system. Beam-pointing and power fluctuations influencing the SPM inside the fiber can cause CEP fluctuations [169]. Additionally, air-fluctuations on the beam-path between fiber output and chamber entrance window can increase the phase noise. In the ASL setup, the latter two CEP jitter sources are currently not detected and cannot be accounted for.

3.2.2 ASL-Beamline Layout

The ASL beamline is an interferometer developed for pump-probe spectroscopy of gaseous targets with attosecond precision. A schematic drawing of the ASL beamline is shown in Fig. 3.11.

The attosecond beam is generated via HHG from the near-infrared few cycle-pulse. Since the attosecond beam with central wavelengths λ_{c} from $8\,\mathrm{nm} - 20\,\mathrm{nm}$ would be absorbed in air, the whole interferometer is placed in vacuum. Based on the layout, the beamline can be separated into three major parts, namely the high harmonic generation chamber, a differential pumping section and the experimental chamber. All three sections, joint together by hand-driven gate valves, can be vented independently. As common for any attosecond beamline, the highest pressure is reached in the HHG-chamber, rising to $10^{-2}\,\mathrm{mbar}$ while the gas flow into the HHG target is running. Two turbopumps[16], optimized for high gas loads with pumping speeds of $250\,\mathrm{l\,sec^{-1}}$ each, are attached to the HHG chamber and can reach a base pressure of $10^{-6}\,\mathrm{mbar}$ without HHG gas-flow.

[16] Adixen; MDP 5011

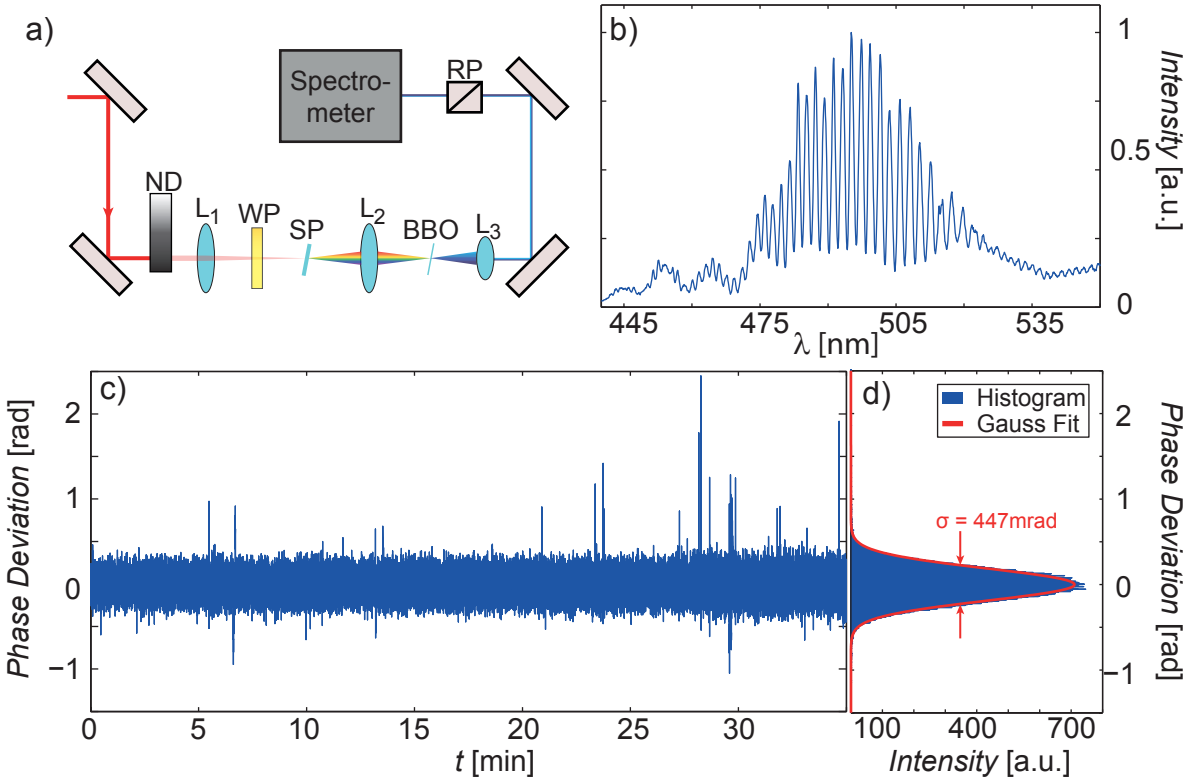

Figure 3.10: Operation of the ASL slow-loop system. Subfigure **(a)** illustrates the beam path of the slow-loop detection system. The modulation, imposed on the spectral intensity measurement **(b)**, encodes the CEP. By Fourier-transformation, the modulation frequency is calculated and stabilized by a PID feed-back to the intra-beam dispersion. Long-range measurements prove the CEP stability of the system **(c)** with a typical rms noise of $\sigma^{\mathrm{rms}} = 447\,\mathrm{mrad}$ **(d)**.

Between the high harmonic generation and the experimental chamber, a differential pumping section is introduced with two turbopumps[17] of $300\,\mathrm{l\,sec^{-1}}$ and $80\,\mathrm{l\,sec^{-1}}$ pumping speed, respectively. Decreasing the gas pressure towards the experimental chamber is the main task of the differential pumping section. In combination with a vacuum skimmer, the pressure level is reduced by at least two orders of magnitude.

The experimental section is pumped by a large $1200\,\mathrm{l\,sec^{-1}}$ turbopump[18] to achieve best vacuum conditions, necessary to operate the high voltage time-of-flight electron detector. The low pressure regime with less background gas pollution also supports higher contrast in the spectroscopic measurements on gaseous targets. Typically, we reach base pressures of $10^{-8}\,\mathrm{mbar}$. Even during operation with the HHG gas and target gas, the pressure in the experimental chamber is typically below $8 \cdot 10^{-5}\,\mathrm{mbar}$.
The turbopumps are backed by two oil-free scroll pumps[19], where one is reserved for the HHG chamber and the second for the differential pumping and experimental section. The flexible connection hoses between turbo- and scroll pumps are vibrational isolated against the optical table.

[17] Pfeiffer Vacuum GmbH; HiPace® 300 and 80
[18] Pfeiffer Vacuum GmbH; HiPace® 1200
[19] Dr. Ing. K. Busch GmbH; Fossa FO 0015/0035 A

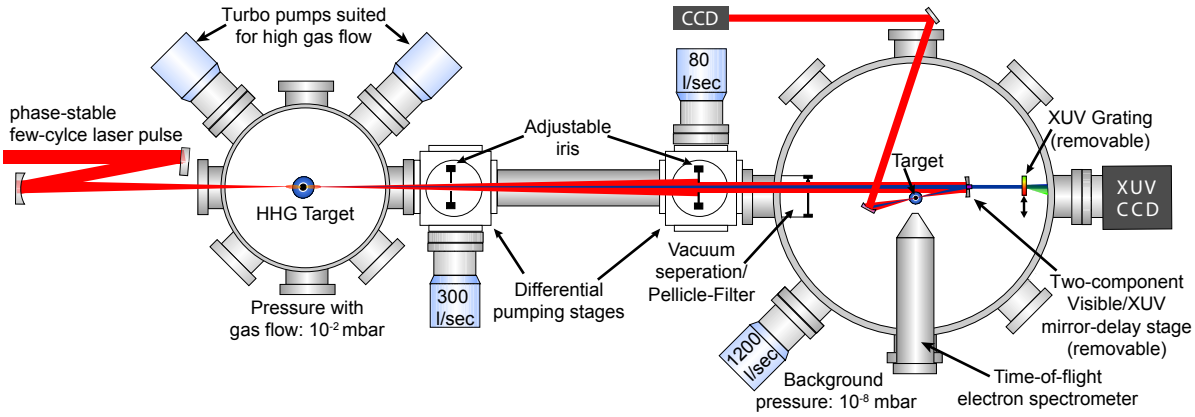

Figure 3.11: Scheme of the ASL-Beamline. The figure illustrates the main components and their arrangement within the experimental setup. A detailed description is given in the text. Adapted from [119].

Vibrational isolation of the interferometer against mechanical jitter is crucial for attosecond experiments, since an interferometric stability better than 10 as demands vibrational amplitudes lower than 3 nm. Mechanical vibrations are mostly generated by the rotation of the turbopumps. For the ASL beamline, we use posts that connect optical components via the intra-vacuum breadboard directly to the honeycomb optical table. The vacuum chambers, connected with the rotating turbopumps, rest on separate optical posts. Flexible, edge-welded bellows decouple the sensitive optical components from the vacuum chambers.

3.2.3 Generation and Characterization of High Harmonics

The few-cycle NIR laser beam is focused by a spherical mirror, $f^{\mathrm{HHG}} = 75\,\mathrm{cm}$, into a thin nickel tube (HHG-Target) with an inner diameter of $d_{\mathrm{inner}} \sim 2.5\,\mathrm{mm}$. The target is filled with neon or argon, depending on the required cut-off energy (see chapter 2). From the mode size on the focusing mirror $d = 10\,\mathrm{mm}$, the focal length f^{HHG} and the central wavelength $\lambda_0 = 700\,\mathrm{nm}$ for the few-cycle pulse, based on Gaussian beam optics, a focal spot size of about 67 µm in the HHG target is calculated. The focus size allows peak intensities on the order of $10^{14}\,\mathrm{W\,cm^{-2}}$, which are high enough to drill the entrance and output holes for the laser beam through the nickel tube.

The backing pressure of the target is adjusted using a flow controller, where a motorized gate valve regulates the flow to a given pressure set-point. The gas target can be moved in all three dimensions with a single step accuracy better than 50 nm. Backing pressure and target position are varied iteratively to meet phase-matching conditions for the specific energy window around 90 eV of high harmonic radiation.

After its generation, the XUV radiation co-propagates together with the NIR laser beam to the experimental chamber. Here, we use an XUV sensitive CCD-camera to characterize the spatial profile of the XUV beam. Together with a movable diffraction grating, the camera serves also as spectrometer. To protect the CCD chip from overexposure by the strong NIR field, a 500 nm-thick foil of Zirconium[20] is placed on the beampath to block photons below 50 eV energy. For energy calibration, thin transmission filters are introduced into the XUV

[20] Lebow Co; EUV-Filter foils

beam, where strong absorption edges based on inner shell excitations are observed. For the energy range between 60 eV and 140 eV, we use aluminum (Al) and silicon-nitride filters (Si_3N_4) foils, where L-edge absorptions at 72 eV and 100 eV are observed as illustrated in Fig. 3.12 (a).

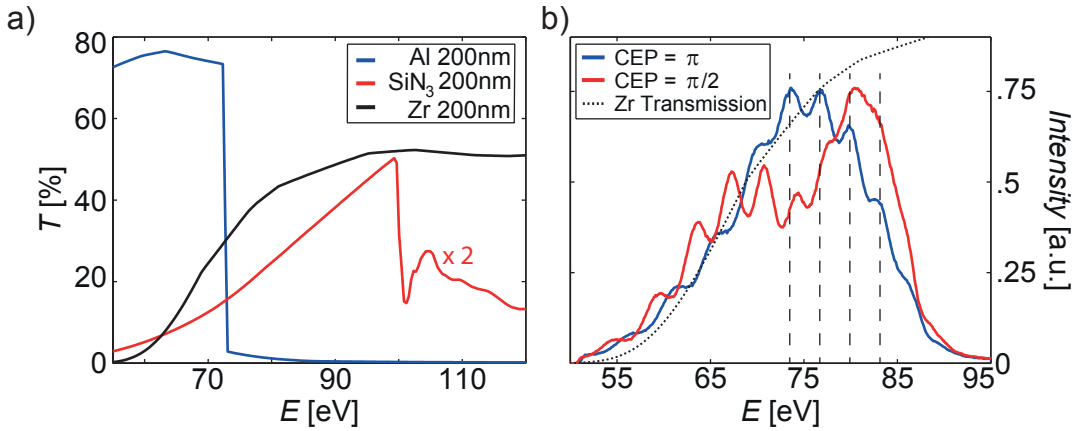

Figure 3.12: Filter transmission and HHG spectra. The left figure **(a)** illustrates the spectral transmission of different EUV filters and calibration foils. Subfigure **(b)** demonstrates the CEP dependence of the XUV spectra. From the superimposed dashed lines with an energy spacing of 2×1.6 eV the central wavelength of the driving pulse can be estimated to $\lambda_c = 729$ nm.

Applying the full fiber output power to the harmonics target, the HHG cut-off can increase up to 110 eV, corresponding to the 78^{th} harmonic. To generate isolated attosecond pulses within the reflectivity curve of the XUV optics, the harmonics cut-off should vary between 80 eV and 93 eV. Adjusting an iris in front of the HHG-target, the laser intensity can be controlled, thereby shifting the harmonics cut-off energy to appropriate values. Setting the CEP and dispersion, the temporal waveform of the NIR driving pulse is optimized to isolate a single attosecond pulse in the HHG cut-off. Generally, the isolation of a single attosecond pulse with high flux is an iterative process, where dispersion, HHG-target position, laser intensity and target pressure must be tuned iteratively.

Figure 3.12 (b) demonstrates the influence of the CEP on the HHG spectrum. As expected for the sine-like waveform of the NIR field (blue curve) the whole spectrum is modulated, since photons generated at different half-cycles can interfere. The cut-off energy is found to be slightly lower for sine-like waveforms. The cosine-like waveform (red curve) shows an increased cut-off energy, while spectral modulation is restricted to the low-energy spectral part. Accordingly, isolated attosecond pulses are discernible from non-isolated, based on measuring the XUV spectrum which is significantly faster than the temporal measurement recording a streaking trace.

3.2.4 Experimental Chamber

From the HHG-target, the few-cycle NIR and attosecond XUV beams co-propagate to the two-component visible/XUV focusing mirror. At the entrance to the experimental chamber, the two beams are spatially separated using a concentric pellicle-foil-filter. The central part forms a 150 nm-thin metal foil which is transparent for the attosecond pulse but opaque for the near-infrared femtosecond pulse. Mounted on a translation stage, the filter for spatial

separation can be moved out of the beam and replaced by the XUV transmission filters. The holder supports maximum four different filters. Located just at the entrance of the experimental chamber, the filters act as loosely sealed vacuum separators, improving the pressure in the experimental chamber.

Optical Components

After spatial separation, the NIR and XUV beams propagate onto the two-component mirror. The outer part, formed as mirror of one inch diameter with a central hole, is coated with a thin layer of boron carbide, which enhances the reflectivity to about 10 % for the NIR beam. The inner mirror with a diameter of 3 mm carries a Mo/Si multilayer coating to enhance the XUV reflectivity. At ASL we use different XUV mirrors with central photon energies of 80 eV, 85 eV and 93 eV. The bandwidth of 6.5 eV is equal for all XUV mirrors and supports pulse durations of about $\tau_{\text{atto}} = 280$ as. The maximum reflectivity amounts to 42 %, 41 % and 35 % for the different multilayer coatings. A typical reflectivity curve for the 93 eV mirror is shown in Fig. 3.13.
A custom-designed holder can manipulate the two mirrors independently with five degrees of freedom. The full stack is mounted onto a translation stage to drive the mirrors out of the beam and observe the spatial profile of the attosecond pulse on the XUV camera. The blazing diffraction grating is mounted onto the same stage and can similarly be positioned in the beam to resolve the XUV spectrum on the camera. Tip-tilt for the beam pointing can be controlled independently for the inner and outer mirror, respectively. Moreover the z-position of the outer-mirror can be adjusted to achieve temporal overlap for the interferometer. Using two manual stages the inner mirror is aligned concentric inside the outer mirror hole.

Delay between inner and outer mirror is driven by a high-precision piezo-actuated translation stage with a single step width of 3 as. The maximum travel range of the delay-stage is 100 µm, covering a maximum delay range between NIR and XUV of 660 fs. To increase the temporal stability of the interferometer, the piezo-stage features a self-referencing feedback-loop. With a focal length of $f = 12.5$ cm, inner and outer beams are focused onto the streaking target. Spatial overlap of both foci is achieved with the independent tip-tilt movement of the outer mirror. A pick-off mirror behind the focus sends the beam through an AR-coated lens to a CCD camera to image the focal plane. Besides the spatial overlap, the imaging system is also used to set the temporal overlap of the interferometer: assuming spatial overlap, the NIR intensity captured by the CCD becomes delay-dependent if the NIR laser illuminates the full double-mirror without spatial filtering by the pellicle filters.

For the ASL setup, focal spot sizes of NIR and XUV beams were not measured experimentally. Focal spot sizes of comparable systems have been reported to yield about 5 µm for the XUV beam, and between 25 µm – 100 µm for the NIR beam. [119,169]. For the AS-5 streaking setup, presented in the following section, the focal spot sizes of the NIR and XUV beams were measured based on the photoemission signal from nanostructured targets [119,148,151], which were found to be in good agreement with the values stated above. Therefore, for the ASL streaking setup, similar focal spot sizes can be assumed.

Target System

At ASL so far only gaseous compounds were under investigation. The gases enter the experimental chamber via feedthrough and are guided through a thin glass nozzle to the interaction

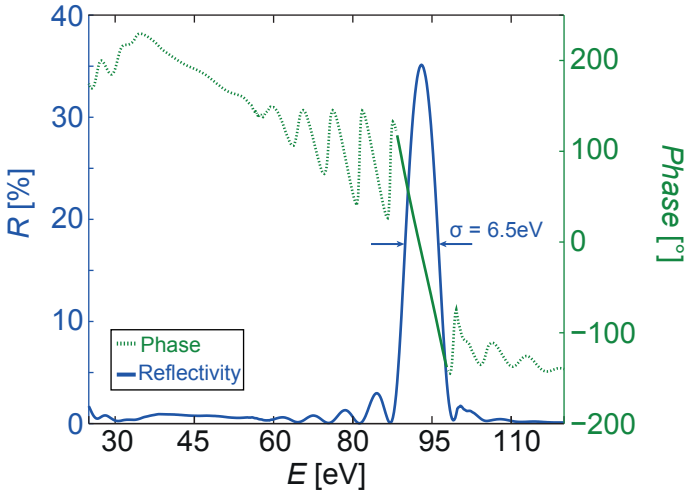

Figure 3.13: XUV mirror reflectivity curve. Simulated reflectivity and phase as a function of photon energy for the double mirror coating with peak reflectivity at 93 eV. Courtesy of Alexander Guggenmos.

volume. The opening of the nozzle varies between 50 µm and 200 µm. The target, manufactered from insulating soda-lime glass, is coated with a thin graphite layer to prevent charge-up. The nozzle is mounted onto an open-loop three-dimensional stage for position adjustment with an absolute single step precision of 30 nm.

For liquid target compounds we use a bubbler system, which contains feedthroughs for input and output. A driving gas, e.g. neon, is applied to the input and bubbles through the liquid. Molecules or atoms evaporate from the liquid and are guided together with the driving gas through the output tube to the gas nozzle in the experimental chamber. If necessary, the evaporation rate can be increased by heating the bubbler vessel.

Input and output of the bubbler can be closed separately by quarter-turn valves. The driving gas pressure is controlled with a needle valve which gives slight control on the ratio between molecules/atoms from the driving gas and the liquid, respectively. The output pressure to control the target density inside the experimental chamber is set with a fine-precision valve. For measurements on the pure driving gas, the bubbler system can be bypassed.

Electron Spectrometer and Data Acquisition System

For electron detection a commercial time-of-flight (TOF) spectrometer[21] is used. The TOF is equipped with an electrostatic lens to increase the solid angle for electron detection. Inside the drift tube with $l_{\text{drift}} = 350\,\text{mm}$, the electrons are shielded from stray fields by μ-metal plates. After the drift tube, the electrons are post-accelerated by several kilovolts onto a double stack multi-channel plate, where every photoelectron triggers a cascade of secondary electrons to result in a voltage drop of several tens of millivolts. To increase the dynamical range or the signal-to-noise ratio (SNR) a fast voltage amplifier[22] can be used.
A fast digitizer card[23], triggered by the laser system, detects each voltage drop, presuming it is below the threshold setting. With an ultimate bin-width of 100 ps, the digitizer card

[21] Stefan Kaesdorf - Geräte für Forschung und Industrie, ETF 10
[22] Becker und Hickl GmbH, HFAC-26 Wide Band Amplifier
[23] FAST ComTec Communication Technology GmbH, Multiple-Event Time Digitizer P7887

counts the number of bins between trigger and individual event, thereby measuring the flight time for each electron individually. Integrated over many events, the TOF detector directly acquires the photoelectron spectrum.

The digitizer card accumulates a specified number of laser shots and stores the photoelectron spectrum, i.e. number of electrons per TOF-bin as column separated file on a PC. Post-processing steps, like the conversion of the raw TOF spectrum to a photoelectron energy spectrum, as well as data analysis are done on a desktop PC.

3.2.5 Gas Phase Streaking

The usability of the ASL setup as an attosecond spectroscopic device is best demonstrated by streaking measurements on a common target. Due to the high ionization cross section between $40\,\text{eV} - 150\,\text{eV}$ [170], neon gas is widely used for reference and calibration measurements in attosecond streaking. In Fig. 3.14 (a) an experimental streaking measurement, taken at ASL, is displayed. With an XUV photon energy centered at 93 eV, the final kinetic energy of electrons ionized from the Ne 2p-shell is centered around 71 eV, as indicated by the black solid line. The low background indicates a reasonable focal shape of the NIR together with nearly perfect spatial overlap with the XUV beam. In the displayed streaking spectrogram, photoelectrons ionized from the Ne 2s-shell are discernible from the noise background, as indicated by the black dashed line. It should be mentioned that the lens-voltage on the TOF was optimized for collection of photoelectrons with final energies around 70 eV, reducing the collection efficiency of the 2s-electrons and explaining the low signal intensity.

The detached streaking trace demonstrates isolated attosecond pulses, with vanishing satellite contributions. Low broadening of the streaking trace while the electrons are up- and downstreaked, indicates a good interferometric stability. The streaking trace outline (black solid line in Fig. 3.14 (a)) is retrieved from the spectrogram by fitting a Gaussian function to the energy spectrum for each delay scan, as indicated exemplary in Fig. 3.14 (b). Since the streaking trace represents the NIR vector potential, the electric field $E(t)$ can be calculated.

Commonly, the streaking trace is analyzed in the Fourier domain (see also Eqs. (2.6) and (2.7)), obtaining the spectral amplitude $E(\omega)$ and phase $\Phi(\omega)$ of the NIR laser field. While the spectral amplitude, displayed in Fig. 3.14 (c), is slightly modulated, the spectral phase exhibits residual higher order terms, mostly third order dispersion that is not fully compensated and should give rise to pre- or post pulses in the temporal domain Before back-transformation into the time domain, the spectral amplitude is filtered with a super-Gaussian filter function. Spectral components outside the range between $450\,\text{nm} - 1250\,\text{nm}$ can not be related to the spectrum of the incident NIR laser beam and are withdrawn. After reverse Fourier transformation, the phase $\Phi(t)$ and the electric field strength $E(t)$ are obtained, as displayed in Fig. 3.14 (d). From the temporal intensity $I(t) \sim E^2(t)$, a pulse duration (FWHM) of $\tau_{\text{fs}} = 5.2\,\text{fs}$ is measured, which is in reasonable agreement with the FRAC measurements presented before. For the central wavelength $\lambda_0 = 730\,\text{nm}$, the pulse duration τ_{fs} equates about two optical cycles. Roughly 8 fs before the center of the main pulse, a weaker, almost single-cycle pre-pulse is observed, which could be expected from residual third-order terms in the spectral phase. The pre-pulse intensity is less than one tenth of the main pulse maximum intensity. The latter is calculated from the field strength yielding $I^{max} = 2.1 \cdot 10^{12}\,\text{Wcm}^{-2}$.

Using an LSGPA algorithm [118] for the retrieval, not only the spectral and temporal pro-

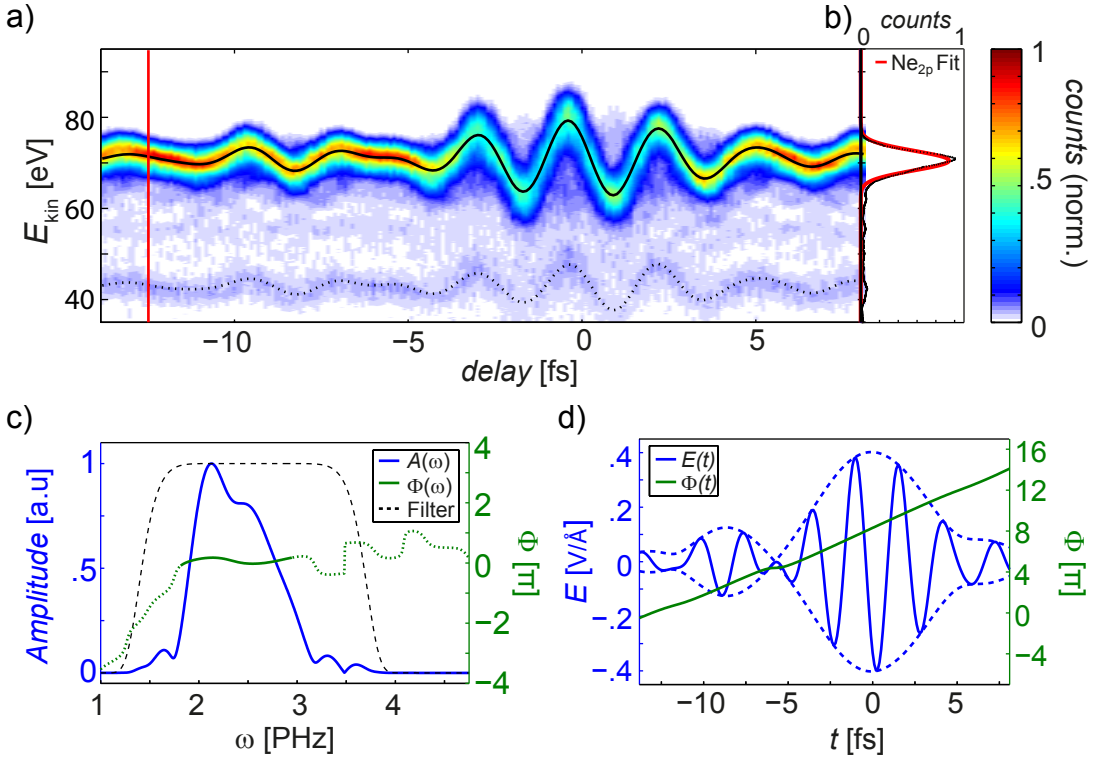

Figure 3.14: Experimental streaking data. The streaking spectrogram obtained in neon gas is illustrated in **(a)**. Photoelectrons emitted from the 2p-shell follow the solid black line, while 2s-emission follows the dashed black line. The solid red line indicates the delay step for the displayed photoelectron spectrum **(b)**. Subfigures **(c)** and **(d)** show the spectral and temporal domain of the NIR streaking field, obtained from a Fourier analysis on the solid black line.

file of the NIR streaking pulse is extracted, but also the spectral and temporal profile of the XUV attosecond pulse can be retrieved. After background subtraction, the retrieved spectrogram, shown in figure 3.15 (b), is in considerable agreement with the measurement displayed in (a). The derived attosecond pulse amplitudes and phases in the spectral and temporal domain are illustrated in subfigures 3.15 (c) and (d), respectively. Since the spectral phase contains non-compensated positive second order distortions, the streaking spectrogram shows less linewidth for the falling edges. Positive group delay dispersion (GDD) is inherent to the attosecond generation process, given that harmonics stem predominantly from short trajectories [95]. The filter foil for spatial separation and also the XUV focusing mirror add negative GDD, which partially compensate the attochirp of short trajectories. From the spectral width of the XUV mirror of 6.5 eV, pulse durations of $\tau_{\mathrm{atto}}^{\mathrm{theo}} = 280\,\mathrm{as}$ are anticipated. The retrieved attosecond pulse duration is $\tau_{\mathrm{atto}} = 306\,\mathrm{as}$ (intensity FWHM), being reasonably close to the expected Fourier-limit.

3.3 AS-5 Setup

The IR-IR cross correlation measurements and the experiments on attosecond streaking from metallic nanostructures were conducted at the AS-5 infrastructure at MPQ. While this chapter

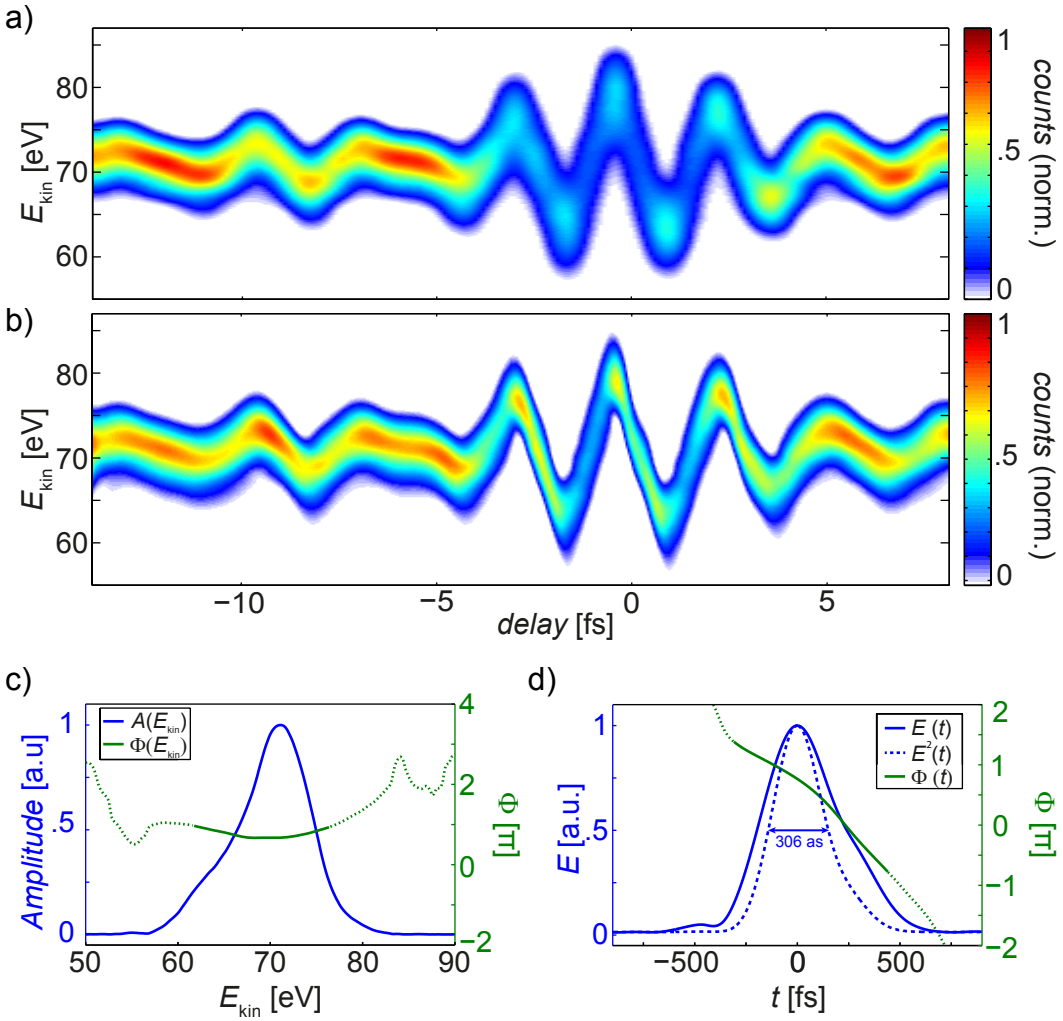

Figure 3.15: LSGPA retrieval. In **(a)** the retrieved spectrogram of the measurement in figure 3.14 is displayed. The spectral and temporal domain of the attosecond pulse analysis is shown in **(b)** and **(c)**.

only mentions the main parameters, it concentrates on pronounced differences to the ASL setup and special considerations or modifications for experiments on nanostructure targets. A thorough description of the setup can be found in e.g. [116, 147, 148, 151].

3.3.1 Laser System and CEP Stabilization

The AS-5 setup uses a Ti:Sa laser system. It consists of a Ti:Sa oscillator, whose output is amplified in a nine pass CPA design, resulting in pulse energies exceeding 2 mJ. Since the laser system is shared with the Petawatt Field Synthesizer (PFS), the laser repetition rate yields 500 Hz or 1 kHz for the AS-5 experiments. The pulses are compressed in a hybrid scheme, consisting of two prism pairs together with 16 reflections on high-dispersive mirrors, which reduce the pulse duration to 27 fs before the fiber. For spectral broadening, the pulses are focused with a lens of $f = 1.75$ m into a hollow core fiber of 275 µm inner diameter and one meter length. A static filling with neon of 3 bar absolute pressure generates an octave span-

ning spectrum that is hereafter temporally compressed by ten reflections on chirped mirrors, resulting in few-cycle pulse durations below 6 fs.

The fast-loop stabilization in the AS-5 laser system is similar to ASL, where a feedback-loop acts on an AOM to change the pump power to the oscillator cavity. While the ASL slow-loop compensates CEP drifts only up to the amplifier output, the AS-5 scheme is located behind the fiber output, capable of compensating drifts introduced on the beampath or directly by the fiber itself. The slow-loop feedbacks to a translation stage in the hybrid compressor, where one of the prism pairs is moved for dispersion compensation. Typical values for the shot-to-shot phase noise range from 300 mrad to 650 mrad depending on the daily performance. Recently, a feed-forward stabilization scheme[24] was installed, where phase noise as low as 220 mrad could be achieved. However, during the experiments presented here, the feed-forward scheme was not yet installed.

The distance between laser output on the first floor to the experimental setup on the ground floor is more than eight meters. Two commercial stabilization setups after the laser output and before the fiber are necessary to reduce beam pointing fluctuations. However, due to the long beam path, the pulse parameters are prone to higher noise, making high-sensitive experiments challenging.

3.3.2 AS-5 Beamline Layout

The operation principle of the AS-5 beamline, commissioned in 2012, is qualitatively identical to the ASL-beamline. Its layout is displayed in Fig. 3.16, illustrating the four main sections comprising the high-harmonic generation, spectrometer, filter section, and the experimental chamber.

In the streaking experiments, the attosecond pulses are generated in neon gas, where

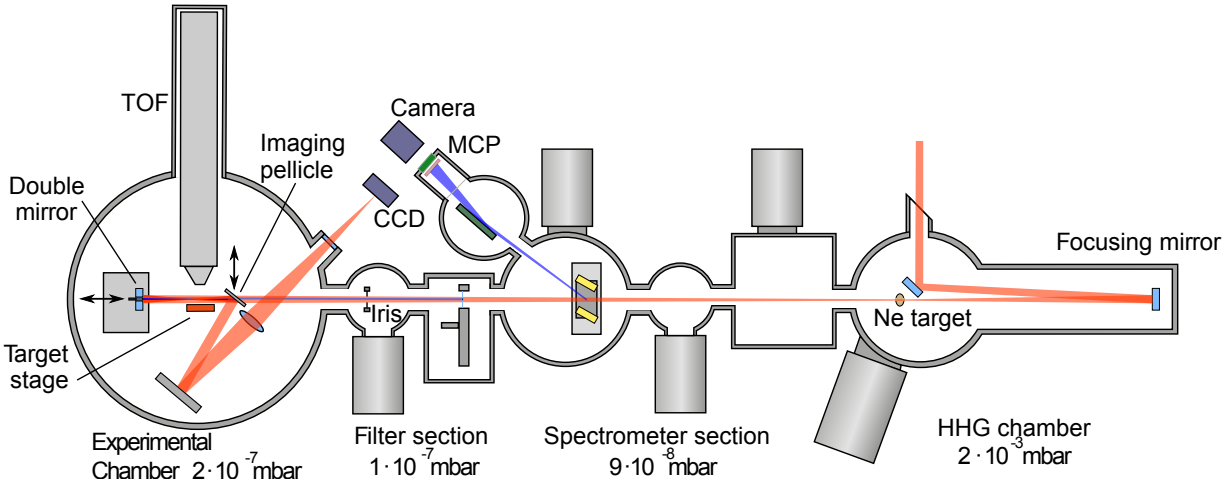

Figure 3.16: Schematic illustration of the AS-5 beamline. The layout displays the setup using the short focal length XUV mirror as described in Sec. 3.3.3. Adapted from [116, 148].

the NIR field is focused by a spherical mirror with $f^{\mathrm{HHG}} = 50\,\mathrm{cm}$ into a 2.5 mm wide nickel tube. Spectrum and spatial profile of the high harmonic radiation is characterized within

[24] Spectra-Physics™; Rainbow CEP 4™

the spectrometer section, using a flat-field corrected, grazing incidence grating and an MCP with phosphor screen. For the given pulse energy and duration, the high-harmonic cut-off typically exceeds 120 eV. After spatial separation in the filter section, the XUV and NIR radiation is reflected by a double mirror inside the experimental chamber with focal length $f^{\mathrm{XUV}} = 12.5\,\mathrm{cm}$. The inner mirror carries a XUV optimized coating, isolating a single attosecond pulse, centered at 93 eV with 7.5 eV bandwidth. Both beams are focused under a small angle of 5° relative to the incident beam in front of the TOF[25]. After traversing the focus, the NIR beam is coupled out of the chamber and imaged with a CCD camera.

The nanotargets are positioned in the focus using a three-dimensional stage: movement of the target along the beam propagation direction is done by an open-loop stage, movement in the focal plane is conducted by closed-loop stages, where each stage has a single step width of 30 nm.

As reported in [151], the XUV focal spot size was found to be around 5 µm, measured as full width at half maximum. The minimum focal spot size for the NIR beam is estimated to be larger than 25 µm, measured as FWHM of the focal intensity profile.

3.3.3 Short Focal Length Double-Mirror

For the studies of plasmonic excitations on nanotargets (see also chapter 4), the excited plasmons are pumped and probed on distant positions ($\sim 10\,\mu\mathrm{m}$) of the target. Since pump and probe beam from inner and outer mirror, respectively, should ideally not overlap, the focal spot sizes should be smaller than 10 µm. The latter is achieved by reducing the focal length to $f^{\mathrm{XUV}} = 2.5\,\mathrm{cm}$. Since for short focal length astigmatic aberration become more severe, the beam path is adopted to almost direct back-reflection. A small downtilt of the double-mirror ensures that the focal spot does not overlap with the incoming XUV beam. The near back-reflection scheme affords a removable pellicle (R = 8 % and T = 92 %) to out couple the beam onto the imaging-CCD without blocking the incoming beam (see Fig. 3.16).

To measure the focal spot size of the NIR and XUV beam, respectively, we exploit the emission of photoelectrons in a strong field process (NIR) and direct, linear photoionization (XUV). For the focal spot size measurements, etched metal nanotips are moved in the focal plane, while the photoemission signal $S(x, y)$ from the NIR or XUV beam is recorded. The strong field photoemission, triggered by the NIR beam is in particular for low intensities restricted to the tip apex, where field enhancement is observed. For the given central wavelength of the NIR beam, a single photon carries the energy of about 1.7 eV, which is not enough to overcome the work function of gold, reported to be around 4.8 eV [171]. For emission of an electron, at least $n = 3$ photons must be accumulated, therefore the photoelectron signal $S(x, y)$ is proportional to $I^n \sim E^{2n}$, with n, I and E being the order of photoemission, laser intensity and field strength, respectively. From the photoelectron signal $S(x, y)$, the focal spot size, defined as FWHM of the laser intensity profile, can be calculated. Assuming the spatial profile for the focal spot to be described by a Gaussian function in horizontal and vertical dimension, the spot size is given by:

$$\mathrm{FWHM}\{I(x,y)\} = \sqrt{n}\cdot\sqrt{2}\cdot\mathrm{FWHM}\{S(x,y)\} = \sqrt{6}\cdot\mathrm{FWHM}\{S(x,y)\} \quad . \tag{3.7}$$

[25] Stefan Kaesdorf - Geräte für Forschung und Industrie; ETF11 - elongated drift tube

The measurements of the NIR focal spot sizes for inner and outer mirror are displayed in Figs. 3.17 a) and b), respectively. The calculated FWHM diameters according to Eq. (3.7) are listed in table 3.1. The focal spots for inner and outer mirror are elongated along the vertical direction, which could result from the downtilt of the double mirror. Averaged over the horizontal and vertical directions, the intensity FWHM diameter of the inner and outer mirror yield approximately 7.1 µm and 5.4 µm. As expected, the outer mirror spot size is found to be smaller compared to the inner mirror, resulting from the larger beam diameter on the mirror. However the outer mirror focus spot size is larger with respect to the inner mirror than one would expect from simple scaling based on the beam diameter ratio of 2:1 on outer and inner mirror. The latter could result from stronger diffraction effects due to the holey shape of the outer mirror.

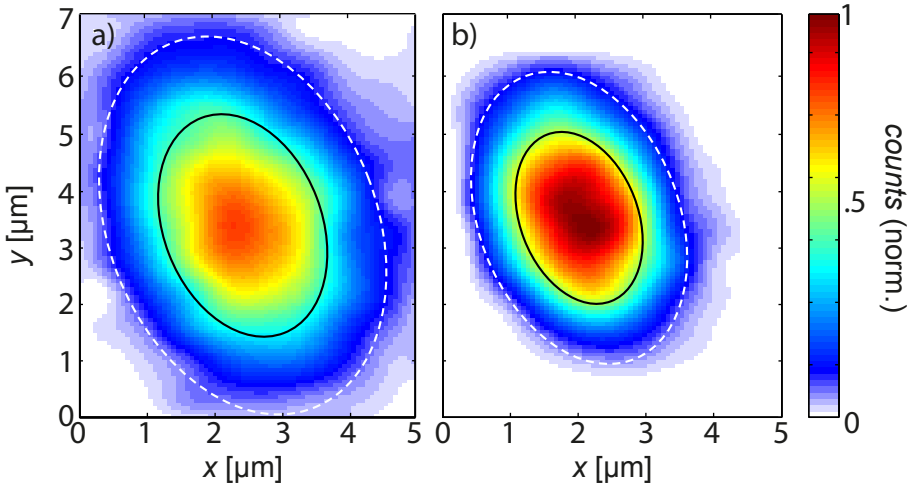

Figure 3.17: NIR focal spot size. Illustration of the photoelectron signal $S(x, y)$ measured for the inner **(a)** and outer **(b)** mirror. Solid black lines, and dashed white lines indicate the FWHM and $1/e^2$ diameters, respectively.

Despite the measurements being performed with low NIR intensities, at the onset of strong field emission, the photoelectrons could still be excited by more than the minimum number of three electrons. The given values equate a lower limit for the focal spot sizes, since with higher photoemission orders, according to Eq. (3.7) the calculated spot sizes would increase with the square root of the photoemission order n.

The XUV focal spot size is measured in a similar way. The XUV photon energy of $E = (93.0 \pm 3.75)\,\mathrm{eV}$ permits direct electron transition into a continuum state and since the field strength of the XUV pulse is small, nonlinear processes can be neglected. Photoionization after excitation with an XUV photon can thus be considered a linear one photon process. Accordingly, moving the tip across the focus and recording the photoelectron signal gives, unlike the NIR case, a shadow image convoluted with the XUV focal spot size.

In Fig. 3.18 (a), the photoelectron signal from XUV photoionization is displayed for moving the tip vertically through the focal plane, measuring the vertical XUV focal spot diameter. With respect to the vertical axis, the tip appears to be mounted under a small angle, which is corrected in the retrieval of the focal diameter. The photoelectron signal is almost homogeneous. Several strong emission sites can be observed, which could result from the target

	Inner Mirror		Outer Mirror	
	vertical	horizontal	vertical	horizontal
FWHM [µm]	8.41 ± 0.75	5.78 ± 0.56	6.51 ± 0.61	4.30 ± 0.70
$1/e^2$ [µm]	14.25 ± 0.90	9.78 ± 0.67	11.03 ± 0.73	7.28 ± 0.84

Table 3.1: Size of the intensity focal spot of inner and outer mirror, calculated from the photoelectron signal $S(x, y)$ displayed in Fig. 3.17. All numbers are given in micrometers.

structure perpendicular to the focal plane: since photoexcited electrons can only escape from within a thin surface layer, locally higher count rates can be expected for a corrugated surface.

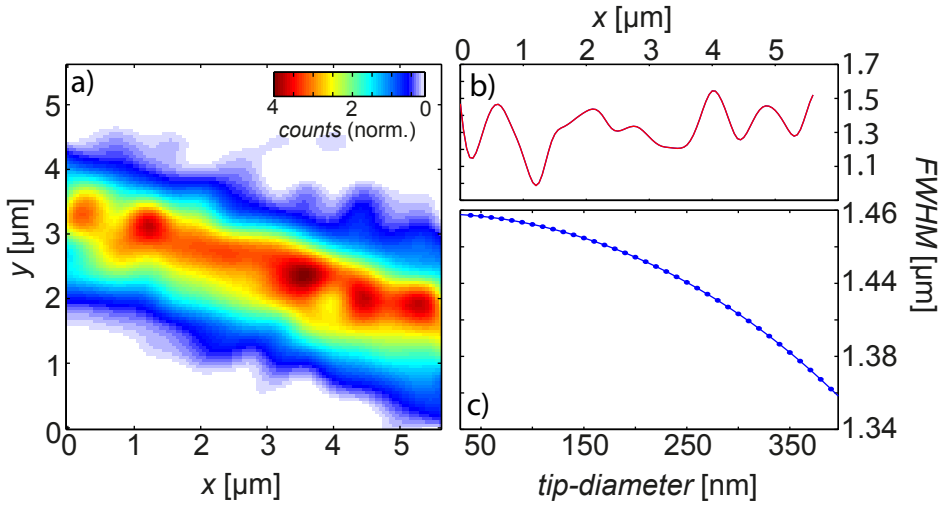

Figure 3.18: XUV focal spot size. Illustration of the photoelectron signal $S_{\mathrm{XUV}}(x, y)$ measured for XUV photoionization **(a)** for reflections from the inner mirror. The convoluted focal spot size **(b)** is extracted from a Gaussian fit to the photoelectron signal. The deconvoluted focal spot size as a function of tip-diameter is displayed in **(c)**.

For the XUV focal spot a Gaussian function is expected, while the nanotip is described by a rectangular function with a width given by the tip diameter. The convoluted signal is therefore again described by a Gaussian function with increased FWHM. The vertical FWHM focal spot size, extracted from a Gaussian fit to the experimental photoelectron signal from Fig. 3.18 (a), is displayed along the horizontal axis in Fig. 3.18 (b), giving $f_{\mathrm{conv}}^{\mathrm{ver}} = (1.49 \pm 0.07)$ µm as weighted mean value. From the SEM image 3.2, the tip diameter, far from the apex, is estimated with $d = 300$ nm, giving an deconvoluted XUV focal spot size of $f_{\mathrm{XUV}}^{\mathrm{ver}} = (1.40 \pm 0.06)$ µm. The deconvoluted focal spot size, as a function of the tip diameter is illustrated in Fig. 3.18 (c). Since the deconvoluted spot size changes by less than 10 % for tip-diameters ranging from 100 nm to 350 nm, a rectangular shaped tip with fixed diameter is a well-suited approximation even for nanotaper geometries with full opening angles up to 12°. Moving the nanotarget horizontally through the beam, yields $f_{\mathrm{XUV}}^{\mathrm{hor}} = (1.05 \pm 0.1)$ µm using the same retrieval algorithm [148].

Chapter 4

Cross-Correlation Measurements of Surface Plasmon Polaritons

4.1 Introduction

Surface plasmons emerge as coherent, collective response of free charge carriers to external electric fields at a conductor-dielectric-interface and gained vast interest in recent decades. Their key property, which allows to confine electromagnetic radiation beyond the diffraction limit to sub-wavelength spatial scales gives rise to multifaceted applications such as spectroscopy [172–174], sensing [175–178] and enhanced nonlinear emissive processes [179, 180]. Only in recent years, electronic circuitry became another essential application in the field of plasmonics, which is rapidly growing in significance. Up to date, information technology relies on the transfer of charges to realize functional operations in conventional, silicone-based circuitry. However, with shrinking spatial dimensions of operational building blocks for increased computational speed and data transfer rates, silicone-based circuitry starts to experience fundamental limits, e.g. by increased tunneling currents, which demands a paradigm shift for future electronic devices. While photonics bears the potential to take computational power to a new level [161], the typical spatial dimensions for photonic devices are on the wavelength level, i.e. micron range [181]. Since plasmonics allows to confine electromagnetic radiation to nanoscale spatial dimensions, this technology offers the possibility to bridge the gap between conventional and lightwave circuitry [30] and is accordingly considered as fundamental cornerstone in future information technologies [182, 183].

Confinement and enhancement of electric fields is observed simultaneously for localized surface plasmons (LSP) and propagating surface plasmon polaritons (SPP). Especially the latter allow to transport signals and thereby information along a conductor/dielectric interface [184], which makes SPPs highly desirable for ultrafast waveguide applications. In several studies various types of plasmonic waveguides were investigated in terms of plasmon propagation length, where the geometric structures range from single metal films [185–189] and multilayer systems formed as metal/insulator/metal (MIM) slabs [190, 191] to more sophisticated structures like chains of metal nanoparticles [192–195] and metallic nanowires [196–199]. While static measurement methods are capable to capture SPP propagation lengths for plasmonic waveguides, recent advances in time-resolved instrumentations offer the opportunity to resolve dynamic properties of SPP propagation, which is a crucial prerequisite for the understanding and development of SPP-based circuitry. For instance Wulf *et al.* applied

ultrafast near-field microscopy to investigate dispersion effects on the temporal waveform of SPP pulses, where they demonstrated that the temporal envelope at a central wavelength of 1550 nm with 120 fs duration remains unchanged while propagating along Au waveguides [200]. Based on numerical calculations, the authors predict insignificant temporal broadening of the SPP pulses for a wide range of geometries even for durations as short as 10 fs, which is well in the few-cycle regime at the respective telecommunication wavelength. In another study on tapered waveguide geometries, where the SPPs, centered around 800 nm, are launched at a diffraction grating, Berweger *et al.* could demonstrate experimentally SPP pulse durations around 16 fs with full waveform-control [159]. Exciting the SPPs with ultrashort few-cycle NIR pulses, ultimate SPP pulse durations as short as 7.7 fs were only recently achieved for a similar geometry [201].

Besides propagation effects on SPP pulse durations, the group velocity of surface plasmons centered around 0.8 µm for various waveguide geometries was investigated. At the vacuum interface of macroscopic, atomically flat Au films, large group velocities around $0.95\,c$ were reported from experimental studies, which are in almost perfect agreement with numerical simulations based on finite-difference time-domain (FDTD) calculations [202]. Nanostructured waveguides, whose dimensions approach the characteristic length scale of the SPP wavelength, exhibit in general smaller group velocities as would be expected from plain surfaces [55, 203]. The latter could be demonstrated experimentally on different nanowire geometries [197, 200, 204]. Only recently, the adiabatic focusing effect itself and its impact on SPP propagation was determined experimentally, revealing a group delay around 10 fs for SPPs propagation along an Au nanotaper of about 8.5° opening angle and 20 nm apex radius [160].

In this chapter pump-probe measurements are presented, which employ the nonlinear multi-photon photoemission from sharp Au super-tips to characterize the temporal dynamics of surface plasmon polaritons. First results based on this approach were reported in Ref. [148], while the present chapter includes an enlarged data basis and revised analysis methods. The SPPs are generated using a few-cycle NIR laser pulse, which is focused to a diffraction grating engraved into the target surface. After their excitation, the plasmons propagate onto a tapered nanowire towards a super-tip apex of 5 - 10 nm radius. At the nanoscale tip apex, where multi-photon photoemission is observed, the SPP electric field is temporally overlapped with a few-cycle NIR laser pulse of variable delay. The photoemission yield of the cross-correlated electric fields, recorded by a time-of-flight detector, is, due to its nonlinear dependence, a highly sensitive probe for the electric field strength. Given that the NIR pulse parameters are known, the delay-dependent photoemission yield gives access to fundamental SPP properties, e.g. pulse duration, field amplitude and central frequency. Additionally, the delay-dependent measurement reveals the SPP propagation time between excitation point at the grating and probing at the super-tip apex. Together with the propagation distance, calculated based on the sample geometry, the average SPP group velocity can be retrieved from the delay-dependent photoemission measurements.

4.2 Approach

The experiments are performed at the AS-5 infrastructure, using the short focal length double mirror with $f = 2.5$ cm as presented in the previous chapter. Briefly, an octave-spanning few-cycle NIR pump beam is focused by the outer part of the double mirror onto a grating

supertip sample (see Sec. 3.1.2) to excite surface plasmon polaritons. The linear grating with step width of 1.3 µm is written on the shank side of a pyramidal cone with 42° full opening angle (see Fig. 3.3). Accordingly, for an incidence angle orthogonal to the cone axis, ideal phase matching demands an excitation wavelength of $\lambda = 633\,\text{nm}$. Since we use an octave-spanning few-cycle laser pulse, centered around 740 nm, phase matching on the grating is achieved for a broad range of incidence angles. Nevertheless, for the linear geometry of the grating a reduced spectral bandwidth for the SPP compared to the NIR laser pulse has to be expected. Subsequent to their excitation, the surface plasmon polaritons propagate towards the apex of the pyramidal cone, where they pass over onto a sharp needle, attached to the cone apex. The latter, referred to as super-tip, features a full opening angle of roughly 5° and extends about 1.5 µm from the cone. Propagating along the super-tip, surface plasmons are adiabatically focused and ultimately enhanced at the super-tip apex, whose radius measures 5 - 10 nm. A second NIR probe pulse with variable delay is focused from the inner part of the double mirror setup onto the super-tip apex. Here, the electric field of the NIR probe pulse interferes, depending on the delay, constructively or destructively with the SPP electric field.

The electric field at the super-tip apex is probed by exploiting the electron photoemission process: in the multiphoton regime, where several photons are accumulated for the emission of a single electron, the yield of photoelectrons is nonlinearly depending on the electric field strength. Accordingly, the interference between SPP and NIR electric field imprints on the delay-dependent photoemission yield, detected by a time-of-flight spectrometer, which gives rise to a cross-correlation signal of photoelectrons. For the samples under study which are coated with Au, the material work function yields $\Phi = 5.4\,\text{eV}$ [205]. Accordingly, at least $n = 3$ photons at a central wavelength of 740 nm are necessary to accumulate for a single electron to overcome the surface barrier.

To investigate the effects of adiabatic focusing on the SPP group velocity, the SPP propagation distance is altered by varying the spatial separation Δy between NIR probe and SPP pump laser pulse as depicted in Fig. 4.1 (a). The separation is verified by scanning the sample spatially through the focal plane while recording the multi-photon emission yield, in lines with the procedure presented in Sec. 3.3.3. The sample position is thereby controlled using closed-loop stages with minimum step length of 30 nm. Especially for small separations between NIR probe and SPP pump laser pulse, and given the double mirror focal spot sizes as listed in Tab. 3.1, it must be expected that the focal spot of the NIR pump pulse partially overlaps with the NIR probe field at the super-tip apex. Therefore, most generally, the strong-field photoemission yield $I_{\text{SPP}}(\tau)$ is featured from three independent contributions and reads as

$$I_{\text{SPP}}(\tau) = \int_{-\infty}^{\infty} \left[E^{\text{pu}}_{\text{apex}}(t - \Delta t^{\text{SPP}}_{\text{ref}}) + E_{\text{SPP}}(t - \Delta t_{\text{SPP}}) + E^{\text{pr}}_{\text{apex}}(t - \tau) \right]^{2n} dt \quad , \qquad (4.1)$$

where τ describes the temporal delay, $E^{\text{pu}}_{\text{apex}}$ and $E^{\text{pr}}_{\text{apex}}$ represent the NIR pump and probe electric fields at the position of the super-tip apex, indicated by the label 2 in Fig. 4.1 (a). The variable $\Delta t^{\text{SPP}}_{\text{ref}}$ signifies the temporal shift induced by the difference in optical path length between NIR pump and probe beam to reach the super-tip apex. The electric field of the surface plasmon polariton is described by E_{SPP}, where Δt_{SPP} represents the temporal shift of the SPP electric field, which gives access to the propagation time and thereby to the average group velocity of the SPP.

For all measurements, Δt_{SPP} is extracted from a fit based on Eq. 4.1 to the experimental data. For the fitting routine, the time-dependence of all electric fields is described by a Gaus-

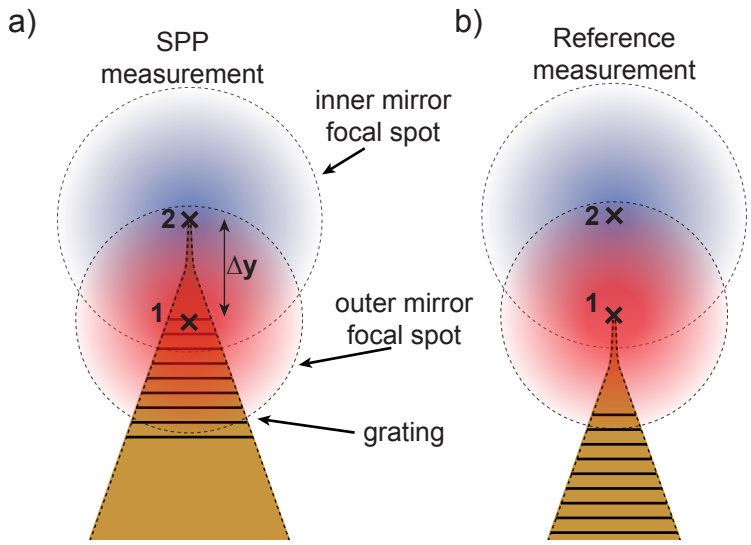

Figure 4.1: Sketch of experimental geometry for SPP and reference measurements. In **(a)** the geometry for the SPP measurement is shown with the outer beam (red) being focused onto the grating, where a surface plasmon is excited which propagates towards the super-tip apex. The delayed NIR probe field, reflected from the inner mirror (purple) is focused onto the super-tip apex and features multi-photon emission. For small displacements, the NIR pump and probe beam overlap spatially at the super-tip apex which needs to be considered in the analysis. For the reference measurements, illustrated in **(b)**, the displacement between inner and outer mirror focal spot is kept constant, while the super-tip apex is moved into the focal spot of the outer mirror. The position of focal spot centers of outer and inner mirror are indicated by the numbers 1 and 2. Temporal properties of both beams are expected to be identical, while different colors for inner and outer beam focal spots, were chosen only for better graphical distinction. Adapted from [148].

sian envelope function with duration σ and a phase term oscillating at central frequency ω:

$$E_k^l(t) = A_k^l \cdot \exp\left[-4\ln(2)\cdot\left(\frac{t}{\sigma_k}\right)^2\right]\cdot\exp\left[-\mathrm{i}(\omega_k t + \varphi_{\mathrm{CE}})\right] \quad , \tag{4.2}$$

where the index k labels either the electric field of SPP or the NIR pulses at the position of the super-tip apex. The latter subdivides into pump and probe beam reflected from outer and inner part of the double mirror as indicated by the l-index. While electric field amplitudes together with the temporal characteristics of the SPP field, i.e. σ_{SPP} and ω_{SPP}, are free parameters in the fitting algorithm, the respective properties of the NIR pump and probe pulses are determined from separate reference measurements, as illustrated in Fig. 4.1 (b).

For the reference measurements, the displacement between NIR pump and probe beam is kept constant, while the super-tip apex is repositioned in the center of the outer mirror focal spot. Since in this configuration, no SPP field is excited at the grating, the strong field photoemission signal from the apex is entirely determined by the NIR laser fields and readily described with

$$I_{\mathrm{ref}}(\tau) = \int_{-\infty}^{\infty}\left[E_{\mathrm{grat}}^{\mathrm{pu}}(t-\Delta t_{\mathrm{ref}}) + E_{\mathrm{grat}}^{\mathrm{pr}}(t-\tau)\right]^{2n} dt \quad , \tag{4.3}$$

where the index ‚grat' indicates the grating position of the sample in SPP measurement geometry, which is equivalent to the label 1 in Figs. 4.1 (a), (b). Fitting the experimental data

of the reference measurements with Eq. (4.3), while the temporal profiles of the NIR fields are modeled according to Eq. (4.2), gives access to the NIR pulse duration σ_{NIR} and its central frequency ω_{NIR}. Here, it is intrinsically assumed that pump and probe beam feature identical temporal profiles, since both beams are derived from different spatial components of the same NIR laser field. Pulse duration and central frequency of the NIR field are subsequently used in the fitting routine on the SPP measurements from where ultimately the temporal properties of the SPP electric field are retrieved, as described above.

A major obstacle derives from the AS-5 double-mirror holder being not realized as gimbal mount, but constructed as three point suspension for which different tip/tilt angles yield intrinsically a finite translational displacement between inner and outer mirror. Therefore, the optical path lengths of the interferometer arms, realized by the inner and outer mirror, depend on the displacement Δy between the respective focal spots. Based on geometrical considerations of the experimental setup and sample, the optical path lengths can be evaluated theoretically, as demonstrated in detail in the appendix A. In addition to the optical path lengths, the calculations yield also the expected temporal shifts Δt_{ref} and $\Delta t_{\mathrm{ref}}^{\mathrm{SPP}}$ between NIR pump and probe field in the reference and SPP measurements. In general, both values are not equal, since the NIR pump and probe field are superimposed at different positions, i.e. at the center of the inner mirror focal spot in the SPP measurement versus at the center of the outer mirror focal spot in the reference measurement. However, for the small displacements $\Delta y \leqq 13\,\mu\mathrm{m}$, the difference is found on the sub-femtosecond timescale and therefor much smaller than SPP propagation times.

The experimentally resulting SPP time shift Δt_{SPP} includes two contributions, namely t_{prop}, which describes the propagation time of the SPP from its excitation position to the super-tip apex, and $t_{\mathrm{path}}^{\mathrm{pump}}$, which represents the optical path length of the NIR pump beam from the outer mirror to the grating surface (see also appendix A). Temporal overlap between SPP electric field and NIR probe field at the super-tip apex is accordingly described by the condition

$$t_{\mathrm{path}}^{\mathrm{probe}} + \Delta t_{\mathrm{SPP}} = t_{\mathrm{path}}^{\mathrm{pump}} + t_{\mathrm{prop}} \quad , \tag{4.4}$$

where $t_{\mathrm{path}}^{\mathrm{probe}}$ introduces the optical path length of the NIR probe beam reflected by the inner mirror. Rearranging the above equation and introducing the optical path length difference $\Delta t_{\mathrm{int}} = t_{\mathrm{path}}^{\mathrm{probe}} - t_{\mathrm{path}}^{\mathrm{pump}}$ between the beams reflected from inner and outer mirror, yields

$$t_{\mathrm{prop}} = \Delta t_{\mathrm{int}} + \Delta t_{\mathrm{SPP}} \quad . \tag{4.5}$$

Together with the propagation length of the SPP l_{SPP}, given as the distance between super-tip apex and SPP excitation position on the grating, the mean group velocity of the SPP v_{SPP} can be calculated. Similar as the optical path length difference Δt_{int}, the SPP propagation length is derived from the sample geometry, as shown in appendix A.

4.3 Theoretical Modeling

Complementary to the experiments, we perform theoretical calculations, where the interaction of the NIR pump or probe pulses with the grating super-tip sample is retrieved from an FDTD simulation. Based on the electric field calculations, we simulate the full experiment, where the yield of multi-photon ionization is calculated from Keldysh theory. The electric SPP and NIR fields as obtained from the cross-correlation simulations is hereafter compared to the results from FDTD calculations. This comparison serves as a benchmark for the validity of the

retrieval algorithm. The sample geometry is modeled on the basis of the SEM micrographs displayed in Figs. 3.3 (a) - (d), with super-tip's radius $R = 10\,\text{nm}$ and 5° full opening angle. The refractive index data for Au is taken from Ref. [206]. The temporal waveforms of the incident NIR pump and probe pulses are described by Gaussian envelope functions with pulse durations of $\sigma = 6.4\,\text{fs}$ and central wavelength around $\lambda = 700\,\text{nm}$, while focal spot sizes for the inner and outer mirror are modeled with a spatial FWHM diameter of 5.5 µm and 4.1 µm, respectively. The FDTD simulation is performed using a commercial software package[1].

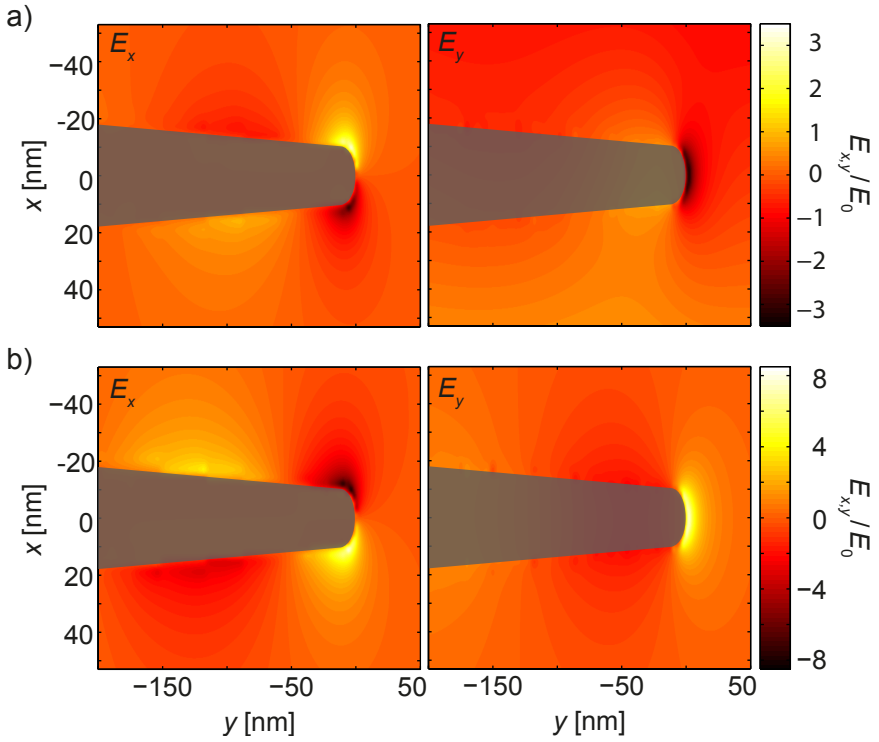

Figure 4.2: Electric near-field calculations for the super-tip geometry. In **(a)** the x (left) and y-component (right) of the electric near field in the xy-plane is displayed, given that only the NIR probe beam is focused to the super-tip apex. Subfigure **(b)** illustrates the situation, where the pump beam excites an SPP on the grating, which experiences adiabatic focusing whilst propagating to the super-tip apex. Adapted from [148].

Figure 4.2 displays the resulting electric fields at the super-tip apex, where in (a) only the NIR probe beam with the spatial profile of the inner mirror focal spot is focused onto the apex. The left panel illustrates the x-component, the right panel the y-component of the electric near field in the xy-plane. The incident laser field amplitude is chosen to unity, for which the field enhancement at the super-tip apex is directly discernible from the depicted result. In lines with previous FDTD calculations for a nanoscale sharp apex [207], field enhancement factors between 3 to 4 are observed. In a separate simulation, with the results illustrated in Fig. 4.2 (b), the effect of the grating structure is explored, where the NIR pump beam with spatial profile of the outer mirror is focused onto the grating. The focus position on the grating is chosen to match a displacement of $\Delta y = 6.5\,\mu\text{m}$, as defined by the measurement

[1] Lumerical Solutions Inc., FDTD Solutions 8.9

geometry, illustrated in Fig. 4.1 (a). The adiabatic focusing effect of the surface plasmon is clearly revealed from the FDTD simulations, indicating a strong field component along the y-direction at the super-tip apex with enhancement factors around 8. This finding is in general agreement with reports in literature, where the direct illumination of a nanoscale apex demonstrated lower field enhancement as compared to an adiabatically focused SPP on the same geometrical structure [208]. The quantitative comparison to literature values is delicate, since minute changes in experimental parameters, e.g. laser wavelength, tip opening angle or SPP propagation length can alter the electric field strength at the apex significantly.

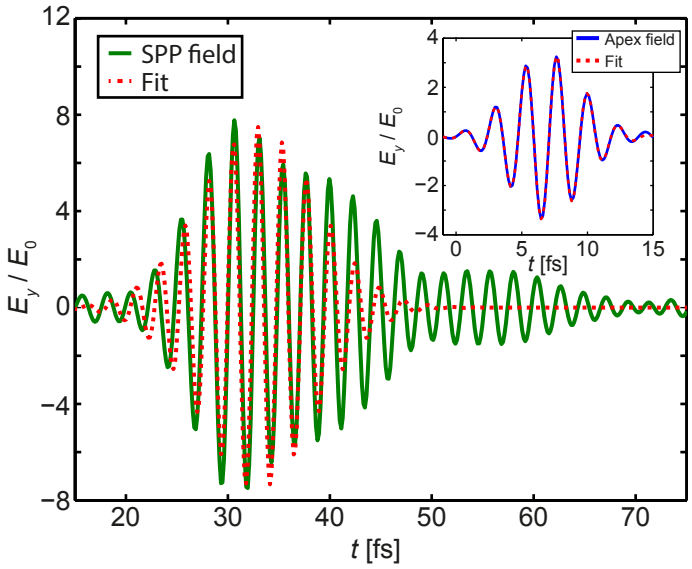

Figure 4.3: Electric field of the SPP at the super-tip apex. The normalized y-component of the SPP electric field at the super-tip apex in dependence of time is illustrated by the green solid line and fitted according to Eq. (4.2), as displayed by the red dotted line. The inset shows the respective results for the NIR field exciting directly the super-tip apex. For both illustration, figure and inset, the time axis zero point represents the arrival time of the NIR field at the grating structure of the sample. Therefore, the inset reveals the optical path length difference between NIR pump and probe pulses in the FDTD simulation geometry. Adapted from [148].

Since FDTD simulations are performed in the temporal domain, the results allow to directly retrieve the SPP propagation time. The normalized y-component of the SPP electric field at the super-tip apex position in dependence of time is illustrated in Fig. 4.3, with the time axis' zero point representing the arrival of NIR beam at the grating structure of the sample. While the electric field at the super-tip apex in case of direct excitation, displayed as inset to Fig. 4.3 represents the temporal profile of the incoming NIR laser field to high accuracy, the SPP electric field yields larger pulse durations and an asymmetric temporal envelope, where the falling edge of the SPP electric field towards larger time-values reveals a flatter decrease than the rising edge. Also, the pulse is slightly chirped with long wavelength components arriving first, as has been found for SPP propagating on similar geometries [209]. However, especially for the short propagation distances below 10 µm, the absolute chirp is considerably low [210] and is neglected within the first approximation. Therefore, despite the asymmetric envelope, the electric fields at the super-tip apex for SPP and direct excitation are fitted by

Gaussian envelope functions, oscillating at a central frequency as defined by Eq. (4.2). From the resulting fits, the times for the maximum electric field strength, $t_{\text{center}}^{\text{SPP}}$ and $t_{\text{center}}^{\text{NIR}}$, are revealed, which reflect the arrival time of SPP respective NIR field at the super-tip apex for the separate simulations, relative to the time axis' zero point, i.e. the SPP excitation time. Accordingly, for the SPP simulation the retrieved time of $t_{\text{center}}^{\text{SPP}} \approx 32.9\,\text{fs}$ represents directly the SPP propagation time. For the separation of $\Delta y = 6.5\,\mu\text{m}$, the SPP propagation length calculates to $l_{\text{SPP}} \approx 6.9\,\mu\text{m}$ (see appendix A) and therefore, the SPP mean velocity, calculated from the FDTD simulations yields

$$v_{\text{SPP}} = \frac{l_{\text{SPP}}}{t_{\text{center}}^{\text{SPP}}} \approx 0.7\,c \qquad , \tag{4.6}$$

where c describes the speed of light. While the FDTD simulations allow direct access to the temporal profile and propagation time of the SPP electric field, the experimental observable, i.e. the photoionization yield from an NIR-SPP cross-correlation measurement demands a more sophisticated analysis method. Therefore, corresponding simulations to reproduce the experiment are performed.

For the simulation of auto- and cross-correlation measurements [148], the photoionization rate $P(\gamma(t))$ from the super-tip apex is modeled in the framework of multiphoton excitation. The time-dependence of the photoemission rate is introduced by a time-dependent Keldysh parameter $\gamma(t)$, where the electric field and thereby the ponderomotive potential $U_p(t)$ is considered as time-dependent:

$$\gamma(t) = \frac{\Phi}{2U_p(t)} = \frac{\omega\sqrt{2\Phi m_{\text{e}}}}{eE(t)} \qquad . \tag{4.7}$$

With the above expression the ionization probability according to Eq. 2.29, is determined by [148]

$$P(\gamma(t)) \propto \exp\left[-\frac{2\Phi}{\hbar\omega}\cdot\left[\left(1+\frac{1}{2\gamma(t)^2}\right)\operatorname{arsinh}(\gamma(t)) - \frac{\sqrt{(1+\gamma(t)^2)}}{2\gamma(t)}\right]\right] \qquad , \tag{4.8}$$

where ω and Φ represent the central laser frequency and work function for gold, and $E(t)$ is the electric field as retrieved in FDTD simulations. The pump-probe scheme is modeled by superimposing the results from the separate calculations, illustrated in Figs. 4.2 (a) and (b), with variable delay τ. The delay axis follows the typical convention for streaking experiments, where larger values signify an advanced probe field, in lines with the experimental representation. Electrons are excited from a thin surface layer of 5 nm thickness and restricted to the super-tip apex by weighting the initial positions for photoemission with a Gaussian profile of 20 nm FWHM diameter, centered at the super-tip apex. Upon photoexcitation, electron propagation through the electric fields is computed classically, based on a Velocity-Verlet algorithm [211]. Electrons recolliding with the super-tip during their propagation are assumed to undergo elastic backscattering at the sample. The full auto- and cross-correlation traces are ultimately obtained by summing up the respective photoelectrons, averaged over final energies and CEP values, for each delay step.

The results of numerically simulated photoemission yields for NIR auto- and SPP cross-correlations are displayed in Figs. 4.4 (a) and (b). The results are fitted with the analytical models based on Eqs. (4.3) and (4.1). By definition, the NIR auto-correlation simulation,

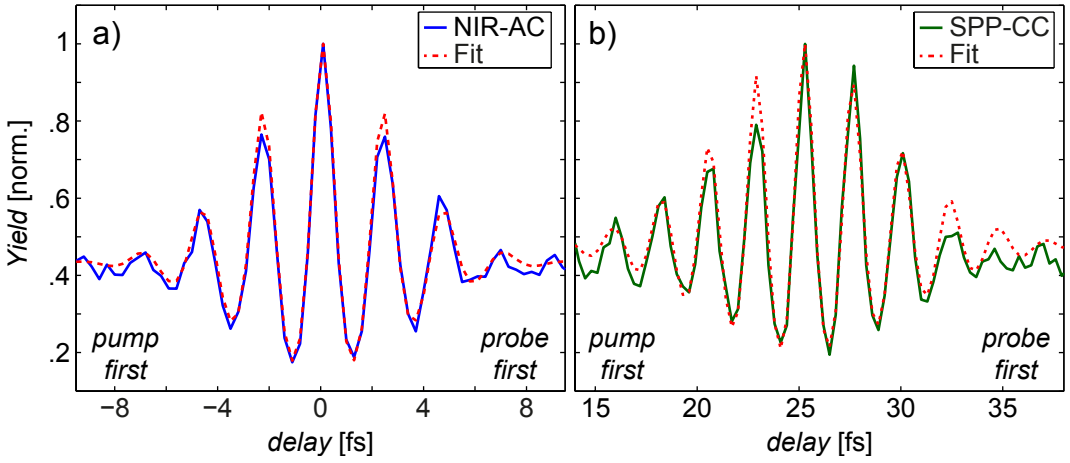

Figure 4.4: Simulated NIR auto- and SPP cross-correlation. In **(a)** the result for the NIR auto-correlation simulation is illustrated (blue solid line), where NIR pump- and probe beam are focused onto the super-tip apex. The resulting NIR auto-correlation trace is fitted (red dashed line) according to Eq. (4.3), from which the NIR pulse duration, central wavelength and amplitude can be extracted. Similarly, in **(b)** the SPP cross-correlation, where the NIR pump beam is focused on the grating to excite an SPP, is simulated (green solid line) and fitted (red dashed line) according to Eq. (4.1). The SPP cross-correlation simulation is calculated at a displacement of $\Delta y = 6.5\,\mu\text{m}$. Adapted from [148].

shown in (a), is centered around zero, since here the NIR pump and probe beams derive from the same source. Fitting the NIR auto-correlation simulation, parameters like field amplitude, pulse duration and central wavelength can be extracted. Comparing the pulse parameters retrieved from the FDTD field calculations, i.e. inset in Fig. 4.3, to the results from the simulated auto-correlation measurement, displayed in Fig. 4.4 (a), demonstrates ideal agreement between the different retrieval algorithms: deviations between both procedures amount to less than 2 %, where an NIR central wavelength between 701 - 706 nm and pulse duration around 6.4 - 6.5 fs is obtained.

NIR pulse parameters are hereafter used as input values to Eq. (4.1) to fit the SPP cross-correlation simulation in Fig. 4.4 (b). While from both retrieval algorithms similar values for the SPP central wavelength are obtained, ranging between 697 - 700 nm, the SPP pulse duration differs for the different approaches. Directly extracted from FDTD calculations, the pulse duration yields about 13.3 fs while from cross-correlation simulations a value of 10.9 fs is obtained. However, within the 95 % confidence level, the results from both retrieval methods still overlap. It should be mentioned that, due to the asymmetric temporal envelope of the SPP electric field, defining the SPP pulse duration is more challenging than for the NIR electric field. Accordingly, error margins of the SPP pulse duration for either retrieval algorithm, are generally larger as compared to the extracted NIR pulse duration.

From the fit to the SPP cross-correlation simulation, the resulting delay time is obtained with $\Delta t_{\text{SPP}} \approx 25.3\,\text{fs}$, which represents the necessary delay of the NIR probe field to overlap temporally with the SPP electric field at the super-tip apex. Based on Eq. (4.5) and the optical path length difference of $\Delta t_{\text{int}} \approx 6.9\,\text{fs}$, as can be observed in the inset of Fig. 4.3, the SPP propagation time yields $t_{\text{prop}} \approx 32.2\,\text{fs}$. With the SPP propagation length of 6.9 µm at a separation of $\Delta y = 6.5\,\mu\text{m}$, the mean velocity calculates to $v_{\text{SPP}} \approx 0.7\,c$, which is in perfect agreement with the previous findings based on the FDTD simulation results. Accordingly, the

simulations support the general feasibility to extract SPP properties based on cross-correlation measurements.

4.4 Experimental Results

Prior to the SPP cross-correlation measurements, the translation stage for setting the delay between pump and probe pulses is gauged in a calibration measurement, with the results displayed in Fig. 4.5. Here, the NIR auto-correlation is detected for inner and outer mirror reflections being focused to the super-tip apex. For the separation of $\Delta y = 0$, the double mirror setup represents a collinear interferometer. Accordingly, the delay time t_0 with maximum temporal overlap corresponds to equal optical path lengths of reflections from the inner and outer mirror. Fitting the experimental data from the calibration measurements by a model expressed in Eq. (4.3), yields $t_0 = -86.1\,\mathrm{fs}$, where the value is exclusively determined by the initial alignment of the double mirror interferometer. To obtain the correct delay axis, all experimental data is shifted by the value of t_0 in the following analysis.

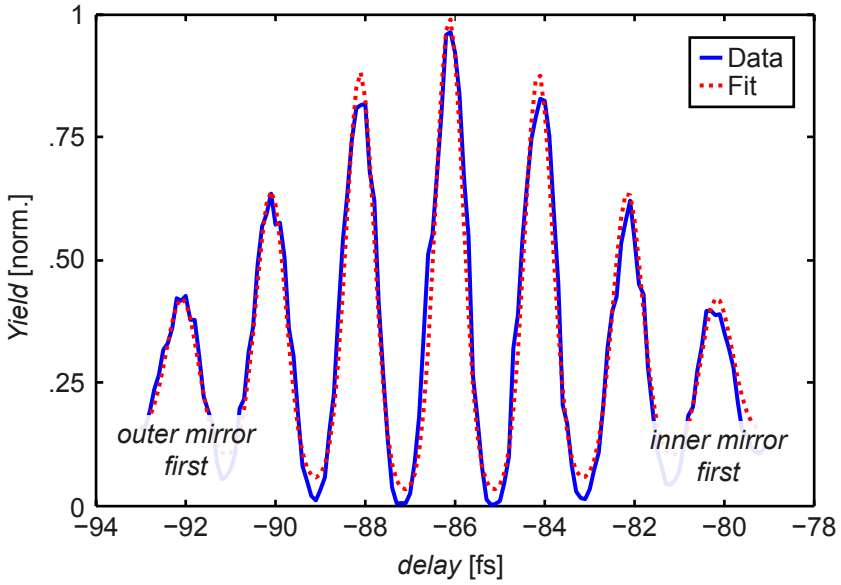

Figure 4.5: Calibration NIR auto-correlation measurement. The blue solid line represents the experimental data of a calibration measurement, while the fit to the data based on a model according to Eq. (4.3) is shown as red dotted line. Adapted from [148].

The NIR auto- and SPP cross-correlation measurements are all performed on the same sample on different days. Regardless from day-to-day fluctuations of the laser system, the NIR pulse parameters for all measurements are found in reasonable agreement. Within the same day, the NIR laser fields are found to vary only marginally over the typical integration time in the range of 60 min for a single measurement. Since the alignment of the super-tip sample in the focal spots is a lengthy procedure, three SPP cross-correlation measurements were performed without corresponding reference measurement. For these data sets, the NIR pulse parameters are taken from a different reference measurement, performed on the same day. In total, SPP cross-correlation measurements are acquired for nine different displacements ranging between $13\,\mu\mathrm{m} \geqq \Delta y \geqq 4\,\mu\mathrm{m}$. The mathematical models expressed by Eqs. (4.1) and

(4.3), which are used to fit the experimental data from SPP cross- and NIR auto-correlation measurements, contain multiple free parameters. To improve the convergence of the fitting algorithm, experimental raw data is Fourier filtered in the spectral domain using a super-Gaussian filter function, which rejects frequency components that are not contained in the original spectrum of the NIR laser field. For better resolution, the raw data sets are zero-padded before calculating the Fourier transforms.

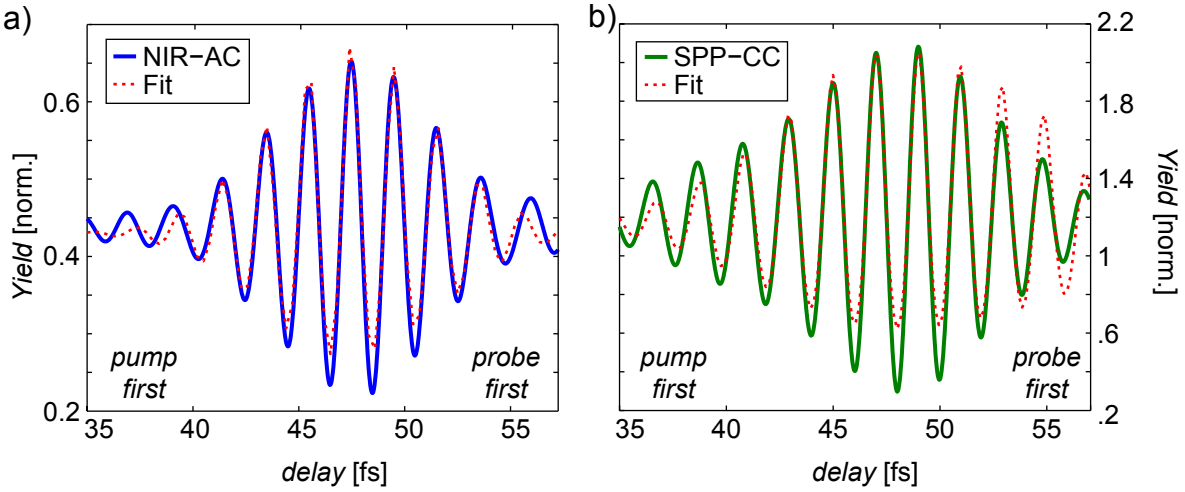

Figure 4.6: Experimental results for NIR auto- and SPP cross-correlation measurements. Photoionization yield per laser shot of NIR auto- (blue solid line) and SPP cross-correlation (green solid line) traces, acquired at a displacement of $\Delta y = 8\,\mu\text{m}$ between inner and outer mirror focal spot, are displayed in **(a)** and **(b)** together with their respective fits (red dashed lines). Adapted from [148].

In figures 4.6 (a) and (b), the results for an NIR auto- and SPP cross-correlation measurement are illustrated together with the respective fits, exemplary for the displacement of $\Delta y = 8\,\mu\text{m}$. Based on the fit to the reference measurement, the temporal profile of the NIR laser field is described by a pulse duration of $\sigma_{\text{NIR}} = 8.5\,\text{fs}$ and central wavelength around $\lambda_{\text{ref}} = 610\,\text{nm}$. The SPP cross-correlation reveals a larger pulse duration, which is retrieved from the fit as $\sigma_{\text{SPP}} = 11.5\,\text{fs}$, while the SPP central wavelength of $\lambda_{\text{SPP}} = 610\,\text{nm}$ is identical with the NIR laser field result. For the asymmetry of the SPP electric field envelope, the description by a Gaussian function in the fitting algorithm is a strong simplification, which appears, however, to still be justified given the generally good agreement between fit and experimental data.

From the SPP cross-correlation measurement, a delay shift of $\Delta t_{\text{SPP}} = 48.7$ is obtained. Using Eq. (4.5) and the calculated optical beam path difference Δt_{int} from Tab. A.2, the SPP propagation time can be retrieved, yielding $t_{\text{prop}} = 114.9\,\text{fs}$. Under consideration of the propagation length $l_{\text{SPP}} = 8.46\,\mu\text{m}$, the mean velocity of the SPP for the separation of $\Delta y = 8\,\mu\text{m}$ calculates to $v_{\text{SPP}} \approx 0.25\,c$. The analysis of all data sets is summarized in Tabs. 4.1 and 4.2, displaying the results of NIR reference and SPP cross-correlation measurements.

Δy [µm]	λ_{ref} [nm]	σ_{ref} [fs]	Δt_{ref} [fs]
5	620 ± 10	9.6 ± 1.1	34.9
6	610 ± 70	8.9 ± 1.2	39.8
7	600 ± 70	7.6 ± 0.9	42.7
8	610 ± 60	8.5 ± 0.9	47.5
9	650 ± 50	9.1 ± 0.8	49.0
12	640 ± 120	7.9 ± 1.5	67.2

Table 4.1: Experimental results for the NIR auto-correlation measurements. The error bars indicate the 95 % confidence level, obtained by the fitting algorithm. The errors to the reference shifts Δt_{ref} are four orders of magnitude lower than the mean values and are therefore omitted. Adapted from [148].

Δy	λ_{SPP} [nm]	σ_{SPP} [fs]	Δt_{SPP} [fs]	Δt_{int} [fs]	l_{SPP} [µm]	t_{prop} [fs]	v_{SPP} [c]
4	590 ± 50	7.4 ± 0.6	22.4	32.2	4.18	54.6	0.255
5	620 ± 60	9.7 ± 1.1	34.0	40.7	5.25	74.7	0.234
6	640 ± 100	13.3 ± 2.3	40.1	49.2	6.32	89.3	0.236
7	610 ± 20	7.5 ± 0.2	43.7	57.7	7.39	101.4	0.243
8	610 ± 80	11.5 ± 1.5	48.7	66.2	8.46	114.9	0.245
9	630 ± 20	10.4 ± 2.0	50.1	74.8	9.53	124.9	0.255
10	640 ± 80	10.1 ± 1.7	54.7	83.3	10.60	138.0	0.256
12	650 ± 160	10.7 ± 3.5	71.1	100.3	12.75	171.4	0.248
13	650 ± 60	8.2 ± 0.8	75.4	108.8	13.82	184.2	0.250

Table 4.2: Experimental results for the SPP cross-correlation measurements. For parameters resulting from the fitting algorithm, the error bar indicates the 95 % confidence level. Error levels to Δt_{SPP} are at least four orders of magnitude lower than the averaged values and are accordingly not considered. Adapted from [148].

4.5 Analysis, Interpretation and Discussion

From the NIR auto-correlation traces, the pulse durations and central wavelength of the NIR laser field can be retrieved. As tabulated in Tab. 4.1, the NIR pulse duration for all reference measurements range between 7.6 - 9.6 fs, where the individual values, under consideration of the error bars, agree reasonably well. The residual spread is likely caused by day-to-day variations in the spectral broadening stage of the laser system. The central wavelengths retrieved from the NIR auto-correlation measurements yield between 600 - 650 nm, where the spread of individual values is again negligible. While the retrieved value is contained in the NIR laser spectrum, the central wavelength for Ti:Sa systems that are spectrally broadened in a hollow core fiber is typically around $\lambda_{\mathrm{ref}} \approx 750\,\mathrm{nm}$. This discrepancy results possibly from the high localization in the measurement: in contrast to spatially averaging methods using spectrometers, the central wavelength retrieval as presented here relies on the multiphoton emission process, which is spatially confined to the region of the super-tip apex. For the short focal length of the double mirror, aberration effects could introduce a spatial variation of the central wavelength across the profile of the focal spot, which potentially yields different values

of λ_{ref} for highly localized measurement schemes compared to spatially averaging methods. Deviations, resulting from the retrieval algorithm can be safely neglected, as is demonstrated from the theoretical calculations: comparing the resulting pulse duration and central wavelength of the NIR electric field retrieved from the simulated auto-correlation yields identical values as the analysis of time-domain based results from the FDTD calculations.

Based on the retrieved NIR laser pulse parameters, the SPP cross-correlation measurements are analyzed to extract the pulse duration σ_{SPP}, central wavelength λ_{SPP} and delay shift Δt_{SPP} for the SPP electric field. The resulting values with their respective error margins are tabulated in Tab. 4.2 for different displacements. The central wavelength of the SPP is retrieved between $\lambda_{\mathrm{SPP}} = 590\text{-}650\,\mathrm{nm}$, which is in reasonable agreement with the theoretical expectation of $\lambda = 630\,\mathrm{nm}$, for which, under consideration of $\lambda_{\mathrm{NIR}} = 740\,\mathrm{nm}$ and the sample geometry, ideal phase-matching is achieved. With increasing displacement, the SPP wavelength appears redshifted, regardless of two data sets, measured at $\Delta y = 5$ and $\Delta y = 6$. For macroscopic metal-dielectric interfaces and also for nanostructured geometries, it was found that the SPP propagation length increases with the respective central wavelength [197, 212]. Accordingly, separate spectral components of broadband SPP pulses exhibit different propagation lengths, which implies that the power spectral density and thereby λ_{SPP} depends on the SPP propagation length. Our finding of redshifted SPP pulses with increasing displacement is qualitatively anticipated from the propagation length studies presented in Refs. [197, 212]. However, the quantitative analysis of the redshift effect for our sample geometry is difficult, since geometrical aspects for the SPP propagation along the pyramidal cone and the nanotaper must be considered separately. It should be noted that, given the large error bars on λ_{SPP}, the effect of redshifted SPP pulses with increasing propagation length is not unambiguously resolved in our experiments. Especially, since the redshift effect is anticipated to reduce the SPP spectral bandwidth, while the associated increase of SPP pulse duration with increasing displacement, is not clearly detectable. Also, the quantitative impact of the redshift, depends strongly on the initial spectral width of SPP pulses and thereby on NIR pulse durations and phase-matching conditions on the grating geometry, which are difficult to control with high accuracy.

The SPP pulse durations, retrieved from the cross-correlation measurements, yield typically larger values as compared to the NIR field, which is in agreement with the presented theoretical simulation. Since the grating geometry, which is used for phase matching between SPP and NIR pump field, is optimized only for a single NIR wavelength, the spectral bandwidth of the SPP is expected to be reduced relative to the NIR pulse, as has been reported for related sample geometries [209]. Accordingly, increased SPP pulse durations as compared to the NIR pump field are anticipated. The spectral selectivity of the grating is counteracted by the single grooves, where phase-matching is supported over a broad spectral range [213, 214]. As retrieved from experimental data tabulated in Tab. 4.2, the specific grating geometry of our samples supports SPP pulse durations on the order of 10 fs. Within the error margins, the results for individual measurements agree reasonably well, where the spread is most likely introduced by day-to-day-variations of the NIR pump pulse duration. As was found from the FDTD calculations, illustrated in Fig. 4.3, the temporal envelope of the SPP electric field is not symmetric in time. Therefore, extracting the SPP pulse duration based on modeling the plasmon's temporal envelope by Gaussian functions yields only approximative results. However, as can be observed in Fig. 4.6 (b), experimental data and fit according to Eq. (4.1) coincide reasonably well, at the expense of increased error margins.

Besides pulse duration and central wavelength, the cross-correlation measurements re-

veal the delay shift Δt_{SPP}, which together with the internal delay Δt_{int} and the propagation distance l_{SPP} yields the averaged SPP group velocity. The FDTD and cross-correlation simulations indicate both $v_{\mathrm{SPP}}^{\mathrm{theo}} \approx 0.7\,c$, whereas for plane surfaces, the SPP velocity, calculated from Eqs. (2.21) and (2.20), is expected around $0.9\,c$ for an SPP wavelength of $\lambda_{\mathrm{SPP}}^{\mathrm{sim}} \approx 710\,\mathrm{nm}$. Employing Eq. (2.25), under consideration of our sample geometry with $r_{\mathrm{apex}} = 10\,\mathrm{nm}$ and half opening angle of 2.5°, the adiabatic focusing effect adds an additional group delay around $\Delta t_{\mathrm{group}} = 5.86\,\mathrm{fs}$. Therefore, the averaged SPP group velocity yields approximately $0.73\,c$, which is reasonably close to the FDTD results. Note that the intersection between super-tip and pyramidal cone has not been considered and is expected to add additional delays. Accordingly, the reduced SPP group velocity as extracted from FDTD simulations, is fully explained by geometrical effects, while the grating geometry appears to have no influence on the SPP group velocity.

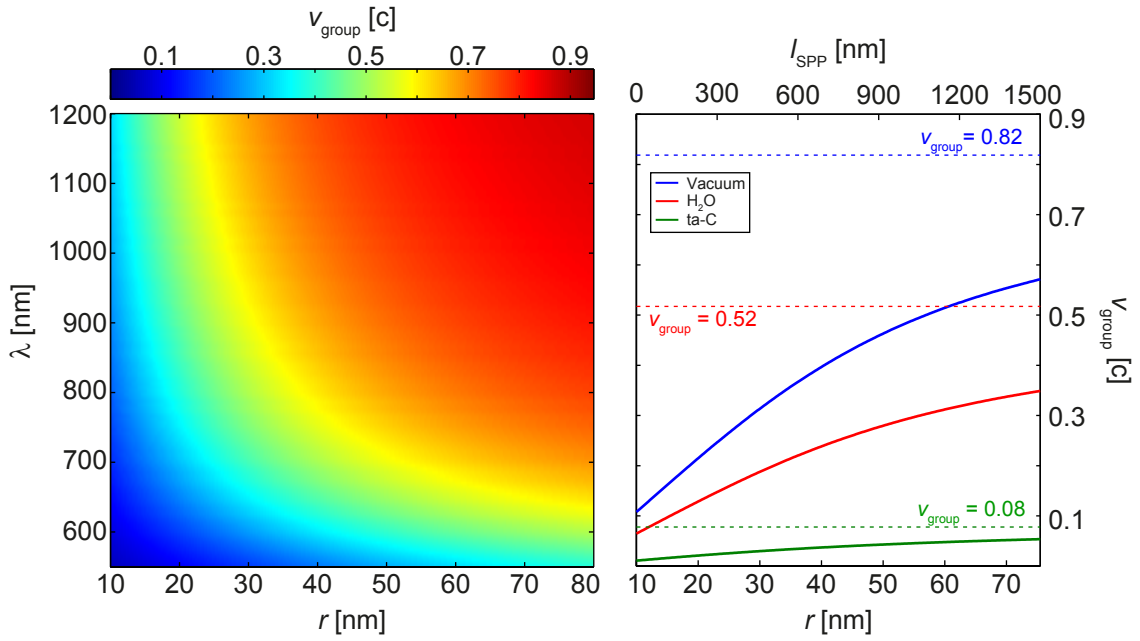

Figure 4.7: Adiabatic focusing effect of super-tip geometry. In **(a)** the SPP group velocity is shown in dependence of wavelength and super-tip radius. Regardless of the local radius, the SPP group velocity decreases with decreasing wavelength. In **(b)** the SPP group velocity for $\lambda_{\mathrm{SPP}} = 630\,\mathrm{nm}$ is illustrated in dependence of the local super-tip radius (bottom x-axis) and SPP propagation length (l_{SPP} on top x-axis) for selected dielectric media (solid lines) together with the respective limiting value for macroscopic surfaces (dashed lines).

The experimental results listed in Tab. 4.2, reveal values around $v_{\mathrm{SPP}} = 0.25\,c$ with marginal spread between individual displacement measurements. Since the experimentally retrieved SPP wavelength is found around $\lambda_{\mathrm{SPP}} \approx 630\,\mathrm{nm}$, the direct comparison between FDTD simulations and measurements is deceptive: as illustrated in Fig. 4.7 (a), the SPP group velocity reduces with decreasing wavelength for any sample geometry. Macroscopic vacuum-Au-interfaces, modeled by the optical constants according to Ref. [53] facilitate SPP group velocities around $0.82\,c$ for the given experimental SPP wavelength. Accordingly, the geometrical delay introduced by the super-tip is calculated to be around 5.32 fs. Compared to the large propagation times revealed by the individual displacement measurements, the group

delay is minor and can therefore not explain the small experimental SPP group velocities. The cross-over between super-tip and pyramidal cone is presumed to introduce additional group delays, which are challenging to account for, since a precise parameterization of the geometry remains elusive. However, while the intersection radius is larger than in case of the super-tip and affects only a very limited propagation length, the additional group delay is expected to be small in comparison to the influence of the super-tip.

Since the dielectric environment affects the plasmon properties considerably, surface adsorption layers are a source for additional delays and must be considered, especially as experimental vacuum conditions of 10^{-6} - 10^{-7} mbar are not in the range of ultra-high vacuum (UHV). A typical contamination in vacuum technology are water adsorption layers. For our sample geometry the effect of H_2O [215] is illustrated in Fig. 4.7 (b), which illustrates the SPP group velocity at $\lambda_{\mathrm{SPP}} = 630\,\mathrm{nm}$ in dependence of the local nanowire radius and the SPP propagation distance l_{SPP} from the super-tip apex. While the SPP group velocity reduces, the short propagation length of 1.5 µm along the super-tip adds only about 16.1 fs. Since the group velocity for macroscopic Au-water-interfaces facilitate still about $0.5\,c$, an H_2O contamination cannot exclusively explain the small experimental SPP group velocities. Another prominent contamination in any vacuum facility are carbon based compounds, which can be transfered to the sample during the measurement process. Here, also the sample generation process itself and especially the regular revision of the sample geometry in SEM instrumentations, are a common source for carbon and hydrocarbon contaminations [216]. In figure 4.7 (b) the influence of a thin film of tetrahedrally coordinated amorphous carbon (ta-C) [217] on the SPP group velocity is illustrated. In contrast to water adsorbtion, the SPP group velocity in case of a ta-C film reduces significantly, where the limiting value for macroscopic interfaces yields only about $v_{\mathrm{SPP}} \approx 0.08\,c$, which is even smaller than the experimental observation. The geometrically introduced group delay ranges around 161.7 fs and is thereby larger than the obtained propagation times for the smallest displacement measurements. While a uniform tetrahedrally coordinated amorphous carbon film would result in even smaller propagation velocities, a partial coverage can easily explain the small obtained SPP group velocity. Despite theoretical calculations indicate that surface adsorption layers are possibly the origin for reduced SPP propagation velocities, an experimental approach to determine the actual chemical environment and also the degree of contamination, i.e. surface coverage, is highly desirable. One possibility are work function measurements of the sample surface using an SEM to detect adsorbates locally. Another option is Raman spectroscopy, which typically achieves high sensitivity at the expense of spatial averaging.

Besides the dielectric environments, further effects influence the SPP group velocity, including surface roughness and non-local implications on the plasmons dispersion relation. The latter sets un upper limit to the field confinement, which can be achieved by SPPs being focused by a conical nanostructure [218]. Typically non-local effects, where electron-electron interaction of the metal cannot be neglected, are predominantly important for small geometries. Therefore, for the presented sample geometry with $r_{\mathrm{apex}} \approx 10\,\mathrm{nm}$, a significant impact on the SPP dispersion relation is only expectable in closest vicinity of the super-tip apex [219], which is insufficient to explain the low SPP group velocities. In contrast, surface roughness can influence the plasmon dispersion relation [220] without requirements on the charactersitic length scales of the sample geometry. Despite the sample production comprises a smoothing step employing Argon-Ion sputtering, an influence on v_{SPP} needs to be considered, since already small surface roughness values of 10 Å r.m.s. yield a detectable influence on the SPP dispersion relation and reduction in phase velocity [221]. Besides the residual surface rough-

ness, special attention must be directed on the influence of the grating structure itself, since it was demonstrated for sinusoidal gratings that the impact on the dispersion relation depends non-linearly on the grating depth [52]. However, a detailed, spectrally resolved theoretical or experimental analysis of the influence on the SPP dispersion relation for our sample's grating geometry has not been reported. Accordingly, a quantitative estimation of the impact on the SPP group velocity due to the grating geometry remains currently elusive. Together with spatially resolved measurements of the sample's surface roughness, the impact of residual surface roughness can in principle be estimated, while the influence of the grating would ideally demand an extensive experimental study with optimized sample geometry.

4.6 Conclusion and Outlook

By NIR-SPP cross-correlation measurements, I investigated dynamical properties of surface plasmon polaritons, which are excited by few-cycle NIR laser fields focused onto grating couplers and guided along a conical super-tip. The results indicate that SPP pulses close to the few-cycle regime can be efficiently transferred from a macroscopic surface to a nanosized tapered waveguide. The SPPs central wavelength and pulse durations are probed by multiphoton electron emission from the super-tip apex for different SPP propagation lengths. All measurements indicate SPP pulse durations in the range of 10 fs, which is in line with our numerical FDTD simulations and literature values. The central SPP wavelength yields around 0.63 µm, which is anticipated for the respective NIR wavelength and grating geometry under consideration of the phase matching condition. Our theoretical simulations reveal reduced SPP group velocities resulting from the adiabatic focusing on the conical nanotaper, as predicted by theoretical calculations. From the experiment, we extract small SPP group velocities, where the slowing down is not fully explained by the sample geometry. While a partial coverage with adsorption layers on the sample surface can theoretically explain the experimental findings, the small SPP group velocity result potentially from multiple, superimposed effects. To elaborate the quantitative impact of the individual contributions in detail, supplemental experiments are highly desirable.

Cross-correlation measurements, where the electric fields of a few-cycle NIR and SPP pulse are superimposed, can be considered a valuable technique to study the dynamics of ultrafast plasmonic excitations on their natural timescales. Since the multiphoton-emission process demands lower field strengths than the tunneling regime, this technique allows to investigate weak SPP pulses. As the photoemission process does not exclusively rely on the SPP electric field but is facilitated by the presence of the NIR probe field, even lower SPP field intensities are accessible with our approach. The main disadvantage in the cross-correlation measurements is the inability to resolve phase information of the SPP electric fields. While it was shown for the conceptually related optical auto-correlation technique that phase-information is in principle accessible [44], the experimental implementation of different dispersion settings for the individual interferometer arms in case of the cross-correlation experiment is difficult. For strong-field electron emission in the tunneling regime, simulations revealed that phase information, i.e. the CE phase of the SPP electric fields can be retrieved, given that the temporal phase of the NIR laser field can be controlled and is known with high precision. However, other analysis methods, e.g. attosecond streaking, are potentially better suited to gain full amplitude and phase information of SPP pulses, nevertheless at the expense of in-

creased complexity of the experimental setup.
Future experiments would tremendously profit from an improved infrastructure. Especially, replacing the interferometer with a gimbal mount double-mirror stage will improve the experimental setup and simplify the data analysis and interpretation. Enhanced vacuum conditions in the UHV regime would reduce the appearance of adsorption layers significantly. Supplementary, in-situ methods like Raman spectroscopy would allow to characterize the degree of surface contaminations and also its chemical fingerprint and thereby its impact on SPP group velocities.

Prospective studies using the NIR-SPP cross-correlation method on different sample geometries can elaborate the influence of the grating itself on the SPP group velocity. In addition, also the possibility to shape the spatio-temporal properties of the plasmonic fields can be investigated using spatially chirped fan-grating structures or gratings of varying grating constant. Since detailed knowledge of the shaping capabilities and dynamical properties of plasmonic excitations is a necessary prerequisite for the development of lightwave electronics, cross-correlation measurements on SPP electric fields can help to understand plasmonic excitations on shortest timescales.

Chapter 5

Streaking Measurements on Au-Nanotips

5.1 Introduction

With the advent of attosecond streaking spectroscopy [4], Goulielmakis *et al.* demonstrated the experimental characterization of few-cycle NIR laser fields in the temporal domain with attosecond precision [10]. Notably, the streaking technique averages the temporal characteristics of the NIR beam spatially over the probing volume, which is determined by the XUV laser focus. Numerous attosecond streaking experiments on gas phase [4, 9, 10, 13, 14] and solid state targets [15–18, 222, 223] were conducted, where XUV focal spot sizes range on the micrometer scale [224–227]. Shortly after the experimental realization of the attosecond streaking technique, Stockman *et al.* proposed theoretically to combine the temporal resolution of the attosecond streaking technique with the spatial resolution of photoemission electron microscopy (PEEM) within a single device [63]. The capabilities of the so-called ATTO-PEEM can be considered tremendous, since it would allow the 4D-characterization of electric fields on the attosecond temporal and nanometer spatial scale in real-time. The latter is in particular essential in the research field of plasmonics, also referred to as '*optics on the nanoscale*' [228] since the natural time and spatial scales of such collective electron excitations are found in the sub-femtosecond and nanometer dimensions.

Up to date, various methods are employed to characterize the spatio-temporal properties of plasmonic excitations. As recently shown by Yi *et al.* the far-field spectral interferometry (SI) is capable to characterize the coherent propagation of SPPs in the time domain, while resolving full amplitude and phase information [210]. Spectral interferometry was used successfully in multiple studies to probe, amongst others, SPP group and phase velocity, damping dynamics or SPP coupling to excitons [204, 229–232]. Since SI is not a time-domain analysis method of the SPP dynamics, it is restricted to fully coherent processes, for which the temporal information can be unambiguously retrieved from the spectral domain. At least for systems with strong electron-electron interaction and especially for resonance effects, this assumption is a priori not necessarily fulfilled. Additionally, the method relies on measurements of the far-field, directly restricting the sensitivity to dipole-active plasmon modes only. In contrast, the competing method of time-resolved interferometric scanning near-field optical microscopy (tr-SNOM), in scattering or transmissive geometry, directly probes the near-field. Based on the tr-SNOM approach, Nishiyama *et al.* could observe the motion of

plasmonic excitations on the femtosecond time scale by two-photon-induced photoluminescence (TPI-PL) [233]. Similarly to the two-photon-photoluminescence, multiphoton-induced photoluminescence (MPPL) was applied to retrieve plasmon decay times and damping characteristics [234,235]. Other studies rely on upgraded PEEM instrumentations, where typically interferometric two-photon photoemission (2PPE) is applied to resolve plasmonic excitations on the sub-femtosecond timescale [202, 236–240].

While highly demanded in the field of plasmonics, none of these methods provides a direct time-domain measurement of near-field amplitude and phase with attosecond precision, in contrast to attosecond streaking spectroscopy. Initiated by the ATTO-PEEM proposal [63], several theoretical reports analyzed practical implications for the application of the streaking technique on propagating and localized plasmons for different geometries [120–123, 125]. While the retrieval of phase and amplitude for nanoscale fields is found to be potentially more demanding with respect to gas phase streaking experiments, all studies supported the general feasibility of attosecond nanoscale near-field sampling.

In this chapter, the first experimental implementation of attosecond nanoscale near-field streaking as published in Ref. [151] is presented. The measurements are conducted at the attosecond beamline AS-5 as presented in Sec. 3.3 on tapered gold nanotips, characterized in Sec. 3.1.1. After description of the experimental approach, the theoretical framework to model the nanotaper streaking experiments is introduced. Herein, the electric field around the nanotip is calculated in a FDTD simulation, which forms the basis for spatially randomized electron trajectory simulations to obtain a full streaking spectrogram. Generally, theoretical and experimental results are found in fairly good agreement. Supported by theoretical considerations, it is demonstrated that the near-field amplitude and phase can be extracted from the experimental streaking spectrograms. As presented in the analysis and interpretation of the experimental data, we elucidate that the spatial confinement to the nanoscale imprints characteristically on the amplitude and phase of the resulting near field. The achievements are summarized in the last section, which finishes with a brief outlook towards subsequent experiments.

5.2 Experimental Approach

Streaking experiments on etched metal nanotip targets, as displayed in Fig. 3.2, are performed at the AS-5 infrastructure. Figure 5.1 illustrates the experimental realization of the nanotaper streaking experiment, where the nanotip target is mounted parallel to the laser polarization direction, along the y-axis (see indicated coordinate system in Fig. 5.1). The TOF spectrometer is aligned in the same direction, for which the tip apex directly faces the TOF entrance. Two-color laser fields with variable delay between the XUV and near-IR beams, are focused onto the nanotaper target, where near fields are excited by the NIR laser beam. The near field is probed by photoelectrons, emitted after XUV photoionization. To elucidate the near field dependence on the incident laser field, the NIR pulse is characterized in a gas phase streaking experiment. Here, the nanotaper target can be replaced by a gas nozzle, both mounted onto a translational stage.

To position the nanotaper in the laser focus and in front of the TOF spectrometer along the beam propagation direction, the electron count-rates from strong-field NIR emission are

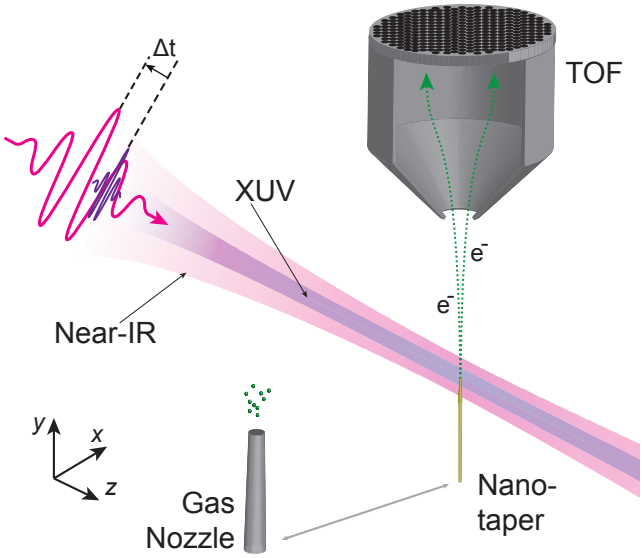

Figure 5.1: Illustration of the experimental setup for the nanotaper streaking experiment. The nanotaper is aligned parallel to the NIR laser polarization and the TOF spectrometer axis along the y-direction. To probe the near field, the nanotaper is positioned in the two-color laser field focus, where the near-IR laser pulse excites the near field, which is hereafter probed by electrons emitted from the nanotaper by XUV photons. For calibration measurements of the NIR laser field, the nanotaper target can be replaced by a gas nozzle. The displayed coordinate system fixes directions in the lab frame and is valid throughout this chapter. Adapted from [151].

maximized. In this procedure, the z-position of the TOF detector and targets are iteratively changed. For positioning the nanotaper within the focal plane, i.e. x-y-plane, we exploit the difference in photoemission schemes between NIR and XUV photoemission. Referring to section 3.3.3, scanning the tip spatially through the focal plane while recording the two-color photoelectron spectrum, the low energy counts in photoelectron spectra display the localization of the NIR laser focus, whereas high energy XUV photoemission yields the convolution of the XUV laser focus with nanotip geometry.

A typical measurement of the photoelectron spectrum is displayed in Fig. 5.2 (a), where the results of focal scanning are illustrated as insets (b) and (c). Integrating the low-energy counts with $E < 19\,\mathrm{eV}$ for different focal plane positions yields the emission plot as illustrated in (b), whereas integrated high-energy XUV emission counts with $E > 70\,\mathrm{eV}$ are shown in (c). The nanotaper, displayed by the outline (black solid line) in Figs. 5.2 (b) and (c), is positioned with its apex in the center of the NIR and XUV focal spots. Accordingly, since the FWHM focal spot size diameter of the XUV laser field yields $d_{XUV} \approx 5\,\mu\mathrm{m}$, the probed nanotaper cross section, illustrated by the white solid line, extends only $2.5\,\mu\mathrm{m}$ from the nanotaper apex along the shank. From that it can already be concluded, that a considerable share of detected photoelectrons will not be emitted from the nanotaper apex, but originates from its shank surface.

Based on Eq. (2.28), from the $2\,U_P$ cut-off energy of NIR photoemission, the intensity of the few-cycle pulse can be calculated. Assuming field enhancement factors of 2 to 3 at the nanotaper apex, for the spectrum, displayed in Fig. 5.2 (a), the obtained cut-off energy around

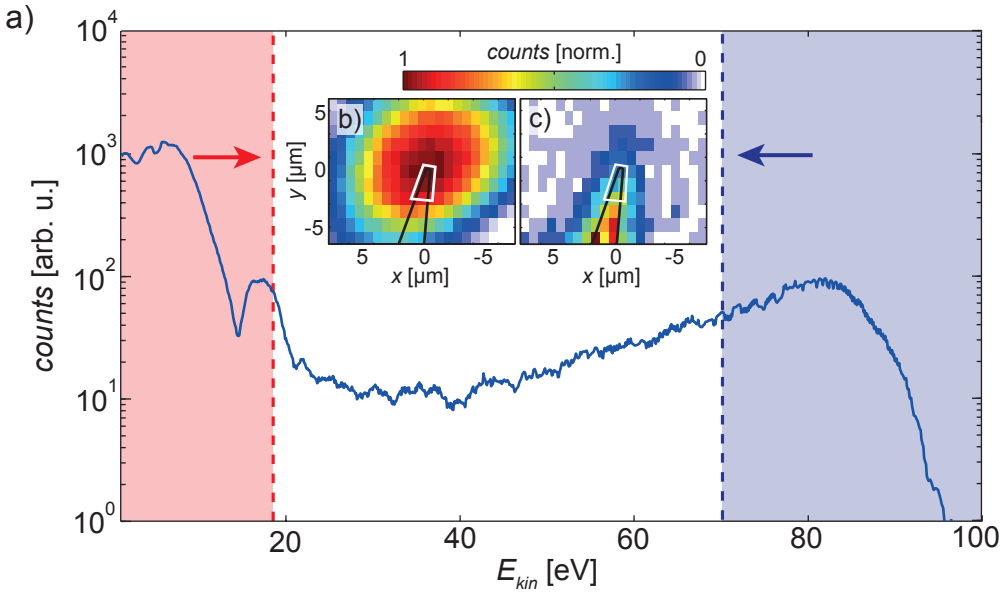

Figure 5.2: Photoelectron spectrum from the nanotaper. The photoelectron spectrum, shown in **(a)**, can be seperated in NIR and XUV photoemission, indicated by the red and blue colored background. The insets, **(b)** and **(c)**, display the separately integrated photoemission signal while scanning the nanotip through the focal plane. The black solid line indicates the position for the nanotip during the streaking experiments, while the white solid line signifies the probed region, given by the FWHM diameter of the XUV focal spot. Adapted from [116, 151].

15 eV implies an NIR-intensity of $\sim 1 \times 10^{11}\,\mathrm{W\,cm^{-2}}$, in accordance to previous reports for similar geometries [79, 241, 242]. As reported by Summers *et al.*, crystalline Au nanowires are found to melt for threshold intensities of $7.5 \times 10^{12}\,\mathrm{W\,cm^{-2}}$ for NIR laser pulses of 32 fs duration at a repetition rate of 2 kHz [243]. The presented phonon-electron interaction model which supports their experimental findings predicts reduced threshold intensities for the thermal breakdown with increasing repetition rates. Since our studies, are performed for smaller repetition rates and shorter pulse duration, which generally yields higher damage threshold intensities, the calculated NIR intensity of $1 \times 10^{11}\,\mathrm{W\,cm^{-2}}$ should be well below the thermal threshold. However, other studies, suggest that optical damage introduced by ablation becomes more severe for ultrashort laser pulses [244–247]. While the reported studies vary for the investigated pulse durations and wavelength, all reported threshold intensities for optical breakdown are found to be larger than the estimated value of $1 \times 10^{11}\,\mathrm{W\,cm^{-2}}$, used here for the nanotaper streaking experiments. Accordingly, it can be concluded, that intensities in the low $10^{11}\,\mathrm{W\,cm^{-2}}$ regime are not yet sufficient to damage the nanostructures. This was confirmed also both by the repeatability of streaking measurements and scanning electron microscopy.

In the experimental spectrum, high energy photoelectrons, exceeding 50 eV, are attributed to photoemission induced by XUV photons. The large width of the XUV photoemission spectrum is partly explained by the density of states (DOS) of the Au band structure. As illustrated in Fig. 5.3, the calculated convolution (blue solid line) of the XUV-mirror reflectivity curve (green dashed line) with experimentally observed DOS function of polycrystalline Au [248] results in a considerable broadening of the photoemission peak, centered around 83 eV. However, the broadening observable in experimental data (red markers), es-

pecially towards lower energies, is not fully explained by the DOS-broadening. One possible explanation of the additional broadening of the photoemission peak are scattering effects of photoexcited electrons at the nanostructure surface. Several methods can be applied to account for inelastically scattered electrons, typically referred to as background [249–252]. Since our analysis method and extraction of the streaking traces relies only on the highest energetic electron counts in the falling edge of the spectrum, inelastically scattered electrons are not further considered and background subtraction, which always holds intrinsic assumption on the underlying scattering process, is omitted. Besides scattering effects, a second contribution for the broadening in the XUV photoemission spectrum are contaminations, forming adlayers on the nanotaper surface. Most commonly, vacuum infrastructures suffer from water or hydrocarbon molecules adsorbed to any surface in the vacuum chambers. The valence ionization potential of water is reported around 12.6 eV [253–256], whereas valence ionization potentials of hydrocarbons range typically between 8 eV-26 eV [257]. Accordingly, low-energetic electrons are potentially not emitted from gold, but from the surface contamination layer. Under consideration of the AS-5 vacuum conditions of 10^{-8} mbar, a contamination layer is highly likely. To exclude the effects of scattering and photoelectron emission from contamination layers, the streaking trace retrieval algorithm relies exclusively on high energetic electrons, which are assumed to be emitted from the Au 5d-band. As will be shown below, for the chosen experimental geometry, surface contamination layers are furthermore not expected to change the temporal dynamics of the near field.

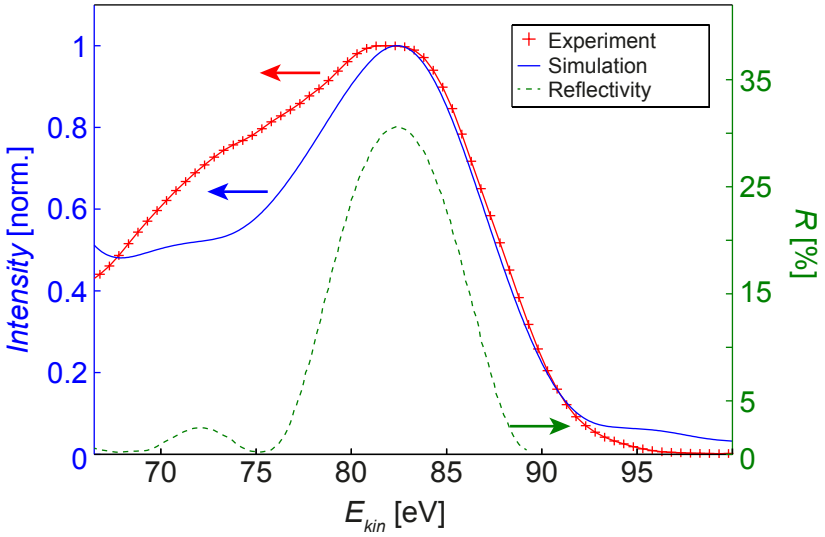

Figure 5.3: Broadening of the Au valence band emission. Normalized photoelectron spectrum (blue solid line) calculated as convolution of the XUV mirror reflectivity curve (green dashed line) with the DOS measurements of the Au valence band reported in Ref. [248]. The reflectivity curve has been shifted by about 10 eV towards lower energies. While from the calculation of the convolution between mirror reflectivity curve and the Au DOS spectrum, a broadening of the photoelectron spectrum can be anticipated, the experimental data (red markers) reveal even larger spectral width of the emission peak.

Given the strong XUV photon absorption and the high target density, typical reference measurements in neon gas yield about 1.5 electron counts per laser shot from XUV photoionization. Accordingly a delay range of 12 fs with precision of 100 as is sampled with decent

statistics within 5 - 10 min. For the nanotaper, positioned with the apex in the laser focus, the XUV-electron count rate is found to vary between $(1.5 - 3) \times 10^{-2}$ per laser shot. Besides the reduced cross section for photoionization from the Au 5d as compared to the Ne 2p shell, the major cause for the low electron count-rates is the small geometrical cross section of the nanotaper. Relating XUV-illuminated nanotaper cross section with the integrated geometrical cross section of the XUV focal spot, where the FWHM focal spot size was assumed to 2.5 µm, yields a factor around 50. Moreover, only the first atomic layers of the Au nanotaper will contribute to detectable electron counts, whereas electrons photoexcited deep in the bulk are prone to inelastic scattering and therefore do not escape from the sample. Since the overall target density is considerably reduced in the case of solid nanosized targets as compared to gas phase experiments, count-rates in the nanotaper streaking experiments are significantly lowered.

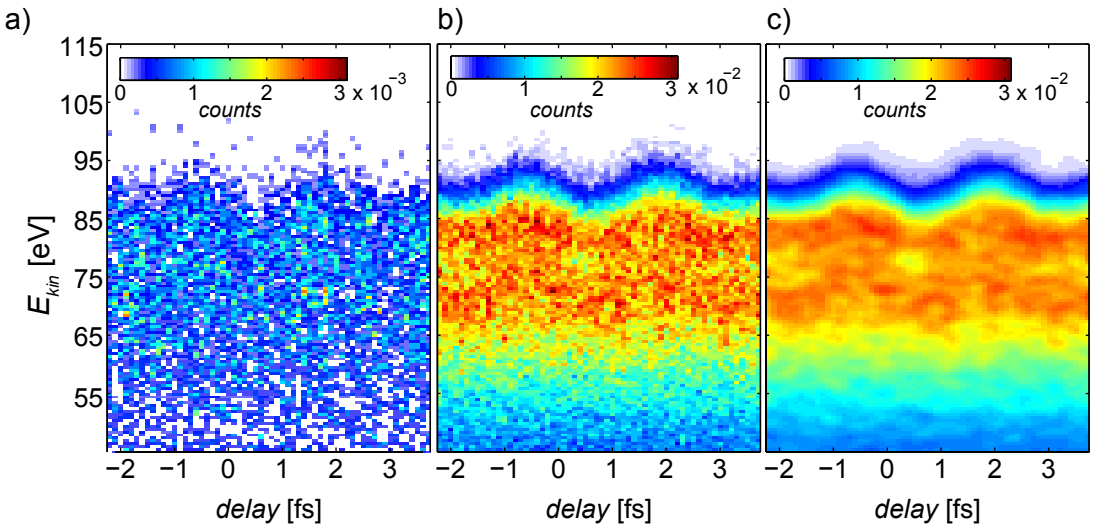

Figure 5.4: Superimposing streaking spectrograms. Single spectrograms on the nanotip, illustrated in **(a)** are acquired at identical integration times as neon gas reference scans, i.e. 7500 laser shots per delay scan. To achieve informative statistics, several individual scans are superimposed, as shown in **(b)**, where 30 scans are overlaid, which yields in total 225 k laser shots per delay scan. The cascaded measurement approach allows to discern longterm drifts and instabilities in laser power or CEP. With a 2D moving averaging filter, binning effects are removed and the spectrogram is smoothed **(c)**.

To reach informative statics in the streaking spectrogram, the necessary acquisition time amounts to several hours, which is on the typical time scale where laser stability can be maintained. While power fluctuations and pointing instabilities are manageable, the CEP stability ranging between 1.5 - 6 h for the few-cycle laser pulse is the major weak point in long-integrative measurements with the AS-5 setup. To reduce the risk of a drop in the CEP-lock during data acquisition, streaking spectrograms on the nanotaper are cascaded to several short-integrative scans with an integration time that is comparable to gas reference measurements. Drifts in power or CEP during the cascaded measurement can be ruled out by reference measurements, taken before and after each nanotaper measurement cascade. Given that no drifts are present, individual nanotaper scans of a measurement cascade are superimposed to a single streaking spectrogram. As demonstrated in Fig. 5.4 (a), individual nanotaper streaking scans do typ-

ically not yield conclusive statistics, which can be achieved by superimposing multiple scans as shown in (b). To reduce the effect of binning, the spectrograms are processed with a 2D averaging filter, where the result is displayed in Fig. 5.4 (c). Depending on daily laser stability, the cascades are comprised of different numbers of integrated scans, where small data sets comprise only four, while large data sets reach up to 30 individual scans.

5.3 Theoretical Modeling

For a better understanding of the experimental data, we perform theoretical simulations. The near fields around the nanostructure are calculated with a finite-difference time-domain (FDTD) method, where we use a commercial software[1] to solve Maxwell's equations. Spatially, the incident NIR laser field is modeled by a Gaussian beam profile with an intensity FWHM diameter of $d_{\mathrm{NIR}}^{\mathrm{sim}} = 15\,\mu\mathrm{m}$. In the temporal domain, the NIR pulse is modeled according to Eq. 2.5, by a Gaussian envelope function, where the central wavelength is assumed to $\lambda_0^{\mathrm{sim}} = 720\,\mathrm{nm}$ and a pulse duration of $\tau_{\mathrm{NIR}}^{\mathrm{sim}} = 4.5\,\mathrm{fs}$, defined as FWHM in temporal intensity. The CE-phase and higher order phase terms are set to 0 for the simulations, representing a cosine-like waveform. As refractive index for Au, we use (spline-interpolated) experimental data from Johnson and Christy [206].

The nanotaper geometry is modeled based on typical SEM micrographs as illustrated in Fig. 3.2 (b). A hemisphere with 100 nm radius features the apex of the nanotaper, for which a full opening angle of 10° is assumed. The FDTD simulation box hosting the nanotaper is modeled with lateral sizes of $20\,\mu\mathrm{m} \times 20\,\mu\mathrm{m}$, which is enough to exclude diffraction effects on the simulation box boundaries. In beam propagation direction, the box dimension is chosen to 1.6 µm which has proven to be enough for capturing the full spatial dependence of the near fields around the nanostructure. Perfectly matched layers (PML) on the simulation boundaries damp the reflections of electric fields effectively over the full bandwidth of the incident laser pulse.

The simulation volume is divided into Yee cells, whose size is determined by the mesh grid. Especially for the nanotaper apex, where the geometry varies substantially on the nanometer scale, the mesh-grid must be fine enough to capture the target structure. At the nanotaper shank, given the orthogonal mesh-grid, the geometry is described by a step-terrace model. Accordingly, for the sharp edges at the steps, strong field localization and enhancement are observable, which must be considered as numerical artifacts [207], but can be reduced by mesh refinement techniques. Since the computational efforts scales nonlinearly with the mesh size, we restrict finer mesh-grids to the region of the nanotaper apex and shank. For Yee cells of 2 nm edge length, limited by the computational power of the employed desktop work station, the calculated FDTD fields show no significant contribution from numerical artifacts.

The resulting FDTD simulations for the field component parallel to the tip axis (and laser polarization direction), normalized to the incident field strength, i.e. E_y/E_0, are displayed in Figs. 5.5 (a) and (b). In (a) the normalized E_y-component for the perspective perpendicular to the laser propagation direction is illustrated, while (b) shows the resulting near field in the focal plane, from a perspective parallel to the laser propagation direction. The near field results as superposition of the incident NIR laser field with the scattered field from the nanostructure. At the apex, field enhancement factors around 2 and field localization to dimensions

[1] Lumerical Solutions Inc., FDTD Solutions 8.9

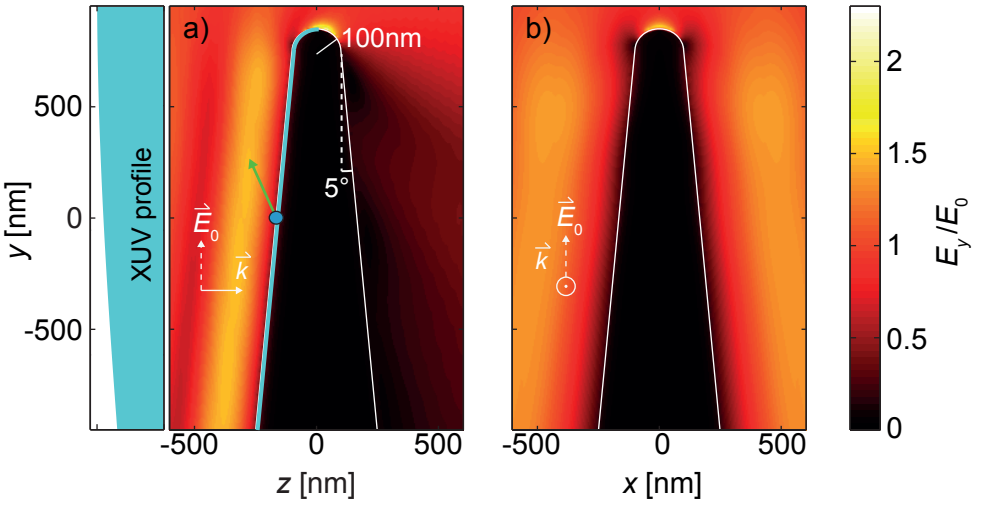

Figure 5.5: FDTD calculations of the near field surrounding the nanotaper target. Both panels show the maximum near field strength along the tip axis E_y, normalized to the incident NIR field strength E_0. While **(a)** displays the result perpendicular to the laser propagation direction, **(b)** demonstrates the result from the parallel perspective. The tip outline is illustrated by the white solid line, while the blue solid line in (a) indicates the region probed by XUV photoemission. The blue solid dots in (a) indicates the representative surface position, from which the nanotaper response function in Sec. 5.3.1 is calculated. The blue shaded area on the left illustrates the XUV focal spot size. Adapted from [151].

below the diffraction limit are observed. The resulting enhancement from our calculations is in good agreement with literature values, reported for similar geometries [207]. In vicinity of the nanotaper shank, the near field amplitude is reduced as compared to the incident NIR field, where suppression to about $0.5\,E_0$ is observed Figs. 5.5 (a) and (b). Moreover, sub-wavelength variation of the near field around the shank can be noticed, indicating surface plasmons propagating along the nanotaper shank. On the left side of Fig. 5.5, the blue shaded area illustrates the spatial profile of the XUV laser focus, with the tip apex positioned in the center. The Gaussian envelope implies, that a considerable share of photoelectrons must be expected to be emitted from the nanotaper shank. A proper discussion of count-rate contributions from different nanotaper positions, as well as the consequences arising from position averaging on the experimental results will follow.

Using the FDTD approach, the near fields of different nanotarget geometries can be investigated and compared in the time domain. Figure 5.6 (a) illustrates the general scheme for which the displayed near fields in (b) are calculated: for different target geometries, the near field is calculated at a representative point $\boldsymbol{r}_0$ on the shank of the nanotargets, facing the incoming laser beam. Here, we compare target geometries of a conical nanotaper (apex radius of 50 nm and full opening angle of 12.5°) with a semi-infinite cylindrical nanotip, consisting of a cylinder with 350 nm radius terminated by a hemisphere. In both cases, the near field is calculated at a distance of 2800 nm from the apex, where the radius of the conical nanotaper at the position $\boldsymbol{r}_0$ yields 350 nm, identical to the radius of the semi-infinite cylinder geometry. Moreover, we use Mie's theory [258] to calculate the analytical solution of the near field in vicinity of the surface of an infinite cylinder with 350 nm radius. In Fig. 5.6 (b) the normalized near-field component E_y is displayed for the different geometries. The results for the nanota-

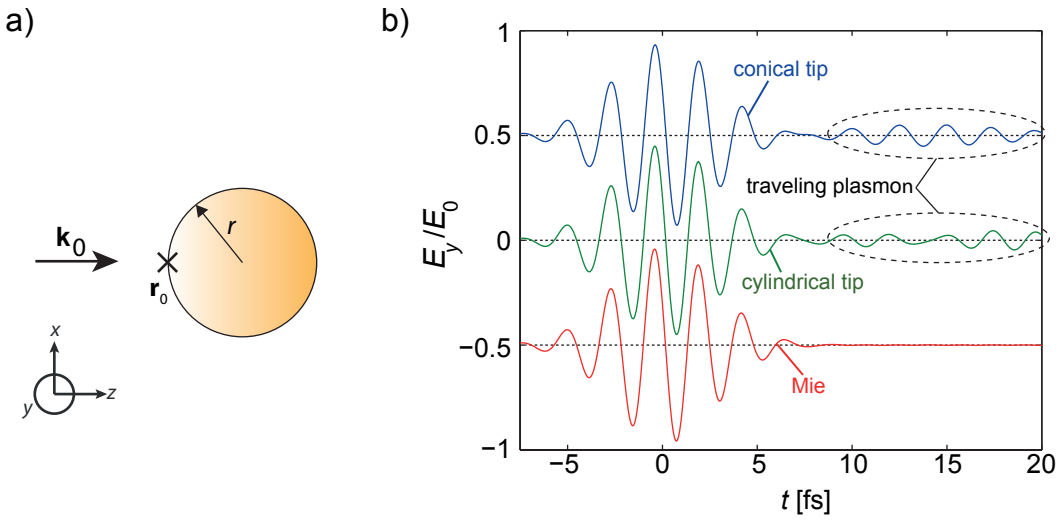

Figure 5.6: Near field calculation in the time domain for different geometries. In **(a)** the geometry for the FDTD calculations is illustrated. The near fields are analyzed on the nanotarget shank surface at the representative position $\boldsymbol{r}_0$, indicating the distance from the apex. We compare the near field results for conical targets ($r_{\mathrm{apex}} = 50\,\mathrm{nm}$ and full opening angle of 12.5°) with cylindrical nanotips (shank diameter 350 nm) and infinite cylinder geometries (cylinder radius 350 nm) for a position at a distance of 2800 nm from the apex, centered in the focus of the incoming laser field $\boldsymbol{E}_0$. In **(b)** the normalized near-field component E_y, parallel to polarization of the incoming electrical field and the tip axis, is displayed for the different geometries. The results for the conical tip and the infinite cylinder were shifted by ±0.5 on the y-axis. After the main pulse, a delayed near-field contribution is obtained for the conical and the cylindrical nanotip, which is in both cases attributed to a surface plasmon, excited at the apex of the nanostructure and propagating along its shank. Adapted from [151].

per tip and the Mie solution are shifted by ±0.5 on the y-axis. As can be observed, the near field calculation for the main pulse between $-7.5\,\mathrm{fs} < \mathrm{t} < 7.5\,\mathrm{fs}$ shows excellent agreement for the different nanotarget geometries. Independent of the geometry, the near-field strength at the nanotarget surface is reduced, yielding typically about half of the incident field. Since a cosine-like input pulse is employed, the near-field phase is apparently shifted for all geometries. In cases of the tapered nanotip and the cylindrical tip, a delayed near-field contribution can be identified, onsetting about 7.5 fs after the center of the main pulse. A full analysis of the near-field dynamics reveals, that the delayed contribution originates from a surface plasmon polariton, excited at the nanotaper apex and propagating along the shank. The delay between the main pulse and the SPP depends on the representative position $\vec{r}_0$ and its distance from the apex. For short distances, the delay reduces, and ultimately overlaps with the main pulse within the interval of -7.5 to 7.5 fs and yields small distortion to the phase and amplitude of the main pulse. For the tapered nanotip, the plasmonic contribution is generally found stronger than for the semi-infinite nanocylinder. Since the tapered geometry connects shank and apex smoothly, while for the cylindrical nanotip the plasmonic excitation is prone to scattering and reflection on the transition between apex and shank, this finding can be anticipated. For the streaking experiment, where a large area from the nanotaper shank is probed, the plasmonic excitations are averaged out, which results in a broadening and smearing-effect for the streaking traces. In conclusion, despite the plasmonic excitation propagating along the nanotaper shank being absent for the Mie calculation of an infinite cylinder, all target

geometries yield approximately similar results for the response of the nanotarget to the main pulse. Apparently, all geometries offer a reasonably good approximation of the nanotaper tip.

While field enhancement factors as high as 30 have been reported for nanostructured targets [207] with smaller apex radii, it should be stressed, that our targets where not fabricated for maximum field enhancement factors. The target geometry we present here was chosen to maximize the signal strength in the streaking experiment, which, as will become more clear with the discussion on the apex contribution below, is supported by tips of larger apex radius.

5.3.1 Response Function

The FDTD calculations yield the spatio-temporal properties of the near field $\mathbf{E}_{\mathrm{nf}}(\mathbf{r},t)$, resulting from the interaction between incident laser field $\mathbf{E}_{\mathrm{input}}(\mathbf{r},t)$ with the metallic nanostructure. While the interaction is fully described in the framework of linear Maxwell's equations, a response function $\mathbf{G}(\mathbf{r},t)$ can be found, which determines the near-field characteristics for any given input pulse. The response function, generally represented by a matrix, is only valid for a given nanostructure geometry and input beam. For convenience, the response function is expressed in the Fourier domain, where the relation yields

$$\mathbf{E}_{\mathrm{nf}}(\mathbf{r},\omega) = \mathbf{G}(\mathbf{r},\omega)\cdot\mathbf{E}_{\mathrm{input}}(\omega) \qquad , \tag{5.1}$$

with $\mathbf{r}$ describing the position on the nanotarget surface and ω the frequency. In our experimental streaking setup, only the near-field component parallel to the polarization direction of the incident laser field is probed. Therefore, the vector relation in Eq. 5.1 reduces to a scalar equation. To obtain the near-field phase, the response function must be separated into an absolute value and its associated phase term, yielding

$$G(\mathbf{r},\omega) = abs(G(\mathbf{r},\omega))\cdot\exp\{i\varphi(G(\mathbf{r},\omega))\} \qquad , \tag{5.2}$$

where absolute value and phase of the response function is normalized to the input beam. To include peculiarities resulting from the numerical simulations, the input pulse is retrieved as free-space response from FDTD calculations at the position of the apex without nanotip present. The results for absolute value and phase of the response function for different geometries, calculated at representative points, are illustrated in Figs. 5.7 (a) and (b).

The results for the tapered nanowire are shown in blue, where the response function is calculated for the position indicated by the blue solid dot shown in Fig. 5.5 (a) at a distance of 750 nm from the apex. The geometry was modeled with an apex radius of 50 nm and full opening angle of 10°. The absolute value of the tapered nanowire's response function is smaller than unity over a broad spectral range. This finding was already anticipated from the FDTD calculations displayed in Fig. 5.6 (b), where the near-field strength appears reduced on the nanotarget surface. The modulations in the absolute value are assigned to SPPs, excited at the apex and propagating along the shank of the tapered nanowire. A similar oscillatory behavior is observed for the phase of the response function. Below the onset of intraband transitions around 550 nm, the phase of the response function increases, approaching the regime where the near field follows the incoming field instantaneously. In the long wavelength regime, the response function phase oscillates, as a result from the plasmon propagation along the shank, around a mean value of about -1 rad.

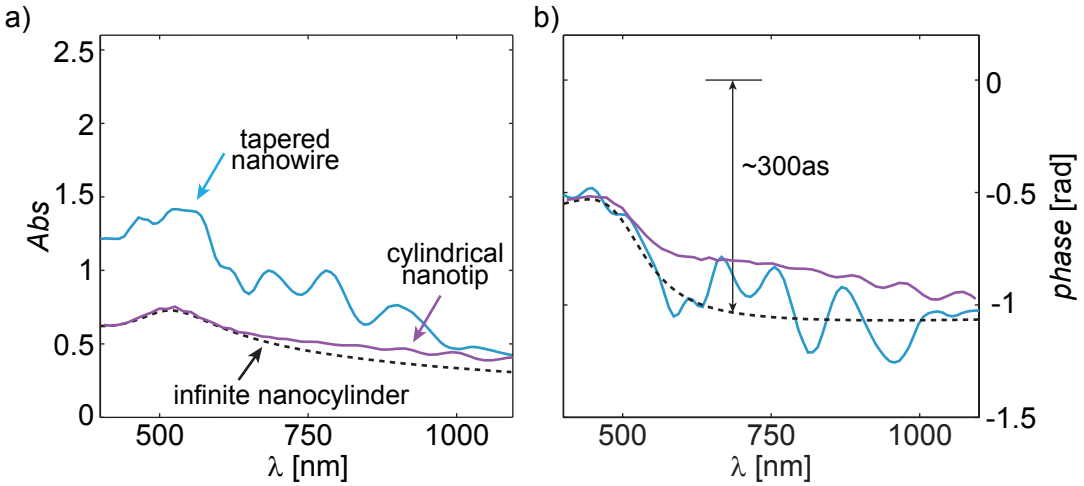

Figure 5.7: Response functions for different target geometries. Absolute value **(a)** and phase **(b)** of response functions calculated at representative target positions (see text) for different target geometries. For the cylindrical nanotip (purple solid line), modeled with 200 nm diameter, and the tapered nanowire (blue solid line), modeled with hemispherical apex of $r_{\mathrm{apex}} = 50$ nm and full opening angle of 10°, the plasmonic excitations propagating along the shank of the nanotarget yield modulations in the absolute value and phase of the response functions. Based on the analytical Mie-solution for an infinite nanocylinder with 200 nm diameter, the phase shift of the near field is predicted with 300 as. Adapted from [151].

Motivated by the time domain calculations, where different geometries were found to yield comparable results, the response functions for an infinite cylinder and a cylindrical nanotip, both with diameter of 200 nm, are calculated. The latter is terminated by a hemisphere of $r_{\mathrm{apex}} = 100$ nm to model the apex, positioned in the focal center of the incident laser field. For the infinite cylinder, Mie's theory is applied to calculate an analytical solution, while the results for the nanocylinder are obtained using the FDTD method.

While the response function's absolute values for the tapered nanowire and infinite cylinder show no perfect agreement, the response function phases coincide considerably well. The absolute value from the Mie calculation, is smaller than unity over the full bandwidth, yielding a near-field attenuation over the full spectrum. For the tapered nanowire, in the short wavelength regime, the absolute value exceeds unity, yielding an effective near-field enhancement over the incident laser field. However, it should be noted, that the laser spectrum bears almost no spectral intensity for the wavelength regime below 600 nm. Averaged over the full spectrum, near field attenuation, which is anticipated from the FDTD calculations, results also for the nanotaper geometry. Since for the infinite cylinder no plasmonic excitations propagate along the surface, the absolute value and phase of the response functions are rather flat without oscillatory behavior, which is predominantly observed for the tapered nanowire geometry. The cylindrical nanotip result is obtained as transition between the findings for the infinite cylinder and tapered nanowire. As already observed in the time domain, an SPP, excited at the apex, propagates along the shank of the cylindrical nanotip. Accordingly, the response function for the cylindrical nanotip geometry shows the oscillatory behavior, as already observed for the tapered nanowire. Since the transition from apex to shank for the cylindrical nanotip is less smooth as compared to the nanotaper geometry, the coupling of plasmonic excitations from apex to shank is less efficient. Therefore, in comparison to the

tapered nanowire, the oscillatory behavior is less pronounced for the cylindrical nanotip.

The oscillatory course for the response function in case of the tapered nanowire and cylindrical nanotip geometry depends on the representative position on the nanotarget for which the response function is calculated, in particular its distance from the apex. The latter is comprehensible, since the SPP spreads from its excitation position at the nanotarget apex. As will be shown below, integrating over different positions, the oscillations in the response functions are averaged out yielding approximately the results as obtained from the Mie calculation. For 720 nm, representing the central wavelength of the NIR laser pulse, the phase shift from the Mie calculation is predicted to be about -1.05 rad, which is equivalent to about 300 as in the time domain.

5.3.2 Streaking Simulations

Since streaking experiments suffer from considerable averaging effects over different positions from the nanotarget, it is a-priori not clear what can be extracted from the experimental streaking spectrograms acquired on nanotarget systems. Accordingly, it is instructive to perform full streaking simulations. We use a classical Monte-Carlo algorithm to simulate the streaking spectrograms, while the near field $\mathbf{E}_{\mathrm{nf}}\left(\mathbf{r}\left(t\right),t\right)$ in vicinity of the nanotarget is calculated in an FDTD approach as presented above. Photoexcited electrons are initialized at the nanotarget surface according to the XUV laser pulse parameter, which is modeled by Gaussian functions in time and space, with FWHM focal spot diameter of 5 µm and FWHM pulse duration of 220 as. Initial kinetic energies of photoexcited electrons are distributed according to experimentally obtained nanotaper XUV photoemission spectra. The emission angle is fully randomized, while we integrate electrons emitted initially within a cone of full opening angle of 45°, corresponding to the solid detection angle of the TOF. Since streaking energy shifts by the near field are found to be substantially lower than the initial kinetic energy, the approach to integrate over initialized emission angles appears justified. For the small streaking intensities below $10^{12}\,\mathrm{W\,cm^2}$, emission angles are hardly changed from the near field propagation. After emission, photoelectrons are propagated in the electric near fields in a full three-dimensional simulation based on the classical equation of motion

$$\mathbf{v}(t) = -\frac{e}{m_{\mathrm{e}}}\int_{t_0}^{t}\mathbf{E}_{\mathrm{nf}}\left(\mathbf{r}\left(t'\right),t'\right)dt' + \mathbf{v}_0 \tag{5.3}$$

where $\mathbf{r}(t)$ describes the electron positions at time t, t_0 the emission time and $v_0 = \sqrt{2E_{\mathrm{kin}}\,/\,m_e}$ the initial velocity which can be calculated based on the initial kinetic energy E_{kin} and the electron mass m_e. The individual electron emission time t_0 is chosen randomly. The propagation calculation according to Eq. (5.3) is performed numerically based on a Velocity-Verlet algorithm [211]. The trajectory calculations are continued until each delay step yields converged results.

A typical streaking spectrogram resulting from the Monte-Carlo simulations is displayed in Fig. 5.8 (a), while a measurement on the nanotaper is illustrated in (b). For the simulated streaking spectrogram, electrons are propagated in the near field, calculated for a cylindrical Au-nanotip with apex and a shank radius of 100 nm. The apex is positioned in the center of the XUV and NIR focal spots. In the near field calculations, the incident NIR intensity was assumed as $10^{12}\,\mathrm{W\,cm^{-2}}$ with a pulse duration of 4.5 fs.

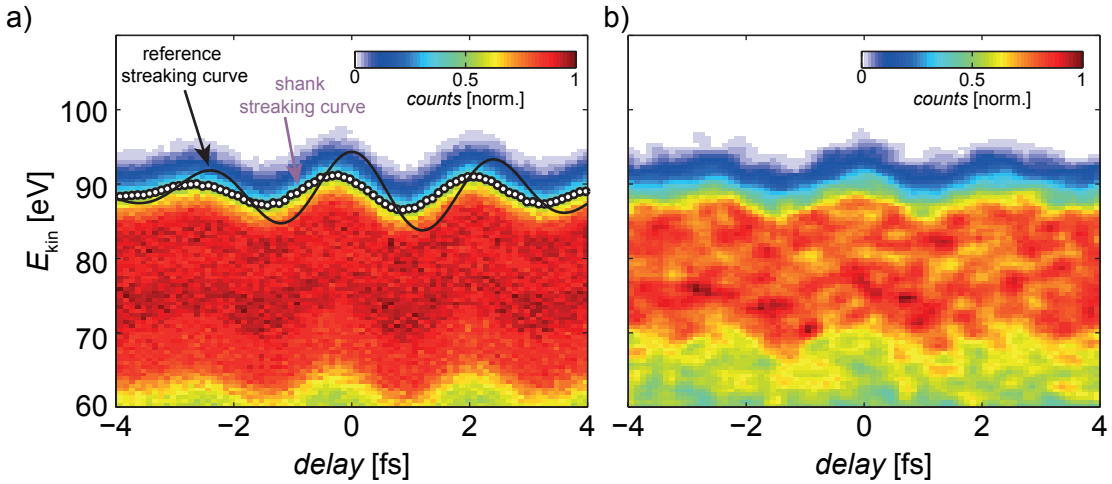

Figure 5.8: Simulated streaking spectrogram. In **(a)** the simulated streaking spectrogram obtained for trajectory simulations in the near field surrounding a cylindrical nanotip with 100 nm diameter is shown. For comparison the experimentally obtained spectrogram is displayed in **(b)**, demonstrating the striking agreement between simulation and experiment. From the simulated streaking spectrogram the streaking trace is retrieved in a Fermi-fitting procedure (displayed as white dots) and compared with the reference streaking curve, calculated as the vector potential of the incident field. Adapted from [151].

The comparison between experimentally obtained and simulated spectrograms yields good agreement. Since the statistics is considerably higher, the simulated streaking spectrogram appears smoother as compared to the experimental result. From the streaking spectrogram, the streaking trace is retrieved using a Fermi fitting routine, which will be explained in the following section. The retrieved streaking trace, displayed as white dots, is compared to the reference streaking trace, representing the vector potential of the incident laser field. The latter is shifted on the y-axis to the mean value of the nanotaper streaking trace. The retrieved nanotip streaking trace is phase shifted with respect to the reference vector potential of the incoming laser field by about 300 as. This result is in striking accordance with the predictions from response function calculations, shown in Fig. 5.7, for representative points on the shank of different nanotarget geometries. The amplitude of the nanotip streaking trace is reduced, yielding about half of the incoming field, as is anticipated from the response function calculations. Apparently, despite the averaging over different emission spots on the nanotip shank, still a well-defined streaking trace is obtainable from the streaking spectrogram. The latter is a direct consequence from the comparable flat response function of the cylindrical nanotip over the full laser bandwidth, as shown in Fig. 5.7. Since the response functions, calculated for representative points on the nanotarget shank, yield identical results for phase shift and amplitude, it is assumed that the spectrogram predominantly comprises electrons emitted from the nanotaper shank rather than from the apex. A proper count-rate analysis, following below, will support this suggestion.

Comparing the response function calculations with the retrieved streaking trace rests implicitly on the assumption, that streaking experiments on the nanotargets probe the phase and amplitude of the electric near field. As will be derived in the next section, this assumption holds only for a specific parameter range, depending on the nanotarget geometry and the properties of the incident NIR and XUV laser pulses.

Trajectory calculations assuming tapered nanotarget geometries suffer from numerical artifacts in FDTD simulations, where hot-spot formation on the shank is observed for orthogonal mesh grids. Since the hot-spots are considered as unphysical numerical artifacts, Monte-Carlo simulations are performed in near fields, calculated for cylindrical nanotip geometries. The discussion based on the response functions, demonstrated that the different geometries influence the retrieved results only marginally.

5.3.3 Streaking Regimes for Nanoscale Near-Field Streaking

As presented in Chap. 2.3 and demonstrated in Ref. [126] the streaking trace for electrons propagating through highly localized electric fields allows not necessarily the retrieval of amplitude and phase of the respective near field. Instead, based on the adiabaticity parameter δ as defined in Eq. (2.44), three different streaking regimes need to be distinguished. To elaborate the respective streaking regime of the present experiment, we calculate the range of δ-values. Since the near-field decay length is determined by the geometrical features of the target, represented here by the nanotargets' radius, it is assumed that $l_{\mathrm{nf}} \approx 50$ - $150\,\mathrm{nm}$. The photoelectrons initial velocity in polarization direction depends on the emission angle, where the electrons initial velocities range between $v_0 \approx 3.8$ - $5.5\,\mathrm{nm\,fs^{-1}}$ for emission angles between $0°$ - $45°$, relative to the laser polarization direction. Assuming the laser period as $T_0 = 2.5\,\mathrm{fs}$, which corresponds to a central wavelength of $750\,\mathrm{nm}$, the adiabaticity parameter yields around $\delta \approx 3.5$ - 15. As apparent from Fig. 5.8, the photoelectrons' energy gain through propagation in the electric near field yields only about $5\,\mathrm{eV}$, whereas their initial kinetic energy around $90\,\mathrm{eV}$ is significantly higher. Therefore, we can employ the zeroth order approximation for the solution of Newton's equation, which is the only necessary requirement to apply the generalized theory presented in Ref. [126].

For the calculated adiabaticity parameter range, the streaking experiment is found in the ponderomotive regime. For simplicity, after comparison with Fig. 2.6, we set the incident-field function $f_0 = 0$, for which the phase of the streaking trace is exclusively determined by surface-function f_{surf}, both defined in Eqs. (2.45a) and (2.45b). In the limit of $\delta \to \infty$, the streaking experiment resembles the ideal ponderomotive case, where the streaking trace represents the near-field vector potential. From the surface-field function, the expected phase deviation for finite δ-values in comparison to the ideal case can be estimated according to

$$\varphi_{\mathrm{A}} = \arctan\left(\frac{\Im(f_{\mathrm{surf}})}{\Re(f_{\mathrm{surf}})}\right) = \arctan\left(\frac{1}{2\pi\delta}\right) \xrightarrow[\delta=3.5]{} 4.54 \times 10^{-2} \quad . \tag{5.4}$$

For the NIR field's central wavelength of $750\,\mathrm{nm}$, the above phase deviation is equivalent to a shift around $18\,\mathrm{as}$ in the time domain. In conclusion, even for small adiabaticity parameters of $\delta \sim 3$, the streaking regime can be considered ponderomotive, where the difference between near-field phase, retrieved from the streaking trace reveals only marginal shifts on the order of tens of attoseconds relative to the phase of the near-field vector potential.

The streaking regime can also be derived numerically by trajectory calculations for electrons emitted at representative points of a nanocylinder target geometry. Thereby, the above simplification of $f_0 = 0$ is dispensable. For the numerical analysis, we assume a constant electron emission angle of $15°$ relative to the cylindrical tip axis. The near field is retrieved from an FDTD simulation, where the target geometry is modeled by an Au nanocylinder target with $100\,\mathrm{nm}$ apex radius. The resulting electron trajectories after propagation through the near field are compared to the near-field vector potential, calculated numerically at the

electron emission points. The results for three different positions on the nanotaper shank surface are illustrated in Fig. 5.9, where dashed and solid lines represent the respective near-field vector potentials and the numerically calculated streaking traces. We compare representative positions on the nanocylinder shank surface with distances of 300 nm, 2000 nm and 3000 nm from the nanotip apex. As observable from the magnified inset, the shift between streaking traces and the near-field vector potential yields about 20 as, which is in excellent agreement with the predictions from the generalized theoretical approach. Accordingly, also the numerical calculation demonstrates that the nanotaper streaking experiment is performed in the ponderomotive regime, where the full phase and amplitude information of the near field can be retrieved from the streaking trace.

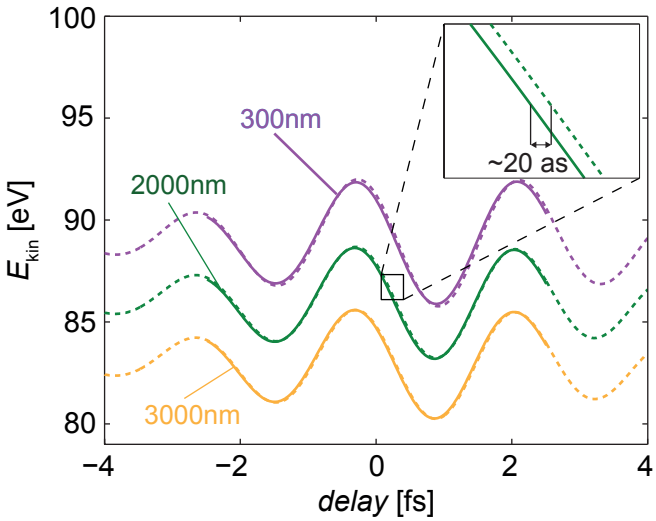

Figure 5.9: Comparison between electron trajectory calculations and the near-field vector potentials. Near-field vector potentials (dashed lines) are calculated at representative points on the nanotip surface, at 300 nm, 2000 nm and 3000 nm distance from the apex. Trajectories for electrons, emitted at the same positions under 15° emission angle relative to the tip axis are calculated (solid lines) and compared to the near-field vector potential. The curves for 2000 nm and 3000 nm are down shifted by 3 eV and 6 eV to separate overlapping traces. From the inset, for the shank position 2000 nm from the apex, the difference between near-field vector potential and streaking trace is evaluated with 20 as, demonstrating a predominantly ponderomotive streaking regime. Adapted from [151].

5.3.4 Streaking from Different Positions on the Nanotaper

In the experimental streaking setup, the measurement averages over different emission sites on the nanotaper. Since the measured spectrograms reveal well-defined streaking traces, it can be concluded, that the near-field phase and amplitude is only weakly dependent on the position on the shank. This argument is supported by Monte-Carlo simulations which showed almost perfect agreement with the experimental results as displayed in Fig. 5.8. However, it is illustrative to investigate phase and amplitude dependence of the near field on different shank positions. To analyze the dependence of near-field vector potentials at different positions on the nanotarget, the near fields are calculated as Mie solutions for infinite nanocylinders with varying radii. The refractive index for the Au nanocylinders is taken from Ref. [259]. The

incident laser field is modeled by a Gaussian envelope with pulse duration of 4.5 fs as FWHM intensity and central wavelength of 720 nm.

Figure 5.10 (a) and (b) show the phase shift and relative amplitude of the vector potential, normalized to the incoming laser field. The results are calculated from the near-field component parallel to the laser polarization at the time, where maximum electric field strength is obtained. The plots display the results for an infinite nanocylinder, outlined by the white solid line, with 100 nm radius. Over the entire front side of the cylinder shank facing the incoming laser field, i.e. $-90 < \theta < 90$, the streaking phase shift can be considered independent on the emission position, encoded by θ. In contrast, on the backside of the nanocylinder, the phase shift is strongly dependent on the emission position, where positive phase shifts are observed. As for the phase, the relative streaking amplitude shows low position dependence, where only towards the pole positions at $\theta = \pm 90°$ a decrease of the near-field amplitude is observable. The backside emission yields almost no streaking amplitude, which is anticipated since Au is opaque over the bandwidth of the NIR laser field. The field is effectively blocked on the shadow side of the nanocylinder, in contrast to transparent media, where field enhancement for the backside emission is reported [260, 261].

For this experiment, electron emission on the nanocylinder backside is highly unlikely, since Au is almost opaque for XUV photons centered around 93 eV. On the other hand, electron excitation on the target front side and subsequent propagation through the nanocylinder to the backside can be excluded due to the mean free path in the range of several nanometer. Accordingly, backside contributions can be safely neglected.

In Figs. 5.10 (c) and (d) the streaking phase shift and relative amplitude for different cylinder radii is plotted in dependence of the angle θ as defined in (a). The streaking phase shift is observed to be flat over a large θ-range for the nanocylinder radius varying between 50 nm and 1500 nm. Accordingly, the different emission sites of a nanocylinder with fixed radius are observed to be in phase, where only large radius nanocylinders yield an increasing variation for emission sites on the nanocylinder poles, i.e. at $\theta = \pm 90°$. Since the absolute values differ with the nanocylinder radius, a nanotaper geometry comprises emission sites which are not fully in phase. However, for the nanotaper geometry discussed above with full opening angles of 12.5° and 50 nm apex radius, the nanotaper radius varies between 50 nm to about 350 nm across the XUV focal spot radius of 2.5 µm. Accordingly, the absolute streaking phase shifts from Fig. 5.10 (c) vary approximately between -260 as and -400 as for different radii on the nanotaper shank surface. The maximum phase shift difference calculates to less than 140 as, which is small compared to the duration of a single optical cycle, yielding 1250 as. Therefore, even for the different radii on a nanotaper, the emission sites can still considered to be in phase.

The relative amplitudes, shown in Fig. 5.10 (d) exhibit a stronger dependence on the emission site, indicated by θ, where the relative amplitudes decrease towards the pole emission at $\theta = \pm 90°$, while the amplitude attenuation is more pronounced for nanocylinders with large radius. The simultaneous emission of electrons prone to different streaking amplitudes will result in a broadening of the streaking trace in the spectrogram, as it is observed in the experiments and Monte-Carlo simulations, demonstrated in Figs. 5.8 (a) and (b).

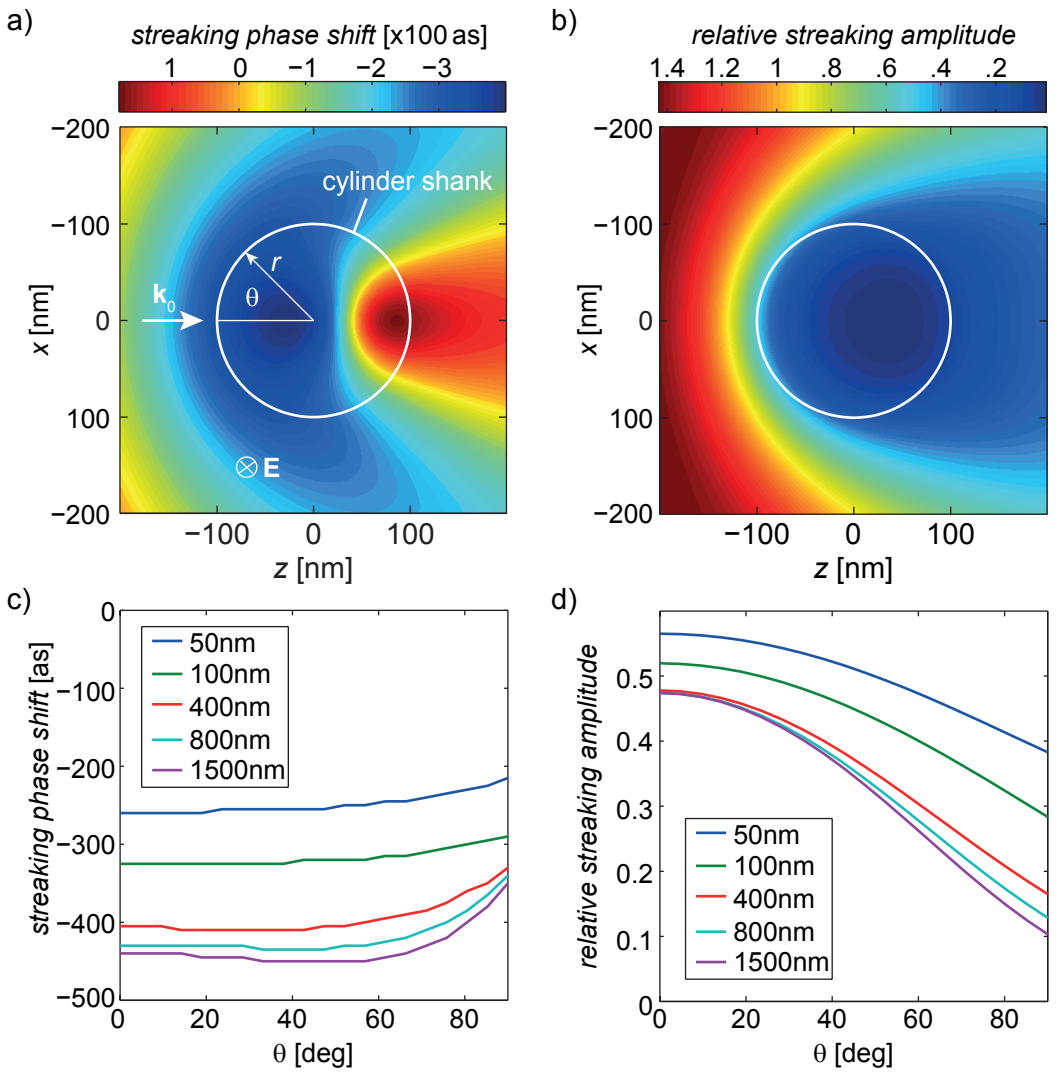

Figure 5.10: Averaging effects for different streaking target emission sites. Streaking phase shift **(a)** and amplitude **(b)**, calculated from the near-field vector potential for an infinite cylinder of 100 nm radius. For **(c)** and **(d)** the streaking phase shift and vector potential amplitude is evaluated for different nanocylinder radii in dependence of angle θ. Adapted from [151].

5.3.5 Reconstruction of the Near Field in Vicinity of the Nanotaper Apex

The tapered nanowire shows field enhancement and localization at the apex. On that basis, for electrons emitted from the apex and thereby probing the enhanced near field region, an increased streaking amplitude can be anticipated. To investigate the near field around the apex, we perform trajectory simulations for electrons emitted from specific positions around the nanotip apex. The near field is calculated in an FDTD simulation, where the geometry is modeled by a cylindrical nanotip of 100 nm radius. In Figs. 5.11 (a) and (b) the near-field component parallel to the tip axis, is displayed at the time-step where maximum electric field strength is observed. The illustrations depict the cylindrical tip, indicated as white outline, in perspective parallel to the laser propagation direction (a) and perpendicular to the laser propagation direction, i.e. in the focal plane, in (b). Trajectory calculations, displayed in Fig. 5.11 (c), are done for electrons emitted at various points. The specific emission sites range between $0\,\mathrm{nm} - 200\,\mathrm{nm}$ from the apex point and are indicated as color-coded dots in (a) and (b). As expected the trajectories of electrons emitted at the apex show larger amplitudes since those propagate through the enhanced near-field region. Compared to the emission from the shank, the streaking amplitude of electrons emitted from the apex spot increases by a factor of $4 - 5$, which is anticipated for field enhancement factors around 2, as observed in FDTD calculations shown in Figs. 5.11 (a) and (b). However, compared to the initial photoelectron energy, the energy gain of 10 eV from propagation in the enhanced near-field region is still comparably small. For emission points with increasing distance from the apex point, streaking amplitudes decrease monotonically and converge towards the streaking amplitude for nanotip shank emission. Besides the differences in streaking amplitudes, the near-field phase varies considerably for the individual emission positions. While for the near field in vicinity of the nanocylinder shank a negative phase shift of about $-300\,\mathrm{as}$ with respect to the incoming field is predicted, the near-field phase at the apex point experiences a positive phase shift of roughly 250 as, as illustrated in Fig. 5.11 (d). Like the streaking amplitude, the near field phase shift is found to change monotonically between apex point and shank emission position.

While the near-field characteristics, i.e. phase shift and relative amplitude, are discussed based on trajectory calculations, it is implicitly assumed that electrons propagating through the apex near field are streaked ponderomotively. It was found that despite the field enhancement at the apex, electron energy gain from the near field is small with respect to their initial energy after photoexcitation. Therefore, it can be concluded that electrons emitted from the apex will not leave the near field considerably faster as compared to the case of photoemission from the shank of the nanotip. Since the near-field decay length is mostly determined by geometrical aspects, it is safe to assume that decay lengths at the nanotip apex and shank are similar. The latter is also supported by the FDTD results displayed in Figs. 5.11 (a) and (b). Accordingly, the assumption that the streaking regime remains unchanged for emission from the nanotip apex appears justified. Therefore, the spatio-temporal properties of the near field are fully revealed by trajectory calculations.

While the theoretical calculations on the nanotaper shank prove that the near-field phase shift and relative amplitude do not differ considerably for different emission spots, the analysis of the apex near field demonstrates the opposite. Surprisingly the Monte Carlo simulation presented above in Fig. 5.8 shows a detached streaking trace with no obvious contribution from the nanotip apex, which is expected with larger streaking amplitude and a phase shift by about

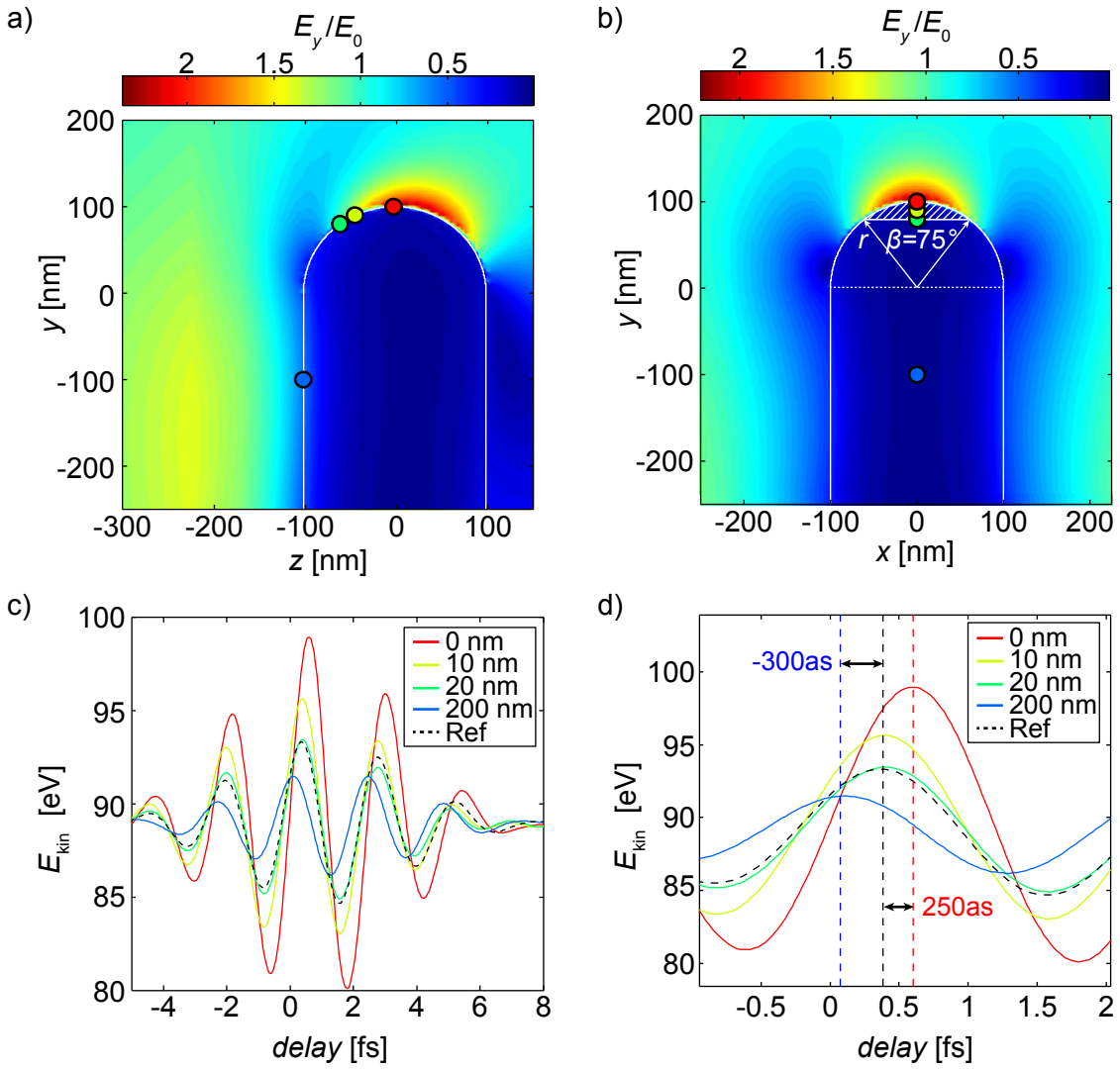

Figure 5.11: Near-field and trajectory calculations for the nanotip apex. The near field component E_y, normalized to the incident field E_0, in vicinity of a gold nanotip is displayed from the perspective parallel **(a)** and perpendicular **(b)** to the laser propagation direction. For photoemission from individual positions on the apex, indicated by colored dots in **(a)** and **(b)**, electron trajectories are calculated and displayed in **(c)**. In a zoomed perspective **(d)**, the phase of the near field shift at the apex is evaluated to 250 as, significantly deviating from the finding at the shank of −300 as. Adapted from [147].

570 as relative to the emission from the nanotip shank. Since the contribution of electrons emitted from the apex is neither observable in the simulated spectrogram in Fig. 5.8 (a), nor in the experimentally acquired spectrogram shown in (b), the signal from electrons propagating through the apex near field must be significantly weaker than the shank emission. Without consideration of details for the photoemission process, the number of detected electrons n_S for emission from a specific region S on the nanotip surface yields

$$n_P \propto \Phi_S^{\mathrm{XUV}} \cdot A_S \cdot f_{\mathrm{rep}} \cdot T_{\mathrm{acq}} \quad , \tag{5.5}$$

where Φ_S^{XUV} is the number of XUV photons per surface area S, A_S is the respective surface area, f_{rep} is the laser repetition rate and T_{acq} denotes the total acquisition time. The relation between electrons emitted from the apex and shank of the nanotip is therefore determined by the relation of surface areas between different emission sites, weighted by the Gaussian profile (FWHM focal diameter of 2.5 µm) of the XUV photon irradiance. The apex surface area, where field enhancement is obtained, is approximated by the white-hatched profile in Fig. 5.11 (b), over which the photon irradiance is assumed to be constant. The cross section for field enhancement is obtained from the illustration in Fig. 5.11 (b) and yields about $0.172\,r^2$. For the shank surface, modeled as rectangle with a width equal to the nanotip diameter, the Gaussian photon flux profile has to be considered. Accordingly the relation yields

$$\frac{n_{apex}}{n_{shank}} \approx \frac{0.172 \cdot r^2}{2r \cdot \frac{\sqrt{\pi}}{2} \cdot \frac{\mathrm{FWHM_{XUV}}}{2\sqrt{\ln 2}}} = 0.172 \cdot \frac{r}{\mathrm{FWHM_{XUV}}} = 3.2 \times 10^{-3} \quad , \tag{5.6}$$

where in the last step the nanotip radius of 100 nm and FWHM focal spot size of 5 µm was used. From the above evaluation, the number of electrons, excited by XUV photons and emitted from the apex is about three orders of magnitude lower as compared to the electron counts emitted from the shank of the nanotip. To reach similar statistics for apex emission, the overall acquisition time has to increase by a factor of 300, which explains, why the apex was not observed in the simulated and experimental streaking spectrograms in Figs. 5.8 (a) and (b).

While changing the experimental parameters to increase the count-rates for apex emission is difficult, Monte-Carlo simulations are easily tuned to increase the overall count-rate from the apex emission. To increase the number of XUV photons per surface area in the simulation, the XUV focal spot size is reduced by one order of magnitude to $d_{\mathrm{XUV}}^{\mathrm{FWHM}} = 0.5\,\mu\mathrm{m}$. As displayed in Fig. 5.12 the resulting streaking trace based on the apex emission (black solid line) is discernible from the streaking trace for the shank emission (green solid line). Despite the increase of statistics to yield in total 7×10^5 trajectories per delay step, a logarithmic scale is necessary to uncover the apex contribution. For the depicted simulation, the NIR intensity was chosen to $3 \times 10^{12}\,\mathrm{W\,cm^2}$ to increase the streaking amplitude for electrons emitted from the apex even further. Thereby streaking traces from shank and apex emission are separated energetically by about twice the mirror bandwidth. A detailed discussion of possible steps to increase the XUV flux experimentally, will be discussed in the outlook to this chapter.

5.4 Experimental Results

The theoretical results above support the general feasibility to sample nanoscale electric fields and to retrieve their spatio-temporal characteristics via attosecond streaking. As described in

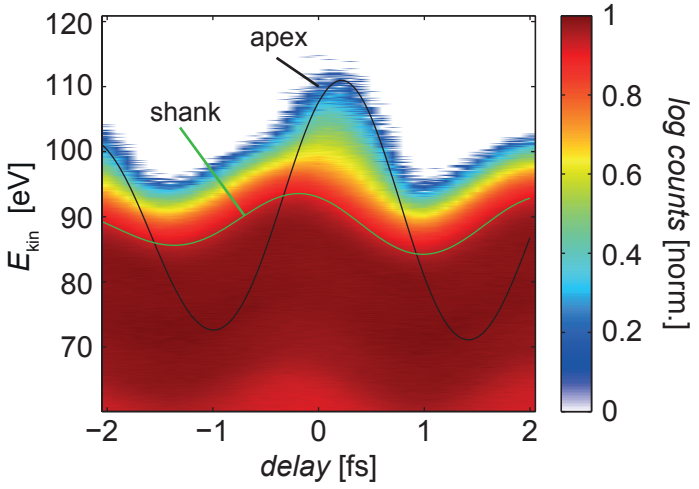

Figure 5.12: Monte-Carlo simulation for visibility of apex contribution. The emission from the nanotip apex yields about three orders of magnitude less counts than the emission from the nanotip shank. For the displayed Monte-Carlo simulation, the total number of trajectories is increased to 7×10^5, while the XUV focal spot size is decreased to 0.5 µm thereby raising the XUV photon irradiance. To separate the different emission sites energetically, the NIR intensity is chosen to $3 \times 10^{12}\,\mathrm{W\,cm^{-2}}$, yielding about twice the XUV mirror bandwidth as separation. Adapted from [151].

Sec. 5.2, cascaded streaking scans on the nanotaper are recorded. After superimposing several scans and subsequent filtering, the nanotaper streaking traces are extracted from the spectrograms and compared to streaking traces obtained from reference measurements on neon gas.

As illustrated in Figs. 5.13 (a) and (b), the smoothed nanotaper spectrogram is compared to the reference measurement performed on neon gas atoms. For each delay step, the photoelectron spectrum of the nanotaper yields a broad feature whose width exceeds 20 eV as can be observed in (c). As already discussed above (see Sec. 5.2), the broadening of the photoelectron spectrum is attributed to scattering effects and potential surface contaminations. While the origin of electron energies below 80 eV is not clear, the high-energy cut-off, can be assigned exclusively to the emission from the Au-5d valence band. In contrast, as displayed in (b) and (d), the photoelectron reference spectrum obtained on neon gas, resembles for each delay step the bandwidth of the XUV focusing mirror and is therefore well described by a Gaussian function. For the nanotaper streaking spectrogram, the delay-dependent energy shift is only discernible in the high-energy cut-off of the spectrum. Accordingly, typical methods to extract the streaking trace, as e.g. described in Ref. [262], cannot be applied. Instead, as illustrated in Figs. 5.13 (c) and (d), for each delay-step, the electron energy spectrum is fitted with a Fermi function, defined as

$$f(E_{\mathrm{kin}}) = \frac{A}{\exp\left(\frac{E_{\mathrm{kin}}-E_0}{\Delta E}\right)+1} \qquad \text{with} \quad E_{\mathrm{kin}} \in [E' - 6\,\mathrm{eV}\,,\, E' + 20\,\mathrm{eV}] \tag{5.7}$$

where A, E_0 and ΔE are free parameters in the fitting routine. Since the Fermi-function is only fitted to the high-energy cut-off regime but not to the full electron spectrum, the fitting routine is restricted to the interval $\Delta E_{\mathrm{kin}} = [E' - 6\,\mathrm{eV}\,,\, E' + 20\,\mathrm{eV}]$. The variable E' denotes the energy, where the electron counts are halved with respect to the maximum counts for each

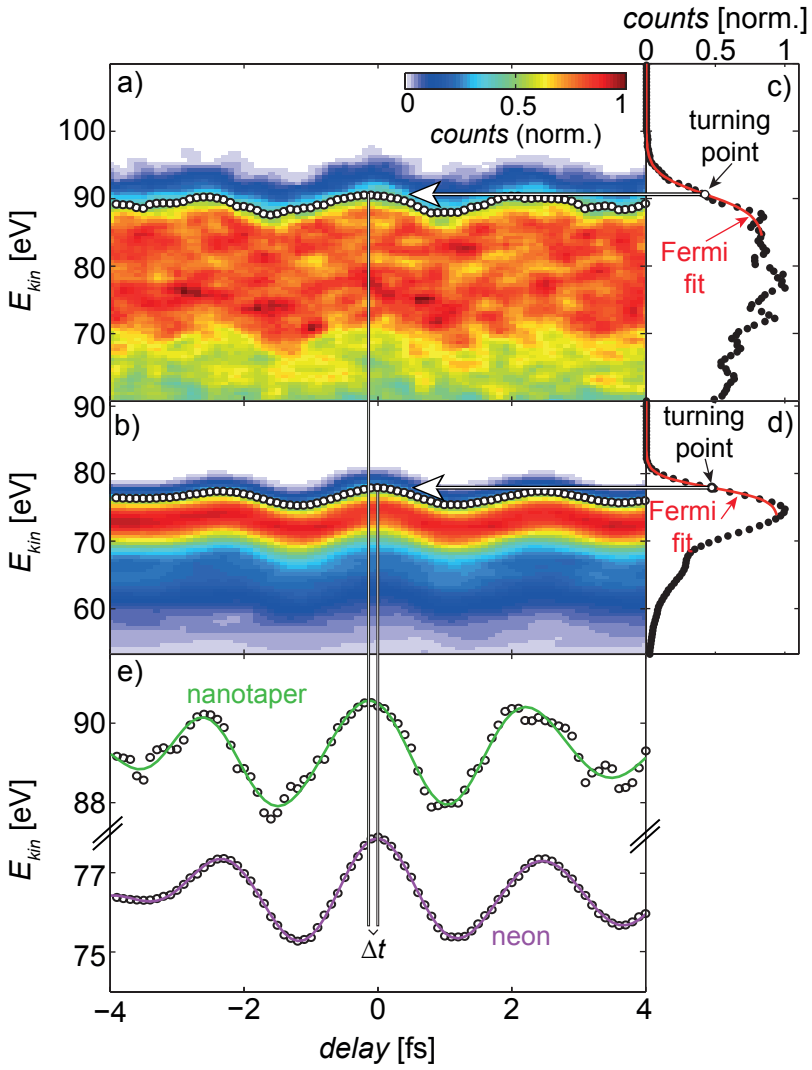

Figure 5.13: Experimental results from nanotaper streaking. Streaking spectrograms obtained on the nanotaper and, as a reference, on neon gas are illustrated in **(a)** and **(b)**. To extract the streaking traces we apply a Fermi-fitting routine on the photoelectron spectrum for each delay step of the streaking spectrograms on the nanotaper **(c)** and neon gas **(d)**. The streaking traces from the nanotip and the reference measurement are filtered in the Fourier-domain and compared in **(e)**. Adapted from [151].

delay step. As indicated in Figs. 5.13 (c) and (d), the Fermi-fit returns the turning points E_0 for each delay step, which specify the streaking trace displayed as white solid dots in the spectrograms in (a) and (b). For consistency, also the gas phase reference streaking trace is extracted based on the Fermi-fitting method, while here also conventional fitting routines are applicable.

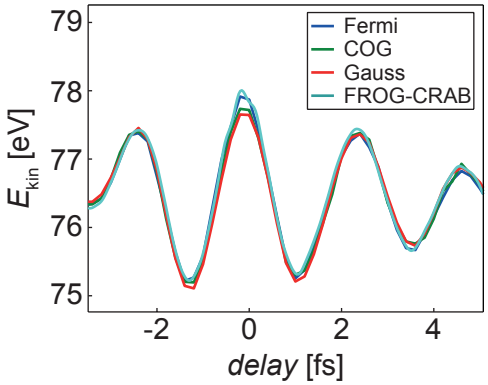

Figure 5.14: Comparison of different streaking trace extraction methods. To demonstrate the robustness of the Fermi-fitting method, we compare streaking traces that are extracted by different methods from the reference streaking spectrogram on neon gas. Besides the Fermi-fitting method, we use a center-of-gravity (COG) analysis, a Gauss-method, where Gaussian functions are fitted to the electron spectrum and a FROG-CRAB algorithm as presented in Ref. [118]. While minor differences in the streaking amplitudes can be observed, all extraction routines give the same phase information. Adapted from [151].

To demonstrate the robustness of the Fermi-fitting routine, we compare the results from different streaking trace extraction methods applied on a reference spectrogram. The results, where individual streaking traces are shifted to a common baseline, are illustrated in Fig. 5.14. While the Gaussian peak finding procedure (Gauss) and center-of-gravity analysis (COG) reveals minor differences in the streaking amplitude, the Fermi-fitting routine yields almost perfect agreement with the FROG-CRAB retrieval algorithm as presented in Ref. [118]. For the gas reference measurements, the streaking trace extraction via the Fermi-fitting method is found to depend on the interval ΔE_{kin}. While the only requirement to choose the upper limit is fulfilled if electron counts converge to zero, in the lower bound, electron counts should ideally converge towards an arbitrary constant value. While the latter is approximately fulfilled for the nanotaper spectrum with its broad, plateau like structure below 80 eV, the lower limit for fitting the gas measurement should not fall short of the Gaussian peak maximum in photoelectron spectra. Most importantly, the comparison exhibits that all retrieval routines coincide almost perfectly in their phase information, which supports that the Fermi-fitting is a suitable method to extract the streaking traces from the spectrograms.

Extracted streaking traces obtained from the nanotaper and gas measurements are filtered in the Fourier domain, where all spectral components outside the NIR laser spectrum are omitted. The comparison between streaking traces, as illustrated in Fig. 5.13 (e), yields a phase shift of $\Delta t = (-200 \pm 50)$ as between the nanotaper trace (solid green line) and the neon reference (solid purple line) for the displayed measurement. Given the error bar, the experimentally retrieved phase shift is in considerable good agreement with theoretical predictions.

5.5 Analysis, Interpretation and Discussion

Previous studies revealed that the maximum electric field amplitude in the laser focus is found to be significantly larger than obtained from gas phase streaking experiments [263]. The gas phase measurements average the NIR laser field strength over the entire focal volume of the XUV laser pulse. As result from the averaging effect, the NIR field strength is underestimated. In addition, misalignment between NIR and XUV laser beams is difficult to exclude in gas phase streaking measurements, where non-perfect overlap between focal spots results likewise in reduced NIR field strengths. In contrast, the nanotaper sample is reliably positioned in the center of the NIR laser focus, where the positioning procedure employs the nonlinear strong-field photoionization signal. Moreover, the tapered nanowire sample probes the incident laser field only locally, where averaging effects can be safely neglected. Accordingly, the direct comparison between near-field strength extracted from nanotaper measurements and NIR laser field amplitudes retrieved from gas phase streaking measurements is difficult. To compensate for averaging effects, correction factors are applied to the NIR laser field strengths, as retrieved from gas phase measurements. Therefore, the NIR-induced strong-field photoionization signal is employed, which is dominated by photoemission from the nanotaper apex. Since the cut-off energy depends non-linearly on the NIR laser field strength, the strong-field photoemission signal represents a reliable local probe of the incident laser field strength at the nanotaper apex position. For the respective target geometry, we assume field enhancement at the nanotaper apex: in lines with previous [207] and based on the presented FDTD calculations, the enhancement factors are estimated to yield around 2 for taper geometries of 100 nm apex radius. Based on this method, we extract correction factors for NIR field strength from gas streaking measurements around 3.

In reverse, the correction factors resolve the discrepancy, which arises from the comparison of the strong-field cut-off energy and NIR field strength, retrieved from gas phase streaking experiments. Without correction factors, field enhancement factors around 12 would be demanded at the nanotaper apex to, explain the cut-off energies of strong-field photoelectron emission. Based on the SEM micrographs, such field enhancement factors are unrealistically high, supported also by literature values [207].

The corrected incident NIR electric field, obtained for the measurement presented in the previous section in Fig. 5.13 (b), is displayed in Fig. 5.15 (a) together with the near field, extracted from the associated nanotaper streaking spectrogram. The amplitude relation between near field and incident fields yields about 0.34 which is in considerable good agreement with the response function predictions based on the FDTD calculations. The phase shift between the near field and the incident field is evaluated to about (-200 ± 50) as which is again found in good agreement with theoretical predictions.

Results for the phase shift and relative amplitude for the full data set, are displayed in Figs. 5.15 (b) and (c). In total it comprises 11 individual measurements, which were acquired under different experimental conditions, i.e. varying days and samples. Relative phases and amplitudes result from the time-domain spectrograms as mean values, averaged over the respective delay range of the streaking measurement. For the phase shift, two data points yield positive values, in strong discrepancy to the other measurements, which are all negative. Regardless of those two outliers, all data points lie within a confined range, which suggests considerable good reproducibility. The reason for the positive phase shifts is not fully clear, especially since those values do not overlap with the standard deviation of the

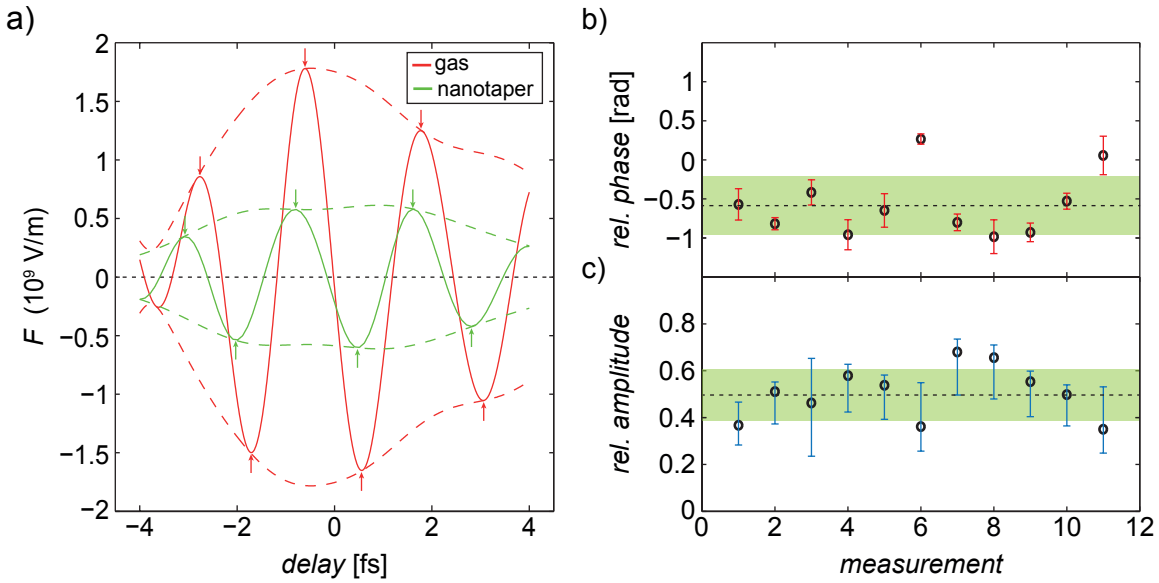

Figure 5.15: Representative electric near field and resulting phase shift and relative amplitudes for the full data set. Subfigure **(a)** shows the near field and the corresponding corrected incident laser field, both retrieved from the streaking traces displayed in Fig. 5.13 (e). Solid lines represent the real part, dashed lines the envelope of the near field (green) and the NIR field (red). In **(b)** and **(c)**, the relative phase and amplitude values of the full data set, comprising 11 individual nanotaper streaking cascades are illustrated. Weighted mean values are shown as dashed black lines, with their respective standard deviation illustrated as green shaded area.

weighted average value, indicated by the green shaded area. Generally, it was found, that phase measurements at the AS-5 setup are prone to higher instabilities as compared to other laser parameters, e.g. amplitudes. The weighted average phase shift, indicated by the black dashed line, yields (-240 ± 155) as, which is in remarkably good agreement with the prediction of -300 as, resulting from the streaking simulation on a cylindrical nanotip with 100 nm apex radius. The relative amplitudes for the individual measurements coincide almost perfectly, where all data points, given their respective standard deviation, overlap with the weighted average of (0.50 ± 0.10), illustrated as black dashed line in (c). As for the phase shift, the averaged relative amplitude demonstrates excellent agreement with the theoretical expectation of 0.54, resulting from the MC simulations on the cylindrical nanotip.

Response function calculation

The results as shown in Figs. 5.15 (b) and (c), represent phase shift and relative amplitude values that are averaged over the temporal delay. More informative than the averaged values are the response functions, which can be understood as a unique property of the investigated sample geometry. Since the response functions are resolved in the spectral domain, the near-field properties can be retrieved for arbitrary incident fields, whose spectra are exclusively composed of wavelength components within the range covered by the response function. To calculate the response function, the experimental data from the near field and the NIR laser field are transformed into the Fourier domain. As described before, a spectral filter respects

only wavelength components between 500 - 1100 nm which are contained in the incident NIR laser spectrum. The results from discrete Fourier transformation are shown as gray crosses in the response functions for relative amplitude and phase, displayed in Figs. 5.16 (a) and (b). Since the data sets, acquired on different days and samples, do not necessarily cover the same delay range, nor the same sampling rate, individual data sets yield different spectral resolution for the response function. To compensate the different data set lengths, we apply zero padding in the time domain to increase the overall spectral resolution and interpolate the response functions linearly. Thereby, an averaged response function can be calculated from all data sets, shown as solid dots in Figs. 5.16 (a) and (b), while individual data sets are weighted by their respective electron count-rates in streaking spectrograms. The error bars on the average response indicate the standard deviation.

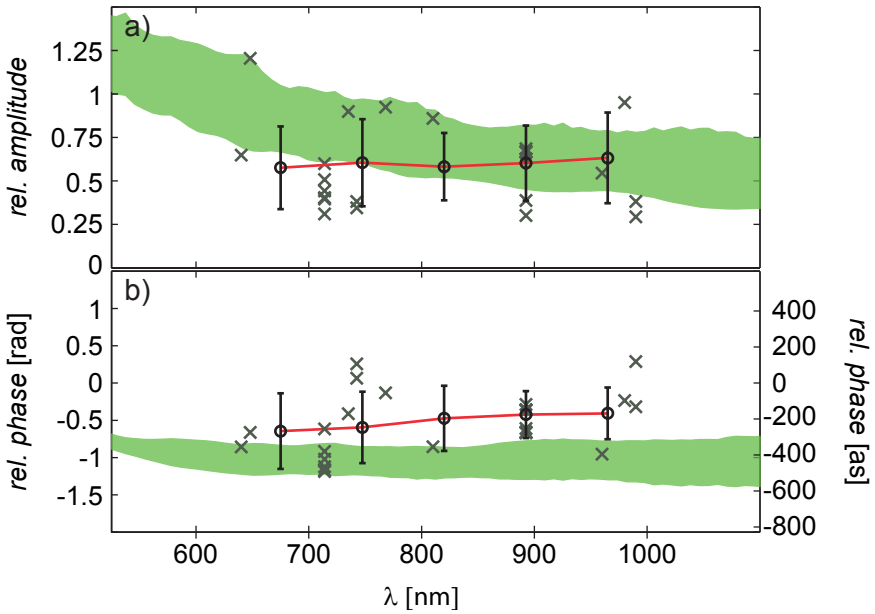

Figure 5.16: Experimental response functions of relative amplitude and phase. The normalized amplitude response of the near field in vicinity of the nanotaper is illustrated in **(a)**, whereas the relative phase response is displayed in **(b)**. Data points obtained by discrete Fourier transformation for the different data sets, acquired on different days and samples, are shown as gray crosses. The averaged response, weighted with the respective electron count rate, is calculated after zero-padding and linear interpolation and represented by solid dots. The error bars indicate the standard deviation. Theoretical predictions on the expected response functions for the tapered nanowire geometry, considering different emission points, are indicated as green shaded areas. Adapted from [151].

We compare the experimentally resulting relative amplitude and phase response to theoretical predictions, indicated by the green shaded areas in Fig. 5.16. The latter is calculated as average of response functions at 10.000 points on a nanotaper surface, where the response functions at individual points is weighted by the spatial profile of the XUV laser focus. The width of the green shaded area represents the standard deviation from the respective average response function. For calculation of the average response function, the nanotaper geometry is modeled as conical tip with 10 ° opening angle and 50 nm apex radius.

Since the response function of the nanotaper is not strongly dependent on the wave-

length, it follows that the relative amplitude and phase is directly discernible from the electric fields in the time domain. Generally, the averaged relative amplitude calculated from experiment is in reasonably good agreement with the theoretical expectations, which supports, that FDTD is a valid approach to simulate light-matter interactions for incident field intensities up to $10^{12}\,\mathrm{W\,cm^{-2}}$.

The spread of relative amplitudes for the individual measurements (gray crosses) is found to be considerably larger than expected from theoretical calculations. One explanation for the increased spread of relative amplitude could be deviations for the retrieved NIR field correction factors. Since the latter depends strongly on the local nanotarget geometry at the apex, systematic errors in estimating the enhancement factors affect the relative amplitude of the response function. Especially for the different samples, slight variations in the nanotaper apex radius are likely. Moreover, the theoretical model does not incorporate surface roughness of the sample. As has been observed for Ag surface, corrugations on the level of several nanometer results in highly localized hot-spot formation and significant field enhancement [63,264] at localized surface regions. Accordingly, the theoretical calculations for non-corrugated surfaces could underestimate the spread in relative amplitudes.

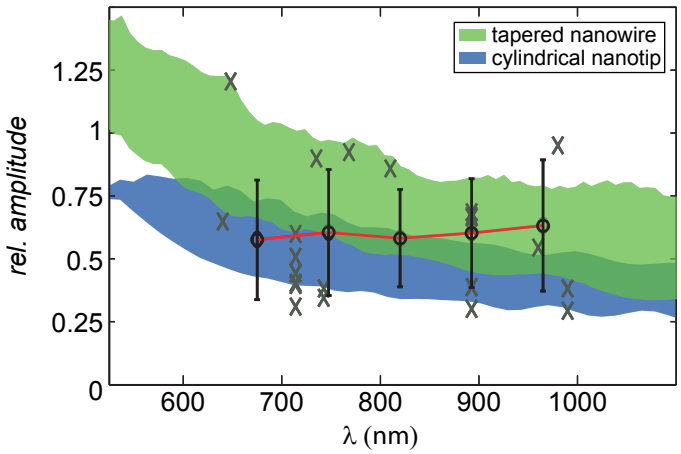

Figure 5.17: Comparison of response functions for different sample geometries. The shaded areas represent the expected amplitude response of a tapered nanowire geometry (green) and a cylindrical nanotip (blue). For the nanotaper, a full opening angle of 10° and apex diameter of 50 nm is assumed. For the nanocylinder model, an apex diameter of 100 nm was chosen. The NIR laser beam is modeled similar for both geometries. Adapted from [151].

While the relative amplitude in the long wavelength regime matches the predictions almost perfectly, for shorter wavelengths it appears to deviate systematically. As discussed in the above sections, the specific sample geometry influences the response functions. While the influence was found to be rather weak, it could still explain the deviations of relative amplitudes for short wavelengths. As illustrated in Fig. 5.17 the average response function of a cylindrical nanotip with 100 nm apex radius (blue shaded area) shows better agreement for short wavelengths, but falls short for the long wavelength range, whereas the situation is reversed for the tapered nanowire geometry (green shaded area, as already illustrated in Fig. 5.16 (a)). Potentially both model geometries, i.e. cylindrical nanotip and tapered nanowire are oversimplifications of the real target geometry. Based on the experimental data from streaking measurements, the target geometry appears to be a mixture of both theoretical models.

The phase shift response function of the near field is plotted in Fig. 5.16 (b), where average values are found to vary between −0.6 rad to −0.4 rad. As for the relative amplitude, the average relative phase response is a flat function for which the phase shift between near field and NIR laser field can already be retrieved from the time-domain data. In comparison to the theoretical expectations, which predict −0.6 rad to −1.1 rad, as illustrated by the green shaded area, the experimentally obtained phase response function for the near field appears to be slightly shifted towards larger values. However, given the error bar of the averaged phase response and the variance of theoretical values, the agreement between experimental data and theoretical expectations is still decent. Since theoretically calculated phase shifts are obtained from FDTD calculation, the agreement with the experimental data suggests, that phase shifts can be understood as a unique property of the near field, given as collective free-electron-like polarization response of the Au to the incident laser field. To support this statement, other possible contributions to the phase shift need to be considered.

As already discussed in Sec. 2.3.2, streaking experiments generally measure relative temporal delays between electrons, emitted from different ground states. The delay, measured in the temporal domain, manifests as phase shift. To discuss the nature of apparent phase shifts, one ideally refers to an absolute scale. Despite recent approaches [22], experimental observation of absolute photoionization delays is difficult, whereas the theoretical calculation of absolute time delays is feasible. From theoretical modeling, the absolute delay for photoemission from the neon 2p-shell is predicted below 10 as [265–267], given an XUV photon energy around 93 eV. Since we observe relative delays in the range of hundreds of attoseconds, the reference measurement in neon gas can be considered instantaneous, when compared to the streaking results from nanotapers.

Screening of the NIR streaking field

To identify additional contributions to the photoemission delay from nanotapers, we compare our results to experimental studies in literature. While there are no streaking experiments on nanoscale target geometries published, we refer to experimental studies on solid state target systems as presented in Refs. [15,16,18,268] and their theoretical interpretations [139–143,145, 146]. In the case of noble metal targets, the few-cycle NIR laser is effectively screened on the target surface, in contrast to XUV photons that can penetrate the target material deeply [18]. Therefore, all electrons that are excited deep inside the metal require to propagate to the metal surface before being exposed to the NIR streaking field. Since electrons excited at the metal surface experience the streaking field immediately, the two different emission channels will be delayed by the propagation time of the deeply excited electrons inside the metal. For magnesium, the screening length of NIR laser fields was found in the range of several Angstrom, i.e. within a single atomic layer [18]. While photoexcitation deep in the bulk is feasible, inelastic scattering processes limit the electron emission depth to about 1 nm from the metal surface. Based on purely classical considerations, the expected delay is around 500 as for the two emission channels, where 100 eV XUV photon energies are assumed. More sophisticated analysis, under consideration of quantum mechanical effects for the electron propagation inside the metal, report smaller values but are found on the same order of magnitude [143–145]. Those theoretical predictions are also in good agreement with experimental observation in RABBITT experiments, where noble metal targets are compared to gas phase results [268]. However, for all the presented studies, the NIR streaking field is polarized perpendicular to the target surface, in contrast to the nanotaper streaking experiment presented here, where

the NIR streaking field, probed by the XUV electrons is polarized parallel to the sample surface. While Maxwell's equations demand screening of the field component perpendicular to the metal surface, the parallel field component is found to be continuous. Accordingly, for our sample geometry, which probes only the parallel field component, the NIR laser field strength can be assumed constant within the emission depth that is considerably shorter than the laser wavelength. Delays resulting from screening effects at the metal-vacuum interface are therefore omitted.

Propagation effects

Whilst photoexcited electrons propagate through the metal to the sample surface, additional time delays need to be considered, which are potentially introduced by interactions with the crystal lattice or delocalized and bound electrons. For the high excess energy, resulting in photoelectron energies in the range of 90 eV an almost free-electron like dispersion can be assumed [18]. Furthermore, since propagation along different lattice directions is averaged for the polycrystalline sample, resonant interactions of the excited electron inside the metal, e.g. inter- or intraband transitions, are expected to be weak [145, 146]. The interaction of photoexcited electrons with their respective hole states is negligible, given the short screening length on the Angstrom level for delocalized valence band states. As theoretical studies demonstrated, expected delays from electron-hole interactions are found on the level of several attoseconds, which yields a marginal contribution with respect to the observed delays in our nanotaper experiment. The formation of shake-up states, where together with the electron emission a second electron is excited to a higher-energetic state, is considered as additional source for photoionization delays in atomic systems [14, 269]. The solid state analogue, i.e. excitation of valence band states to form a plasmon in the bulk or at the surface of the metal target, has to be considered in the case of the nanotaper. Since the excitation of plasmons comes for the sake of an energy loss of the emitted electron, potential delays are only imprinted to electrons detected at lower energies. In contrast, the Fermi-fitting procedure to extract the streaking traces from nanotaper streaking spectrograms, relies exclusively on electrons detected with highest photon energies, for which no energy loss due to plasmon excitation is observed. While the plasmon excitation mechanism could explain the large spectral bandwidth of XUV photoemission in the nanotaper experiments, it can be ruled out as contribution to the phase shift.

Time delays from image and space charge

Besides the discussed interactions inside the metal, photoexcited electrons are prone to additional temporal delays while propagating in vacuum. Firstly, the emission of electrons creates an image charge on the nanotaper and yields a positive potential, which affects the obtained streaking delays. Generally, the strength of this static Coulomb-interaction scales linearly with the amount of charge. While excitation by XUV photons reveals only marginal image charge, NIR strong-field emission of electrons at the nanotaper apex is several orders of magnitudes stronger. However, according to Maxwell's equations, the Coulomb-attraction acts perpendicular to the nanotaper surface. In line with the argumentation above, for our geometry, where only fields parallel to the nanotaper axis are probed, the additional image charge has no effect on electrons emitted from the nanotaper shank. As the count-rate approximation demonstrated, for the given target size and XUV photon flux, the experimental signal is fully assigned to the emission from the nanotaper shank. Electrons emitted from the nanotaper

apex, which are affected by the positive potential, are not discernible in the measurement. Phase shift contributions resulting from image charge effects are therefore excluded for our experimental observations. Secondly, space charges from many-electron photoionization could influence the individual photoelectrons and thereby the measured photoemission delay. Again, the low XUV- photoionization rate for the nanoscale target, where less than one electron per laser shot is detected should not yield a significant amount of space charge in vicinity of the shank, in contrast to the apex region, where strong field emission boosts the number of free electrons. In consideration of the spacing between tip shank and apex, and the NIR laser field-strength, the dipole-moment from space charge at the apex shouldn't influence electrons emitted from the shank significantly. Moreover, it is stressed, that in literature on the photoemission delay from metal targets [15, 16, 18, 268], no space charge effects are reported, despite higher XUV ionization rates and stronger NIR streaking fields. Accordingly, space charge effects are not considered to influence the relative phase shift between nanotaper and gas phase streaking measurement.

Position and Dispersion Effects

Other possible sources for the relative phase delay between nanotaper and gas measurements arise from target positioning and dispersion effects. Due to the Gouy phase shift and the strong localization of the nanotaper target, a finite phase shift would be expected, if the nanotaper position in beam propagation direction deviates from the z-position of the NIR laser focus [270]. While we found our procedure to position the nanotaper in the NIR laser focus to work reliable and reproducible, we estimated the effect of Gouy phase shifts to the streaking curve experimentally. However, moving the gas target along the NIR laser focus, while keeping the position of the TOF detector fixed, no significant phase shifts were observable. Remaining deviations between the different traces could be fully attributed to the limited CEP stability. Dispersion effects can alter the phase shifts additionally. Here, previous reports [116, 147] discussed the influence of the neon gas jet on the NIR laser field. Given the marginal refractive index difference between neon gas and vacuum, and the low gas density in the experiments, it can be concluded that expectable phase shifts arising from the propagation of the NIR laser pulse through the neon gas jet, should be vanishingly small. Experimental findings, where we compare neon streaking traces for different target gas pressures, support this assumption.

Influence of adsorbates

Besides the dispersion effects on the reference measurement, adsorbates on the nanotaper surface could potentially alter the relative phase shift, especially under consideration of the experimental vacuum conditions around 10^{-7} mbar. To elucidate the influence of adsorbate layers, we perform calculations based on Mie theory for an infinite cylinder geometry of 150 nm radius, where we assume a fixed adsorbate layer thickness of 5 nm. The resulting phase shift for laser wavelength of 720 nm is displayed in Fig. 5.18 as a function of refractive index n. Significant phase shifts are only obtained for large refractive index materials as adsorbates. Typically simple carbon molecules and water are the main source for adsorbate contamination, for which the real and imaginary part of refractive index is expected to yield $\mathrm{Re}(n) < 2.5$ and $\mathrm{Im}(n) < 5$, illustrated by the red broken line in Fig. 5.18. As resulting from the simulation, even for the large adsorbate layer thickness, the expectable delay could not explain the experimental observation.

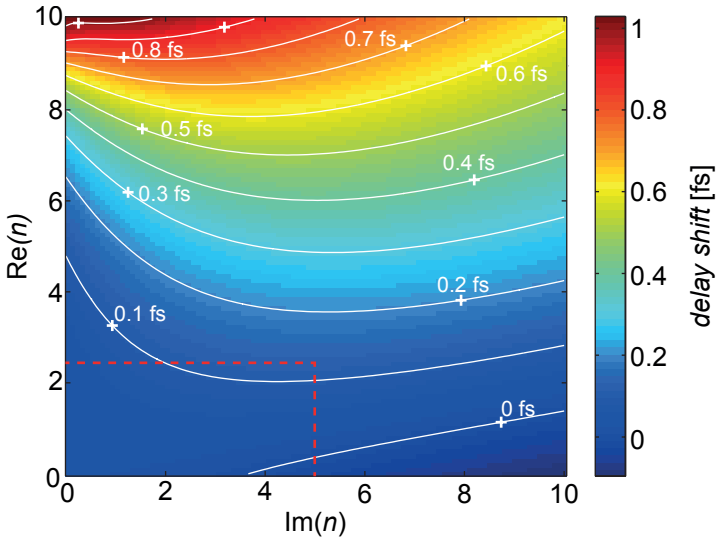

Figure 5.18: Influence of adsorbates on the near-field phase. Calculated phase shifts of the near field at the surface of a Au nanotaper in dependence of the real and imaginary part of the refractive index n. For the simulation an adsorbate layer thickness of 5 nm was assumed, while the geometry is modeled by an infinite cylinder of 150 nm radius. The result is obtained analytically from Mie theory, assuming an excitation wavelength of 720 nm. Adapted from [151].

Based on geometrical considerations of the nanotaper streaking experiment, potential sources for photoemission delay, that were partially discussed in previous studies, could be excluded to explain the experimental observations. Moreover, it was found that misalignment and dispersion effects will not contribute significantly to the phase delay. Since the experimental findings are well compatible with theoretical predictions from FDTD calculations, it appears justified to attribute the phase shift to the near field in vicinity of the nanotarget. Experimentally retrieved phase shifts and relative amplitudes are resulting as nanotaper response to the incident laser field. The outcome can be considered a unique property of the nanoscale target geometry.

5.6 Conclusion and Outlook

In this chapter, I presented the first successful application of the attosecond streaking technique on nanoscale target geometries, published in [151]. From the streaking spectrograms on tapered Au nanowires, the streaking trace is extracted by a novel fitting routine and hereafter compared to conventional streaking traces obtained in neon gas. For the two streaking traces, an average phase shift of $\Delta\tau = (270 \pm 100)$ as is observed. The experiments are complemented by theoretical calculations based on a classical approach: first, the interaction of the Au nanotaper with the incident NIR laser field is retrieved from FDTD simulations. Second, classical trajectory calculations yield electron propagation in the near field resulting from FDTD simulations resembling the pseudo-streaking traces from specific nanotaper emission sites.

Together with the simulations, it was demonstrated that the streaking experiment is performed in the ponderomotive streaking regime, where the full temporal information of the

near field is accessible. Despite significant spatial averaging, the MC simulations showed good agreement with experimental streaking spectrograms. This finding is supported by trajectory calculations for specific emission sites, which yield a weak dependence of the near-field amplitude and phase over a wide range of spatial parameters. The theoretically predicted phase shift amounts to 300 as, which is in good agreement with experimental results. Response functions, which determine the phase and amplitude changes as a unique property of the considered target geometry, are calculated from theoretical and experimental data and found in decent agreement. In conclusion, the presented streaking experiments probed the nanoscale electric field in vicinity of a nanotaper shank. The analysis showed, that for the specific geometry of our experimental setup, space charge effects can be ruled out in explanations for the observed phase shift. Supported from classical calculations, amplitude and phase shifts are explained as unique property of the nanoscale target dimensions, resulting from the interaction between few-cycle laser fields and the free-electron gas of the Au nanotaper.

While field enhancement at the nanotaper apex is expected from theoretical simulations, count-rate approximations for the experimental geometry support that the near-field region around the apex yield no significant contribution to the streaking spectrograms. Since field enhancement is considered one of the main properties of plasmonic systems, it remains to demonstrate experimentally that streaking spectroscopy can be applied to localized, enhanced electric fields. One possibility for the detection of enhanced near fields, includes a change of the target geometry. As has been shown by theoretical simulations in Ref. [147], for nanocylinder geometries, where the shank faces the detector, a larger target surface is prone to field enhancement. Since the detection signal strength scales with the target surface, such geometries facilitate the characterization of localized, enhanced fields. However, more preferable are approaches, where the detection signal strength is increased independent on the target geometry. Analyzing Eq. (5.5), the essential parameters to increase the detection signal for XUV photoemission from the apex are XUV photon flux Φ_S^{XUV}, the repetition rate f_{rep} and the acquisition time T_{acq}. Given the long measurement times in the range of several hours for the present study, the potential to increase acquisition times is considered marginal. However, higher CEP stability could allow a factor of 1 to 2 for future experiments. Increasing the repetition rate could yield orders of magnitude larger count rates, as compared to the AS-5 laser system, working at modest repetition rates of maximum 1 kHz. The most significant rise of apex detection signals is achieved by increasing the XUV photon flux. In a two-step approach, the XUV focal spot size should be decreased while additionally the photon flux from the attosecond source should be strengthened. Concluded from the HHG efficiency scaling, the latter can be realized by reducing the central energy of XUV photons to form the isolated attosecond pulse. Thereby, a five fold increase of XUV photons and accordingly in electron counts from the nanotarget appears a reasonable estimation. Since the substrate surface corrugations for XUV reflecting optics should not exceed the Angstrom-level, reduction of the focal length is hampered by the availability of smoothly polished substrates. Ultimately, the focal length is limited by geometrical constraints of the experimental setup. Nevertheless, the reduction of focal spot size bears potential for 50 to 100 fold higher electron count rates. All changes together would induce up to 10.000 times larger detection signals for which XUV photoemission from the nanotaper apex should be discernible. With implementing an innovative CEP stabilization scheme and the short focal length XUV mirror as presented in Sec. 3.3, first steps towards this directions are already performed.

Improvements of the detection signal opens further opportunities to study more complex

phenomena such as plasmonic excitation with attosecond precision. Particularly, the propagation and localization of plasmons are interesting features, subject to further investigations in order to unravel the dynamics of collective correlated electron excitations. Plasmonic supertip targets and fan/chirped grating targets, as presented in Secs. 3.1.2 and 3.1.3, seem perfectly suited to conduct first streaking experiments shedding light on complex electron dynamics. While contamination adlayers on the sample surface are not expected to alter the static properties of nanoscale near fields considerably, the influence on dynamical properties, e.g. in plasmon propagation, can be significant. Extended investigations on innovative target geometries are hence preferably performed under an improved vacuum environment, which ideally comprises tools to characterize the surface quality and contamination levels experimentally. Since plasmonic excitations are considered the basic building block to bridge the gap between conventional and lightwave circuitry, a thorough understanding of the dynamics of localized near fields is highly desirable. With the nanoscale attosecond streaking technique, a valuable tool is demonstrated, which paves the way towards the development of more advanced petahertz electronics.

Chapter 6

Attosecond Streaking of Molecular Photoemission

6.1 Introduction

After Einstein's explanation of the photoelectric effect by the quantum nature of light [71], the photoionization (PI) process became one of the most-studied phenomena in physics. Based on Hertz's experimental findings [64], for a long time, the electron-detachment from bound states in atomic or solid state targets was considered to happen instantaneous. However, pioneering theoretical works by Eisenbud [132], Wigner [130] and Smith [133] posed first questions on this simple picture of photoionization. The experimental verification became possible only recently with the advent of attosecond science [3], where attosecond streaking spectroscopy was applied to investigate the detachment of electrons from different initial states of atomic neon. In their experimental study, Schultze *et al.* obtained a time delay of around 20 as between the emission of photoelectrons from neon 2s and 2p orbitals [14]. Based on numerous theoretical calculations (see e.g. Ref. [134] for an overview), and under consideration of influences from the experimental method, the time delay is interpreted as Eisenbud-Wigner-Smith (EWS) delay, which originates from phase shifts accumulated by the photoelectron wave packet while propagating through the binding potential of the atomic nucleus during the ionization process. In reverse, the interpretation implies, that time delays measured in attosecond streaking experiments hold information about the orbital potential landscape encountered by the photoelectrons during the photoionization process. Given the high temporal resolution, not only static orbital potentials can be detected but even dynamic changes upon NIR interaction or collective electron interactions are acquired directly in the time domain.

Streaking spectroscopy has been widely applied to atoms [14, 266, 271, 272] and solid state systems [15, 16, 18, 222, 268], whereas molecular targets came only recently into focus of attosecond experiments [32, 273, 274]. In contrast to atoms, molecules offer the opportunity to shape the orbital landscape by choosing appropriate chemical constituents, which in turn serves to validate individual aspects in theoretical modeling. Unique for molecular targets is the reduced symmetry, which, especially in case of atoms and partly also for solid state systems, simplifies the analysis considerably. Since the complexity in calculations scales with the number of particles involved, the effort in photoionization simulations for molecules is dramatically increased as compared to atoms, but is, however, significantly lower with respect to solid state systems. Only recently, first time-resolved experimental studies of the

photoionization process from N_2O were reported, where the maximum photoionization delay for photon-energies between 20 - 40 eV yields around 160 as [34]. Calculations based on a full quantum mechanical scattering theory attributed the large delays to the trapping potential of a shape resonance, where in case of N_2O, effects of electron-electron interactions are reported to be of negligible influence [275].

In contrast, a different type of resonance, i.e. the atomic giant dipole resonance (GDR), typically involve collective effects [35], which include correlations between electrons of the same (intraband) as well as distinct (interband) atomic subshells. Gradually the dynamical properties of such resonances and especially the role of electron-electron-interactions come into focus of time-resolved experiments. However, despite Verhoef *et al.* reporting first attosecond streaking measurements on atomic xenon (Xe) in the energy range of the GDR at 97.5 eV [276], detailed experimental studies on this topic remain currently still elusive. Nevertheless, time-domain based measurements of electron dynamics in vicinity of photoionization resonances are of fundamental importance, especially since the generic link between excitation lifetime and spectral width of the resonance, as observed for single channel excitations e.g. in Ref. [277], is not strictly fulfilled in the presence of repulsive interactions between electrons [38]. The necessity of experimental studies to investigate the effect of collective excitations on photoionization delays derives also from deficiencies in accurate theoretical modeling: in case of xenon, where the electron interaction in the energy range of the GDR was simulated by two different approaches, the results show severe qualitative and quantitative disagreement [37, 38]. Accordingly, attosecond streaking spectroscopy on atoms and molecules in the energy range of GDRs can help to elaborate the role of collective electron interactions within atomic and molecular orbitals.

In this chapter, first experimental results from attosecond streaking measurements on ethyl iodide (EtI) are presented. For photoionization, XUV photons with central energy of 80 eV and 93 eV are employed, both well-located in the energy range of the giant dipole resonance of atomic iodine [278, 279]. The EWS delay for electrons emitted from the ethyl iodide 4d shell is retrieved from the streaking delay difference between photoionization from ethyl iodide 4d and neon 2p orbitals, as obtained from experimental streaking spectroscopy. With the present experimental setup, streaking traces from both targets are recorded simultaneously making this approach less sensitive to instabilities of the laser system. The results are interpreted based on full-quantum calculations and semi-classical trajectory simulations. Besides the effects of collective electron excitations, the influence of the molecular orbital landscape on the resulting photoionization delays is discussed.

6.2 Resonances in Atomic and Molecular Photoionization

In the range of 100 eV, the photoionization cross section of the xenon 4d orbitals, is strongly enhanced, which is typically attributed to a giant dipole resonance (GDR), where collective electron effects are considered to play a major role [35, 170]. In case of iodine atoms a similar enhancement of the photoionization cross section for the 4d shell can be observed, however at a slightly different excitation energy range. The strong qualitative agreement to the findings for xenon poses the question, whether the enhanced photoionization cross section in case of iodine is likewise explained by the occurrence of a giant dipole resonance. To resolve this question, it is instructive to shed light on the microscopic picture of a GDR and clarify its

physical properties and the potential influence on photoionization delays, as obtained in attosecond streaking experiments.

Originally, the term giant dipole resonance indicates a strong enhancement of photoabsorption cross sections of atomic nuclei in various species, typically observed over a broad range of several mega-electronvolt (MeV) photon energies [280]. In nuclear physics, the phenomenon is attributed to a collective excitation of nuclear particles, where protons and neutrons conduct oscillations in opposite directions, which represents to good approximation a dipolar oscillation mode [281]. In atomic physics, D. L. Ederer performed photoionization experiments [170], which revealed a qualitatively identical profile of the photoionization cross section of the xenon 4d shell to the previously observed GDRs obtained in nuclear physics. Remark, however, that the absolute values for photoionization cross sections in atomic physics are by several order of magnitude larger compared to nuclear physics, while the maximum is observed at significantly lower photon energies, in the range of several tens of electronvolts. Besides the similarity in the qualitative outline, theoretical calculations indicate that collective effects play a major role in the explanation of the photoionization cross section of xenon [35]. Ultimately, motivated by the latter observation, many-body physics theoreticians introduced the term atomic giant dipole resonance to describe the enhanced photoionization cross section of d-shell electrons for atoms with proton numbers in close vicinity of xenon ($Z_{\mathrm{Xe}} = 54$) [36].

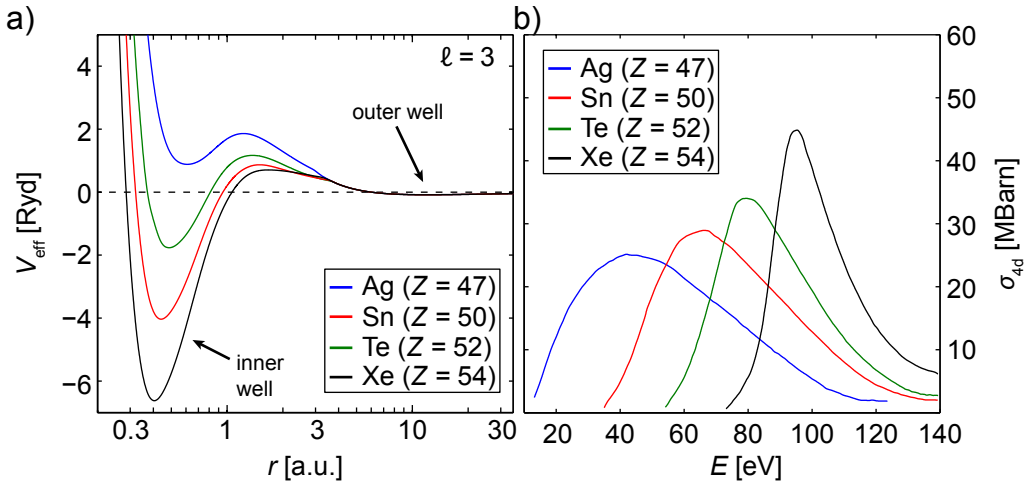

Figure 6.1: Effective potentials and photoionization cross sections of heavy atoms around xenon. In **(a)** the effective atomic potentials for electrons with orbital quantum number $\ell = 3$ are displayed in dependence of the radial distance from the nucleus for different atomic species. For small radii, the employed Herman-Skillman potentials [282] feature short range potentials, but evolve for large radii into Coulomb-like potentials. The additional centrifugal potential results in a positive potential barrier, whose height and width depends sensitively on the atomic number. Reprinted from Ref. [283]. As illustrated in **(b)**, the centrifugal barrier gives rise to a giant dipole resonance in the photoionization cross section $\sigma_{4\mathrm{d}}$. Here, the latter is calculated for single-particle excitations regardless of collective effects. Reprinted from Ref. [284].

On a microscopic level, the profound explanation for the formation of GDRs in specific atomic species becomes already apparent from the effective single-electron potentials. Since the giant dipole resonance is observed for photon-induced transitions of d-shell electrons to f-symmetric continuum states, i.e. $nd \rightarrow \epsilon f$ with n representing the principal quantum num-

ber, also the centrifugal potential of the emitted photoelectron needs to be considered. Accordingly, in one dimension, the effective atomic potential V_{eff} can be expressed as [283]

$$V_{\text{eff}}(r) = -V_{\text{HS}}(r) + \frac{\ell(\ell+1)}{r^2} \quad , \tag{6.1}$$

where r describes the radial distance from the nucleus, ℓ represents the quantum number of orbital angular momentum and V_{HS} designates the Herman and Skillman potential [282], which represents a short range potential that develops into a Coulomb-like potential far from the nucleus. In Fig. 6.1 (a), the resulting effective potentials for f-symmetric wave functions, i.e. $\ell = 3$, in dependence of the radial distance from the nucleus is illustrated for different atomic numbers. Apparently, the effective potentials form a double-valley structure, with an inner and outer well, which are separated by a positive centrifugal barrier. In a semi-classical picture, the latter explains, why the photoionization cross sections is comparably low in vicinity of the ionization threshold, since photoelectrons require enough excess energy to overcome the centrifugal barrier. Likewise in a quantum-mechanical picture, due to the potential barrier, the wave function of the f-symmetric continuum state yields only small amplitudes at the positions of the inner well. Naturally, this changes for f-wave functions describing states whose excess energy exceeds the positive potential barrier. Accordingly, the wave function overlap between bound d-shell electrons and the f-symmetric continuum states, which determines the photoionization cross section, increases for excess energies approaching the barrier height. In the opposite limit, where the f-wave continuum state exceeds the potential barrier by far, the oscillatory behavior of its wave function similarly reduces the overlap with the bound state and the photoionization cross section decreases. In between both limits, where the wave function of the continuum state becomes resonant to the inner potential well, the photoionization cross section is maximized, forming a distinct peak, referred to as atomic giant dipole resonance.

The height and position of the centrifugal barrier strongly depends on the depth and width of the inner well and therefore on the atomic number Z. Accordingly, as displayed in Fig. 6.1 (b), the position and width of the giant dipole resonance, observed in the photoionization cross section, changes significantly for different atomic species. With increasing atomic numbers, the centrifugal barrier height decreases, while beyond a certain threshold the inner potential well becomes deep enough to support additional bound states. This phenomenon is typically termed as collapse of the f-symmetric wave function into the inner well, for which dipole transitions between bound states of same principal quantum number are observable. For neutral atoms this process is observed approximately around $Z = 57$, i.e lanthanum, while for negatively charged ions similar manifestations are reported already for barium ($Z_{\text{Ba}} = 56$) or cesium ($Z_{\text{Cs}} = 55$) [284].

Since the giant dipole resonance is well described by the effective atomic potential under consideration of the centrifugal term for large orbital quantum numbers, its properties remain almost unchanged in different environments. Therefore, the large absolute values of photoionization cross sections, but also peak position and width of atomic GDRs can still be observed for the respective atomic species bound in solids or molecules. However, the atomic GDR shall not be confused with molecular shape resonances, which are conceptually directly related to the giant dipole resonances in atoms but concern typically molecular orbitals, e.g. binding valence band orbitals. While for the latter the chemical surrounding can change the properties of the molecular shape resonance tremendously, inner-shell orbitals of atoms where GDRs are present, are hardly affected by the molecule's constituents [285].

For the qualitative explanation of giant dipole resonances, it is sufficient referring to single-particle excitations. However, as demonstrated in numerous theoretical calculations (see e.g. Refs. [286, 287] for an overview), to accomplish reasonable quantitative agreement with experimentally obtained cross sections demands to take collective effects into account. In the single-particle description, without consideration of many-body interactions, the resonance peaks typically shift towards the ionization threshold, while its sharpness and the absolute values in photoionization cross sections are overestimated [288]. Besides intrachannel effects, where electrons of the same sub-shell are correlated, also interchannel coupling, where electrons of distinct atomic shells are mutually affected, can be observed in the presence of a giant dipole resonance. The latter manifests in increased photoionization cross sections for distinct atomic subshells in the energy range of the giant dipole resonance, which has been experimentally verified for photoionization from 5s and 5p orbitals of xenon at photon energies between 90 eV and 100 eV [289].

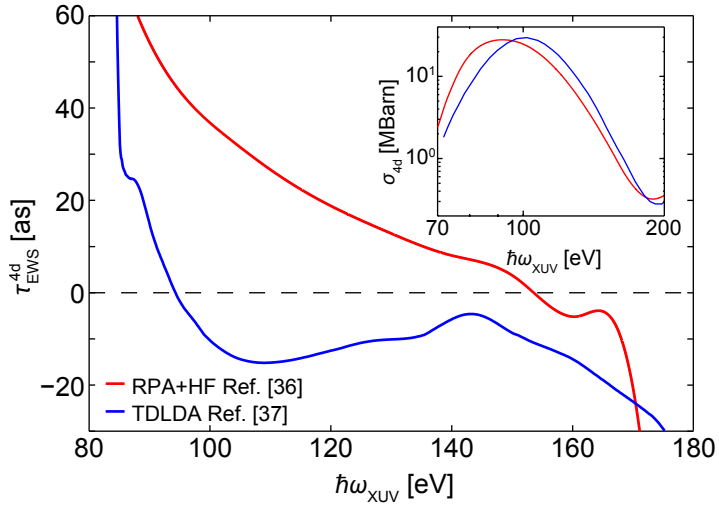

Figure 6.2: Theoretical calculations of photoionization delays for electrons emitted from the xenon 4d-shell. Comparison of theoretical predictions for the photoionization delay from xenon 4d orbitals, where both approaches, i.e. random phase approximation with exchange (RPAE) and time-dependent local density approximation (TDLDA) consider collective effects. The inset illustrates the 4d photoionization cross sections as obtained for the respective methods. Reprinted from Refs. [37] (RPAE) and [38] (TDLDA).

The effects of inter- and intrachannel coupling in photoionization processes is also investigated in theoretical simulations to elaborate its influence on the results of time-domain measurements. The latter are of specific importance, since time-resolved approaches offer the opportunity to disentangle individual photoionization channels and can thereby resolve their degree of mixing. As illustrated in Fig. 6.2, calculations employing the random phase approximation with exchange (RPAE) on the photoionization from the xenon 4d shell indicate positive EWS delays over the entire energy range, where the giant dipole resonance is present (see inset) [37]. More recently, Magrakvelidze *et al.* published a complementary theoretical study on the photoionization process from the xenon 4 d-shell, where the time-dependent local density approximation (TDLDA) is employed to consider collective electron effects [38]. As shown in Fig. 6.2, Magrakvelidze *et al.* predict a negative photoionization delay in the

presence of the giant dipole resonance, which is interpreted as generic behavior: since the interaction between the emitted electron with the remaining shell electrons facilitates a repulsive potential, the expected EWS-delay is negative. So far only few experimental reports on the photoionization delays on xenon exist, e.g. Refs. [81,276,290], which are currently not capable to resolve the discrepancy between the theoretical approaches, that both in principle include collective electron interaction effects.

The latter motivates further experimental studies on giant dipole resonances and the effect of collective interactions on photoionization delays. In the presented theoretical and experimental studies, the GDR in iodine is investigated employing the attosecond streaking technique. While xenon is a rare gas, where all orbitals are fully occupied, atomic ground state iodine lacks one electron in the 5p shell. Accordingly, as compared to xenon a stronger interorbital coupling between electrons in the p- and d-shell is anticipated [284]. For experimental convenience, not atomic iodine, but ethyl iodide is investigated, which complicates the theoretical treatment and accordingly the interpretation of results significantly. Nevertheless, the comparison between theoretical predictions and experimental results on photoionization delays from iodine, offers an ideal test scenario to validate theoretical approaches to model coupling strengths and collective effects in photoionization. In the presented experimental study, photoemission from the iodine 4d-shell is referenced to photoionization from the neon 2p-shell. The experimental approach, where photoionization from distinct atomic shells within the same atom are referenced against each other, as e.g. chosen by Verhoef *et al.* in Ref. [276], is especially in the presence of strong interchannel coupling disadvantageous, since the latter affects measurement signal and reference simultaneously.

6.3 Theoretical Approach

6.3.1 Quantum Scattering Theory

Photoionization delays result from phase shifts, which are experienced by the emitted electron during the ionization process. Since the latter is understood as half-scattering process, photoionization delays can be obtained from a quantum scattering theoretical description. While for isolated atoms, specific geometrical symmetries can be exploited in the simulations, molecular targets demand typically more complex approaches for the extraction of photoionization delays. Only recently, first theoretical simulations on different diatomic molecules, i.e. molecular nitrogen (N_2) and carbon monoxide (CO) were reported, where the ionization matrix elements together with the respective scattering phases are calculated in the molecular frame (MF) [274]. D. Baykusheva and H.-J. Wörner published an advanced theoretical approach, where photoionization delays are obtained in the laboratory frame and include emission angle averaging, which is common for many experimental apparatus [275]. Besides single-photon transitions, their method is additionally capable to obtain photoionization delays for two-photon ionization processes, which allows to simulate full attosecond interferometric experiments, e.g. the reconstruction of attosecond beating by interference of two-photon transitions (RABBIT).

For the calculation of photoionization delays from the 4d orbitals in ethyl iodide[1], based on the quantum scattering theory, the single-photon transition approach as described in full

[1]Quantum scattering simulations are performed in the group of H.-J. Wörner by D. Baykusheva.

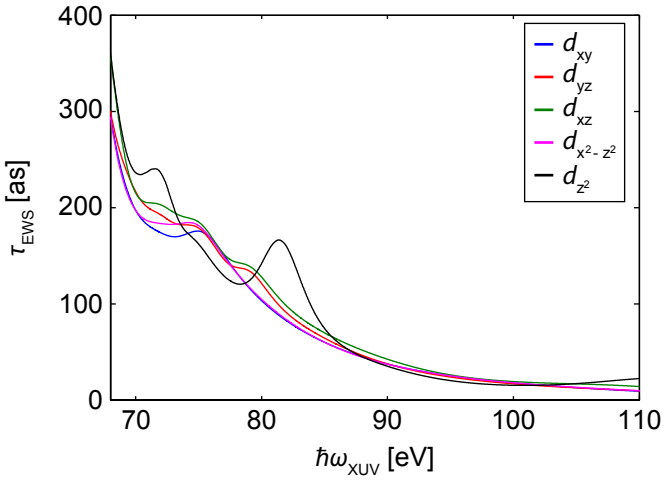

Figure 6.3: Orbitally-resolved photoionization delays calculated from quantum scattering theory. Qualitatively and quantitatively the photoionization delays from individual orbitals are found in reasonable agreement. Since all orbitals contribute about equally to the photoionization yield, the experimentally observable delay is obtained as mean value, averaged over all orbitals. Courtesy of D. Baykusheva.

details in Ref. [275] is employed. Here, the photoionization process is modeled in dipole approximation together with single active electron approximation (SAE), where the respective transition matrix element is expressed in the laboratory frame. The ethyl iodide initial state is calculated in a Hartree-Fock (HF) approach, where the basis set 6-311 G** is employed. Polarization of the initial state by the presence of an NIR streaking field is not considered in the quantum scattering method. The final state is likewise obtained from an HF formulation, employing the frozen-core approximation, for which the orbital potentials are considered to remain unchanged by the ionization process. With a geometrical transformation of the laser polarization direction, using generalized Euler angles, the transition matrix element is obtained in the molecular frame, where, following Eq. (2.48), the photoionization delay is calculated as the derivative of the transition matrix element's argument with respect to energy. To consider averaging effects for randomized ethyl iodide orientations, the photoionization delay of particular emission directions and molecule orientations is weighted by the corresponding cross section and integrated over the full solid angle. Similarly, the averaging of the detection system is considered by integrating over the respective solid angle, i.e. a full opening cone angle of 45° around laser polarization.

The resulting averaged photoionization delays, expressed in the laboratory frame, are illustrated in Fig. 6.3 for individual orbitals of the 4d shell of ethyl iodide. Within the energy range, where in the photoionization cross section a resonance peak is observed, i.e. between 70 eV and 110 eV, all photoionization delays yield positive values. Qualitatively, all orbitals show a similar behavior, where EWS delays increase with decreasing XUV photon energies. The latter finding is a generic behavior for XUV photon energies approaching the ionization limit. Minor deviations are observed especially for the d_{z^2}-orbital, where EWS delays around 72 eV and 82 eV traverse a local maximum. However, since individual orbitals contribute about equally to the total photoionization yield, the latter effect is smeared out in the orbital-averaged curve, which can be obtained from experimental streaking measurements.

6.3.2 Density Functional Theory

Since the computing effort scales exponentially with the number of involved particles, the calculation of electronic ground states for many-particle systems like molecules or heavy atoms as quantum-mechanically exact solution via Schrödinger's equation is typically not feasible. Even within the Born-Oppenheimer approximation, where the motion of the nuclei is neglected, an exact solution of Schrödinger's equation for many electrons is currently out of reach. An alternative approach is pursued in density functional theory (DFT), where the ground state energy is expressed as functional of the electron density $n(\mathbf{r})$ [291]. The electron density is constructed from auxiliary functions, which solve the single-particle Schrödinger's equation, wherein the many-body interaction is considered by the exchange-correlation potential $V_{\mathrm{XC}}(\mathbf{r})$ [292]. Local density approximation theory (LDA), is a specific model for the exchange-correlation potential, which derives from the formulation of a homogeneous electron gas. In the descriptions of atomic and molecular systems, LDA theory considers the electron gas density to vary locally, while within such limited regions, the electron gas is assumed spatially homogeneous.

For electronic systems, where screening effects become significant, and also for the description of excited ionization states, results from density functional theory in the LDA formulation yield less agreement with experimental findings. An alternative is a time-dependent approach, referred to as time-dependent density functional theory (TDDFT), where the electron density $n(\mathbf{r}, t)$ is still calculated from auxiliary functions, which are now a solution to the time-dependent Schrödinger equation [293]. The exchange correlation potential in TDDFT can still be expressed in a local density approximation based on the homogeneous electron gas, which is accordingly referred to as TDLDA.

For the retrieval of photoionization delays, the electronic structure of atomic iodine is calculated in LDA and TDLDA simulations[2]. Due to the vast number of electrons, calculations are restricted to atomic iodine, while simulations of the entire ethyl iodide molecule remain elusive. The resulting photoionization cross section $\sigma_{4\mathrm{d}}$ for the transition $4d \rightarrow \epsilon f$ and the asymmetry parameter $\beta_{4\mathrm{d}}$, both obtained by LDA and TDLDA calculations, are illustrated in Figs. 6.4 (a) and (b), together with experimental data taken on different iodine compounds. The asymmetry parameter β, generically defined by

$$\frac{d\sigma}{d\Omega} = \frac{\sigma}{4\pi}\left(1 + \beta \cdot \frac{3\cos^2(\theta) - 1}{2}\right) \quad , \tag{6.2}$$

where Ω and θ represent the solid angle and angle between laser polarization and electron emission direction, respectively, considers the orientation dependence in the photoemission process. For both parameters the results from TDLDA calculations yield generally better qualitative and quantitative agreement with experimental data than with predictions from LDA-theory. The absolute values of photoionization cross sections appear overestimated for both LDA and TDLDA calculations, where experimental results yield cross sections, which are only about half the size of theoretical predictions from TDLDA simulations. While experimental values of cross sections on ionized iodine atoms [298] are found in good agreement with TDLDA calculations, theoretical reports raised generic concerns [299] about the quantitative analysis of experimental results on neutral iodine cross section measurements. However, qualitatively, the resonance in photoionization cross section for the transition $4d \rightarrow \epsilon f$ is fully

[2]LDA and TDLDA calculations are performed in the group of A. Landsman by L.-W. Pi

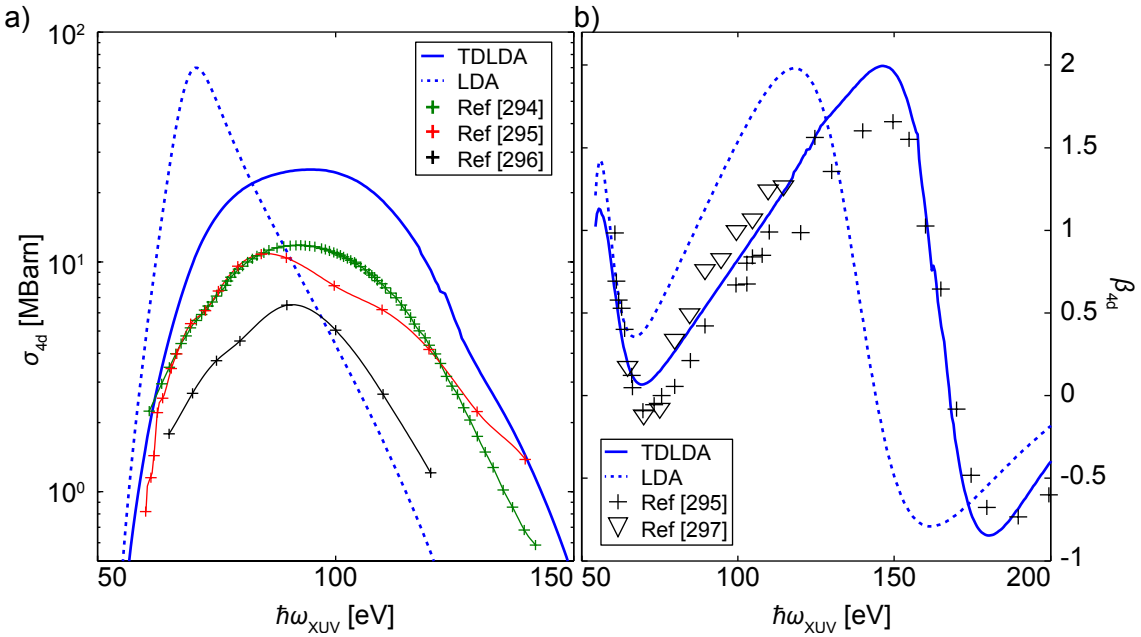

Figure 6.4: Cross sections and asymmetry parameters calculated from DFT simulations. The resulting cross sections σ_{4d} and asymmetry parameters β_{4d} for photoionization from the 4d shell of iodine are shown in **(a)** and **(b)**, each indicating the results from LDA and TDLDA simulations by broken and solid blue lines, respectively. For comparison, results from experimental studies on different iodine compounds (i.e. diatomic, molecular iodine Ref. [294], methyl iodide Ref. [295], atomic iodine Ref. [296] and chloromethyl-methyl iodonium Ref. [297]) are plotted together with theoretical simulations. For comparability, the absolute values from Ref. [294], obtained on diatomic, molecular iodine, are halved. Since the results from TDLDA calculations on atomic iodine are found in reasonable agreement with results on molecular compounds, it can be concluded that cross section and asymmetry parameter are not strongly influenced by the molecular constituents.

retrieved from TDLDA simulations with the maximum cross section centered around XUV energies of 90 eV and an approximate FWHM of 30 eV. Since the experimental data represents measurements on different iodine compounds, i.e. pure atomic [296] and molecular [294] iodine, but also more complex molecules [295,297], it can be concluded that cross sections and asymmetry parameters for photoionization from inner shells are hardly influenced by molecular constituents, but are almost exclusively determined by the atomic properties.

The latter is a priori not fulfilled for photoionization delays, since here the interaction of the emitted electron with molecular orbitals could potentially influence the apparent delays. Nonetheless, the retrieval of photoionization delays from (TD)LDA simulations on atomic iodine is instructive: as outlined in Sec. 6.2 previous theoretical reports on the photoionization delay of electrons emitted from the xenon 4d orbitals revealed substantially different results. Since the electronic structure differs only by one electron, iodine and xenon can be considered to possess similar physical properties, which is also supported by the 4d photoionization cross sections of both species. Accordingly, complementary (TD)LDA simulations on the photoionization delays for atomic iodine could potentially dissolve remaining ambiguities of the generic effect of collective interactions on the photoionization delays, which arose from previous theoretical reports on xenon.

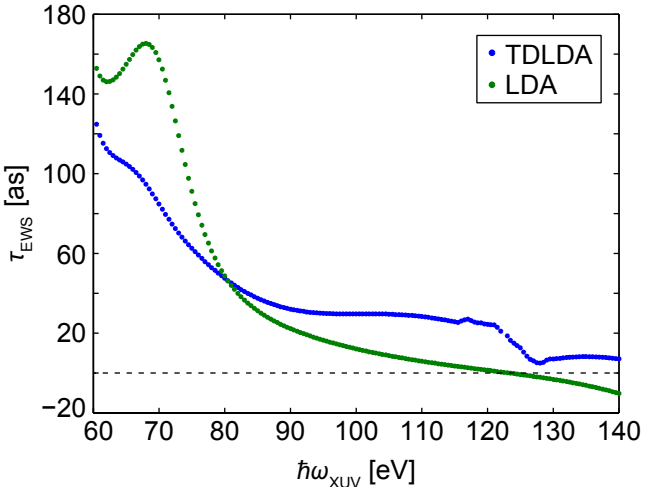

Figure 6.5: Photoionization delays calculated from LDA/TDLDA simulations on atomic iodine. The photoionization delays are calculated in dependence of the photon energy from the electronic structure of atomic iodine, which is determined by LDA and TDLDA calculations. For both calculations, the respective EWS delay yields positive values, while only in the high energy regime, i.e. $\hbar\omega_{\mathrm{XUV}} \geq 125\,\mathrm{eV}$ the influence of the Cooper minimum becomes apparent by negative delay values.

The extracted photoionization delays, in dependence of the XUV photon energy for electrons emitted from the 4d shell of atomic iodine, are displayed in Fig. 6.5 for simulations based on LDA and TDLDA calculations in green an blue, respectively. In agreement with the previous results from quantum scattering theory, the photoionization delay is increasing with decreasing XUV photon energy. For calculations based on LDA theory, the EWS delay reveals a distinct peak at around the same XUV photon energy, where the photoionization cross section from LDA calculations is maximized. In contrast, for the TDLDA calculations, where the cross section maximum is observed around 90 eV, no clear delay peak is obtained. Remarkably, for both theories, the EWS delay is positive, where only for high XUV photon-energies beyond 120 eV, the influence of the Cooper-minimum at around 160 eV causes a change in sign. This finding is in contrast to previous simulations employing the TDLDA approach on atomic iodine, where for XUV photon energies exceeding 90 eV negative EWS delays are reported [300], which are attributed to collective interactions of electrons within the 4d shell of iodine. The discrepancy in theoretical results is conceptually identical with the outcome of simulations on xenon, where similar theoretical approaches yield differing results. At present, the disagreement between calculations on both atomic targets remains elusive. Here, experimental measurements in the respective energy range are highly desirable to resolve remaining ambiguities.

6.3.3 Semi-classical Calculations

In the semi-classical calculations[3], described in full details in Ref. [301], the streaking process is modeled in two steps, where the first incorporates the single-photon ionization from the streaking target by the XUV laser field. In the second step, the liberated electron is propagated in the orbital potential landscape of the ionized streaking target and the superimposed NIR

[3]Semi-classical simulations are performed in the group of A. Landsman by L. Ortmann and T. Zimmermann.

laser field. Subsequently, individual electron trajectories of randomized emission directions are integrated within a full cone angle of 45° around the NIR laser field polarization direction, which yields a streaking spectrogram. Finally, the theoretically calculated spectrograms are analyzed using the same approach as for the analysis of the experimental measurements to obtain the streaking delay. All necessary input variables in the semi-classical calculations, e.g. NIR laser intensity, central energy and spectral width of the XUV pulse or NIR pulse duration, are motivated by experimental parameters.

The electronic ground states of neon and ethyl iodide are both calculated in two different approaches, i.e. the Hartree-Fock method (HF) and configuration interaction single (CIS) description, where the respective basis sets 6-31 G** and cc-pVTZ are employed. In the CIS approach, the ground state is calculated based on Dyson orbitals, which result as overlap integral between the wave functions of the neutral and ionized streaking target. Thereby, shake-up states, where photoemission is accompanied by the transition of electrons into higher-lying orbitals are particularly included in the calculations. However, the analysis of occupation probabilities reveals that excited ionic states are hardly populated, which is also supported by experimental findings. In the Hartree-Fock description, Koopman's theorem is implicitly employed, assuming that the orbital structure of the ionized streaking target is identical to its neutral ground state (frozen orbital approximation).

In the semi-classical calculations, full streaking spectrograms $S(p)$ are calculated from the photoelectron's wave functions

$$S(p) = \left| \langle p | P_{\mathrm{D}} | \psi^{(1)}(t) \rangle \right|^2 \qquad , \tag{6.3}$$

where p represents the momentum, while the projector P_{D} rejects the bound part of the photoelectron's wave function $\psi^{(1)}(t)$. Here, it is implicitly assumed that the spectrogram is calculated for large times t, where bound and dissociative parts of the electron wave packet are clearly separated and the NIR laser pulse vanished. Employing the single active electron approximation (SAE), the photoelectron's wave function is given by

$$\psi^{(1)}(t) = -\frac{i}{\hbar} \int_{t_0}^{t} U_0(t - t')\, H_{\mathrm{XUV}}\, U_0(t' - t_0)\, \psi^{(0)}(t_0) dt' \qquad , \tag{6.4}$$

where $\psi^{(0)}(t_0)$ describes the electron ground state, with t_0 expressing a time prior to the arrival of the NIR laser field at the streaking target. Before photoionization by the XUV laser field at time t', the photoelectron wave function is propagated with the propagator $U_0(t' - t_0) = \exp\left[-\frac{i\, H_0(t'-t_0)}{\hbar}\right]$, where the Hamiltonian H_0 yields the ground state energy E_0 of the neutral neon atom or ethyl iodide molecule. In the semi-classical calculations not only the orbital potential of the streaking target (i.e. neon atoms or ethyl iodide molecules), but also the NIR laser field is considered by the Hamiltonian. However, since the NIR probe field in streaking experiments is typically weak enough to exclude strong-field processes, it can be assumed that the ground state wave function of the respective streaking target is an eigenstate of the effective Hamiltonian H_0 for all times prior to the photoionization process, for which $\psi^{(0)}(t')$ is easily obtained. The interaction with the XUV laser field is typically expressed using the dipole approximation with $H_{\mathrm{XUV}} = -\boldsymbol{\mu}_e\, \mathbf{E}_{\mathrm{XUV}}$, where $\boldsymbol{\mu}$ is the dipole operator and $\mathbf{E}_{\mathrm{XUV}} = \boldsymbol{\epsilon}\, E_{\mathrm{env}}(t) \cdot \cos(\omega_{\mathrm{XUV}}\, t)$ describes the XUV laser pulse by its envelope function $E_{\mathrm{env}}(t)$ and central frequency ω_{XUV}. As result, the partially dissociative electron wave function $\psi_{\mathrm{XUV}}(t') = H_{\mathrm{XUV}}(t')\, \psi^{(0)}(t')$ is obtained. Ultimately, the ionized wave function $\psi_{\mathrm{XUV}}(t')$ is again propagated with $U_0(t - t')$ until large times t, where the electric field

of the NIR laser pulse has vanished. However, in the last propagation step, the propagator $U_0(t-t')$ needs to consider the Hamiltonian of the entire ionized ethyl iodide molecule H_{mol} in the presence of the NIR laser field, for which the eigenstates are generally not obtained analytically. Since the kinetic energy of photoelectrons in streaking experiments is typically large, the latter propagation can be performed using the classical Wigner method [301–303].

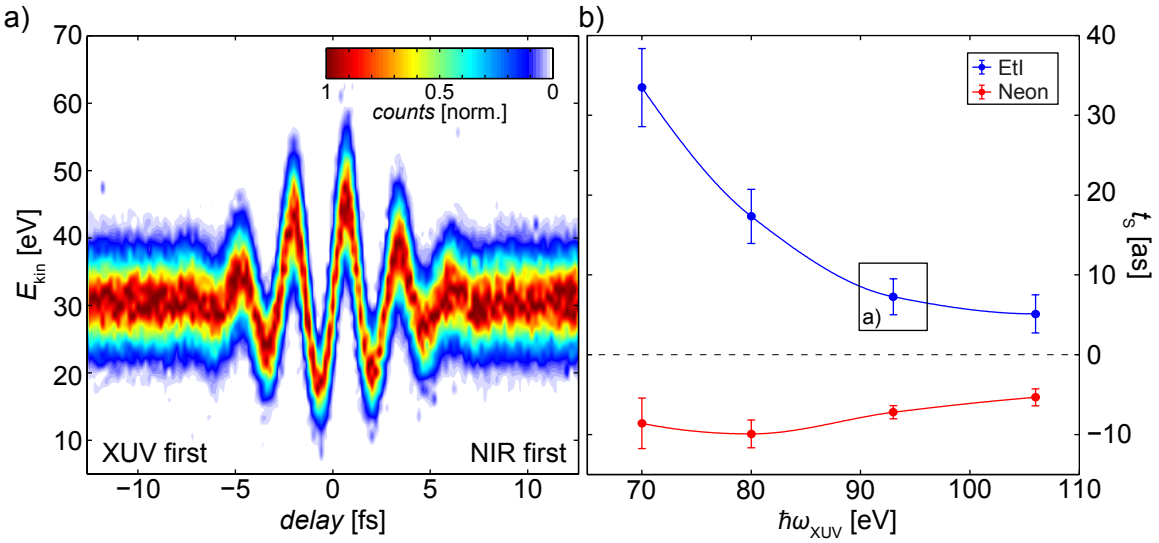

Figure 6.6: Simulated streaking spectrogram and associated streaking delays. The streaking spectrogram on ethyl iodide, calculated based on the semi-classical approach, is illustrated in **(a)**, where the central energy and spectral width of the XUV laser field is given by 93 eV and 6.5 eV, respectively. In **(b)** the streaking delays t_S for photoemission from ethyl iodide 4d (blue) and neon 2p orbitals (red) are displayed in dependence of the central XUV photon energy, where the result obtained from the spectrogram shown in **(a)** is highlighted by a black rectangle. For the shown streaking delays, electronic ground states of neon and ethyl iodide are calculated based on the configuration interaction single description (CIS). Courtesy of L. Ortmann and T. Zimmermann.

A typical streaking spectrogram on ethyl iodide, resulting from the semi-classical calculations is shown in Fig. 6.6 (a), where the central XUV photon energy and spectral width (FWHM) yield 93 eV and 6.5 eV. From the simulations, the binding energy of electrons ionized from the 4d-band of ethyl iodide yields about 61 eV, which is slightly larger than experimental literature values, but is still within the typical error bar of several electronvolts for electronic ground state calculations. From the analysis of photoionization probabilities, it is found that individual orbitals of the five-fold, degenerated 4d band of ethyl iodide contribute equally to the photoemission yield in the spectrogram. Accordingly, the retrieved streaking delays represent to good approximation the averaged mean value of individual orbital emission. Together with the respective streaking spectrogram calculated for photoionization from the neon 2p orbital, the streaking delay t_S for both targets can be retrieved. Therefore, the simulated spectrograms are analyzed using the same procedure as applied to experimentally obtained streaking spectrograms, which is explained in detail in Sec. 6.4. Briefly, the streaking traces from the neon and ethyl iodide emission bands are extracted from the spectrograms by Gaussian peak fitting and are hereafter transferred into the spectral domain, where the streaking delay difference between both emission channels is calculated from the difference in spectral

phase. To investigate the dependence of streaking delays on the XUV photon energy, spectrograms are simulated for different XUV photon energies. For both targets, the resulting streaking delays in the range of 70 - 106 eV are shown in Fig. 6.6 (b), where the electronic ground states of ethyl iodide and neon are calculated based on the CIS description. However, it should be pointed out that the illustrated streaking delays of neon and ethyl iodide are not corrected for measurement specific effects, e.g. Coulomb-laser-coupling, which explains the negative values for the streaking delay in case of neon. Across the full investigated energy range, the streaking delay for photoionization from ethyl iodide is larger as compared to the photoionization from neon 2p orbitals. Accordingly, the relative streaking delay difference between photoionization from ethyl iodide and neon is positive, for which electrons emitted from the ethyl iodide appear to reach the detector later as compared to electrons photoionized from neon.

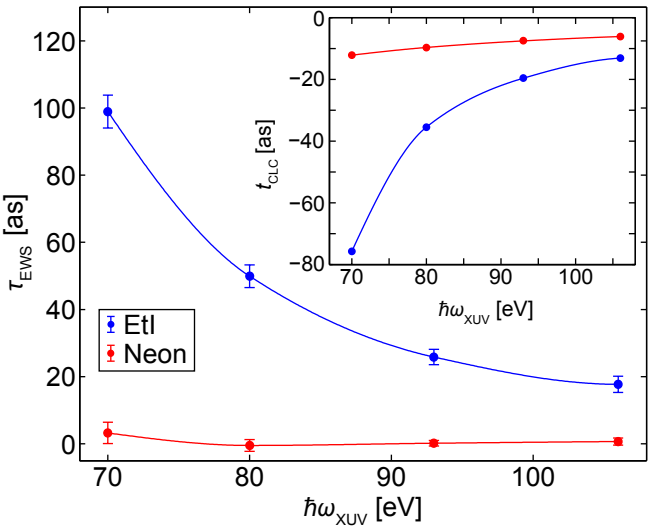

Figure 6.7: Eisenbud-Wigner-Smith delay from semi-classical calculations. Relative Eisenbud-Wigner-Smith delay for electrons ionized from the 4d orbital of ethyl iodide (blue) and neon 2p orbitals (red) in dependence of the XUV photon energy. Electronic ground states of both streaking targets are calculated using the configuration interaction singles description. The inset displays the delay, introduced by the NIR field via Coulomb-laser-coupling for photoemission from the respective streaking targets. The CLC-contribution was calculated classically following the expression given in Eq. (2.49). Courtesy of L. Ortmann and T. Zimmermann.

While the difference between streaking delays, resulting from semi-classical calculations, is directly comparable to the experimental findings, the comparison to quantum scattering theory and LDA/TDLDA calculations, where the influence of the NIR laser field is not considered, is inadmissible. As stated in Eq. (2.51), the few-cycle field introduces phase shifts on the emitted electrons via Coulomb-laser-coupling and polarization effects of the streaking target. While the latter can be assumed to have a negligible influence for the comparably weak NIR laser fields, the Coulomb-laser-coupling term t_{CLC} can change the streaking delays significantly, especially for photoelectrons of small kinetic energies. As shown in Ref. [134] and expressed in Eq. (2.49), the additional delay t_{CLC}, introduced by Coulomb-laser-coupling, can be approximated in a fully classical calculation. Subtracting the CLC-delays from the streaking delay t_{S}, as obtained from the semi-classical calculations and illustrated in Fig. 6.6 (b),

reveals the Eisenbud-Wigner-Smith delay τ_{EWS} for photoionization from neon and ethyl iodide, where the latter is directly comparable to the results from quantum scattering theory. In Fig. 6.7, the EWS-delays for photoionization from neon (red) and ethyl iodide (blue) are illustrated in dependence on the XUV photon energy, while the respective CLC-delay t_{CLC}, assuming a central wavelength of $\lambda_{\mathrm{NIR}} \approx 800\,\mathrm{nm}$ for the NIR laser field, is displayed as inset. Apparently, the EWS-delay for photoionization from the ethyl iodide 4d orbitals is strongly increasing with decreasing XUV photon energies, which is in qualitative agreement with the previous results from quantum scattering theory and (TD)LDA simulations. Electrons photoionized from neon 2p orbitals experience only small delays over the entire energy range. However, as in case of ethyl iodide, the neon EWS-delay starts to increase while approaching the ionization threshold. This finding is in considerable agreement with photoionization delays from neon obtained from RPAE calculations, where many-body effects are included [37].

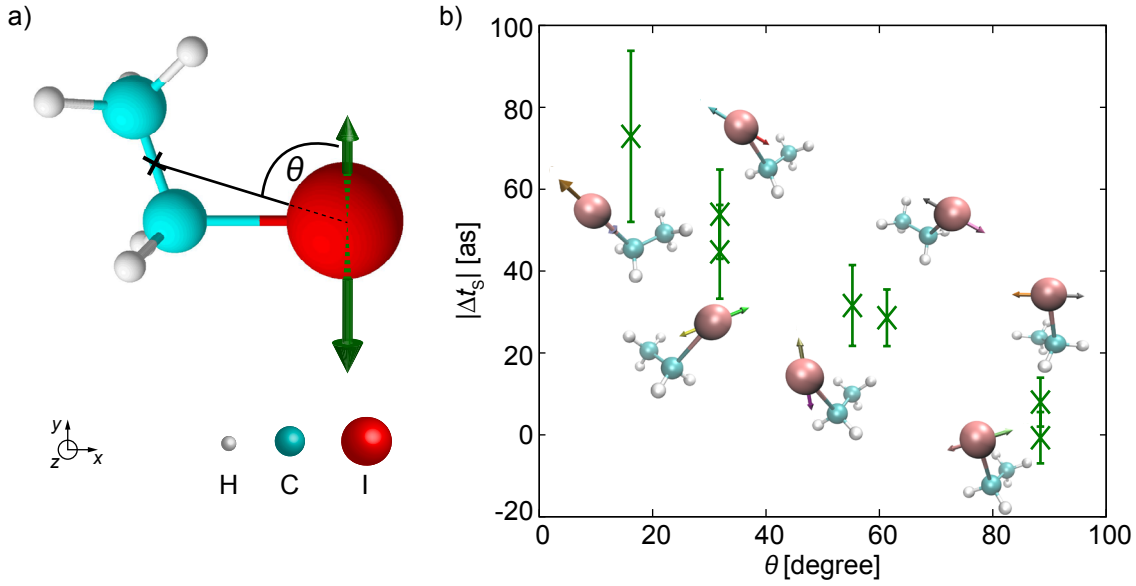

Figure 6.8: Orientation dependence of streaking delays from ethyl iodide. The geometry underlying the analysis of the orientation dependence of streaking delays is illustrated in **(a)**, where the absolute value of photoionization delay and emission direction of electrons is indicated by the length and direction of the solid green arrow. The emission angle θ is defined with respect to the connecting line between the iodine atom and the carbon bond center (black cross). Here, arbitrary emission directions are projected into the xy-plane, defined by the iodine and the two carbon atoms. In **(b)** the absolute values of differential streaking delays Δt_{S} are illustrated in dependence of the emission angle θ. The small pictographs represent a 3D illustration of the photoelectron emission direction. Courtesy of L. Ortmann and T. Zimmermann.

While the streaking delays, illustrated in Fig. 6.6 (b), are calculated for randomized ethyl iodide emission directions, the semi-classical simulations allow to resolve the streaking delay as a function of the emission angle of the photoelectron. To elaborate the influence of the molecular potential landscape on the streaking delay, it is instructive to analyze the streaking delay difference Δt_{S} between photoelectrons ionized from the ethyl iodide 4d orbitals and emitted in opposite directions. Accordingly, the isotropic case, where the streaking delay is independent on the emission direction, demands $\Delta t_{\mathrm{S}} \approx 0$. The streaking delay difference is

evaluated in dependence of the emission angle, which is given relative to the connection line between the iodine atom and the central point of the carbon-carbon bond. The general geometry to analyze the orientation dependence of the streaking delay is illustrated in Fig. 6.8 (a), while the resulting streaking delay difference for photoionization by XUV photons of 80 eV central energy, is shown in (b). In total, the streaking delay difference is evaluated for seven independent orientations, where the largest delay difference is observed between the emission parallel and anti-parallel to the carbon-iodine bond, which yields about 71 as. In contrast, the delay of photoelectrons emitted approximately parallel to the ethyl group, i.e. $\theta \approx 90°$, is found to be almost isotropic, where the streaking delay difference is close to zero. While the anisotropy of streaking delays for photoionization from ethyl iodide is evident from Fig. 6.8 (b), the streaking delay difference makes no statement on the absolute orientation dependence of streaking delays. Here, it is found that photoelectrons emitted away from the ethyl group, along the carbon iodine bond direction, experience the largest absolute streaking delays in the range of 80 as, whereas the streaking delay in emission directions being approximately orthogonal to the connection line between iodine atom and central point of the carbon-carbon bond of the ethyl group yield only around 15 as. Remarkably, the latter is considerably close to photoionization delays in emission directions, which traverse the ethyl group almost through the center. The large photoionization delay for electrons emitted away from the ethyl group parallel of the carbon-iodine-bond, indicates a positive electrostatic potential in close vicinity of the iodine atom.

6.4 Experimental Results

A typical streaking spectrogram, measured with XUV photons at central energy of 93 eV is illustrated in Fig. 6.9 (a). Here, the conversion from time-of-flight to energy, is facilitated by the generic relation between flight time t_{TOF} and kinetic energy E_{kin}:

$$E_{\mathrm{kin}}\,[\mathrm{eV}] = s \cdot \frac{1}{t^2_{\mathrm{TOF}}\,[\mu\mathrm{s}]} \qquad , \tag{6.5}$$

where the parameter s represents a fitting constant. The latter is calibrated by the XUV photoionization signal from neon, where the central kinetic energy is set to 58 eV and 71 eV for the respective XUV photon energies of 80 eV and 93 eV. Accordingly, it is assumed that XUV photoionization from neon is dominated by the photoemission from the 2p shell, as supported by experimentally obtained partial cross section [170], where the binding potential yields 21.6 eV.

The highest-energetic photoemission band in the streaking spectrogram features a broad band of comparably low count rate, where the photoelectron peak is located around 80 eV (for NIR and XUV not being in temporal overlap). Based on the respective photoelectron's binding energy in the range of 8 - 18 eV, the high energy emission line is attributed to photoionization from the valence band of the ethyl iodide molecule. For the XUV bandwidth of 6.5 eV, in total six individual orbitals contribute to the high-energy band, where the largest photoionization cross-section is reported for the σ-bond orbital between the carbon and iodine atom [304]. For the latter a binding energy of $I_{\mathrm{b}} = 11.7$ eV is predicted, which is in reasonable agreement with the emission peak from streaking measurements indicating an experimentally obtained binding potential of 13 eV.

The low energetic emission band between 35 and 40 eV results from photoionization of

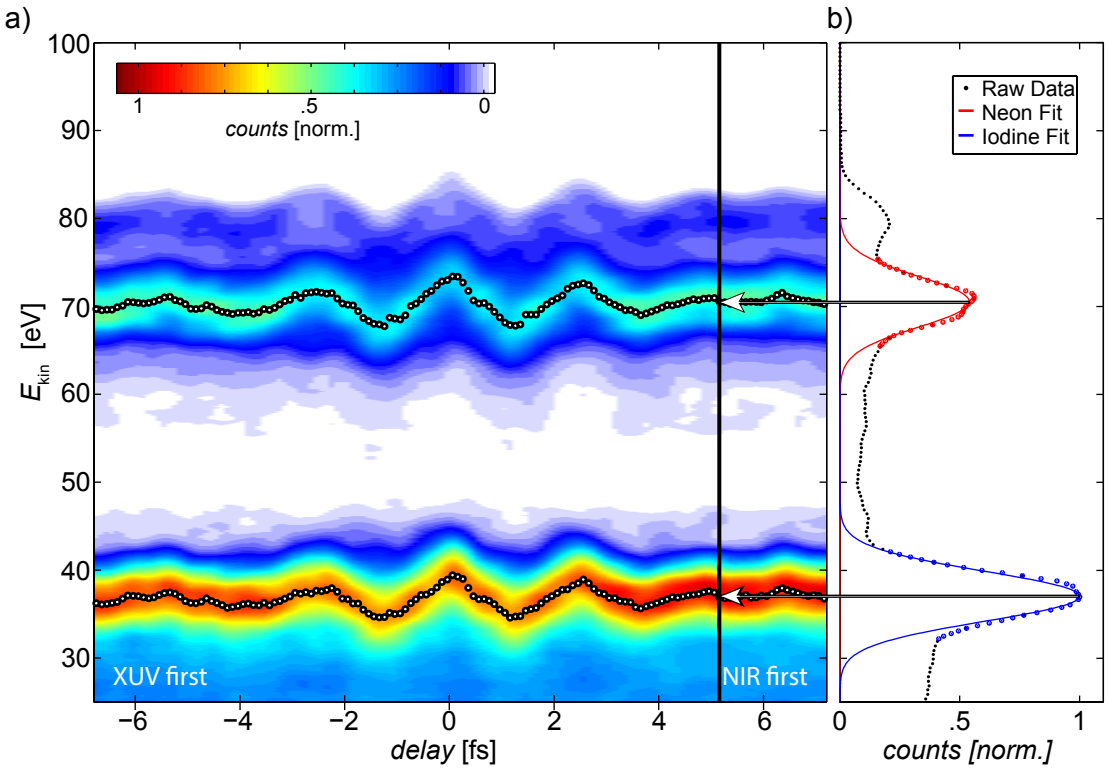

Figure 6.9: Streaking spectrogram on ethyl iodide and neon. In **(a)** a streaking spectrogram, integrating 20k laser shots per delay steps of 100 as and acquired simultaneously on ethyl iodide and neon for an XUV photon energy of 93 eV, is displayed. The black line indicates the respective delay value for which the normalized photoelectron spectrum in **(b)** is illustrated. For each delay scan, Gaussian functions are fitted to the neon 2p and iodine 4d emission, where the energy values of the maximum photoelectron counts define the raw streaking traces, outlined by white dots in **(a)**.

the 4d orbital of iodine atoms, bound in the ethyl iodide molecules. Since the 4d shell of iodine is only partially filled, the electronic state gives rise to a spin doublet, where the respective binding potentials are reported to yield 57.5 eV and 59.2 eV for the $4d_{5/2}$ and $4d_{3/2}$ configuration, respectively [296, 305]. While the photoelectron energy around 36 eV is anticipated for the reported binding potentials, the double peak structure indicating the spin doublet state is not resolved in the streaking spectrogram. Since the photoelectron spectrum results as convolution of the density of states and the XUV bandwidth, the double peak structure is smeared out, yielding only a single peak of enhanced width.

While the assignment of individual streaking lines is supported by the respective binding potentials, an exchange of streaking targets verified this finding experimentally: by removal of the neon driving gas, the streaking line assigned to the photoionization of neon vanishes, whereas the high and low-energetic emission lines attributed to ionization from the ethyl iodide molecule remain unchanged. Ultimately, to allocate the low-energy emission unambiguously to the iodine atom, the ethyl iodide molecule is replaced by ethanol, for which only the high-energy emission is observable in the streaking spectrograms.

Retrieval of Streaking Delays

To calculate the photoionization delay between the respective orbital emissions, the streaking traces are extracted from the spectrogram. Therefore, for each delay scan, the photoemission yield from the neon 2p and ethyl iodide 4d orbitals is fitted independently by Gaussian functions. In Fig. 6.9 (b), a typical photoelectron spectrum is displayed, for an arbitrary delay, indicated by the black solid line in Fig. 6.9 (a). In the fitting algorithm, applied to the neon and ethyl iodide emission lines, only a limited energy range around the respective peak maximum is taken into account. The latter is indicated by the red and blue dots in Fig. 6.9 (b), which visualize the considered data points within their respective energy range. The resulting Gauss fits are illustrated as red and blue solid lines. The central energies, for which the Gaussian function of each delay scan is maximized, designate the streaking traces for the respective emission orbitals, represented as dots in the streaking spectrogram in Fig. 6.9 (a). As can be observed, for temporal overlap between NIR and XUV laser fields, the photoelectron spectra of valence band and neon emission are not fully separated. While the neon peak, due to the strong photoionization cross section of the 2p orbital and the high target density, is clearly resolved for any delay, the valence band emission peak disperses to an extent, where Gaussian peak fitting is unfeasible. Accordingly, the valence band emission is not further considered in determining photoionization delays. Similar peculiarities of overlapping photoelectron spectra are found for an XUV-photon energy of 80 eV, where the excess energy of photoelectrons ionized from the iodine 4d orbital is only marginally larger than above-threshold ionization (ATI) from the ethyl iodide molecule induced by the few-cycle laser field. Therefore, in streaking measurements with 80 eV photons, the maximum NIR intensity is limited to $I_{\mathrm{NIR}} \lessapprox 4 \cdot 10^{11}\,\mathrm{W\,cm^{-2}}$, where the ATI cut-off does not exceed 15 eV.

For the retrieval of streaking time delays, streaking traces acquired from the neon 2p and iodine 4d emission bands are Fourier transformed into the spectral domain, which yields the spectral amplitude and phase, as illustrated in Figs. 6.10 (a) and (b). Prior to Fourier transformation, all time-based datasets are zero-padded to increase the resolution in spectral amplitude and phase. Since phase and time shifts are inherently connected, the streaking delay t_{S} between the two emission lines is calculated from the difference in spectral phase

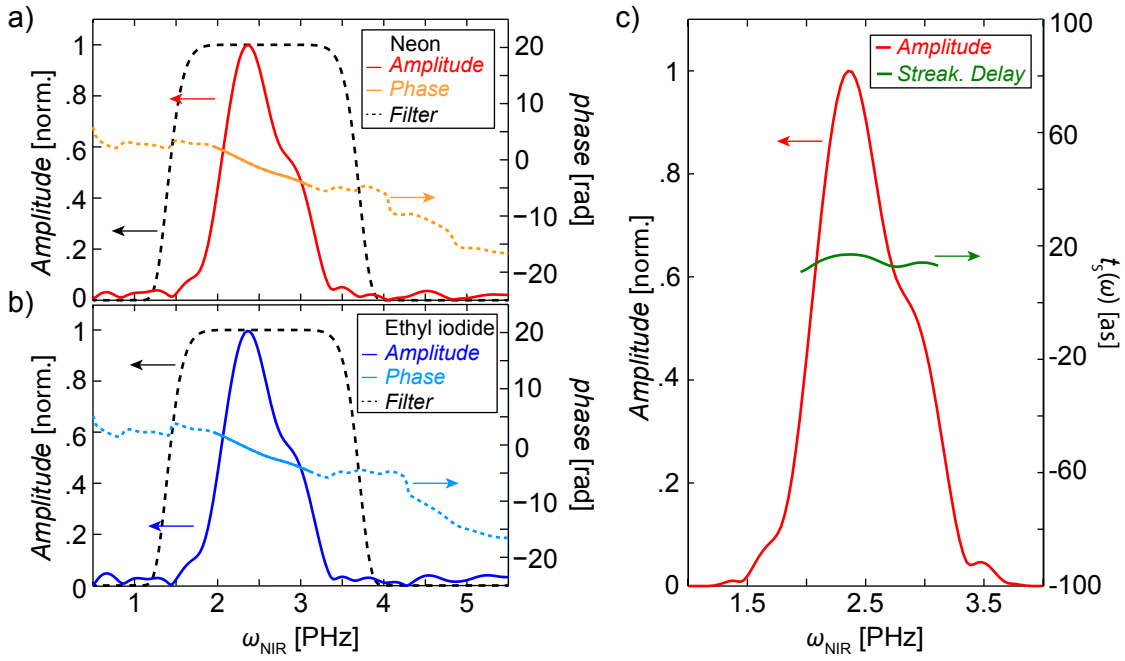

Figure 6.10: Spectral amplitude and phase of streaking traces. In **(a)** and **(b)** the spectral amplitude and phase of the streaking traces, retrieved from the neon 2p and iodine 4d emission, respectively, are displayed in dependence of the angular frequency ω of the NIR laser field. Spectral intensities below the threshold of $0.1 \cdot I_{\max}(\omega)$ (i.e. spectral amplitude threshold of $A(\omega) \leq \sqrt{0.1} \cdot A_{\max}(\omega)$) are considered as noise level, for which the spectral phase $\Phi(\omega)$ is blanked, illustrated by the light red/blue broken lines. The Fourier filter, which confines the respected angular frequency range to the NIR laser spectrum, is displayed as black broken line. In **(c)** the streaking delay $t_S(\omega)$, calculated using Eq. (6.6), is shown together with the filtered spectral amplitude of the neon streaking trace, which is used as weighting factor to calculated the weighted mean value $\overline{t_S}$.

according to

$$t_{\mathrm{S}}(\omega) = \frac{\Phi_{\mathrm{Iod}}(\omega) - \Phi_{\mathrm{Ne}}(\omega)}{\omega} \quad , \tag{6.6}$$

where $\Phi_{\mathrm{Iod}}(\omega)$ and $\Phi_{\mathrm{Ne}}(\omega)$ represent the spectral phase of the iodine and neon streaking trace, while ω stands for the NIR laser angular frequency. As illustrated in Fig. 6.10 (c), the resulting streaking delay $t_{\mathrm{S}}(\omega)$ is generally a flat function of angular frequency, for which the average is calculated according to

$$\overline{t_{\mathrm{S}}} = \sum_{\omega} \frac{I_{\mathrm{Ne}}(\omega) \cdot t_{\mathrm{S}}(\omega)}{I_{\mathrm{Ne}}(\omega)} \tag{6.7}$$

where the spectral intensity $I_{\mathrm{Ne}}(\omega)$ of the neon 2p streaking trace is employed as weighting factor.

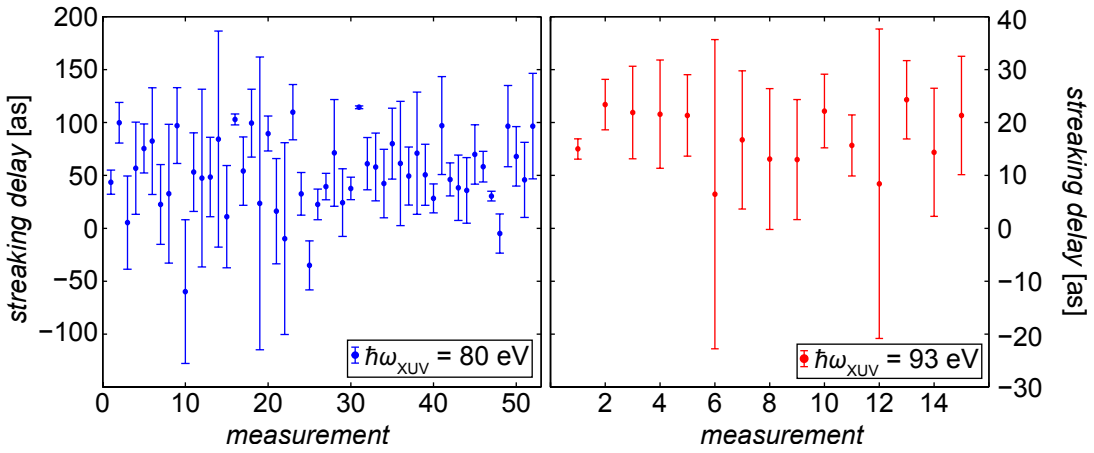

Figure 6.11: Streaking delay difference between photoionization from ethyl iodide 4d and neon 2p orbitals. Retrieved streaking delay difference between the ethyl iodide 4d and neon 2p-orbital emission from all measurements, where **(a)** and **(b)** illustrate the results for XUV photon energy of 80 eV and 93 eV, respectively.

To reveal the energy dependence of the streaking delay, spectrograms are acquired at different XUV photon energies, i.e. 80 and 93 eV. In contrast to measurements at $\hbar\omega_{\mathrm{XUV}} = 93$ eV, measurements at 80 eV XUV photon energy suffer from significantly reduced photon flux, for which the integration time is increased to 40k laser shots to obtain adequate statistics. Simultaneously, the delay step size is increased to 200 as in order to preserve the total acquisition time, limited by the CEP stability of the few-cycle laser field. The results, comprising all measurements at XUV photon energies of 80 and 93 eV, are illustrated in Figs. 6.11 (a) and (b), respectively. From the individual measurements, the average streaking delay is obtained as 68.4 ± 39.6 as and 18.1 ± 4.3 as for 80 eV and 93 eV photon energy.

Likewise, the streaking delay difference between the neon 2p and ethyl iodide 4d streaking traces can be illustrated in the temporal domain. Therefore, the streaking traces are filtered in the spectral domain, as indicated in Figs. 6.10 (a) and (b), where an appropriate filter function rejects all frequency components that are not contained in the input spectrum of the NIR laser field. The back-transformed, filtered streaking traces for neon and ethyl iodide emission are displayed in Fig. 6.12 as red and blue solid line, respectively, together with the superimposed

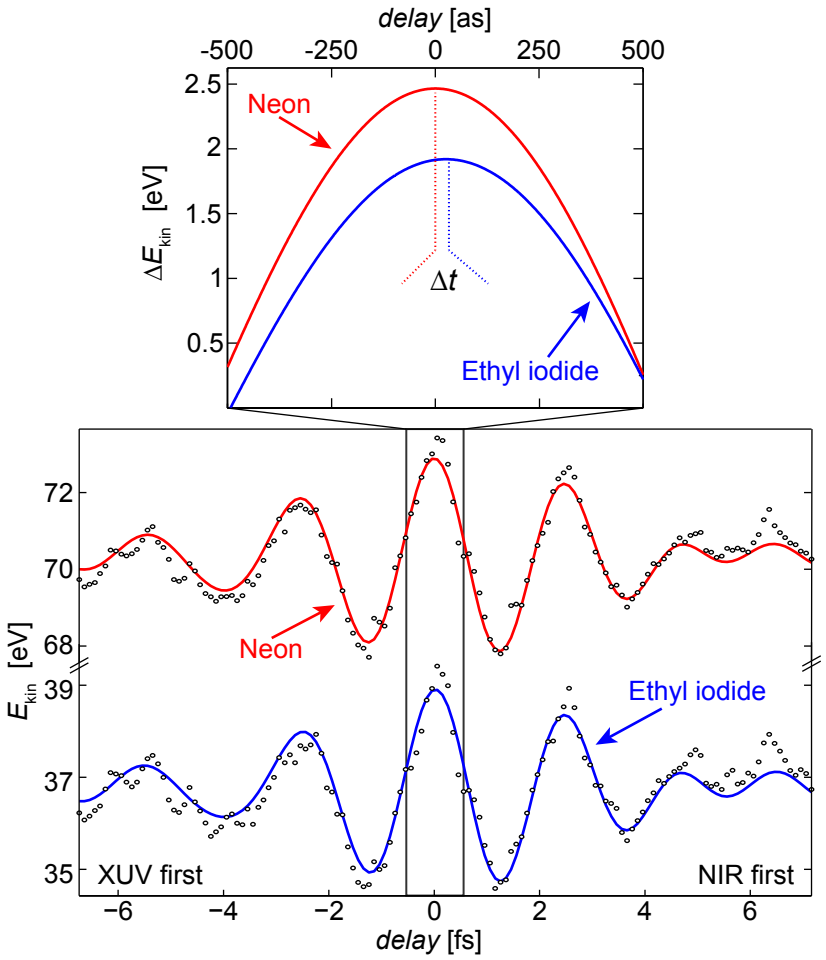

Figure 6.12: Filtered streaking traces for ethyl iodide and neon. The bottom figure illustrates the streaking traces from the neon 2p and ethyl iodine 4d emission as obtained from Fig. 6.9 **(a)** together with the respective Fourier filtered data, displayed as red and blue solid lines. Since the streaking delay is on the order of tens of attoseconds, the shift between the two streaking traces is only observed on a magnified delay axis, as shown on the top, where just a narrow range of 1 fs around the maximum streaking amplitude is displayed.

raw data points representing the unfiltered streaking traces. For the small streaking delays on the order of tens of attoseconds, the resulting shift is only apparent for a magnified delay axis, illustrated at the top of Fig. 6.12, which shows only a small delay range around the maximum streaking amplitude.

6.5 Analysis, Interpretation and Discussion

On average, the analysis of the streaking spectrograms, acquired simultaneously on neon and ethyl iodide, reveal positive streaking delay differences between electrons emitted from the iodine 4d and neon 2p orbitals for both XUV central photon energies at 80 eV and 93 eV. The bar chart representations of streaking delays, illustrated in Figs. 6.13 (a) and (b) for the respective XUV photon energy, demonstrates the accumulation of individual streaking delay results in vicinity to the weighted mean values, i.e. 68 as and 18 as, respectively. Generally, the data set measured at central XUV photon energy of 80 eV is prone to larger variance, where few individual values even yield negative streaking delays. This finding is mainly attributed to the reduced XUV photon flux for measurements at central energy of 80 eV. Considering the emission from the 4d orbitals of ethyl iodide, the count rate yields only about 0.07 electrons per laser shot, which is significantly lower as compared to the measurement at 93 eV photon energy. Since the overall acquisition time for a full streaking spectrogram is limited by the laser stability, the integration time per delay step cannot be increased enough to compensate the small count rates. Accordingly, the signal strength and thereby also the signal-to-noise ratio (SNR) reduces and statistical errors will affect the photoionization delays more severely.

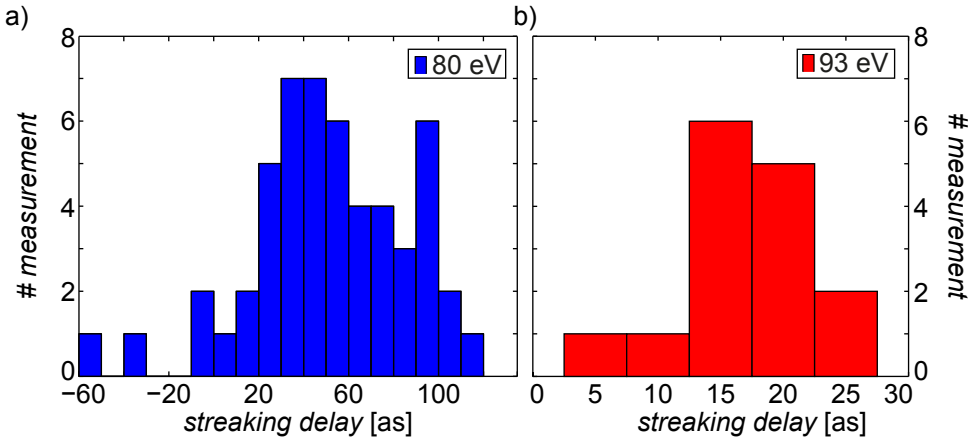

Figure 6.13: Bar plot representation of streaking delay differences. Subfigures **(a)** and **(b)** display the obtained streaking delay difference between electrons emitted from the ethyl iodide 4d shell with respect to the emission from neon 2p orbitals. For the larger variance in the 80 eV measurements, shown in **(a)**, the streaking-delay bin width is chosen to 10 as, while the measurements employing XUV photons at central energy of 93 eV, as shown in **(b)** use 5 as bin width.

While the generic behavior of reduced XUV photon flux results in decreasing count rates, which affects the photoelectron yield from neon 2p and ethyl iodide 4d orbitals simultaneously, the measurements at 80 eV photon energy suffer additionally from an increased noise floor: besides the generation of free electrons by XUV induced photoionization, the presence of

the NIR laser field facilitates also ATI from ethyl iodide. For NIR intensities in the range of $10^{11}\,\mathrm{W\,cm^{-2}}$, which are typically employed in the experiment, electrons generated by ATI reach energies between $15-20\,\mathrm{eV}$. Accordingly, for the binding potential of about 57 eV of the ethyl iodide 4d shell, photoelectron spectra from NIR ATI and single-photon XUV ionization are found to partially overlap. The latter is in particular significant for XUV and NIR laser pulses in temporal overlap, where for specific half-cycles, electrons ionized from the ethyl iodide 4d orbitals loose kinetic energy to the NIR laser field, i.e. electrons are downstreaked in energy. For the experiments described here, the ATI is an undesired background. The combination of small signal strength and large background counts for measurements employing XUV photons of 80 eV reduces the signal-to-noise ratio considerably, which explains the large variance of individual results, illustrated in Fig. 6.11 (a) and Fig. 6.13 (a). However, taking the size of the full data set, yielding 52 independent measurements, into account, enough statistics is achieved to observe accumulation of individual results around a mean value even for measurements recorded with 80 eV XUV photon energy.

Correlation between streaking delay and field amplitude

All streaking spectrograms are acquired in the ponderomotive streaking regime, where the shift in the photoelectron's kinetic energy is related to the vector potential of the NIR laser field, as expressed in Eq. (2.40). Therefore, the NIR field intensity can be directly retrieved from the streaking traces in the spectrograms. The general dependence of the streaking delay on the intensity is displayed as semilogarithmic scatter plot in Fig. 6.14 for measurements at both XUV photon energies. Here, for all measurements, the intensity is calculated from the streaking traces obtained from photoionization of the neon 2p orbitals. As can be observed, the streaking intensities for measurements employing 80 eV photons hardly exceed $4\times10^{11}\,\mathrm{W\,cm^2}$. As outlined before, approximately around this intensity, the streaking trace of the ethyl iodide 4d emission overlaps significantly with electron excited via multi-photon ionization for half cycles, where photoelectrons are downstreaked. For large intensities, the data analysis is typically not robust and streaking delays can not be reliably extracted.

While on the ordinate the accumulation of individual results around the respective mean values is again apparent for both data sets, a correlation between streaking delays and intensities is not discernible. The sample correlation coefficient $r_{t_\mathrm{s},I}$ between the NIR laser intensity I_NIR and streaking delay t_s, is calculated according to

$$r_{t_\mathrm{s},I} = \frac{\sum_i (t_\mathrm{s}^i - \overline{t_\mathrm{s}}) \cdot (I_\mathrm{NIR}^i - \overline{I_\mathrm{NIR}})}{\sqrt{\sum_i (t_\mathrm{s}^i - \overline{t_\mathrm{s}})^2} \cdot \sqrt{\sum_i (I_\mathrm{NIR}^i - \overline{I_\mathrm{NIR}})^2}} \quad , \tag{6.8}$$

where the summation index i extends over the number of individual measurements and $\overline{t_\mathrm{s}}$, $\overline{I_\mathrm{NIR}}$ represent arithmetic mean values. For both data sets, i.e. streaking spectrograms employing XUV photons at 80 eV and 93 eV, correlation coefficients yield only about -0.013 and 0.187, respectively. The larger value of the correlation coefficient for measurements with 93 eV photons derives mainly from the small data set size, comprising in total 15 individual measurements. Accordingly, it can be concluded that streaking delays and NIR laser field intensities are not strongly correlated, which is in agreement with findings from previous experiments on the photoionization delay from neon orbitals [14].

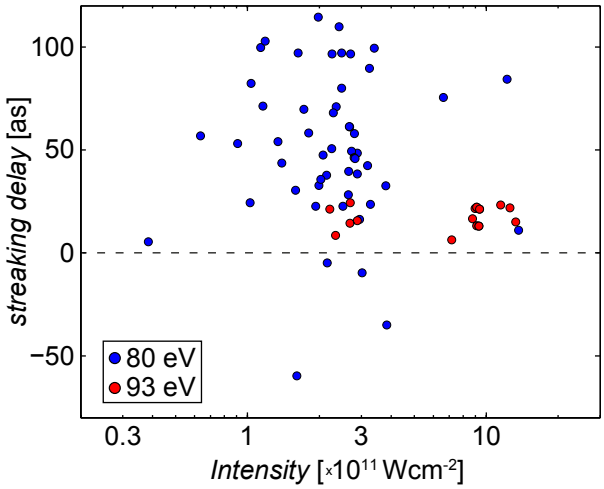

Figure 6.14: Scatter plot of streaking delay versus streaking intensity. While the data points accumulate on the ordinate around the mean value, a correlation between intensity and streaking delay is not apparent. This qualitative result is supported by calculating the correlation coefficient $r_{t_s,I}$, which yields -0.013 and 0.187 for data sets at 80 eV and 93 eV XUV photon energy.

Impact of the experimental instrumentation on streaking delays

In Fig. 6.14, the plotted intensity is extracted from the streaking trace resulting from the neon 2p emission. A complementary analysis, where the intensity is retrieved from the streaking trace of photoemission from the ethyl iodide 4d shell, reveals similar correlation coefficients yielding -0.100 and 0.175 for measurements with XUV photons of 80 eV and 93 eV. However, absolute values of intensities retrieved from the ethyl iodide 4d streaking traces are found to be larger by a factor of 2-3 in comparison to intensities extracted from the neon 2p emission. This finding is notable, since electrons emitted from both targets experience the same NIR laser field, for which the identical NIR intensities should be retrieved. However, the electrostatic lens of the TOF detector, which is employed to enhance the signal strength in all measurements, affects the obtained streaking amplitudes and thereby the results on the retrieved laser field intensity: by application of a positive lens voltage, the detectors acceptance angle is increased, where maximum values about 45° full opening angle, centered around laser polarization direction are achievable. Accordingly, the measurement signal is averaged over different emission directions. Since the streaking amplitude, i.e. the NIR induced shift in the photoelectron's kinetic energy, depends on the emission direction, measurements using the electrostatic lens of the detection system average over a broader range of streaking amplitudes. While maximum streaking amplitudes are exclusively obtained for photoemission parallel to the NIR laser polarization direction, averaging over emission directions can only reduce the detected streaking amplitude. Therefore, the extracted NIR laser intensity, as shown in Fig. 6.14, appears lower, since in the measurements the electrostatic lens increases the acceptance angle of detection.

Generally, while using the electrostatic lens, the acceptance angle depends on the photoelectron's kinetic energy. Therefore, count-rate amplification is only observed within a specific range of kinetic energies, which is chosen by setting an appropriate lens voltage. Here, in every ethyl iodide streaking measurement, the lens voltage is chosen to maximize the yield of pho-

toelectrons ionized from the neon 2p orbitals. Therefore, the acceptance angle for electrons of less kinetic energy, e.g. photoelectrons ionized from the ethyl iodide 4d shell, is smaller and the respective measurement signal is averaged only over few emission directions. Accordingly, the NIR intensities, retrieved from streaking traces of the ethyl iodide 4d orbitals, are expected to appear larger, as compared to the intensity, extracted from the neon streaking trace.

Since the electrostatic lens introduces an additional positive potential, the conversion from time-of-flights to kinetic energies depends on the respective lens voltage, where the full dependence is generally only obtained from electron trajectory simulations. The generic approach for the conversion from flight-time to energy, expressed in Eq. (6.5), considers the lens voltage only through the fitting parameter s. While the effect of the electrostatic lens is potentially oversimplified in the generic approach, streaking amplitudes could appear larger after the conversion to energy scale. However, since the binding potentials for the ethyl iodide valence band and ethyl iodide 4d orbitals are obtained in reasonable agreement with literature values, the applicability of the generic conversion procedure appears to be justified and flaws are expected to be of minor influence.

Spectral reshaping introduced by the electrostatic lens can affect the obtained streaking amplitudes and subsequently the retrieved NIR intensities. More important for the scope of this experiment is to elaborate the influence of the electrostatic lens on the retrieved photoionization delays. The previous work by Schultze *et al.* revealed that spectral reshaping by an arbitrary, generally energy-dependent function has no effect on the detected photoionization delays [14]. However, the latter finding was demonstrated to become invalid in the presence of chirped attosecond pulses [81]: here, the energy-dependent amplification profile of an electrostatic lens adds a systematic error on the extracted photoionization delays, which is in general additionally dependent on the method employed to extract the streaking traces from associated spectrograms. Other effects on the photoelectron's spectral shape, e.g. an energy-dependent photoionization cross-section of the target, act in a similar manner and change the photoionization delays systematically in the presence of chirped attosecond pulses. For the present experiment, a FROG-CRAB analysis of streaking spectrograms on pure neon, which are acquired prior and subsequent to measurements on ethyl iodide, reveal a negligible chirp of employed XUV attosecond pulses at both central energies of 80 eV and 93 eV. The streaking spectrograms on ethyl iodide, e.g. in Fig. 6.9 (a), support this finding qualitatively, since streaking trace outlines do not show the typical features of spectral thinning or broadening during the streaking process, as would be common for chirped attosecond pulses (see also Fig. 2.5 (b) and Chap. 2.3). Therefore, the obtained streaking delay difference between photoionization from the ethyl iodide 4d shell and neon 2p orbitals is found to be insensitive to spectral reshaping, while systematic errors are assumed to be absent.

Comparison to streaking delays from semi-classical calculations

For the comparison between experimentally obtained streaking delays and theoretical predictions, illustrated in Fig. 6.15, the semi-classical approach, which considers the influence of the NIR laser field, is employed. Since experimental results represent the relative streaking delay, the difference between individual streaking delays of ethyl iodide 4d and neon 2p orbitals, as shown in Fig. 6.6 (b) is calculated from theoretical simulations. Herein, the electronic ground states of ethyl iodide and neon are calculated by different methods based on the Hartree-Fock (SC-HF) and configuration interaction singles (SC-CIS) description. While the experimental

finding at XUV photon energy of 93 eV is almost ideally predicted by theoretical simulations, the result for 80 eV is considerably larger as expected from semi-classical calculations. However, given the large error bar of the measurement, theory and experiment do still overlap within their respective standard deviation. The latter is valid for both methods, employed to calculate the electronic ground state of streaking targets, which yield generally only a small variation in the streaking delay difference between photoionization from the ethyl iodide 4d and neon 2p orbitals over the entire considered XUV photon energy range.

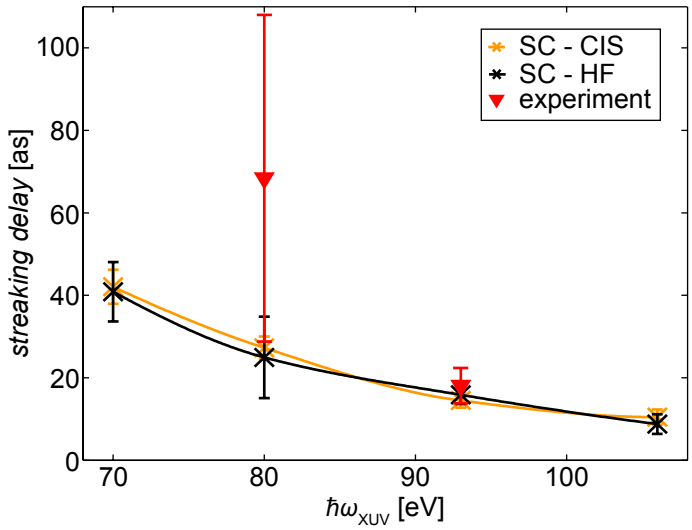

Figure 6.15: Comparison of streaking delay differences. Experimental results on streaking delay differences between ethyl iodide 4d and neon 2p orbitals, together with the respective error bars, are illustrated as red solid triangles and compared to results from theoretical predictions. The latter are based on the semi-classical approach, where electronic ground states of ethyl iodide and neon are calculated using the Hartree-Fock and configuration interaction singles description.

While experimental results are to a large extent in reasonable agreement with semi-classical calculations, the comparison to different theoretical methods, which typically reveal the Eisenbud-Wigner-Smith delay, is inadmissible. However, together with the results from semi-classical calculations, the EWS-delay can be directly retrieved from experimental data. Therefore, the theoretically obtained streaking delay t_S^{Ne} for photoionization from the neon 2p orbitals, illustrated as red solid line in Fig. 6.6, is added to the experimental results, which hereafter represent the pure streaking delay for photoionization from the ethyl iodide 4d shell. As expressed in Eq. (2.51), the latter still incorporates the NIR induced Coulomb-laser-coupling delay t_{CLC}. The CLC-delay can be calculated classically according to Eq. (2.49), where the results are illustrated as inset in Fig. 6.7. After subtraction of the CLC delay, the results describe the Eisenbud-Wigner-Smith delay, obtained from experimental data.

Comparison of Eisenbud-Wigner-Smith delays

The comparison of EWS delays, illustrated in Fig. 6.16, yields a similar qualitative set of results based on different theoretical approaches and experimental data, where EWS-delays are positive within the entire investigated energy range between 70 eV and 106 eV. In agreement

with experimental data, the EWS-delays are found to increase with decreasing XUV photon energy, as predicted by all considered theoretical methods. The qualitative coincidence is especially remarkable given the different levels of theories, where EWS-delays calculated with the semi-classical approach (SC-HF and SC-CIS) and quantum scattering theory (QuScat) consider the entire ethyl iodide molecule, whereas (TD)LDA simulations are exclusively performed on atomic iodine. However, especially at low XUV photon energies, the quantitative agreement between different theoretical methods is poor. In contrast, in the high XUV photon energy regime, results from individual methods differ by less than 25 as and are found to agree reasonably well with experimental findings.

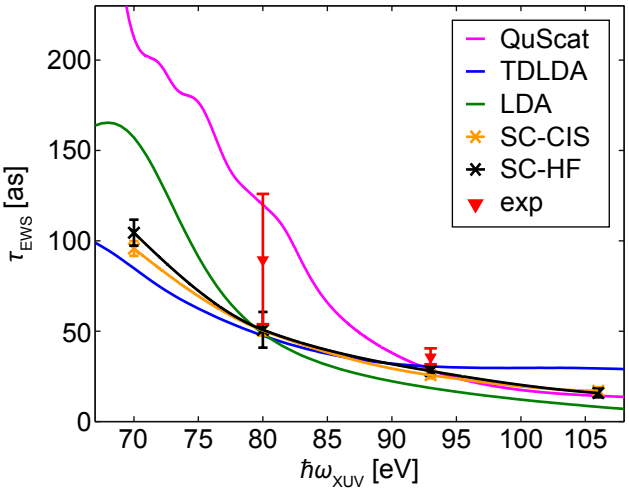

Figure 6.16: Comparison of EWS delays. Simulations on the EWS-delays for photoionization from the ethyl iodine 4d orbitals are based on different theoretical approaches, including quantum scattering theory (QuScat) and semi-classical Wigner method (SC-HF, SC-CIS), while (TD)LDA simulations are performed on atomic iodine. For semi-classical calculations the molecular orbital ground state is retrieved from Hartree-Fock and configuration interaction singles schemes. The weighted average values from measurements at XUV photon energies of 80 eV and 93 eV are illustrated as red solid triangles.

Theoretical results on the full ethyl iodide molecule, i.e. quantum scattering theory (QuScat) and semi-classical calculations (SC-HF and SC-CIS), are found to be almost identical for XUV photon energies larger than 93 eV. Here, the experimental result on the EWS-delay is slightly larger than expected from theory, but, under consideration of the respective error bars, is still in accordance with theoretical predictions. At low XUV photon energies, EWS delays obtained from quantum scattering theory are much larger as compared to semi-classical calculations, where the difference at 80 eV XUV photon energy yields around 70 as. At the current stage the discrepancy of both methods in the low energy regime remains elusive, especially since EWS-delays are generally independent of the NIR laser field, while its inclusion is the major conceptual difference between both theoretical methods. Given the large error bar at low XUV photon energy, the experimental results overlap simultaneously with either theoretical prediction, therefore no further conclusions can be drawn from the measurements on the validity of the theoretical models. However, it should be emphasized that EWS-delays obtained from experimental data and semi-classical simulations rely on the calculation of Coulomb-laser-coupling delays by the expression given in Eq. (2.49), which is obtained as

classical analogue to a fully quantum mechanical calculation of photoionization from atomic hydrogen [137]. Most generally, the magnitude of t_{CLC} depends on the final state of the emitted photoelectron, specifically its angular momentum. But, as illustrated by Dahlström *et al.*, the difference of Coulomb-laser-coupling delays between distinct final states is considerably small, especially with increasing excess energy of photoelectrons [306]. Accordingly, the latter effect is potentially not strong enough to explain the magnitude of the quantitative mismatch between results from quantum scattering theory and the semi-classical approach. Another source for quantitative discrepancies could derive from different basis sets in the calculation of the ethyl iodide ground state. While the agreement between theoretical predictions and experimental results on the binding potential of the considered orbitals is typically a strong justification for the application of a specific basis set, photoionization delays are highly sensitive to the detailed spatial dependence of the orbital potential landscape. Additionally, since photoelectrons traverse the molecule, photoionization delays can be affected significantly by multiple molecular orbitals. Both is not necessarily reflected by the pure binding potential of orbitals, from where photoelectrons are ionized by the XUV attosecond laser field. For unambiguous comparability of different methods, ideally identical basis sets are employed in both theoretical approaches. Moreover, additional features, e.g. cross section and asymmetry parameter, could be retrieved from calculations using different basis sets and compared to experimental findings, which would further support the justification of a specific basis set.

While molecular orbitals can affect the photoionization delays, the comparison between experimental data and results of TDLDA/LDA calculations is difficult, since the latter do not consider ethyl iodide but only atomic iodine. Nevertheless, the comparison to TDLDA and LDA simulations is instructive to resolve generic effects of electron-electron interactions on photoionization delays in the presence of giant dipole resonances. Previous calculations on xenon by Magrakvelidze *et al.*, employing the (TD)LDA approach, predict negative EWS-delays for electrons ionized from the 4d shell by XUV photon energies in vicinity of the GDR [38]. This finding is attributed to a repulsive potential, due to the collective many-electron interaction. Currently, this explanation is still conversely debated, since complementary theoretical calculations on xenon using the random phase approximation with exchange (RPAE) approach, which in principle also considers collective electron excitations, obtain positive EWS-delays [37]. Only recently, Magrakvelidze *et al.* published (TD)LDA calculations on iodine, which yield negative EWS-delays in the XUV photon energy range of the giant dipole resonance (see also next section and Fig. 6.18), in qualitative agreement with their results on xenon [300]. In contrast, the presented simulations in this thesis based on the LDA and TDLDA approach do not predict negative photoionization delays for emission from the 4d orbitals of atomic iodine. This finding is supported by experimental results on ethyl iodide, where, however, the generic repulsive potential of many-electron correlation is possibly concealed by attractive potentials of molecular orbitals, which are traversed by the photoelectron during the ionization process. Experimentally obtained photoionization delays appear to yield better agreement with predictions from TDLDA simulations rather than LDA calculations. However, since for the respective XUV photon energies of 80 eV and 93 eV the difference in EWS-delays between TDLDA and LDA calculations is small, the current data set of measurements on ethyl iodide does not allow to reveal unambiguously the influence of collective effects on the EWS-delay of atomic iodine.

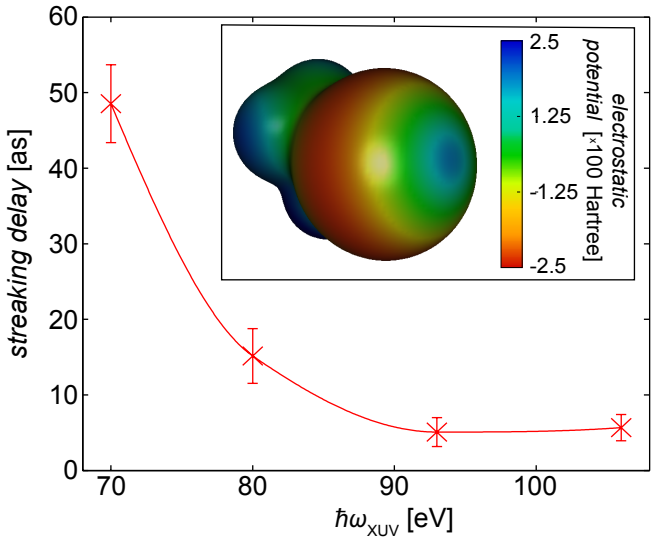

Figure 6.17: Molecular influence on streaking delays. Orientation averaged streaking delay for ethyl iodide relative to atomic iodine, which are both obtained from semi-classical calculations, where the electronic ground state is modeled based on the configuration interaction single approach. As inset, the electrostatic potential around the ethyl iodide molecule is illustrated on a surface of constant electron density, where the positive electrostatic potential at the pole of the iodine atom is referred to as σ-hole. Courtesy of L. Ortmann and T. Zimmermann.

Influence from molecular constituents

Calculations which consider the full ethyl iodide molecule are found to differ from either DFT simulation on atomic iodine, where the discrepancy is attributed to the molecular constituents of the iodine atom. The influence of the ethyl group became already apparent from the analysis of orientation dependence of streaking delays, illustrated in Fig. 6.8, where the largest relative and absolute streaking delays are observed for photoemission along the carbon-iodine bond, directed away from the molecule. This finding indicates an attractive potential in vicinity of the iodine atom, as depicted in the inset to Fig. 6.17. The positive electrostatic potential, referred to as σ-hole [307], is typically observed for covalent binding between carbon and halogen atoms: since the electronic structure of halogens involves one missing electron to a fully occupied p-shell, one of the three degenerated p-orbitals is only half-filled. The single electron located in the respective semi-filled p-orbital resides predominantly between the carbon and iodine molecule inside the covalent binding orbital, whereas the opposed p-orbital lobe is depleted, which gives rise to the observed positive electrostatic potential [308]. Accordingly, for photoelectron trajectories guided through the σ-hole, larger photoionization delays can be expected, due to the attractive potential. Despite the strong directional character of the σ-hole, simulations confirm that larger photoionization delays are even expected after orientation averaging. The resulting streaking delay difference between photoionization from the ethyl iodide molecule and atomic iodine, obtained based on the semi-classical approach, is illustrated in Fig. 6.17. The electronic ground states of ethyl iodide and atomic iodine are calculated using the CIS method. While for large excess energies, almost no difference is obtained, the σ-hole's attractive potential yields about 50 as larger photoionization delays with respect to atomic iodine at low photoelectron kinetic energies. Accordingly, the strong increase of experimentally obtained photoionization delays at low XUV photon energies can

be attributed to the occurrence of a positive potential around the iodine atom, referred to as σ-hole.

6.6 Conclusion and Outlook

In this chapter, streaking measurements on the ethyl iodide molecule are introduced, which represent the first successful application of the attosecond streaking technique on molecular targets. From the measurements, which are carried out at different XUV photon energies, the photoionization delay for electrons emitted from the ethyl iodide 4d shell with respect to photoemission from neon 2p orbitals is retrieved. Complementary to experimental measurements, simulations are performed based on different theoretical approaches, i.e. semi-classical calculations, quantum scattering and density functional theory. While the semi-classical simulations take the full ethyl iodide molecule together with influences of the streaking method on the retrieved photoionization delays into account, quantum scattering theory does not include effects of the measurement technique but is still performed on the full ethyl iodide molecule. In contrast, the density functional theory approach, precisely LDA and TDLDA calculations, considers exclusively atomic iodine without influences from the measurement method. For direct comparability between different theoretical methods and experimental data, the Eisenbud-Wigner-Smith delay is extracted from the data sets. Despite the disparity of individual theoretical methods, their qualitative behavior is identical, where EWS-delays increase with decreasing XUV photon energy, as supported by experimental findings. While the comparison of cross sections and asymmetry parameters, obtained from (TD)LDA calculations, with experimental literature values indicates that collective effects play a crucial role in photoionization from the iodine 4d shell, the generic behavior of negative photoionization delays, predicted for xenon [38] and atomic iodine [300], is not confirmed by the presented experimental results on ethyl iodide. Even under consideration of the molecule's potential landscape, the EWS-delays yield positive values within the entire investigated energy range. However, further experiments (see next paragraph below) are highly recommended, in order to draw an unambiguous conclusion whether collective electron effects result generally in negative photoionization delays.

From the analysis of experimental and theoretical results, the molecular surrounding is found to affect the obtained EWS delays. Typically, the influence of the molecular potential landscape is highly anisotropic, where in case of ethyl iodide a positive potential is located at the pole of the iodine atom, facing away from the ethyl group. The positive potential, referred to as σ-hole, features strictly positive EWS delays, in particular for small photoelectron energies, i.e. low XUV photon energy. Despite the strong anisotropy, the orientation averaged photoionization delay, as obtained from the presented streaking measurements, is found to be considerably larger in ethyl iodide as compared to iodine atoms. This finding is supported by experimental results, where EWS delays for ethyl iodide increase significantly at low photoelectron energies.

Given the high importance of halogen bonds and accordingly the σ-holes in chemical biology [309, 310], drug design [311] and catalysis [312], further photoionization experiments are instructive to resolve magnitude and spatial dependence of the positive potentials and ultimately, to shed light on its dynamical properties. Since the σ-hole in case of pentafluoroethyl iodide (PFI) is predicted to yield a stronger positive potential, larger photoionization

delays can be expected, which holds even for orientation averaged measurements. Accordingly, streaking experiments on PFI, complementary to the above presented ethyl iodide measurements, would likewise allow to test different theoretical models.

Superior to averaging measurement approaches, orientation-resolved schemes allow to obtain additionally information on the anisotropy. However, the latter demands to control the molecule's orientation/alignment with respect the NIR laser field polarization direction, which can be achieved using strong pico- or nanosecond laser pulses [313]. Stereographic measurements, where the streaking delay difference between photoelectrons emitted in opposite directions from ethyl iodide or pentafluoroethyl iodide is detected (exemplary illustrated for results from theoretical calculations in Fig. 6.8) would offer to simplify the experiments, since no additional reference streaking target, e.g. neon gas, is necessary. Besides, Coulomb-laser coupling effects can be neglected, since the latter influences both emission directions in the same manner, for which the delay-difference remains unaffected.

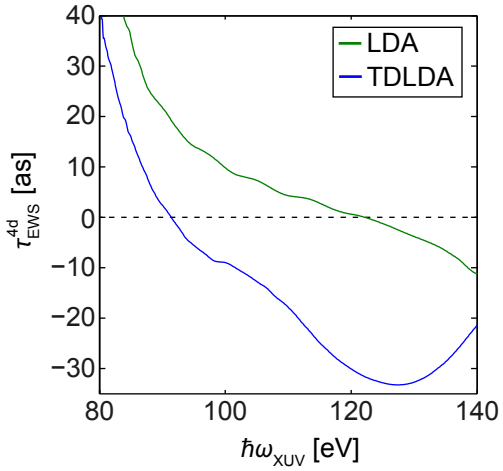

Figure 6.18: Calculated EWS delay for photoionization from atomic iodine using the DFT approach. While the LDA calculations (solid green line), which do not consider collective electron effects are predominantly positive over a wide range of XUV photon energies, the TDLDA results (solid blue line) yield a distinct minimum around 130 eV XUV photon energy. Future experiments in the energy range of minimum photoionization delays should be capable to reveal the generic influence of collective electron effects on photoionization delays unambiguously. Reprinted from Ref. [300].

Apart from measurements on the examination of the σ-hole, the generic effect of collective electron interactions on the photoionization delays remains still elusive. While the presented experimental and theoretical results revealed positive photoionization delays in the presence of giant dipole resonances, recent theoretical studies by Magrakvelidze *et al.*, illustrated in Fig. 6.18, indicate negative EWS-delays for photoionization from iodine 4d orbitals [300]. Since the latter are predicted to be minimal for XUV photon energies in the range of 130 eV, streaking experiments at this XUV photon energy regime are highly appreciated to resolve the discrepancy.

Chapter 7

Summary

In this thesis several experiments are presented, which are conducted to shed light on the dynamics of collective electron phenomena in nanostructures and molecules. The pump-probe measurements on nanoscale targets are performed using the attosecond beamline AS-5, hosted at the Max Planck Institute for Quantum Optics, where in particular the temporal dynamics of surface plasmon polaritons are in the focus of performed experiments. The motivation for time-resolved studies on SPPs derives from their vast potential in technological applications, where surface plasmon polaritons, due to their inherent property of light confinement to sub-wavelength dimensions, are considered for wave guide applications in future information technological developments. The samples, which are investigated in the present thesis, comprise a nanostructured grating geometry, where the SPPs are excited upon illumination by a few-cycle laser pulse, centered in the near-infrared around 750 nm and referred to as pump beam. From the grating, SPPs are guided along a tapered nanowire, towards a sharp apex of 5 - 10 nm radius. At the apex, the SPP electric field is superimposed with a second laser pulse of variable delay, referred to as probe beam, which constitutes a direct replica of the pump beam. The superposition of SPP and laser probe field facilitates multi-photon ionization from the super-tip apex, where the delay-dependent photoelectron yield holds information on the temporal properties of the SPP electric field. The experimental results demonstrate for the first time that ultrashort SPP pulses, generated at nanostructured gratings, engraved on macroscopic surfaces, can be effectively transferred to nanowire geometries: from the measurements minimum SPP pulse durations of 7.4 fs are obtained at the super-tip apex, which represent to date the shortest reported duration of SPP pulses on gold nanostructures. Given the central wavelength around 630 nm, the SPP pulses comprise less than four optical cycles, which constitutes almost the few-cycle regime. These findings emphasize the high potential of SPPs in future information technological applications. Based on the respective experimental setup and target geometry, the SPP group velocity is extracted from the results, which appears reduced as compared to theoretical simulations, which are performed complementarily to experimental studies. It is emphasized, that the applied method, i.e. an SPP-NIR cross correlation in non-collinear geometry, has not been reported in literature. The main advantage in this approach is the capability to detect SPP electric fields, which are too weak to facilitate multi-photon ionization without presence of the probe laser field. However, the incapability to obtain sub-cycle resolution on nanoscale electric fields constitutes the major weak point of the cross-correlation approach, where instead the attosecond streaking technique can be employed.

The expansion of the attosecond streaking method, which was demonstrated on atomic

and solid state systems, to nanostructured target geometries was so far only considered in multiple theoretical calculations. The first experimental realization of sampling of nanoscale electric fields with attosecond precision was demonstrated only recently in measurements performed in the framework of this thesis. Here, the attosecond streaking technique is applied to tapered Au nanowires, where an electric near field builds up in vicinity of the sample surface upon illumination by NIR few-cycle pulses. The near field is subsequently probed by photoelectrons, which are excited from the nanotaper by a synchronized attosecond XUV laser pulse with variable delay. From the experiment a phase shift of around (-240 ± 155) as is obtained for the near field with respect to the incident NIR laser field. This finding is supported by classical trajectory calculations. Based on detailed theoretical simulations, spatial averaging is found to play a minor role for the respective target geometry, since phase shifts are found to be only weakly position depending. The count-rate analysis reveals that photoelectrons are mainly ionized from the nanotaper shank, while photoionization from the nanotaper apex is not resolvable with the current setup. However, future implementations on the infrastructure can help to overcome such deficiencies. Based on general considerations and theoretical calculations, generic prerequisites on the experimental setup in dependency of the target geometry can be formulated to facilitate streaking experiments on nanoscale electric field.

While the pump-probe measurements on nanostructured targets are performed at an existing infrastructure, attosecond streaking experiments on collective electron effects in molecular targets are conducted at the attosecond science laboratory (ASL) in Riyadh, where the entire beamline facility was established and subsequently calibrated within the scope of this thesis. The measurements on ethyl iodide molecules aim towards the investigation of photoionization delays in the presence of collective electron effects, featured by a giant-dipole resonance in the photoionization cross-section from the ethyl iodine 4d orbitals. Comparative studies of photoionization delays in the presence of collective electron effects are largely absent, where only few reports on atomic xenon exist, while open-shell systems like iodine were not yet considered. The analysis of streaking experiments on ethyl iodide at different XUV photon energies yields pure positive photoionization delays, which is supported by three distinct theoretical simulations, conducted within the framework of this thesis, where different levels of theory, i.e. semi-classical, quantum scattering and *ab-initio* calculations, are considered. The experimental findings help to resolve discrepancies in existing theoretical calculations, which reveal contradictory qualitative dependence of photoionization delays in the presence of collective electron excitations. The large increase of photoionization delays with decreasing XUV photon energy, as obtained from the streaking measurements, results from the characteristic potential landscape of the ethyl iodide molecule, where the halogen bond induces a localized positive potential at the iodine atom, referred to as σ-hole. Together with theoretical simulations it is demonstrated that the presence of the σ-hole yields increased photoionization delays even for measurements, where the result is averaged over all emission directions. Given the anisotropic character of the molecular potential landscape, streaking measurements on aligned molecules are one possibility to study the influence of the σ-hole on the intra-molecular electron dynamics.

Appendix A

Geometrical Considerations of Cross-Correlation Measurements

To extract the SPP propagation time from the NIR-SPP cross-correlation measurements, intrinsic differences between the optical path lengths of NIR pump and probe beams must be considered. Since the AS-5 double-mirror setup is not designed as gimbal mount, the optical path length differences between pump and probe beam are not exclusively determined by the sample geometry but also from the double-mirror mount: its three point suspension yields a displacement in beam propagation direction between inner and outer mirror which depends on the tip/tilt angles. In the following, we will derive the optical path length difference between NIR pump and probe beam for different separations Δy.

The geometry of the experimental setup and sample is displayed in Fig. A.1 for the viewpoints parallel to y-axis (a) and x-axis (b). As illustrated in (a) the full double mirror setup, i.e. inner and outer mirror, is tilted downwards to feature a displacement $D = 3.5\,\mathrm{mm}$ between the mirror's focal spots and the incoming beam at a distance f_{out} from inner/outer mirror. During all measurements, the sample is positioned such, that the super-tip apex is placed at the focus of the outer mirror. Instead of the specified focal length, we performed numerical simulation with included spherical aberration effects to estimate the focal length of the outer mirror in the experiment. From that we find a reduction by 200 µm with respect to the specifications, yielding a focal length of $f_{\mathrm{out}} = 2.3\,\mathrm{mm}$, which represents the distance between sample and outer mirror.

D [mm]	f_{out} [cm]	L[cm]	δ [°]	H [µm]
3.5	2.3	4.9	21	1.49

Table A.1: Input parameters for calculation of optical path length differences and expected theoretical delays.

To calculate the optical path length difference between pump and probe beams, we refer to the illustration of the experimental geometry orthogonal to the yz-plane in Fig. A.1 (b). Under consideration of the up/down-tilt of the double-mirror in x-direction, in the projection to the yz-plane, all lengths appear shorter by a factor of $\cos(\alpha)$. The angle α is calculated

from the displacement D and the focal length f_{out} as

$$\alpha = \arcsin\left(\frac{D}{f_{\text{out}}}\right) \quad . \tag{A.1}$$

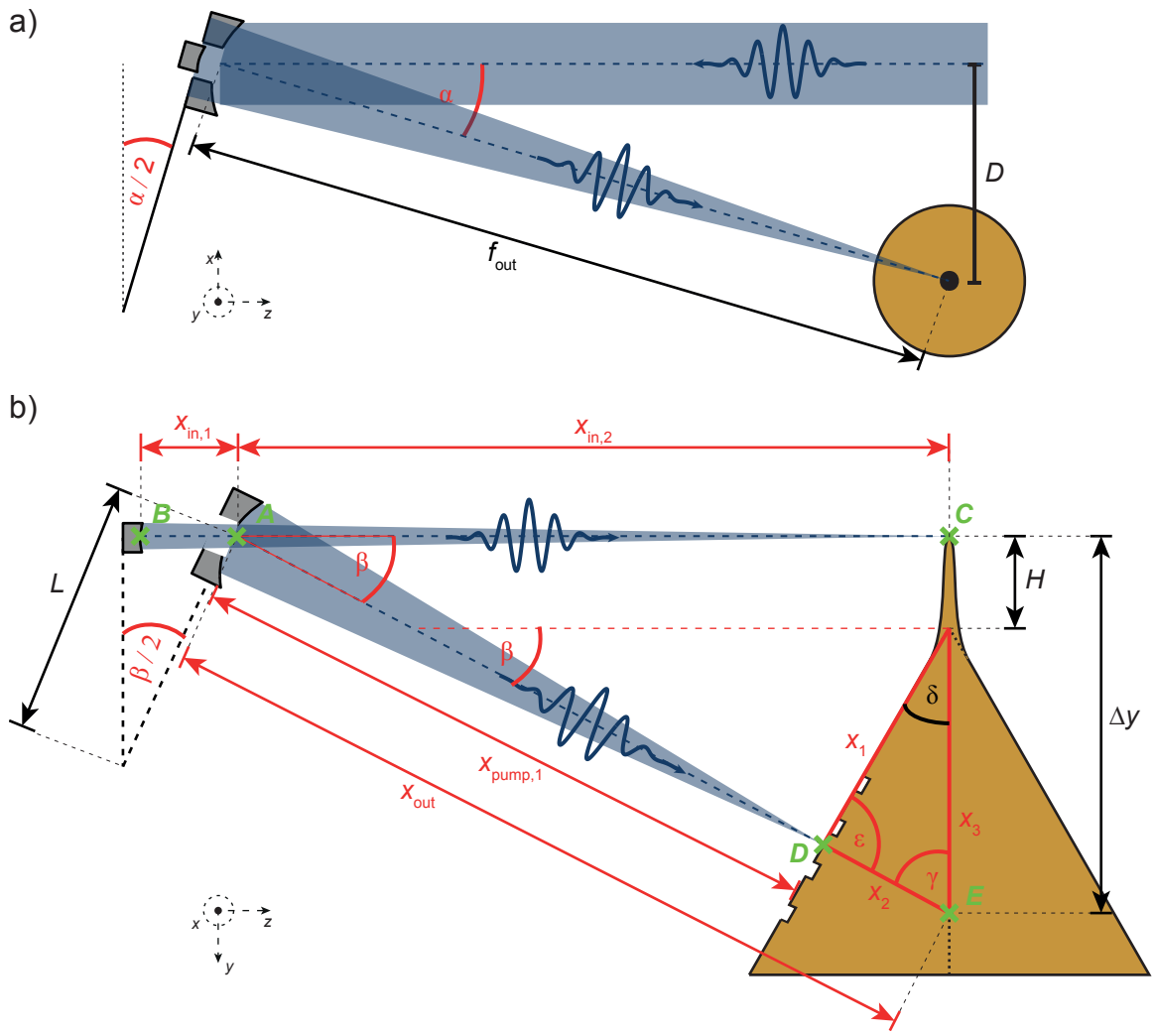

Figure A.1: Evaluation of the optical path lengths of NIR pump and probe beams in cross-correlation measurements. The illustrations displays the experimental geometry of super-tip sample and double-mirror interferometer in the xz-plane **(a)** and yz-plane **(b)**. Input values, listed in Tab. A.1 are color-coded in black, while auxiliary parameters are shown in red. To visualize the pump and probe beam paths, selective points, labeled from A to E are marked by green crosses. Adapted from [148].

The probe beam path can be separated into three individual components, i.e. the propagation along $\overrightarrow{AB}$, $\overrightarrow{BA}$ and $\overrightarrow{AC}$. It should be noted, that the subsection $\overrightarrow{AB}$ is part of the incoming beam path and is therefor not tilted by α in the xz-plane. In contrast, the sections $\overrightarrow{BA}$ and $\overrightarrow{AC}$ represent the probe beam after reflection from the inner mirror, for which the tilting by α has to be taken into account. The first part evaluates to

$$\overrightarrow{AB} = x_{\text{in},1} = L \cdot \sin\left(\frac{\beta}{2}\right) \quad , \tag{A.2}$$

where L describes the length of mirror holder with $L = 4.9 \pm 0.1\,\mathrm{cm}$. The angle β derives from the displacement Δy and the projected focal length x_{out} as

$$\beta = \arcsin\left(\frac{\Delta y}{x_{\mathrm{out}}}\right) = \arcsin\left(\frac{\Delta y}{f_{\mathrm{out}} \cdot \cos(\alpha)}\right) \quad . \tag{A.3}$$

Similarly, the second and third part of the probe beam path are evaluated, for which the up/down-tilting of the double-mirror must be taken into account

$$\overrightarrow{BA} = \frac{x_{\mathrm{in},1}}{\cos(\alpha)} \qquad \overrightarrow{AC} = \frac{x_{\mathrm{in},2}}{\cos(\alpha)} \quad , \tag{A.4}$$

where $x_{\mathrm{in},2} = x_{\mathrm{out}} \cdot \cos(\beta)$ is fully described by the projected focal length x_{out} and angle β. The optical beam path of the probe beam x_{probe} is then given as the sum of all three contributions

$$x_{\mathrm{probe}} = \overrightarrow{AB} + \overrightarrow{BA} + \overrightarrow{AC} \quad . \tag{A.5}$$

The calculation of the pump beam path x_{pump}, defined as the length $\overrightarrow{AD}$, demands the definition of several auxiliary parameters, namely the angles γ, ϵ and the lengths x_1, x_2 and x_3. Since the sum of angles in an arbitrary triangle yields 180°, γ and ϵ evaluate to

$$\gamma = 180^\circ - 90^\circ - \beta = 90^\circ - \beta \tag{A.6}$$

$$\epsilon = 180^\circ - \delta - \gamma = 90^\circ - \delta + \beta \quad , \tag{A.7}$$

where $\delta = 21^\circ$ represents the half opening angle of the pyramidal cone of the super-tip sample. The length x_3 is given by the difference between displacement Δy and height of the super-tip H. Based on the law of sines, the length x_2 is extracted as

$$x_2 = x_3 \cdot \frac{\sin(\delta)}{\sin(\epsilon)} = \frac{\sin(\delta)}{\sin(\epsilon)} \cdot (\Delta y - H) \quad . \tag{A.8}$$

Now the unprojected optical path length of the pump beam can be calculated as the difference between x_{out} and x_2, divided by the factor $cos(\alpha)$

$$x_{\mathrm{pump}}^{\mathrm{SPP}} = \frac{x_{\mathrm{out}} - x_2}{\cos(\alpha)} = \frac{\Delta y}{\sin(\beta)\,\cos(\alpha)} - \frac{\sin(\delta)}{\sin(\epsilon)\,\cos(\alpha)} \cdot (\Delta y - H) \quad . \tag{A.9}$$

The optical path length difference for the NIR-SPP cross-correlation measurements is hereafter ultimately calculated by subtracting Eq. (A.9) from Eq. (A.5). Dividing the resulting path length difference with the speed of light yields the intrinsic temporal delay Δt_{int} of the double mirror setup in SPP measurement configuration. In a similar way, the analysis of optical path length difference between NIR pump and probe beam in the reference measurements yields a theoretical prediction for the temporal shift Δt_{ref}.

The delay shift $\Delta t_{\mathrm{ref}}^{\mathrm{SPP}}$ represents the temporal delay between the NIR probe and pump pulse in SPP measurement configuration at the position of the super-tip apex. Again, the optical path length of the NIR probe pulse is unchanged compared to above, while the path length of the NIR pump pulse results as

$$x_{\mathrm{pump}}^{\mathrm{SPP,\,ref}} = \frac{\cos(\beta) \cdot x_{\mathrm{in},2}}{\cos(\alpha)} = \cos^2(\beta)\frac{x_{\mathrm{out}}}{\cos(\alpha)} = \cos^2(\beta) \cdot f_{\mathrm{out}} \quad . \tag{A.10}$$

Since the absolute values of β-angles are miniscule for all separations Δy in our experiment, the optical path length of the NIR pump beams in SPP and reference measurements, i.e. $x_{\text{pump}}^{\text{SPP, ref}}$ and $x_{\text{pump}}^{\text{ref}}$, is almost identical. Accordingly, the difference between Δt_{ref} and $\Delta t_{\text{ref}}^{\text{SPP}}$ is found to be on the sub-femtosecond timescale.

The SPP propagation length l_{SPP} calculates as the sum of the super-tip height H and the auxiliary parameter x_1 as defined in Fig. A.1. Again, we employ the law of sines to calculate the value of x_1:

$$x_1 = \sin(\gamma) \cdot \frac{x_3}{\sin(\epsilon)} = \sin(\gamma) \cdot \frac{\Delta z - H}{\sin(\epsilon)} \quad . \tag{A.11}$$

Based on the input parameters, resulting from SEM micrographs or dimensional measurements of the experimental setup as listed in Tab. A.1, the respective delay shifts and SPP propagation lengths can be calculated for different displacements Δy between inner and outer mirror focal spots. The results are listed below in Tab. A.2.

Δy [µm]	Δt_{ref}[fs]	$\Delta t_{\text{ref}}^{\text{SPP}}$[fs]	Δt_{int}[fs]	l_{SPP} [µm]
4	28.91	28.91	32.16	4.18
5	36.14	36.14	40.68	5.25
6	43.36	43.37	49.20	6.32
7	50.59	50.60	57.72	7.39
8	57.82	57.82	66.24	8.46
9	65.04	65.05	74.76	9.53
10	72.27	72.28	83.28	10.60
12	86.72	86.74	100.32	12.75
13	93.94	93.97	108.84	13.82

Table A.2: Theoretical delay values and SPP propagation lengths, calculated from the experimental setup and sample geometry.

Bibliography

[1] P. Corkum and F. Krausz. Attosecond science. *Nature Physics*, 3(6):381–387, 2007.

[2] A. Scrinzi, M. Y. Ivanov, R. Kienberger, and D. M. Villeneuve. Attosecond physics. *Journal of Physics B: Atomic, Molecular and Optical Physics*, 39(1):R1, 2005.

[3] F. Krausz and M. Ivanov. Attosecond physics. *Reviews of Modern Physics*, 81(1):163, 2009.

[4] M. Hentschel, R. Kienberger, C. Spielmann, G. A. Reider, N. Milosevic, T. Brabec, P. B. Corkum, U. Heinzmann, M. Drescher, and F. Krausz. Attosecond metrology. *Nature*, 414(6863):509–513, 2001.

[5] M. Schultze, A. Wirth, I. Grguras, M. Uiberacker, T. Uphues, A. J. Verhoef, J. Gagnon, M. Hofstetter, U. Kleineberg, E. Goulielmakis, and F. Krausz. State-of-the-art attosecond metrology. *Journal of Electron Spectroscopy and Related Phenomena*, 184(3):68–77, 2011.

[6] J. J. Macklin, J. D. Kmetec, and C. L. Gordon III. High-order harmonic generation using intense femtosecond pulses. *Physical Review Letters*, 70(6):766, 1993.

[7] P. M. Paul, E. S. Toma, P. Breger, G. Mullot, F. Augé, P. Balcou, H. G. Muller, and P. Agostini. Observation of a train of attosecond pulses from high harmonic generation. *Science*, 292(5522):1689–1692, 2001.

[8] J. Itatani, F. Quéré, G. L. Yudin, M. Y. Ivanov, F. Krausz, and P. B. Corkum. Attosecond streak camera. *Physical Review Letters*, 88(17):173903, 2002.

[9] R. Kienberger, E. Goulielmakis, M. Uiberacker, A. Baltuska, V. Yakovlev, F. Bammer, A. Scrinzi, T. Westerwalbesloh, U. Kleineberg, U. Heinzmann, M. Drescher, and F. Krausz. Atomic transient recorder. *Nature*, 427(6977):817–821, 2004.

[10] E. Goulielmakis, V. S. Yakovlev, A. L. Cavalieri, M. Uiberacker, V. Pervak, A. Apolonski, R. Kienberger, U. Kleineberg, and F. Krausz. Attosecond control and measurement: lightwave electronics. *Science*, 317(5839):769–775, 2007.

[11] M. Drescher, M. Hentschel, R. Kienberger, M. Uiberacker, V. Yakovlev, A. Scrinzi, T. Westerwalbesloh, U. Kleineberg, U. Heinzmann, and F. Krausz. Time-resolved atomic inner-shell spectroscopy. *Nature*, 419(6909):803–807, 2002.

[12] M. Uiberacker, T. Uphues, M. Schultze, A. J. Verhoef, V. Yakovlev, M. F. Kling, J. Rauschenberger, N. M. Kabachnik, H. Schröder, M. Lezius, K. L. Kompa, H.-G.

Muller, M. J. J. Vrakking, S. Hendel, U. Kleineberg, U. Heinzmann, M. Drescher, and F. Krausz. Attosecond real-time observation of electron tunnelling in atoms. *Nature*, 446(7136):627–632, 2007.

[13] P. Eckle, M. Smolarski, P. Schlup, J. Biegert, A. Staudte, M. Schöffler, H. G. Muller, R. Dörner, and U. Keller. Attosecond angular streaking. *Nature Physics*, 4(7):565–570, 2008.

[14] M. Schultze, M. Fieß, N. Karpowicz, J. Gagnon, M. Korbman, M. Hofstetter, S. Neppl, A. L. Cavalieri, Y. Komninos, T. Mercouris, C. A. Nicolaides, R. Pazourek, S. Nagele, J. Feist, J. Burgdörfer, A. M. Azzeer, R. Ernstorfer, R. Kienberger, U. Kleineberg, E. Goulielmakis, F. Krausz, and V. S. Yakovlev. Delay in photoemission. *Science*, 328(5986):1658–1662, 2010.

[15] A. L. Cavalieri, N. Müller, T. Uphues, V. S. Yakovlev, A. Baltuška, B. Horvath, B. Schmidt, L. Blümel, R. Holzwarth, S. Hendel, M. Drescher, U. Kleineberg, P. M. Echenique, R. Kienberger, F. Krausz, and U. Heinzmann. Attosecond spectroscopy in condensed matter. *Nature*, 449(7165):1029–1032, 2007.

[16] S. Neppl, R. Ernstorfer, E. M. Bothschafter, A. L. Cavalieri, D. Menzel, J. V. Barth, F. Krausz, R. Kienberger, and P. Feulner. Attosecond time-resolved photoemission from core and valence states of magnesium. *Physical Review Letters*, 109(8):087401, 2012.

[17] L. Seiffert, Q. Liu, S. Zherebtsov, A. Trabattoni, P. Rupp, M. C. Castrovilli, M. Galli, F. Süßmann, K. Wintersperger, J. Stierle, G. Sansone, L. Poletto, F. Frassetto, I. Halfpap, V. Mondes, C. Graf, E. Rühl, F. Krausz, M. Nisoli, T. Fennel, F. Calegari, and M. F. Kling. Attosecond chronoscopy of electron scattering in dielectric nanoparticles. *Nature Physics*, 13(8):766–770, 2017.

[18] S. Neppl, R. Ernstorfer, A. L. Cavalieri, C. Lemell, G. Wachter, E. Magerl, E. M. Bothschafter, M. Jobst, M. Hofstetter, U. Kleineberg, J. V. Barth, D. Menzel, Burgdörfer, P. Feulner, F. Krausz, and R. Kienberger. Direct observation of electron propagation and dielectric screening on the atomic length scale. *Nature*, 517(7534):342–346, 2015.

[19] E. Dagotto. Correlated electrons in high-temperature superconductors. *Reviews of Modern Physics*, 66(3):763, 1994.

[20] E. P. Wohlfarth. The theoretical and experimental status of the collective electron theory of ferromagnetism. *Reviews of Modern Physics*, 25(1):211, 1953.

[21] M. Imada, A. Fujimori, and Y. Tokura. Metal-insulator transitions. *Reviews of Modern Physics*, 70(4):1039, 1998.

[22] M. Ossiander, F. Siegrist, V. Shirvanyan, R. Pazourek, A. Sommer, T. Latka, A. Guggenmos, S. Nagele, J. Feist, J. Burgdörfer, R. Kienberger, and M. Schultze. Attosecond correlation dynamics. *Nature Physics*, 13(3):280–285, 2017.

[23] R. Pazourek, J. Feist, S. Nagele, and J. Burgdörfer. Attosecond streaking of correlated two-electron transitions in helium. *Physical Review Letters*, 108(16):163001, 2012.

[24] P. Hommelhoff and M. Kling. *Attosecond nanophysics: From basic science to applications*. John Wiley & Sons, 2015.

[25] M. F. Ciappina, J. Pérez-Hernández, A. Landsman, W. Okell, S. Zherebtsov, B. Förg, J. Schötz, L. Seiffert, T. Fennel, T. Shaaran, T. Zimmermann, A. Chacón, R. Guichard, A. Zaïr, J. W. G. Tisch, J. P. Marangos, T. Witting, B. A, S. A. Maier, L. Roso, M. Krüger, P. Hommelhoff, M. F. Kling, F. Krausz, and M. Lewenstein. Attosecond physics at the nanoscale. *Reports on Progress in Physics*, 80(5):054401, 2017.

[26] S. A. Maier. *Plasmonics: fundamentals and applications*. Springer Science & Business Media, 2007.

[27] K. Li, M. I. Stockman, and D. J. Bergman. Self-similar chain of metal nanospheres as an efficient nanolens. *Physical Review Letters*, 91(22):227402, 2003.

[28] A. Schiffrin, T. Paasch-Colberg, N. Karpowicz, V. Apalkov, D. Gerster, S. Mühlbrandt, M. Korbman, J. Reichert, M. Schultze, S. Holzner, J. V. Barth, R. Kienberger, R. Ernstdorfer, V. S. Yakovlev, M. I. Stockman, and F. Krausz. Optical-field-induced current in dielectrics. *Nature*, 493(7430):70–74, 2013.

[29] M. Schultze, E. M. Bothschafter, A. Sommer, S. Holzner, W. Schweinberger, M. Fiess, M. Hofstetter, R. Kienberger, V. Apalkov, V. S. Yakovlev, M. I. Stockman, and F. Krausz. Controlling dielectrics with the electric field of light. *Nature*, 493(7430):75–78, 2013.

[30] E. Ozbay. Plasmonics: merging photonics and electronics at nanoscale dimensions. *Science*, 311(5758):189–193, 2006.

[31] F. Krausz and M. I. Stockman. Attosecond metrology: from electron capture to future signal processing. *Nature Photonics*, 8(3):205–213, 2014.

[32] F. Lépine, M. Y. Ivanov, and M. J. J. Vrakking. Attosecond molecular dynamics: fact or fiction? *Nature Photonics*, 8(3):195–204, 2014.

[33] X. Xie, K. Doblhoff-Dier, S. Roither, M. S. Schöffler, D. Kartashov, H. Xu, T. Rathje, G. G. Paulus, A. Baltuška, S. Gräfe, and M. Kitzler. Attosecond-recollision-controlled selective fragmentation of polyatomic molecules. *Physical Review Letters*, 109(24):243001, 2012.

[34] M. Huppert, I. Jordan, D. Baykusheva, A. von Conta, and H. J. Wörner. Attosecond delays in molecular photoionization. *Physical Review Letters*, 117(9):093001, 2016.

[35] G. Wendin. Collective resonance in the 4d10 shell in atomic Xe. *Physics Letters A*, 37(5):445–446, 1971.

[36] G. Wendin. Collective effects in atomic photoabsorption spectra. III. Collective resonance in the 4d10 shell inXe. *Journal of Physics B: Atomic and Molecular Physics*, 6(1):42, 1973.

[37] A. S. Kheifets. Time delay in valence-shell photoionization of noble-gas atoms. *Physical Review A*, 87:063404, 2013.

[38] M. Magrakvelidze, M. E.-A. Madjet, and H. S. Chakraborty. Attosecond delay of xenon 4d photoionization at the giant resonance and Cooper minimum. *Physical Review A*, 94(1):013429, 2016.

[39] J. C. Maxwell. A dynamical theory of the electromagnetic field. *Philosophical transactions of the Royal Society of London*, 155:459–512, 1865.

[40] J.-C. Diels and W. Rudolph. *Ultrashort laser pulse phenomena*. Academic press, 2006.

[41] H. P. Weber. Method for pulsewidth measurement of ultrashort light pulses generated by phase-locked lasers using nonlinear optics. *Journal of Applied Physics*, 38(5):2231–2234, 1967.

[42] M. Maier, W. Kaiser, and J. A. Giordmaine. Intense light bursts in the stimulated raman effect. *Physical Review Letters*, 17:1275–1277, 1966.

[43] C. Spielmann, L. Xu, and F. Krausz. Measurement of interferometric autocorrelations: comment. *Applied Optics*, 36(12):2523–2525, 1997.

[44] J.-C. M. Diels, J. J. Fontaine, I. C. McMichael, and F. Simoni. Control and measurement of ultrashort pulse shapes (in amplitude and phase) with femtosecond accuracy. *Applied Optics*, 24(9):1270–1282, 1985.

[45] K. Naganuma, K. Mogi, and H. Yamada. Time direction determination of asymmetric ultrashort optical pulses from second-harmonic generation autocorrelation signals. *Applied Physics Letters*, 54(13):1201–1202, 1989.

[46] C. Yan and J.-C. Diels. Amplitude and phase recording of ultrashort pulses. *Journal of the Optical Society of America B*, 8(6):1259–1263, 1991.

[47] J.-H. Chung and A. M. Weiner. Ambiguity of ultrashort pulse shapes retrieved from the intensity autocorrelation and the power spectrum. *IEEE Journal of Selected Topics in Quantum Electronics*, 7(4):656–666, 2001.

[48] D. J. Kane and R. Trebino. Characterization of arbitrary femtosecond pulses using frequency-resolved optical gating. *IEEE Journal of Quantum Electronics*, 29(2):571–579, 1993.

[49] C. Iaconis and I. A. Walmsley. Spectral phase interferometry for direct electric-field reconstruction of ultrashort optical pulses. *Optics Letters*, 23(10):792–794, 1998.

[50] L. Gallmann, D. H. Sutter, N. Matuschek, G. Steinmeyer, U. Keller, C. Iaconis, and I. A. Walmsley. Characterization of sub-6-fs optical pulses with spectral phase interferometry for direct electric-field reconstruction. *Optics Letters*, 24(18):1314–1316, 1999.

[51] A. Baltuška, M. S. Pshenichnikov, and D. A. Wiersma. Amplitude and phase characterization of 4.5-fs pulses by frequency-resolved optical gating. *Optics Letters*, 23(18):1474–1476, 1998.

[52] H. Raether. Surface plasmons on smooth surfaces. In *Surface plasmons on smooth and rough surfaces and on gratings*, pages 4–39. Springer, 1988.

[53] R. L. Olmon, B. Slovick, T. W. Johnson, D. Shelton, S.-H. Oh, G. D. Boreman, and M. B. Raschke. Optical dielectric function of gold. *Physical Review B*, 86(23):235147, 2012.

[54] A. Vial, A.-S. Grimault, D. Macías, D. Barchiesi, and M. L. de La Chapelle. Improved analytical fit of gold dispersion: Application to the modeling of extinction spectra with a finite-difference time-domain method. *Physical Review B*, 71(8):085416, 2005.

[55] M. I. Stockman. Nanofocusing of optical energy in tapered plasmonic waveguides. *Physics Review Letters*, 93:137404, 2004.

[56] E. Kretschmann and H. Raether. Radiative decay of non radiative surface plasmons excited by light. *Zeitschrift für Naturforschung A*, 23(12):2135–2136, 1968.

[57] A. Otto. Excitation of nonradiative surface plasma waves in silver by the method of frustrated total reflection. *Zeitschrift für Physik*, 216(4):398–410, 1968.

[58] B. Hecht, H. Bielefeldt, L. Novotny, Y. Inouye, and D. W. Pohl. Local excitation, scattering, and interference of surface plasmons. *Physical Review Letters*, 77(9):1889, 1996.

[59] S. Park, G. Lee, S. H. Song, C. H. Oh, and P. S. Kim. Resonant coupling of surface plasmons to radiation modes by use of dielectric gratings. *Optics Letters*, 28(20):1870–1872, 2003.

[60] S. T. Koev, A. Agrawal, H. J. Lezec, and V. A. Aksyuk. An efficient large-area grating coupler for surface plasmon polaritons. *Plasmonics*, 7(2):269–277, 2012.

[61] I. P. Radko, S. I. Bozhevolnyi, G. Brucoli, L. Martín-Moreno, F. J. García-Vidal, and A. Boltasseva. Efficiency of local surface plasmon polariton excitation on ridges. *Physical Review B*, 78(11):115115, 2008.

[62] G. Lévêque and O. J. F. Martin. Optimization of finite diffraction gratings for the excitation of surface plasmons. *Journal of Applied Physics*, 100(12):124301, 2006.

[63] M. I. Stockman, M. F. Kling, U. Kleineberg, and F. Krausz. Attosecond nanoplasmonic-field microscope. *Nature Photonics*, 1(9):539–544, 2007.

[64] H. Hertz. Über einen Einfluss des ultravioletten Lichtes auf die elektrische Entladung. *Annalen der Physik*, 267(8):983–1000, 1887.

[65] L. V. Keldysh. Ionization in the field of a strong electromagnetic wave. *Sov. Phys. JETP*, 20(5):1307–1314, 1965.

[66] F. V. Bunkin and M. V. Fedorov. Cold emission of electrons from the surface of a metal in a strong radiation field. *Sov. Phys. JETP*, 21(5):896–899, 1965.

[67] A. M. Perelomov, V. S. Popov, and M. V. Terent'ev. Ionization of atoms in an alternating electric field. *Sov. Phys. JETP*, 23(5):924–934, 1966.

[68] A. M. Perelomov, V. S. Popov, and M. Terent'ev. Ionization of atoms in an alternating electric field: II. *Sov. Phys. JETP*, 24(1):207–217, 1967.

[69] H. Sonnenberg, H. Heffner, and W. Spicer. Two photon photoelectric effect in Cs_3Sb_2. *Applied Physics Letters*, 5(5):95–96, 1964.

[70] F. H. M. Faisal. *Theory of multiphoton processes*. Springer Science and Business Media, 2013.

[71] A. Einstein. Über einen die Erzeugung und Verwandlung des Lichtes betreffenden heuristischen Gesichtspunkt. *Annalen der Physik*, 322(6):132–148, 1905.

[72] M. Krüger. *Attosecond Physics in strong-field photoemission from metal nanotips*. PhD thesis, Ludwig-Maximilians Universität, 2013.

[73] S. Mitra. *Strong-field photoemission dynamics from metallic nanostructures*. Master's thesis, Karlsruhe Institute of Technology, 2016.

[74] P. Agostini, F. Fabre, G. Mainfray, G. Petite, and N. K. Rahman. Free-free transitions following six-photon ionization of xenon atoms. *Physical Review Letters*, 42(17):1127, 1979.

[75] H. G. Muller, A. Tip, and M. J. Van der Wiel. Ponderomotive force and AC–Stark shift in multiphoton ionisation. *Journal of Physics B: Atomic and Molecular Physics*, 16(22):L679, 1983.

[76] V. C. Reed and K. Burnett. Role of resonances and quantum-mechanical interference in the generation of above-threshold-ionization spectra. *Physical Review A*, 43(11):6217, 1991.

[77] M. V. Ammosov, N. B. Delone, and V. P. Krainov. Tunnelling ionization of complex atoms and of atomic ions in an alternating electromagnetic field. *Journal of Experimental and Theoretical Physics*, 64(6):1191–1194, 1986.

[78] M. Schenk, M. Krüger, and P. Hommelhoff. Strong-field above-threshold photoemission from sharp metal tips. *Physical Review Letters*, 105(25):257601, 2010.

[79] B. Piglosiewicz, S. Schmidt, D. J. Park, J. Vogelsang, P. Groß, C. Manzoni, P. Farinello, G. Cerullo, and C. Lienau. Carrier-envelope phase effects on the strong-field photoemission of electrons from metallic nanostructures. *Nature Photonics*, 8(1):37–42, 2014.

[80] H. Niikura, F. Légaré, R. Hasbani, A. D. Bandrauk, M. Y. Ivanov, D. M. Villeneuve, and P. B. Corkum. Sub-laser-cycle electron pulses for probing molecular dynamics. *Nature*, 417(6892):917, 2002.

[81] S. Neppl. *Attosecond time-resolved photoemission from surfaces and interfaces*. PhD thesis, Technische Universität München, 2012.

[82] G. G. Paulus, W. Becker, W. Nicklich, and H. Walther. Rescattering effects in above-threshold ionization: a classical model. *Journal of Physics B: Atomic, Molecular and Optical Physics*, 27(21):L703, 1994.

[83] G. Paulus, W. Nicklich, H. Xu, P. Lambropoulos, and H. Walther. Plateau in above threshold ionization spectra. *Physical Review Letters*, 72(18):2851, 1994.

[84] P. B. Corkum. Plasma perspective on strong field multiphoton ionization. *Physical Review Letters*, 71(13):1994, 1993.

[85] M. Busuladžić, A. Gazibegović-Busuladžić, and D. Milošević. High-order above-threshold ionization in a laser field: Influence of the ionization potential on the high-energy cutoff. *Laser Physics*, 16(2):289–293, 2006.

[86] D. N. Fittinghoff, P. R. Bolton, B. Chang, and K. C. Kulander. Observation of non-sequential double ionization of helium with optical tunneling. *Physical Review Letters*, 69(18):2642, 1992.

[87] X. F. Li, A. L'Huillier, M. Ferray, L. A. Lompré, and G. Mainfray. Multiple-harmonic generation in rare gases at high laser intensity. *Physical Review A*, 39(11):5751, 1989.

[88] A. L'Huillier and P. Balcou. High-order harmonic generation in rare gases with a 1-ps 1053-nm laser. *Physical Review Letters*, 70(6):774, 1993.

[89] K. Miyazaki and H. Sakai. High-order harmonic generation in rare gases with intense subpicosecond dye laser pulses. *Journal of Physics B: Atomic, Molecular and Optical Physics*, 25(3):L83, 1992.

[90] J. K. Crane, R. W. Falcone, M. D. Perry, and S. Herman. High-field harmonic generation in helium. *Optics Letters*, 17(18):1256–1258, 1992.

[91] S. Ghimire, A. D. DiChiara, E. Sistrunk, P. Agostini, L. F. DiMauro, and D. A. Reis. Observation of high-order harmonic generation in a bulk crystal. *Nature Physics*, 7(2):138, 2011.

[92] P. M. Kraus, A. Rupenyan, and H. J. Wörner. High-harmonic spectroscopy of oriented OCS molecules: emission of even and odd harmonics. *Physical Review Letters*, 109(23):233903, 2012.

[93] M. F. Ciappina, J. Biegert, R. Quidant, and M. Lewenstein. High-order-harmonic generation from inhomogeneous fields. *Physical Review A*, 85(3):033828, 2012.

[94] P. Antoine, A. L'Huillier, and M. Lewenstein. Attosecond pulse trains using high–order harmonics. *Physical Review Letters*, 77(7):1234, 1996.

[95] M. Lewenstein, P. Balcou, M. Y. Ivanov, A. L'Huillier, and P. B. Corkum. Theory of high-harmonic generation by low-frequency laser fields. *Physical Review A*, 49(3):2117, 1994.

[96] J. L. Krause, K. J. Schafer, and K. C. Kulander. High-order harmonic generation from atoms and ions in the high intensity regime. *Physical Review Letters*, 68(24):3535, 1992.

[97] T. Ruchon, C. P. Hauri, K. Varju, E. Mansten, M. Swoboda, R. López-Martens, and A. L'Huillier. Macroscopic effects in attosecond pulse generation. *New Journal of Physics*, 10(2):025027, 2008.

[98] Y. Mairesse, A. De Bohan, L. Frasinski, H. Merdji, L. C. Dinu, P. Monchicourt, P. Breger, M. Kovačev, R. Taïeb, B. Carré, H. G. Muller, P. Agostini, and P. Salières. Attosecond synchronization of high-harmonic soft X-rays. *Science*, 302(5650):1540–1543, 2003.

[99] K. T. Kim, C. M. Kim, M.-G. Baik, G. Umesh, and C. H. Nam. Single sub-50-attosecond pulse generation from chirp-compensated harmonic radiation using material dispersion. *Physical Review A*, 69(5):051805, 2004.

[100] R. Lopez-Martens, K. Varjú, P. Johnsson, J. Mauritsson, Y. Mairesse, P. Salieres, M. B. Gaarde, K. J. Schafer, A. Persson, S. Svanberg, C.-G. Wahlström, and A. L'Huillier. Amplitude and phase control of attosecond light pulses. *Physical Review Letters*, 94(3):033001, 2005.

[101] P. Balcou, P. Salieres, A. L'Huillier, and M. Lewenstein. Generalized phase-matching conditions for high harmonics: The role of field-gradient forces. *Physical Review A*, 55(4):3204, 1997.

[102] M. B. Gaarde and K. J. Schafer. Theory of attosecond pulse generation. In *Attosecond Physics*, pages 11–31. Springer, 2013.

[103] L. E. Chipperfield, P. L. Knight, J. W. G. Tisch, and J. P. Marangos. Tracking individual electron trajectories in a high harmonic spectrum. *Optics Communications*, 264(2):494–501, 2006.

[104] M. B. Gaarde, J. L. Tate, and K. J. Schafer. Macroscopic aspects of attosecond pulse generation. *Journal of Physics B: Atomic, Molecular and Optical Physics*, 41(13):132001, 2008.

[105] G. Sansone, E. Benedetti, F. Calegari, C. Vozzi, L. Avaldi, R. Flammini, L. Poletto, P. Villoresi, C. Altucci, R. Velotta, S. Stagira, S. De Silvestri, and M. Nisoli. Isolated single-cycle attosecond pulses. *Science*, 314(5798):443–446, 2006.

[106] B. Shan, S. Ghimire, and Z. Chang. Generation of the attosecond extreme ultraviolet supercontinuum by a polarization gating. *Journal of Modern Optics*, 52(2-3):277–283, 2005.

[107] T. Sekikawa, A. Kosuge, T. Kanai, and S. Watanabe. Nonlinear optics in the extreme ultraviolet. *Nature*, 432(7017):605, 2004.

[108] Y. Oishi, M. Kaku, A. Suda, F. Kannari, and K. Midorikawa. Generation of extreme ultraviolet continuum radiation driven by a sub-10-fs two-color field. *Optics Express*, 14(16):7230–7237, 2006.

[109] H. Mashiko, S. Gilbertson, C. Li, S. D. Khan, M. M. Shakya, E. Moon, and Z. Chang. Double optical gating of high-order harmonic generation with carrier-envelope phase stabilized lasers. *Physical Review Letters*, 100(10):103906, 2008.

[110] X. Feng, S. Gilbertson, H. Mashiko, H. Wang, S. D. Khan, M. Chini, Y. Wu, K. Zhao, and Z. Chang. Generation of isolated attosecond pulses with 20 to 28 femtosecond lasers. *Physical Review Letters*, 103(18):183901, 2009.

[111] H.-C. Bandulet, D. Comtois, E. Bisson, A. Fleischer, H. Pépin, J.-C. Kieffer, P. B. Corkum, and D. M. Villeneuve. Gating attosecond pulse train generation using multicolor laser fields. *Physical Review A*, 81(1):013803, 2010.

[112] M. B. Gaarde and K. J. Schafer. Generating single attosecond pulses via spatial filtering. *Optics Letters*, 31(21):3188–3190, 2006.

[113] E. J. Takahashi, P. Lan, and K. Midorikawa. Generation of isolated attosecond pulses. In *Attosecond Physics*, pages 47–68. Springer, 2013.

[114] Y. C. Lim, T. Westerwalbesloh, A. Aschentrup, O. Wehmeyer, G. Haindl, U. Kleineberg, and U. Heinzmann. Fabrication and characterization of EUV multilayer mirrors optimized for small spectral reflection bandwidth. *Applied Physics A*, 72(1):121–124, 2001.

[115] L. Plaja, R. Torres, and A. Zaır. Attosecond physics. *Springer Series in Optical Sciences*, 177, 2013.

[116] F. Süßmann. *Attosecond dynamics of nano-localized fields probed by photoelectron spectroscopy*. PhD thesis, Ludwig-Maximilians Universität, 2013.

[117] Z. Chang. *Fundamentals of attosecond optics*. CRC Press, 2016.

[118] J. Gagnon, E. Goulielmakis, and V. S. Yakovlev. The accurate FROG characterization of attosecond pulses from streaking measurements. *Applied Physics B: Lasers and Optics*, 92(1):25–32, 2008.

[119] M. Schultze. *Attosecond real time observation of ionization and electron-electron interactions*. PhD thesis, Ludwig-Maximilians-Universität, 2008.

[120] E. Skopalová, D. Y. Lei, T. Witting, C. Arrell, F. Frank, Y. Sonnefraud, S. A. Maier, J. W. G. Tisch, and J. P. Marangos. Numerical simulation of attosecond nanoplasmonic streaking. *New Journal of Physics*, 13(8):083003, 2011.

[121] F. Süßmann and M. F. Kling. Attosecond nanoplasmonic streaking of localized fields near metal nanospheres. *Physical Review B*, 84(12):121406, 2011.

[122] A. G. Borisov, P. M. Echenique, and A. K. Kazansky. Attostreaking with metallic nano-objects. *New Journal of Physics*, 14(2):023036, 2012.

[123] F. Kelkensberg, A. F. Koenderink, and M. J. J. Vrakking. Attosecond streaking in a nano-plasmonic field. *New Journal of Physics*, 14(9):093034, 2012.

[124] J. S. Prell, L. J. Borja, D. M. Neumark, and S. R. Leone. Simulation of attosecond-resolved imaging of the plasmon electric field in metallic nanoparticles. *Annalen der Physik*, 525(1-2):151–161, 2013.

[125] M. Lupetti, J. Hengster, T. Uphues, and A. Scrinzi. Attosecond photoscopy of plasmonic excitations. *Physical Review Letters*, 113(11):113903, 2014.

[126] J. Schötz, B. Förg, M. Förster, W. A. Okell, M. I. Stockman, F. Krausz, P. Hommelhoff, and M. F. Kling. Reconstruction of nanoscale near fields by attosecond streaking. *IEEE Journal of Selected Topics in Quantum Electronics*, 23(3):1–11, 2017.

[127] W. Heisenberg. Über den anschaulichen Inhalt der quantentheoretischen Kinematik und Mechanik. *Zeitschrift für Physik*, 43(3):172–198, 1927.

[128] W. Pauli. *Die allgemeinen Prinzipien der Wellenmechanik*. Springer, 1933.

[129] A. Maquet, J. Caillat, and R. Taïeb. Attosecond delays in photoionization: time and quantum mechanics. *Journal of Physics B: Atomic, Molecular and Optical Physics*, 47(20):204004, 2014.

[130] E. P. Wigner. Lower limit for the energy derivative of the scattering phase shift. *Physical Review*, 98(1):145, 1955.

[131] S. Nagele, R. Pazourek, J. Feist, K. Doblhoff-Dier, C. Lemell, K. Tőkési, and J. Burgdörfer. Time-resolved photoemission by attosecond streaking: extraction of time information. *Journal of Physics B: Atomic, Molecular and Optical Physics*, 44(8):081001, 2011.

[132] L. Eisenbud. *The formal properties of nuclear collisions*. PhD thesis, Princeton University, 1948.

[133] F. T. Smith. Lifetime matrix in collision theory. *Physical Review*, 118(1):349, 1960.

[134] R. Pazourek, S. Nagele, and J. Burgdörfer. Attosecond chronoscopy of photoemission. *Reviews of Modern Physics*, 87(3):765, 2015.

[135] C.-H. Zhang and U. Thumm. Electron-ion interaction effects in attosecond time-resolved photoelectron spectra. *Physical Review A*, 82:043405, 2010.

[136] O. Smirnova, M. Spanner, and M. Y. Ivanov. Coulomb and polarization effects in laser-assisted XUV ionization. *Journal of Physics B: Atomic, Molecular and Optical Physics*, 39(13):S323, 2006.

[137] R. Pazourek, S. Nagele, and J. Burgdörfer. Time-resolved photoemission on the attosecond scale: opportunities and challenges. *Faraday discussions*, 163:353–376, 2013.

[138] J. M. Dahlström, T. Carette, and E. Lindroth. Diagrammatic approach to attosecond delays in photoionization. *Physical Review A*, 86:061402, 2012.

[139] A. K. Kazansky and P. M. Echenique. One-electron model for the electronic response of metal surfaces to subfemtosecond photoexcitation. *Physical Review Letters*, 102(17):177401, 2009.

[140] C. Lemell, B. Solleder, K. Tőkési, and J. Burgdörfer. Simulation of attosecond streaking of electrons emitted from a tungsten surface. *Physical Review A*, 79(6):062901, 2009.

[141] C.-H. Zhang and U. Thumm. Attosecond photoelectron spectroscopy of metal surfaces. *Physical Review Letters*, 102(12):123601, 2009.

[142] C.-H. Zhang and U. Thumm. Effect of wave-function localization on the time delay in photoemission from surfaces. *Physical Review A*, 84(6):065403, 2011.

[143] C.-H. Zhang and U. Thumm. Probing dielectric-response effects with attosecond time-resolved streaked photoelectron spectroscopy of metal surfaces. *Physical Review A*, 84(6):063403, 2011.

[144] C.-H. Zhang and U. Thumm. Streaking and Wigner time delays in photoemission from atoms and surfaces. *Physical Review A*, 84(3):033401, 2011.

[145] E. E. Krasovskii. Attosecond spectroscopy of solids: Streaking phase shift due to lattice scattering. *Physical Review B*, 84(19):195106, 2011.

[146] A. G. Borisov, D. Sánchez-Portal, A. K. Kazansky, and P. M. Echenique. Resonant and nonresonant processes in attosecond streaking from metals. *Physical Review B*, 87(12):121110, 2013.

[147] J. Schötz. *Attosecond experiments on plasmonic nanostructures.* Master's thesis, Ludwig-Maximilians-Universität, 2014.

[148] K. Wintersperger. *Characterisation of Surface Plasmon Polaritons on gold nanotips by non-linear photoemission.* Master's thesis, Ludwig-Maximilians-Universität, 2015.

[149] M. Krüger, M. Schenk, M. Förster, and P. Hommelhoff. Attosecond physics in photoemission from a metal nanotip. *Journal of Physics B: Atomic, Molecular and Optical Physics*, 45(7):074006, 2012.

[150] M. Förster. *Investigation and control of strong-field photoemission from metal nanotips.* PhD thesis, Ludwig-Maximilians Universität, 2015.

[151] B. Förg, J. Schötz, F. Süßmann, M. Förster, M. Krüger, B. Ahn, W. A. Okell, K. Wintersperger, S. Zherebtsov, A. Guggenmos, V. Pervak, A. Kessel, S. A. Trushin, A. M. Azzeer, M. I. Stockman, D. Kim, F. Krausz, P. Hommelhoff, and M. F. Kling. Attosecond nanoscale near-field sampling. *Nature Communications*, 7, 2016.

[152] B. W. Mao, B. Ren, X. W. Cai, and L. H. Xiong. Electrochemical oscillatory behavior under a scanning electrochemical microscopic configuration. *Journal of Electroanalytical Chemistry*, 394(1):155–160, 1995.

[153] B. Ren, G. Picardi, and B. Pettinger. Preparation of gold tips suitable for tip-enhanced raman spectroscopy and light emission by electrochemical etching. *Review of Scientific Instruments*, 75(4):837–841, 2004.

[154] S. Narasiwodeyar, M. Dwyer, M. Liu, W. K. Park, and L. H. Greene. Two-step fabrication technique of gold tips for use in point-contact spectroscopy. *Review of Scientific Instruments*, 86(3):033903, 2015.

[155] M. Eisele, M. Krüger, M. Schenk, A. Ziegler, and P. Hommelhoff. Note: Production of sharp gold tips with high surface quality. *Review of Scientific Instruments*, 82(2):026101, 2011.

[156] M. Lopes, T. Toury, M. L. de La Chapelle, F. Bonaccorso, and P. G. Gucciardi. Fast and reliable fabrication of gold tips with sub-50 nm radius of curvature for tip-enhanced raman spectroscopy. *Review of Scientific Instruments*, 84(7):073702, 2013.

[157] A. Giugni, B. Torre, A. Toma, M. Francardi, M. Malerba, A. Alabastri, R. P. Zaccaria, M. I. Stockman, and E. Di Fabrizio. Hot-electron nanoscopy using adiabatic compression of surface plasmons. *Nature Nanotechnology*, 8(11):845–852, 2013.

[158] S. Berweger, J. M. Atkin, R. L. Olmon, and M. B. Raschke. Adiabatic tip-plasmon focusing for nano-raman spectroscopy. *The Journal of Physical Chemistry Letters*, 1(24):3427–3432, 2010.

[159] S. Berweger, J. M. Atkin, X. G. Xu, R. L. Olmon, and M. B. Raschke. Femtosecond nanofocusing with full optical waveform control. *Nano Letters*, 11(10):4309–4313, 2011.

[160] V. Kravtsov, J. M. Atkin, and M. B. Raschke. Group delay and dispersion in adiabatic plasmonic nanofocusing. *Optics Letters*, 38(8):1322–4, 2013.

[161] M. Garg, M. Zhan, T. T. Luu, H. Lakhotia, T. Klostermann, A. Guggenmos, and E. Goulielmakis. Multi-petahertz electronic metrology. *Nature*, 538(7625):359–363, 2016.

[162] A. Abbott. Saudi arabia opens top-notch laser lab. *Nature*, 518(7539):281–282, 2015.

[163] A. Stingl, R. Szipöcs, M. Lenzner, C. Spielmann, and F. Krausz. Sub-10-fs mirror-dispersion-controlled Ti:sapphire laser. *Optics Letters*, 20(6):602–604, 1995.

[164] U. Morgner, F. X. Kärtner, S. H. Cho, Y. Chen, H. A. Haus, J. G. Fujimoto, E. P. Ippen, V. Scheuer, G. Angelow, and T. Tschudi. Sub-two-cycle pulses from a Kerr-lens mode-locked Ti:sapphire laser. *Optics Letters*, 24(6):411–413, 1999.

[165] R. Ell, U. Morgner, F. X. Kärtner, J. G. Fujimoto, E. P. Ippen, V. Scheuer, G. Angelow, T. Tschudi, M. J. Lederer, A. Boiko, and B. Luther-Davies. Generation of 5-fs pulses and octave-spanning spectra directly from a Ti:sapphire laser. *Optics Letters*, 26(6):373–375, 2001.

[166] L. Xu, T. W. Hänsch, C. Spielmann, A. Poppe, T. Brabec, and F. Krausz. Route to phase control of ultrashort light pulses. *Optics Letters*, 21(24):2008–2010, 1996.

[167] A. Poppe, R. Holzwarth, A. Apolonski, G. Tempea, C. Spielmann, T. W. Hänsch, and F. Krausz. Few-cycle optical waveform synthesis. *Applied Physics B*, 72(3):373–376, 2001.

[168] B. Borchert. *Pushing Frontiers in Carrier-Envelope Phase Stabilization of Ultrashort Laser Pulses*. PhD thesis, Humboldt-Universität zu Berlin, 2014.

[169] W. A. Okell. *Ultrafast measurements in condensed matter*. PhD thesis, Imperial College London, 2014.

[170] D. L. Ederer and D. H. Tomboulian. Photoionization cross cection of neon in the 80 to 600 Å region. *Physical Review*, 133(6A):A1525, 1964.

[171] P. A. Anderson. Work function of gold. *Physical Review*, 115(3):553–554, 1959.

[172] C. Sönnichsen, S. Geier, N. E. Hecker, G. Von Plessen, J. Feldmann, H. Ditlbacher, B. Lamprecht, J. Krenn, F. Aussenegg, V. Z. Chan, J. P. Spatz, and M. Möller. Spectroscopy of single metallic nanoparticles using total internal reflection microscopy. *Applied Physics Letters*, 77(19):2949–2951, 2000.

[173] A. A. Mikhailovsky, M. A. Petruska, K. Li, M. I. Stockman, and V. I. Klimov. Phase–sensitive spectroscopy of surface plasmons in individual metal nanostructures. *Physical Review B*, 69(8):085401, 2004.

[174] A. A. Mikhailovsky, M. A. Petruska, M. I. Stockman, and V. I. Klimov. Broadband near-field interference spectroscopy of metal nanoparticles using a femtosecond white-light continuum. *Optics Letters*, 28(18):1686–1688, 2003.

[175] J. Zhao, X. Zhang, C. R. Yonzon, A. J. Haes, and R. P. Van Duyne. Localized surface plasmon resonance biosensors. *Nanomedicine*, 1(2):219–228, 2006.

[176] J. Homola, S. S. Yee, and G. Gauglitz. Surface plasmon resonance sensors. *Sensors and Actuators B: Chemical*, 54(1):3–15, 1999.

[177] G. Raschke, S. Brogl, A. S. Susha, A. L. Rogach, T. A. Klar, J. Feldmann, B. Fieres, N. Petkov, T. Bein, A. Nichtl, and K. Kürzinger. Gold nanoshells improve single nanoparticle molecular sensors. *Nano Letters*, 4(10):1853–1857, 2004.

[178] D. Monzón-Hernández, J. Villatoro, D. Talavera, and D. Luna-Moreno. Optical-fiber surface-plasmon resonance sensor with multiple resonance peaks. *Applied Optics*, 43(6):1216–1220, 2004.

[179] P. Anger, P. Bharadwaj, and L. Novotny. Enhancement and quenching of single-molecule fluorescence. *Physical Review Letters*, 96(11):113002, 2006.

[180] E. Dulkeith, T. Niedereichholz, T. A. Klar, J. Feldmann, G. Von Plessen, D. I. Gittins, K. S. Mayya, and F. Caruso. Plasmon emission in photoexcited gold nanoparticles. *Physical Review B*, 70(20):205424, 2004.

[181] M. L. Brongersma, R. Zia, and J. A. Schuller. Plasmonics – the missing link between nanoelectronics and microphotonics. *Applied Physics A: Materials Science & Processing*, 89(2):221–223, 2007.

[182] R. Zia, J. A. Schuller, A. Chandran, and M. L. Brongersma. Plasmonics: the next chip-scale technology. *Materials Today*, 9(7):20–27, 2006.

[183] K. F. MacDonald, Z. L. Sámson, M. I. Stockman, and N. I. Zheludev. Ultrafast active plasmonics. *Nature Photonics*, 3(1):55–58, 2009.

[184] Y. Fang and M. Sun. Nanoplasmonic waveguides: towards applications in integrated nanophotonic circuits. *Light: Science & Applications*, 4(6):e294, 2015.

[185] E. N. Economou. Surface plasmons in thin films. *Physical Review*, 182(2):539, 1969.

[186] B. Lamprecht, J. R. Krenn, G. Schider, H. Ditlbacher, M. Salerno, N. Felidj, A. Leitner, F. R. Aussenegg, and J. C. Weeber. Surface plasmon propagation in microscale metal stripes. *Applied Physics Letters*, 79(1):51–53, 2001.

[187] J. A. Dionne, L. A. Sweatlock, H. A. Atwater, and A. Polman. Planar metal plasmon waveguides: frequency-dependent dispersion, propagation, localization, and loss beyond the free electron model. *Physical Review B*, 72:075405, 2005.

[188] R. Charbonneau, P. Berini, E. Berolo, and E. Lisicka-Shrzek. Experimental observation of plasmon–polariton waves supported by a thin metal film of finite width. *Optics Letters*, 25(11):844–846, 2000.

[189] P. Berini. Plasmon-polariton waves guided by thin lossy metal films of finite width: Bound modes of symmetric structures. *Physical Review B*, 61(15):10484, 2000.

[190] J. Chen, G. A. Smolyakov, S. R. J. Brueck, and K. J. Malloy. Surface plasmon modes of finite, planar, metal-insulator-metal plasmonic waveguides. *Optics Express*, 16(19):14902–14909, 2008.

[191] P. Neutens, P. Van Dorpe, I. De Vlaminck, L. Lagae, and G. Borghs. Electrical detection of confined gap plasmons in metal-insulator-metal waveguides. *Nature Photonics*, 3(5):283, 2009.

[192] S. A. Maier, P. G. Kik, H. A. Atwater, S. Meltzer, E. Harel, B. E. Koel, and A. A. G. Requicha. Local detection of electromagnetic energy transport below the diffraction limit in metal nanoparticle plasmon waveguides. *Nature Materials*, 2(4):229, 2003.

[193] M. Quinten, A. Leitner, J. R. Krenn, and F. R. Aussenegg. Electromagnetic energy transport via linear chains of silver nanoparticles. *Optics Letters*, 23(17):1331–1333, 1998.

[194] M. L. Brongersma, J. W. Hartman, and H. A. Atwater. Electromagnetic energy transfer and switching in nanoparticle chain arrays below the diffraction limit. *Physical Review B*, 62(24):R16356, 2000.

[195] S. A. Maier, P. G. Kik, and H. A. Atwater. Observation of coupled plasmon-polariton modes in au nanoparticle chain waveguides of different lengths: Estimation of waveguide loss. *Applied Physics Letters*, 81(9):1714–1716, 2002.

[196] J. R. Krenn, B. Lamprecht, H. Ditlbacher, G. Schider, M. Salerno, A. Leitner, and F. R. Aussenegg. Non–diffraction-limited light transport by gold nanowires. *Europhysics Letters*, 60(5):663, 2002.

[197] B. Wild, L. Cao, Y. Sun, B. P. Khanal, E. R. Zubarev, S. K. Gray, N. F. Scherer, and M. Pelton. Propagation lengths and group velocities of plasmons in chemically synthesized gold and silver nanowires. *ACS Nano*, 6(1):472–482, 2012.

[198] H. Ditlbacher, A. Hohenau, D. Wagner, U. Kreibig, M. Rogers, F. Hofer, F. R. Aussenegg, and J. R. Krenn. Silver nanowires as surface plasmon resonators. *Physical Review Letters*, 95(25):257403, 2005.

[199] A. W. Sanders, D. A. Routenberg, B. J. Wiley, Y. Xia, E. R. Dufresne, and M. A. Reed. Observation of plasmon propagation, redirection, and fan-out in silver nanowires. *Nano Letters*, 6(8):1822–1826, 2006.

[200] M. Wulf, A. de Hoogh, N. Rotenberg, and L. Kuipers. Ultrafast plasmonics on gold nanowires: confinement, dispersion, and pulse propagation. *ACS Photonics*, 1(11):1173–1180, 2014.

[201] M. Müller, V. Kravtsov, A. Paarmann, M. B. Raschke, and R. Ernstorfer. Nanofocused plasmon-driven sub-10 fs electron point source. *ACS Photonics*, 3(4):611–619, 2016.

[202] Y. Gong, A. G. Joly, D. Hu, P. Z. El-Khoury, and W. P. Hess. Ultrafast imaging of surface plasmons propagating on a gold surface. *Nano Letters*, 15(5):3472–3478, 2015.

[203] A. J. Babadjanyan, N. L. Margaryan, and K. V. Nerkararyan. Superfocusing of surface polaritons in the conical structure. *Journal of Applied Physics*, 87(8):3785–3788, 2000.

[204] C. Rewitz, T. Keitzl, P. Tuchscherer, J.-S. Huang, P. Geisler, G. Razinskas, B. Hecht, and T. Brixner. Ultrafast plasmon propagation in nanowires characterized by far-field spectral interferometry. *Nano Letters*, 12(1):45–49, 2011.

[205] M. Uda, A. Nakamura, T. Yamamoto, and Y. Fujimoto. Work function of polycrystalline Ag, Au and Al. *Journal of Electron Spectroscopy and Related Phenomena*, 88–91:643–648, 1998.

[206] P. B. Johnson and R.-W. Christy. Optical constants of the noble metals. *Physical Review B*, 6(12):4370, 1972.

[207] S. Thomas, G. Wachter, C. Lemell, J. Burgdörfer, and P. Hommelhoff. Large optical field enhancement for nanotips with large opening angles. *New Journal of Physics*, 17(6):063010, 2015.

[208] J. Vogelsang, J. Robin, B. J. Nagy, P. Dombi, D. Rosenkranz, M. Schiek, P. Groß, and C. Lienau. Ultrafast electron emission from a sharp metal nanotaper driven by adiabatic nanofocusing of surface plasmons. *Nano Letters*, 15(7):4685–4691, 2015.

[209] S. Schmidt, B. Piglosiewicz, D. Sadiq, J. Shirdel, J. S. Lee, P. Vasa, N. Park, D.-S. Kim, and C. Lienau. Adiabatic nanofocusing on ultrasmooth single-crystalline gold tapers creates a 10-nm-sized light source with few-cycle time resolution. *ACS Nano*, 6(7):6040–6048, 2012.

[210] J.-M. Yi, D. Hou, H. Kollmann, V. Smirnov, Z. Pápa, P. Dombi, M. Silies, and C. Lienau. Probing coherent surface plasmon polariton propagation using ultrabroadband spectral interferometry. *ACS Photonics*, 4(2):347–354, 2017.

[211] W. C. Swope, H. C. Andersen, P. H. Berens, and K. R. Wilson. A computer simulation method for the calculation of equilibrium constants for the formation of physical clusters of molecules: Application to small water clusters. *The Journal of Chemical Physics*, 76(1):637–649, 1982.

[212] J. T. Van Wijngaarden, E. Verhagen, A. Polman, C. E. Ross, H. J. Lezec, and H. A. Atwater. Direct imaging of propagation and damping of near-resonance surface plasmon polaritons using cathodoluminescence spectroscopy. *Applied Physics Letters*, 88(22):221111, 2006.

[213] J. Lu, C. Petre, E. Yablonovitch, and J. Conway. Numerical optimization of a grating coupler for the efficient excitation of surface plasmons at an Ag-SiO_2 interface. *Journal of the Optical Society of America B*, 24(9):2268–2272, 2007.

[214] H. Ditlbacher, J. R. Krenn, A. Hohenau, A. Leitner, and F. R. Aussenegg. Efficiency of local light-plasmon coupling. *Applied Physics Letters*, 83(18):3665–3667, 2003.

[215] G. M. Hale and M. R. Querry. Optical constants of water in the 200 nm to 200 µm wavelength region. *Applied Optics*, 12(3):555–563, 1973.

[216] A. E. Vladár, M. T. Postek, and R. Vane. Active monitoring and control of electron-beam-induced contamination. In *Proceedings of SPIE*, volume 4344, pages 835–843, 2001.

[217] J. I. Larruquert, L. V. Rodríguez-de Marcos, J. A. Méndez, P. J. Martin, and A. Bendavid. High reflectance ta-C coatings in the extreme ultraviolet. *Optics Express*, 21(23):27537–27549, 2013.

[218] R. Ruppin. Effect of non-locality on nanofocusing of surface plasmon field intensity in a conical tip. *Physics Letters A*, 340(1):299–302, 2005.

[219] A. Wiener, A. I. Fernández-Domínguez, A. P. Horsfield, J. B. Pendry, and S. A. Maier. Nonlocal effects in the nanofocusing performance of plasmonic tips. *Nano Letters*, 12(6):3308–3314, 2012.

[220] D.-L. Hornauer. Light scattering experiments on silver films of different roughness using surface plasmon excitation. *Optics Communications*, 16(1):76–79, 1976.

[221] D. Hornauer, H. Kapitza, and H. Raether. The dispersion relation of surface plasmons on rough surfaces. *Journal of Physics D: Applied Physics*, 7(9):L100, 1974.

[222] W. A. Okell, T. Witting, D. Fabris, C. A. Arrell, J. Hengster, S. Ibrahimkutty, A. Seiler, M. Barthelmess, S. Stankov, D. Y. Lei, Y. Sonnefraud, M. Rahmani, T. Uphues, S. A. Maier, J. P. Marangos, and J. W. G. Tisch. Temporal broadening of attosecond photoelectron wavepackets from solid surfaces. *Optica*, 2(4):383–387, 2015.

[223] C. Chen, Z. Tao, A. Carr, T. Szilvási, M. Keller, M. Mavrikakis, H. C. Kapteyn, and M. M. Murnane. Direct time-domain observation of attosecond photoelectron lifetimes and attosecond electron dynamics in occupied bands in solids. In *International Conference on Ultrafast Phenomena*, pages UTh5A–1. Optical Society of America, 2016.

[224] M. Fieß, M. Schultze, E. Goulielmakis, B. Dennhardt, J. Gagnon, M. Hofstetter, R. Kienberger, and F. Krausz. Versatile apparatus for attosecond metrology and spectroscopy. *Review of Scientific Instruments*, 81(9):093103, 2010.

[225] E. Magerl, S. Neppl, A. L. Cavalieri, E. M. Bothschafter, M. Stanislawski, T. Uphues, M. Hofstetter, U. Kleineberg, J. V. Barth, D. Menzel, F. Krausz, R. Ernstorfer, R. Kienberger, and P. Feulner. A flexible apparatus for attosecond photoelectron spectroscopy of solids and surfaces. *Review of Scientific Instruments*, 82(6):063104, 2011.

[226] F. Frank, C. Arrell, T. Witting, W. A. Okell, J. McKenna, J. S. Robinson, C. A. Haworth, D. Austin, H. Teng, I. A. Walmsley, J. P. Marangos, and T. J. W. G. Invited review article: technology for attosecond science. *Review of Scientific Instruments*, 83(7):52, 2012.

[227] R. Locher, M. Lucchini, J. Herrmann, M. Sabbar, M. Weger, A. Ludwig, L. Castiglioni, M. Greif, M. Hengsberger, L. Gallmann, and U. Keller. Versatile attosecond beamline in a two-foci configuration for simultaneous time-resolved measurements. *Review of Scientific Instruments*, 85(1):013113, 2014.

[228] A. Polman and H. A. Atwater. Plasmonics: optics at the nanoscale. *Materials Today*, 8(1):56, 2005.

[229] V. V. Temnov, U. Woggon, J. Dintinger, E. Devaux, and T. W. Ebbesen. Surface plasmon interferometry: measuring group velocity of surface plasmons. *Optics Letters*, 32(10):1235–1237, 2007.

[230] C. Rewitz, T. Keitzl, P. Tuchscherer, S. Goetz, P. Geisler, G. Razinskas, B. Hecht, and T. Brixner. Spectral-interference microscopy for characterization of functional plasmonic elements. *Optics Express*, 20(13):14632–14647, 2012.

[231] Y. Gorodetski, T. Chervy, S. Wang, J. A. Hutchison, A. Drezet, C. Genet, and T. W. Ebbesen. Tracking surface plasmon pulses using ultrafast leakage imaging. *Optica*, 3(1):48–53, 2016.

[232] W. Wang, P. Vasa, R. Pomraenke, R. Vogelgesang, A. De Sio, E. Sommer, M. Maiuri, C. Manzoni, G. Cerullo, and C. Lienau. Interplay between strong coupling and radiative damping of excitons and surface plasmon polaritons in hybrid nanostructures. *ACS Nano*, 8(1):1056–1064, 2014.

[233] Y. Nishiyama, K. Imura, and H. Okamoto. Observation of plasmon wave packet motions via femtosecond time-resolved near-field imaging techniques. *Nano Letters*, 15(11):7657–7665, 2015.

[234] T. Hanke, J. Cesar, V. Knittel, A. Truügler, U. Hohenester, A. Leitenstorfer, and R. Bratschitsch. Tailoring spatiotemporal light confinement in single plasmonic nanoantennas. *Nano Letters*, 12(2):992–996, 2012.

[235] V. Knittel, M. P. Fischer, T. de Roo, S. Mecking, A. Leitenstorfer, and D. Brida. Nonlinear photoluminescence spectrum of single gold nanostructures. *ACS Nano*, 9(1):894–900, 2015.

[236] L. I. Chelaru and F.-J. M. zu Heringdorf. In situ monitoring of surface plasmons in single-crystalline Ag-nanowires. *Surface Science*, 601(18):4541–4545, 2007.

[237] G. Spektor, D. Kilbane, A. K. Mahro, B. Frank, S. Ristok, L. Gal, P. Kahl, D. Podbiel, S. Mathias, H. Giessen, F.-J. Meyer zu Heringdorf, O. M, and A. M. Revealing the subfemtosecond dynamics of orbital angular momentum in nanoplasmonic vortices. *Science*, 355(6330):1187–1191, 2017.

[238] C. Lemke, C. Schneider, T. Leißner, D. Bayer, J. W. Radke, A. Fischer, P. Melchior, A. B. Evlyukhin, B. N. Chichkov, C. Reinhardt, M. Bauer, and M. Aeschlimann. Spatiotemporal characterization of SPP pulse propagation in two-dimensional plasmonic focusing devices. *Nano Letters*, 13(3):1053–1058, 2013.

[239] A. Kubo, K. Onda, H. Petek, Z. Sun, Y. S. Jung, and H. K. Kim. Femtosecond imaging of surface plasmon dynamics in a nanostructured silver film. *Nano Letters*, 5(6):1123–1127, 2005.

[240] F.-J. M. zu Heringdorf, L. I. Chelaru, S. Möllenbeck, D. Thien, and M. Horn-von Hoegen. Femtosecond photoemission microscopy. *Surface Science*, 601(20):4700–4705, 2007.

[241] M. Krüger, M. Schenk, and P. Hommelhoff. Attosecond control of electrons emitted from a nanoscale metal tip. *Nature*, 475(7354):78–81, 2011.

[242] G. Herink, D. R. Solli, M. Gulde, and C. Ropers. Field-driven photoemission from nanostructures quenches the quiver motion. *Nature*, 483(7388):190–193, 2012.

[243] A. M. Summers, A. S. Ramm, G. Paneru, M. F. Kling, B. N. Flanders, and C. A. Trallero-Herrero. Optical damage threshold of Au nanowires in strong femtosecond laser fields. *Optics Express*, 22(4):4235–4246, 2014.

[244] B. C. Stuart, M. D. Feit, S. Herman, A. M. Rubenchik, B. W. Shore, and M. D. Perry. Optical ablation by high-power short-pulse lasers. *Journal of the Optical Society of America B*, 13(2):459–468, 1996.

[245] S. Nolte, C. Momma, H. Jacobs, A. Tünnermann, B. N. Chichkov, B. Wellegehausen, and H. Welling. Ablation of metals by ultrashort laser pulses. *Journal of the Optical Society of America B*, 14(10):2716–2722, 1997.

[246] S. Link, C. Burda, B. Nikoobakht, and M. A. El-Sayed. Laser-induced shape changes of colloidal gold nanorods using femtosecond and nanosecond laser pulses. *The Journal of Physical Chemistry B*, 104(26):6152–6163, 2000.

[247] A. Plech, V. Kotaidis, M. Lorenc, and J. Boneberg. Femtosecond laser near-field ablation from gold nanoparticles. *Nature Physics*, 2(1):44–47, 2006.

[248] I. Lindau, P. Pianetta, K. Y. Yu, and W. E. Spicer. Photoemission of gold in the energy range 30-300 eV using synchrotron radiation. *Physical Review B*, 13(2):492, 1976.

[249] D. A. Shirley. High-resolution X-ray photoemission spectrum of the valence bands of gold. *Physical Review B*, 5(12):4709, 1972.

[250] S. Tougaard and B. Jørgensen. Inelastic background intensities in XPS spectra. *Surface Science*, 143(2-3):482–494, 1984.

[251] S. Tougaard. Quantitative analysis of the inelastic background in surface electron spectroscopy. *Surface and Interface Analysis*, 11(9):453–472, 1988.

[252] J. Végh. The Shirley background revised. *Journal of Electron Spectroscopy and Related Phenomena*, 151(3):159–164, 2006.

[253] C. R. Brundle and D. W. Turner. High resolution molecular photoelectron spectroscopy. II. Water and deuterium oxide. *Proceedings of the Royal Society of London A: Mathematical, Physical and Engineering Sciences*, 307(1488):27–36, 1968.

[254] V. H. Dibeler, J. A. Walker, and H. M. Rosenstock. Mass spectrometric study of photoionization. V. Water and ammonia. *Journal of Research of the National Bureau of Standards, Section A*, 70:459–463, 1966.

[255] D. C. Frost and C. A. McDowell. Excited states of the molecular ions of hydrogen fluoride, hydrogen iodide, water, hydrogen sulphide, and ammonia. *Canadian Journal of Chemistry*, 36(1):39–47, 1958.

[256] V. Čermák. Penning ionization electron spectroscopy. I. Determination of ionization potentials of polyatomic molecules. *Collection of Czechoslovak Chemical Communications*, 33(9):2739–2764, 1968.

[257] G. Bieri, F. Burger, E. Heilbronner, and J. P. Maier. Valence ionization energies of hydrocarbons. *Helvetica Chimica Acta*, 60(7):2213–2233, 1977.

[258] G. Mie. Beiträge zur Optik trüber Medien, speziell kolloidaler Metallösungen. *Annalen der Physik*, 330(3):377–445, 1908.

[259] E. D. Palik. *Handbook of optical constants of solids*. Academic press, 1998.

[260] F. Süßmann and M. F. Kling. Attosecond nanoplasmonic streaking of localized fields near metal nanospheres. *Physical Review B*, 84(12):121406, 2011.

[261] S. Zherebtsov, T. Fennel, J. Plenge, E. Antonsson, I. Znakovskaya, A. Wirth, O. Herrwerth, F. Süßmann, C. Peltz, I. Ahmad, S. A. Trushin, V. Pervak, S. Karsch, M. J. J. Vrakking, B. Langer, C. Graf, M. I. Stockman, F. Krausz, E. Rühl, and M. F. Kling. Controlled near-field enhanced electron acceleration from dielectric nanospheres with intense few-cycle laser fields. *Nature Physics*, 7(8):656–662, 2011.

[262] M. Gerl. *Time-resolved investigation of photoelectron dynamics by attosecond streaking spectroscopy on solids*. Master's thesis, Technische Universität München, 2013.

[263] S. Zherebtsov, A. Wirth, T. Uphues, I. Znakovskaya, O. Herrwerth, J. Gagnon, M. Korbman, V. S. Yakovlev, M. J. J. Vrakking, M. Drescher, and M. F. Kling. Attosecond imaging of XUV-induced atomic photoemission and Auger decay in strong laser fields. *Journal of Physics B: Atomic, Molecular and Optical Physics*, 44(10):105601, 2011.

[264] Y. Zhao, X. Liu, D. Y. Lei, and Y. Chai. Effects of surface roughness of Ag thin films on surface-enhanced raman spectroscopy of graphene: spatial nonlocality and physisorption strain. *Nanoscale*, 6(3):1311–1317, 2014.

[265] A. S. Kheifets and I. A. Ivanov. Delay in atomic photoionization. *Physical Review Letters*, 105(23):233002, 2010.

[266] K. Klünder, J. Dahlström, M. Gisselbrecht, T. Fordell, M. Swoboda, D. Guénot, P. Johnsson, J. Caillat, J. Mauritsson, A. Maquet, R. Taïb, and A. L'Huillier. Probing single-photon ionization on the attosecond time scale. *Physical Review Letters*, 106(14):143002, 2011.

[267] L. R. Moore, M. A. Lysaght, J. S. Parker, H. W. Van Der Hart, and K. T. Taylor. Time delay between photoemission from the 2p and 2s subshells of neon. *Physical Review A*, 84(6):061404, 2011.

[268] R. Locher, L. Castiglioni, M. Lucchini, M. Greif, L. Gallmann, J. Osterwalder, M. Hengsberger, and U. Keller. Energy-dependent photoemission delays from noble metal surfaces by attosecond interferometry. *Optica*, 2(5):405–410, 2015.

[269] J. Feist, O. Zatsarinny, S. Nagele, R. Pazourek, J. Burgdörfer, X. Guan, K. Bartschat, and B. I. Schneider. Time delays for attosecond streaking in photoionization of neon. *Physical Review A*, 89(3):033417, 2014.

[270] D. Hoff, M. Krüger, L. Maisenbacher, A. M. Sayler, G. G. Paulus, and P. Hommelhoff. Tracing the phase of focused broadband laser pulses. *Nature Physics*, 13(10):947–951, 2017.

[271] D. Guénot, K. Klünder, C. L. Arnold, D. Kroon, J. M. Dahlström, M. Miranda, T. Fordell, M. Gisselbrecht, P. Johnsson, J. Mauritsson, E. Lindroth, A. Maquet, R. Taïeb, A. L'Huillier, and A. S. Kheifets. Photoemission-time-delay measurements and calculations close to the 3s ionization cross-section minimum in Ar. *Physical Review A*, 85(5):053424, 2012.

[272] C. Palatchi, J. M. Dahlström, A. S. Kheifets, I. A. Ivanov, D. M. Canaday, P. Agostini, and L. F. DiMauro. Atomic delay in helium, neon, argon and krypton. *Journal of Physics B: Atomic, Molecular and Optical Physics*, 47(24):245003, 2014.

[273] G. Sansone, F. Kelkensberg, F. Morales, J. F. Perez-Torres, F. Martin, and M. J. J. Vrakking. Attosecond time-resolved electron dynamics in the hydrogen molecule. *IEEE Journal of Selected Topics in Quantum Electronics*, 18(1):520–530, 2012.

[274] P. Hockett, E. Frumker, D. M. Villeneuve, and P. B. Corkum. Time delay in molecular photoionization. *Journal of Physics B: Atomic, Molecular and Optical Physics*, 49(9):095602, 2016.

[275] D. Baykusheva and H. J. Wörner. Theory of attosecond delays in molecular photoionization. *The Journal of Chemical Physics*, 146(12):124306, 2017.

[276] A. J. Verhoef, A. Mitrofanov, M. Krikunova, N. M. Kabachnik, M. Drescher, and A. Baltuska. Measurement of attosecond photo-ionization delay in xenon. In *Lasers and Electro-Optics Europe, Conference on International Quantum Electronics Conference*, pages 1–1. IEEE, 2013.

[277] Z. Tao, C. Chen, T. Szilvási, M. Keller, M. Mavrikakis, H. Kapteyn, and M. Murnane. Direct time-domain observation of attosecond final-state lifetimes in photoemission from solids. *Science*, 353(6294):62–67, 2016.

[278] F. C. Faknoux and M. B. Amar. Inner and outer shell ionization for atomic iodine: calculation of cross-sections and angular distribution parameters. *Journal of electron spectroscopy and related phenomena*, 41(1):67–87, 1986.

[279] J. Tremblay, M. Larzilliere, F. Combet-Farnoux, and P. Morin. Photoelectron spectroscopy of atomic iodine produced by laser photodissociation. *Physical Review A*, 38(7):3804, 1988.

[280] G. C. Baldwin and G. S. Klaiber. Photo-fission in heavy elements. *Physical Review*, 71(1):3, 1947.

[281] M. Goldhaber and E. Teller. On nuclear dipole vibrations. *Physical Review*, 74(9):1046, 1948.

[282] F. Herman and S. Skillman. *Atomic structure calculations*. Materials science and technology. Prentice-Hall, 1963.

[283] A. R. P. Rau and U. Fano. Atomic potential wells and the periodic table. *Physical Review*, 167(1):7, 1968.

[284] F. C. Farnoux. Giant resonances in heavy elements: Open-shell effects, multiplet structure and spin-orbit interaction. In *Giant resonances in atoms, molecules, and solids*, pages 153–170. Springer, 1987.

[285] F. Keller and H. Lefebvre-Brion. Shape resonances in photoionization of diatomic molecules: An example in the d inner shell ionization of the hydrogen halides. *Zeitschrift für Physik D Atoms, Molecules and Clusters*, 4(1):15–23, 1986.

[286] H. P. Kelly and Z. Altun. Atomic many body theory of giant resonances. In *Giant resonances in atoms, molecules, and solids*, pages 71–89. Springer, 1987.

[287] G. Wendin. Giant resonances as a probe of collective excitations in atoms and solids. In *Giant resonances in atoms, molecules, and solids*, pages 171–211. Springer, 1987.

[288] J. Connerade. Controlled collapse and the profiles of 'giant resonances'. In *Giant resonances in atoms, molecules, and solids*, pages 3–23. Springer, 1987.

[289] J. B. West, P. R. Woodruff, K. Codling, and R. G. Houlgate. The 4d, 5s and 5p partial photoionization cross sections of xenon above the 4d threshold. *Journal of Physics B: Atomic and Molecular Physics*, 9(3):407, 1976.

[290] H. W. Schweinberger. *A Laser Source for the Generation of Intense Attosecond Pulses and its First Application*. PhD thesis, Ludwig-Maximilians-Universität, 2014.

[291] P. Hohenberg and W. Kohn. Inhomogeneous electron gas. *Physical Review*, 136(3B):B864, 1964.

[292] W. Kohn and L. J. Sham. Self-consistent equations including exchange and correlation effects. *Physical Review*, 140(4A):A1133, 1965.

[293] E. Runge and E. K. U. Gross. Density-functional theory for time-dependent systems. *Physical Review Letters*, 52(12):997, 1984.

[294] F. J. Comes, U. Nielsen, and W. H. E. Schwarz. Inner electron excitation of iodine in the gaseous and solid phase. *The Journal of Chemical Physics*, 58(6):2230–2237, 1973.

[295] D. W. Lindle, P. Kobrin, C. M. Truesdale, T. A. Ferrett, P. A. Heimann, H. G. Kerkhoff, U. Becker, and D. A. Shirley. Inner-shell photoemission from the iodine atom in CH_3I. *Physical Review A*, 30(1):239, 1984.

[296] L. Nahon, A. Svensson, and P. Morin. Experimental study of the 4d ionization continuum in atomic iodine by photoelectron and photoion spectroscopy. *Physical Review A*, 43(5):2328, 1991.

[297] I. Novak, J. Benson, and A. Potts. UV angle-resolved photoelectron spectra of mixed methylene dihalides using synchrotron radiation. *Chemical Physics*, 107(1):129–138, 1986.

[298] H. Kjeldsen, P. Andersen, F. Folkmann, H. Knudsen, B. Kristensen, J. B. West, and T. Andersen. Absolute photoionization cross sections of I^+ and I^{2+} in the 4d ionization region. *Physical Review A*, 62(2):020702, 2000.

[299] M. Y. Amusia, N. A. Cherepkov, L. V. Chernysheva, and S. T. Manson. Photoionization of atomic iodine and its ions. *Physical Review A*, 61(2):020701, 2000.

[300] M. Magrakvelidze and H. Chakraborty. Attosecond time delays in the valence photoionization of xenon and iodine at energies degenerate with core emissions. *Journal of Physics: Conference Series*, 875(3):022015, 2017.

[301] T. Zimmermann, L. Ortmann, C. Hofmann, J.-M. Rost, and A. S. Landsman. Classical Wigner propagation for attosecond streaking. *to be published*, 2017.

[302] E. J. Heller. Wigner phase space method: Analysis for semiclassical applications. *The Journal of Chemical Physics*, 65(4):1289–1298, 1976.

[303] W. H. Miller. The semiclassical initial value representation: A potentially practical way for adding quantum effects to classical molecular dynamics simulations. *The Journal of Physical Chemistry A*, 105(13):2942–2955, 2001.

[304] K. Kimura, S. Katsumata, Y. Achiba, H. Matsumoto, and S. Nagakura. Photoelectron spectra and orbital structures of higher alkyl chlorides, bromides, and iodides. *Bulletin of the Chemical Society of Japan*, 46(2):373–380, 1973.

[305] S. Aksela, H. Aksela, and T. Thomas. $M_{4,5}N_{4,5}X$ Auger electron spectra of iodine and xenon. Many-body effects. *Physical Review A*, 19(2):721, 1979.

[306] J. M. Dahlström, D. Guénot, K. Klünder, M. Gisselbrecht, J. Mauritsson, A. L'Huillier, A. Maquet, and R. Taïeb. Theory of attosecond delays in laser-assisted photoionization. *Chemical Physics*, 414:53–64, 2013.

[307] T. Clark, M. Hennemann, J. S. Murray, and P. Politzer. Halogen bonding: the σ-hole. *Journal of Molecular Modeling*, 13(2):291–296, 2007.

[308] P. Politzer, J. S. Murray, and T. Clark. Halogen bonding: an electrostatically-driven highly directional noncovalent interaction. *Physical Chemistry Chemical Physics*, 12(28):7748–7757, 2010.

[309] M. R. Scholfield, C. M. V. Zanden, M. Carter, and P. S. Ho. Halogen bonding (X-bonding): A biological perspective. *Protein Science*, 22(2):139–152, 2013.

[310] R. Wilcken, M. O. Zimmermann, A. Lange, A. C. Joerger, and F. M. Boeckler. Principles and applications of halogen bonding in medicinal chemistry and chemical biology. *Journal of Medicinal Chemistry*, 56(4):1363–1388, 2013.

[311] S. Sirimulla, J. B. Bailey, R. Vegesna, and M. Narayan. Halogen interactions in protein–ligand complexes: implications of halogen bonding for rational drug design. *Journal of Chemical Information and Modeling*, 53(11):2781–2791, 2013.

[312] F. Kniep, S. H. Jungbauer, Q. Zhang, S. M. Walter, S. Schindler, I. Schnapperelle, E. Herdtweck, and S. M. Huber. Organocatalysis by neutral multidentate halogen-bond donors. *Angewandte Chemie International Edition*, 52(27):7028–7032, 2013.

[313] H. Sakai, C. P. Safvan, J. J. Larsen, K. M. Hilligsøe, K. Hald, and H. Stapelfeldt. Controlling the alignment of neutral molecules by a strong laser field. *The Journal of Chemical Physics*, 110(21):10235–10238, 1999.